Broadband Coherent X-ray Diffractive Imaging and Developments towards a High Repetition Rate mid-IR Driven keV High Harmonic Source

Julius Huijts

NNT : 2019SACLS154

Broadband Coherent X-ray Diffractive Imaging and Developments towards a High Repetition Rate mid-IR driven keV High Harmonic Source

Thèse de doctorat de l'Université Paris-Saclay
préparée à l'Université Paris-Sud

École doctorale n°572 : Ondes et Matière (EDOM)
Spécialité de doctorat: Lasers, Molécules, Rayonnement Atmosphérique

Thèse présentée et soutenue à Gif-sur-Yvette, le 20 juin 2019, par

Julius Huijts

Composition du Jury :

Jérôme Faure Directeur de Recherche, ENSTA-ParisTech (Laboratoire d'Optique Appliquée)	Président
Caterina Vozzi Professeure, Politecnico di Milano (Institute for Photonics and Nanotechnologies)	Rapporteur
Christian Spielmann Professeur, Friedrich Schiller Universität Jena (LS Quantenelektronik)	Rapporteur
Stefan Witte Professeur assistant, Vrije Universiteit Amsterdam (EUV Generation and Imaging ARCNL)	Examinateur
Marc Hanna Chargé de Recherche, Institut d'Optique (Laboratoire Charles Fabry)	Examinateur
Hamed Merdji Directeur de Recherche, Commissariat à l'énergie atomique (LIDYL)	Directeur de thèse

Thèse de doctorat

Abstract

Julius HUIJTS

Broadband coherent X-ray diffractive imaging and developments towards a high repetition rate mid-IR driven keV high harmonic source

Soft X-ray sources based on high harmonic generation are up to now unique tools to probe dynamics in matter on femto- to attosecond timescales. High harmonic generation is a process in which an intense femtosecond laser pulse is frequency upconverted to the UV and soft X-ray region through a highly nonlinear interaction in a gas. Thanks to their excellent spatial coherence, they can be used for lensless imaging, which has already led to impressive results. To use these sources to the fullest of their potential, a number of challenges needs to be met: their brightness and maximum photon energy need to be increased and the lensless imaging techniques need to be modified to cope with the large bandwidth of these sources. For the latter, a novel approach is presented, in which broadband diffraction patterns are rendered monochromatic through a numerical treatment based solely on the spectrum and the assumption of a spatially non-dispersive sample. This approach is validated through a broadband lensless imaging experiment on a supercontinuum source in the visible, in which a binary sample was properly reconstructed through phase retrieval for a source bandwidth of 11 %. Through simulations, the numerical monochromatization method is shown to work for hard X-rays as well, with a simplified semiconductor lithography mask as sample. A potential application of lithography mask inspection on an inverse Compton scattering source is proposed, although the conclusion of the analysis is that the current source lacks brightness for the proposal to be realistic. Simulations with sufficient brightness show that the sample is well reconstructed up to 10 % spectral bandwidth at 8 keV. In an extension of these simulations, an extended lithography mask sample is reconstructed through ptychography, showing that the monochromatization method can be applied in combination with different lensless imaging techniques. Through two synchrotron experiments an experimental validation with hard X-rays was attempted, of which the resulting diffraction patterns after numerical monochromatization look promising. The phase retrieval process and data treatment however require additional efforts. An important part of the thesis is dedicated to the extension of high harmonic sources to higher photon energies and increased brightness. This exploratory work is performed towards the realization of a compact high harmonic source on a high repetition rate mid-IR OPCPA laser system, which sustains higher average power and longer wavelengths compared to ubiquitous Ti:Sapphire laser systems. High repetition rates are desirable for numerous applications involving the study of rare events. The use of mid-IR wavelengths (3.1 μm in this work) promises extension of the generated photon energies to the kilo-electronvolt level, allowing shorter pulses, covering more X-ray absorption edges and improving the attainable spatial resolution for imaging. However, high repetition rates come with low pulse energies, which constrains the generation process. The generation with longer wavelengths is challenging due to the significantly lower dipole response of the gas. To cope with these challenges a number of experimental configurations is explored theoretically and experimentally: free-focusing

in a gas-jet; free-focusing in a gas cell; soliton compression and high harmonic generation combined in a photonic crystal fiber; separated soliton compression in a photonic crystal fiber and high harmonic generation in a gas cell. First results on soliton compression down to 26 fs and lower harmonics up to the seventh order are presented. Together, these results represent a step towards ultrafast lensless X-ray imaging on table-top sources and towards an extension of the capabilities of these sources.

Résumé

Julius HUIJTS

Imagerie par diffraction cohérente des rayons X en large bande spectrale et développements vers une source harmonique au keV pompée par laser moyen-infrarouge à haut taux de répétition

Des sources des rayons XUV et rayons X mous sont des outils extraordinaires pour sonder la dynamique à l'échelle nanométrique avec une résolution femto- voire attoseconde. La génération d'harmoniques d'ordre élevé (GH) est une des sources majeures dans ce domaine d'application. La GH est un processus dans lequel une impulsion laser infrarouge femtoseconde est convertie, de manière cohérente, en fréquences élevées dans le domaine XUV par interaction hautement non-linéaire, typiquement dans un gaz. La GH possède une excellente cohérence spatiale qui a permis de réaliser des démonstrations impressionnantes en imagerie sans lentille. Pour accroître le potentiel de ces sources, deux défis sont à relever : leur brillance et énergie de photon maximum doivent augmenter et les techniques d'imagerie sans lentille doivent être modifiées pour être compatibles avec l'importante largeur spectrale des impulsions attosecondes émises par ces sources. Cette thèse présente une nouvelle approche dans laquelle des figures de diffraction large bande, i.e. potentiellement attosecondes, sont rendues monochromatiques numériquement. Cette méthode est basée uniquement sur la mesure du spectre de la source et la supposition d'un échantillon spatialement non-dispersif. Cette approche a été validée tout d'abord dans le visible, à partir d'un supercontinuum. L'échantillon binaire est reconstruit par recouvrement de phase pour une largeur spectrale de 11 %, là où les algorithmes usuels divergent. Les simulations numériques montrent aussi que la méthode de monochromatisation peut être appliquée au domaine des rayons X, avec comme exemple un masque semi-conducteur utilisé en lithographie EUV. Bien que la brillance cohérente de la source actuelle (qui progresse) reste insuffisante, une application sur l'inspection de masques sur source Compton est proposée. Dans une extension de ces simulations un masque de lithographie étendu est reconstruit par ptychographie, démontrant la versatilité à d'autres techniques d'imagerie sans lentille. Nous avons également entamé une série d'expériences dans le domaine des X-durs sur source synchrotron. Les figures de diffraction après monochromatisation numérique semblent prometteuses mais l'analyse des données demandent des efforts supplémentaires. Une partie importante de cette thèse est dédiée à l'extension des sources harmoniques à des brillances et énergies de photon plus élevées. Ce travail exploratoire permettrait la réalisation d'une source harmonique compacte pompée par un laser OPCPA dans le moyen infrarouge à très fort taux de répétition. Les longueurs d'onde moyen infrarouge (3.1 μm dans ce travail de thèse) sont favorables à l'extension des énergies des photons au keV et aux impulsions attosecondes. Le but est de pouvoir couvrir les seuils d'absorption X et d'améliorer la résolution spatio-temporelle. Cependant, deux facteurs rendent cette démonstration difficile: le nombre de photons par impulsion de la source OPCPA est très limité et la réponse du dipôle harmonique à grande longueur est extrêmement faible. Pour relever ces défis plusieurs configurations expérimentales sont explorées : génération dans un

jet de gaz ; génération dans une cellule de gaz ; compression solitonique et la génération d'harmoniques combinées dans une fibre à cristal photonique ; compression solitonique dans une fibre à cristal photonique et génération d'harmoniques dans une cellule de gaz. Les premiers résultats expérimentaux sur la compression solitonique jusqu'à 26 femtosecondes et des harmoniques basses jusqu'à l'ordre sept sont présentés. En résumé, ces résultats représentent une avancée vers l'imagerie nanométrique attoseconde sur des nouvelles sources 'table-top' et vers une extension des capacités de ces sources.

Acknowledgements

First and foremost I would like to express my gratitude to towards Hamed, for placing his trust in me and for giving me the freedom to satisfy my curiosity during the past years. I have also appreciated the way you look after the atmosphere and social cohesion in the group. I wish to thank Jens for giving me the opportunity to work on such a challenging project, for including me in his group and of course for the Benasque group retreats. I am also grateful to Dr. Vozzi, Dr. Spielmann, Dr. Faure, Dr. Witte and Dr. Hanna for carefully going through my manuscript and for their recognition and positive attitude at my defense. Working in two labs gave me the opportunity to meet many extraordinary people, some of whom I would like to mention here.

Julien, Dominik and Rémy, my fellow thésards from the first day: thank you for sometimes helping me disentangle French bureaucracy, for your French lessons (here I should thank Ariane as well) and for the daily dose of silly jokes. The same goes for Joana, Rana, Quentin, Shatha, Ramona, Maria, Viktoria, Sven, Léa and Xu. A special thanks goes to David, Ahmed and Sara, for their invaluable support during the beamtimes (both scientifically and emotionally). Willem, thank you for always being there when needed, your support was crucial not just to me, but to all our thésards. Finally a thanks to les mecs de la mécanique: Michel, DD et surtout Sylvain. Merci pour tout ce que vous m'avez appris et pour les beaux dispositifs qu'on a développés ensemble.

The boys and girl at ICFO: Barbara, Nicola, Ugaitz, Themis, Tobias, Stefano, Kasra, Maurizio and the others, thanks for the jokes, the parties, the many jarras we shared. You really adopted me into the group. Xara, Vindhiya, Marcos, Sarah, thanks for the candies, the trips and the raki. Xavi, Sema y Juan, gracias por vuestro apoyo, y siempre con una broma, sois los mecánicos más rapidos del mundo. Un agradecimiento especial para Carlos y Vittoria, sin los quales no funcionaría ninguno de los laboratorios de ICFO. Mehdi and Josep, thank you for turning a house into a home.

From Uppsala, I would like to thank Felipe for hosting me and giving me access to the cluster, Benedikt for showing me around and answering my stupid questions and Max for his patience and for accommodating me after an exhausting beamtime in Oxford. From Erlangen, I wish to thank Francesco, Mallika, Robert and Alex for making my stay both pleasant and successful. Un remerciement pour Florent, Gaëtan et Phillip pour la bonne ambiance au LCF et pareil pour Kadda et Andrea à Nanoscopium.

I will finish on a more personal note. Merci les potes, Michele et Xristiana, pour toutes nos petites aventures depuis le début de la thèse. Bedankt aan de Treinboys voor de steun en broodnodige afleiding. Pap, mam, Melch en Crispijn, dank jullie wel voor jullie onaflaatbare steun en rotsvast vertrouwen. Anna, grazie per un sostegno di cui non sapevo neanche di aver bisogno.

Author Contributions

Scientific projects typically require a large degree of collaboration, and this PhD project was no exception. This section specifies the work done by the author himself.

Broadband CDI

I came up with the idea of using a matrix inversion to numerically monochromatize broadband diffraction patterns, and implemented it in Python code, using sparsity and parallelisation. Presented with the problem of inverted noise, I looked up, implemented and tested several regularization methods, out of which I chose CGLS. The phase retrieval code existed in our group as a Matlab code - I transposed it to Python and extended it depending on the data at hand.

Experiment in the visible

I devised the experiment and built the setup (apart from the source). I collected and analyzed the data (helpful discussions with H. Merdji, W. Boutu, F. Guichard and M. Natile are acknowledged).

X-ray simulations

I came up with simulating the application to lithography mask inspection, as well as the application to ICS sources. I contacted the research team of ThomX and plotted the result of their Monte Carlo simulation for my analysis. It was my idea (in discussion with B. Daurer) to use *Condor* to simulate broadband hard X-ray diffraction and I ran the simulations on the cluster (with some initial trouble-shooting by M. Hantke). I initiated the collaboration with S. Fernandez on the ptychographic reconstructions.

Synchrotron beamtimes

I devised the experiments in discussion with H. Merdji and D. Gauthier. I wrote both beamtime applications and was the responsible for both experiments. The data collection at Diamond was together with W. Boutu, D. Gauthier and A. Maghraoui, at Soleil with H. Merdji, D. Gauthier, S. Fernandez, M. Kholodtsova and K. Medjoubi. For both beamtimes I analysed the data (except for the ptychographic reconstruction).

HHG calculations, setup design and experiments

The schemes of the experiments were devised through numerous discussions with J. Biegert. I performed the analysis for the phase-matching pressures and ADK ionization rates. I designed and installed the high pressure gas system and performed the vacuum calculations. The gas-jet based chamber was designed by X. Menino as per my directions, for the gas-cell chamber I did the design and the engineering drawings. I also designed the chamber for the integrated soliton compression and HHG setup, made the engineering drawings and oversaw its fabrication. It was my idea to use a taper to improve coupling between the two PCFs, which I then made together with V. Finazzi. I also made the gas slots and I prepared and cleaved the PCFs. I installed and aligned the different experimental setups and did the data acquisition and analysis (with occasional but crucial support from U. Elu, T. Steinle or H.-W. Sun).

Contents

List of Figures

List of Tables

List of Abbreviations

ARR	**A**nti **R**esonant **R**eflection
ATI	**A**bove **T**hreshold **I**onization
CCD	**C**harge **C**oupled **D**evice
CDI	**C**oherent **D**iffractive **I**maging
CEP	**C**arrier **E**nvelope **P**hase
CGLS	**C**onjugate **G**radient **L**east **S**quares
DFG	**D**ifference **F**requency **G**eneration
FEL	**F**ree **E**lectron **L**aser
FIB	**F**ocused **I**on **B**eam
FROG	**F**requency **R**esolved **O**ptical **G**ating
FWHM	**F**ull **W**idth at **H**alf **M**aximum
HCF	**H**ollow **C**ore **F**iber
HDR	**H**igh **D**ynamic **R**ange
HHG	**H**igh (order) **H**armonic **G**eneration
ICFO	**I**nstitut de **C**iències **FO**tòniques
ICS	**I**nverse **C**ompton **S**cattering
MCP	**M**icro **C**hannel **P**late
MPL	**M**ax **P**lanck institute for the science of **L**ight
NA	**N**umerical **A**perture
NSDI	**N**on **S**equential **D**ouble **I**onization
OPA	**O**ptical **P**arametric **A**mplifier/-fication
OPCPA	**O**ptical **P**arametric **C**hirped **P**ulse **A**mplifier
PCF	**P**hotonic **C**rystal **F**iber
PRTF	**P**hase **R**etrieval **T**ransfer **F**unction
PSF	**P**oint **S**pread **F**unction
QPM	**Q**uasi **P**hase **M**atching
SEM	**S**canning **E**lectron **M**icroscopy
SHG	**S**econd **H**armonic **G**eneration
SPM	**S**elf **P**hase **M**odulation

Chapter 1

Introduction

1.1 Nature's time and length scales

The time and length scales we are used to in our daily lives are determined by how we perceive the world around us: through our own eyes. We generally have a hard time imagining objects that are smaller than what our eyes can see, say, smaller than the width of a human hair. Anything that is faster than 'the blink of an eye' is beyond timescales we are naturally familiar with.

Our eyes offer us only a minute window into the realm of time and length scales that nature has to offer. (Figure 1.1 shows a few examples of processes at short time scales, and objects at small length scales.) For centuries mankind has fought to extend this window by building devices that push the limits of what we can see, in time and space.

1.2 Imaging fast processes

A famous example of an early attempt to image a process too fast for our eyes, is that of Eadward Muybridge in 1878 [5]. The question was whether a galloping horse is ever completely aloft (i.e. none of his feet touching the ground). He set up an ingenious array of cameras, each with its own shutter that was triggered electrically as the horse passed. The shutters were engineered by Muybridge himself and were open for only about a microsecond. The resulting first high-speed video ever made clearly showed the horse with all four feet off the ground (figure 1.2).

Shutter times on sub-microsecond time scales have proven difficult to realize mechanically. To image faster processes, the stroboscopic approach was developed, pioneered by Fox Talbot in 1851 and further developed mainly by Harold Edgerton. The principle behind stroboscopic imaging is that the object is only illuminated during a very brief period of time, by a short light flash. It is thus the length of the light pulse that determines the temporal resolution, not the shutter time. The famous image of a bullet piercing an apple (figure 1.1) was obtained by Edgerton through this technique using a microsecond flash in 1964. Continually improving his technique, he would later use it to make pictures of nuclear explosions with flashes as short as 10 picoseconds.

A limit of the stroboscopic technique is that it cannot be used in a camera array to make a high-speed movie like Muybridge. To make a movie using the stroboscopic technique one has to resort to a pump-probe experiment.

1.2.1 Stroboscopic movies: Pump-probe experiments

In a pump-probe experiment two light pulses are used: one to initiate the dynamics, and one to take a snapshot of it. By repeating the experiment for different delays between pump and probe, the frames of the movie of the dynamics are acquired. George Porter

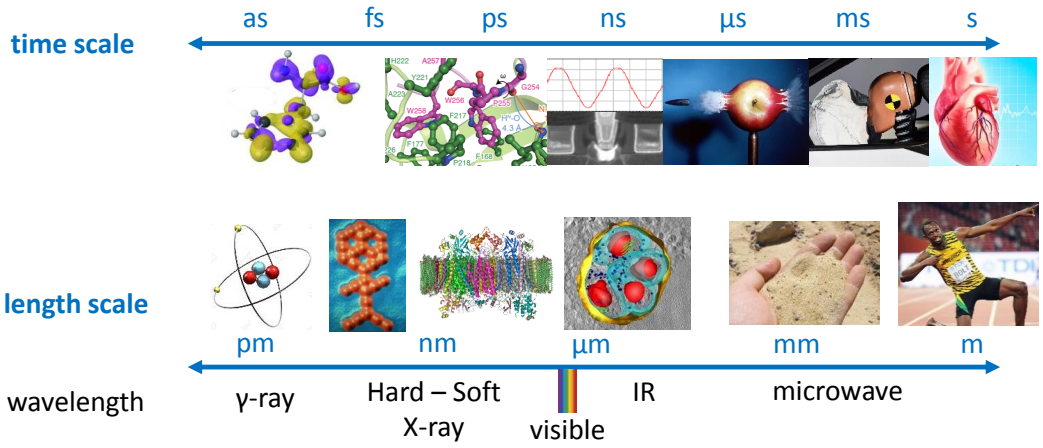

FIGURE 1.1: Examples of Nature's time scales, from right to left: A heart beating on a second time scale; An airbag deploying in milliseconds; A bullet imaged with a microsecond stroboscopic flash [1]; A field-effect transistor switching on a nano- to picosecond time scale; Chemical reactions taking place on a pico- to femtosecond timescale; Charge migration taking place on an attosecond time scale [2].
Examples of Nature's length scales, from right to left: Usain Bolt, fastest man on earth, 1.95 m tall; Sand grains are about a millimeter in size; Soft X-ray microscopy image of parasites in a human cell [3], a few µm large; A membrane protein complex resolved through X-ray crystallography, tens of nanometers in size; 'Molecular man' consisting of 28 CO molecules, 4 nanometer tall, built and imaged through scanning tunneling microscopy [4]; A helium atom has a theoretical diameter of 62 picometer. On the bottom of the figure, the regions of the electromagnetic spectrum corresponding to wavelengths at the depicted length scale.

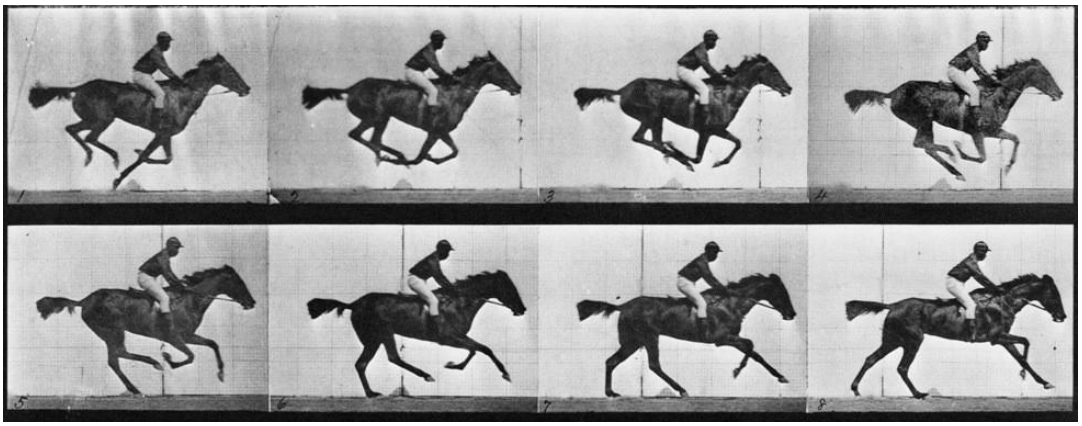

FIGURE 1.2: In 1878 Eadward Muybridge made the first high-speed video using an array of triggered cameras. Several frames show the horse with all four feet off the ground, confirming Muybridge's hypothesis.

can be seen as the founding father of pump-probe experiments: he studied the formation of radicals by an intense flash of light through spectroscopy with a second flash of light [6], later rewarded with the Nobel Prize in Chemistry in 1967 [7]. The advent of the laser [8] and specifically of the femtosecond laser [9] allowed pump-probe experiments on chemical reactions, giving birth to the field of femtochemistry, pioneered by Ahmed Zewail [10] and awarded the Nobel Prize in Chemistry in 1999 [11].

As each frame of the movie in a pump-probe experiment comes from a different instantiation of the dynamics under study, the technique is reserved to repeatable processes. Some schemes are however proposed to record unique events [12, 13].

1.3 Imaging with X-rays

In space, the smallest feature that can be distinguished is determined by the wavelength of the light with which the object is illuminated [14]. Thus to see smaller objects, a shorter wavelength should be used. As can be seen from figure 1.1, X-rays have wavelengths on the order of a nanometer and below, and can be used to image objects down to nanometer resolution. Another benefit of X-rays is their penetrating power: because of their low interaction with matter they can be used to look 'inside' objects, as was already realized by the discoverer of X-rays, Wilhelm Röntgen (Nobel Prize Physics 1901 [15]). X-ray technology has known a tremendous development and is now indispensable to modern science, which has a variety of sources available.

1.3.1 X-ray sources: large scale versus table-top

The most ubiquitous X-ray source (present in any hospital) is an X-ray tube: a relatively small and inexpensive device in which electrons from a cathode impinge on an anode, emitting X-rays in the form of *bremsstrahlung*. For many scientific applications, a brighter source is needed: these have been developed mainly in the form of synchrotrons and, more recently, free electron lasers. These are large scale facilities with multiple beamlines, serving scientific users that need to apply for beamtime in order to do their experiment. More recently, so-called 'table-top' sources have emerged. These are sources that are based on an intense femtosecond laser system, where the X-rays are generated through different physical phenomena. One of these phenomena is High Harmonic Generation (HHG). These HHG sources can produce extremely short pulses of soft X-rays, down to tens of attoseconds, to follow matter on the timescales of electronic motion. This has led to impressive recent developments, such as following the charge migration in a biological molecule on an attosecond timescale (figure 1.1 and [2]). To use these sources efficiently for imaging a number of hurdles need to be taken.

1.3.2 Attosecond lensless X-ray imaging

X-ray lenses are difficult to make. Techniques have been developed to perform imaging without the use of lenses, so-called lensless imaging. Lensless imaging on HHG sources thus in principle represents a way to image objects on attosecond timescales with nanometric resolution. Exciting applications are for example in two revolutions: all-optical magnetic switching and petahertz electronics. All-optical magnetic switching entails the switching of magnetic nanoscale domains by ultrafast laser pulses which could increase speed and energy efficiency of data storage by orders of magnitude [16, 17]. Research on petahertz electronics aims at increasing the switching speed of transistors by orders of magnitude. Today's transistors switch on a nano- to picosecond timescale (figure 1.1), but significant research efforts are currently being made to explore devices that might deliver

switching times on the order of a femtosecond [18, 19]. These dynamics have recently been measured on an attosecond timescale [20–22], but without spatial information. For both research fields, the combination of sub-femtosecond temporal resolution and nanometric spatial resolution provides crucial insight into the electron dynamics, thus favoring the next revolutions in data storage, electronics and computation.

At the moment this is impossible due to a limited source brightness, photon energy and the broadband nature of the sources being incompatible with the methods used for lensless imaging. This thesis work presents a number of small steps in solving these challenges.

1.4 Thesis Outline

This manuscripts consists of two parts. The first part is on broadband coherent diffractive imaging. In Chapter 2 the reader is introduced to CDI and the state of the art of its extension to broadband sources. Then the developed method of broadband CDI through numerical monochromatization is presented. The method is validated on a broadband source in the visible, as shown in Chapter 3. A validation using X-rays is explored through simulations in Chapter 4 and through experiments on synchrotron sources in Chapter 5.

The second part of the manuscript deals with extending the photon energy and increasing the repetition rate of high harmonic sources. The background and state of the art is presented in Chapter 6, together with calculations for an experimental realization on a cutting-edge laser source. Chapter 7 contains the results of several experimental attempts, together with details on the employed setups.

A large part of the necessary theoretical background for this thesis is explained in appendices at the end of the manuscript, with references to relevant textbooks.

Bibliography

[1] Harold Edgerton. Bullet through Apple, 1964. Smithsonian American Art Museum.

[2] F. Calegari, D. Ayuso, A. Trabattoni, L. Belshaw, S. De Camillis, S. Anumula, F. Frassetto, L. Poletto, A. Palacios, P. Decleva, J. B. Greenwood, F. Martín, and M. Nisoli. Ultrafast electron dynamics in phenylalanine initiated by attosecond pulses. *Science*, 346(6207):336–339, October 2014. ISSN 0036-8075, 1095-9203. doi: 10.1126/science.1254061.

[3] Maria Harkiolaki, Michele C. Darrow, Matthew C. Spink, Ewelina Kosior, Kyle Dent, and Elizabeth Duke. Cryo-soft X-ray tomography: Using soft X-rays to explore the ultrastructure of whole cells. *Emerging Topics in Life Sciences*, page ETLS20170086, March 2018. ISSN 2397-8554, 2397-8562. doi: 10.1042/ETLS20170086.

[4] P. Zeppenfeld, C. P. Lutz, and D. M. Eigler. Manipulating atoms and molecules with a scanning tunneling microscope. *Ultramicroscopy*, 42-44:128–133, July 1992. ISSN 0304-3991. doi: 10.1016/0304-3991(92)90256-J.

[5] STANFORD magazine. The Man Who Stopped Time. https://stanfordmag.org/contents/the-man-who-stopped-time.

[6] George Porter and Norrish Ronald George Wreyford. Flash photolysis and spectroscopy. A new method for the study of free radical reactions. *Proceedings of the Royal Society of London. Series A. Mathematical and Physical Sciences*, 200(1061): 284–300, January 1950. doi: 10.1098/rspa.1950.0018.

[7] George Porter. Nobel Lecture - Flash Photolysis and some of its applications, 1967.

[8] T. H. Maiman. Stimulated Optical Radiation in Ruby. *Nature*, 187(4736):493, August 1960. ISSN 1476-4687. doi: 10.1038/187493a0.

[9] R. L. Fork, B. I. Greene, and C. V. Shank. Generation of optical pulses shorter than 0.1 psec by colliding pulse mode locking. *Applied Physics Letters*, 38(9):671–672, May 1981. ISSN 0003-6951. doi: 10.1063/1.92500.

[10] Marcos Dantus, Mark J. Rosker, and Ahmed H. Zewail. Real-time femtosecond probing of "transition states" in chemical reactions. *The Journal of Chemical Physics*, 87 (4):2395–2397, August 1987. ISSN 0021-9606. doi: 10.1063/1.453122.

[11] Ahmed H. Zewail. Nobel Lecture - Femtochemistry - Atomic-scale dynamics of the chemical bond using ultrafast lasers, 1999.

[12] K. Nakagawa, A. Iwasaki, Y. Oishi, R. Horisaki, A. Tsukamoto, A. Nakamura, K. Hirosawa, H. Liao, T. Ushida, K. Goda, F. Kannari, and I. Sakuma. Sequentially timed all-optical mapping photography (STAMP). *Nature Photonics*, 8(9):695–700, September 2014. ISSN 1749-4893. doi: 10.1038/nphoton.2014.163.

[13] Andreas Ehn, Joakim Bood, Zheming Li, Edouard Berrocal, Marcus Aldén, and Elias Kristensson. FRAME: Femtosecond videography for atomic and molecular dynamics. *Light: Science & Applications*, 6(9):e17045, September 2017. ISSN 2047-7538. doi: 10.1038/lsa.2017.45.

[14] E. Abbe. Beiträge zur Theorie des Mikroskops und der mikroskopischen Wahrnehmung. *Archiv für mikroskopische Anatomie*, 9(1):413–418, December 1873. ISSN 0176-7364. doi: 10.1007/BF02956173.

[15] Wilhelm Roentgen. The Nobel Prize in Physics 1901. https://www.nobelprize.org/prizes/physics/1901/rontgen/facts/.

[16] Jean-Yves Bigot and Mircea Vomir. Ultrafast magnetization dynamics of nanostructures. *Annalen der Physik*, 525(1-2):2–30, 2013. ISSN 1521-3889. doi: 10.1002/andp.201200199.

[17] Alexey V. Kimel and Mo Li. Writing magnetic memory with ultrashort light pulses. *Nature Reviews Materials*, 4(3):189, March 2019. ISSN 2058-8437. doi: 10.1038/s41578-019-0086-3.

[18] Ferenc Krausz and Mark I. Stockman. Attosecond metrology: From electron capture to future signal processing. *Nature Photonics*, 8(3):205–213, March 2014. ISSN 1749-4893. doi: 10.1038/nphoton.2014.28.

[19] Takuya Higuchi, Christian Heide, Konrad Ullmann, Heiko B. Weber, and Peter Hommelhoff. Light-field-driven currents in graphene. *Nature*, 550(7675):224–228, October 2017. ISSN 1476-4687. doi: 10.1038/nature23900.

[20] Hiroki Mashiko, Yuta Chisuga, Ikufumi Katayama, Katsuya Oguri, Hiroyuki Masuda, Jun Takeda, and Hideki Gotoh. Multi-petahertz electron interference in Cr:Al 2 O 3 solid-state material. *Nature Communications*, 9(1):1468, April 2018. ISSN 2041-1723. doi: 10.1038/s41467-018-03885-7.

[21] F. Langer, C. P. Schmid, S. Schlauderer, M. Gmitra, J. Fabian, P. Nagler, C. Schüller, T. Korn, P. G. Hawkins, J. T. Steiner, U. Huttner, S. W. Koch, M. Kira, and R. Huber. Lightwave valleytronics in a monolayer of tungsten diselenide. *Nature*, 557(7703): 76, May 2018. ISSN 1476-4687. doi: 10.1038/s41586-018-0013-6.

[22] F. Schlaepfer, M. Lucchini, S. A. Sato, M. Volkov, L. Kasmi, N. Hartmann, A. Rubio, L. Gallmann, and U. Keller. Attosecond optical-field-enhanced carrier injection into the GaAs conduction band. *Nature Physics*, 14:560–564, March 2018. ISSN 1745-2473. doi: 10.1038/s41567-018-0069-0.

Chapter 2

Broadband coherent diffractive imaging

2.1 Introduction

An accurate description of electromagnetic radiation requires information in both amplitude and phase. The Fourier transform (see Appendix A) is an extremely powerful tool in describing the propagation of electromagnetic radiation, giving rise to the vast field of Fourier optics [1–3]. The concept of lensless imaging relies heavily on Fourier optics. In lensless imaging the goal is to create an image of an object, not by employing lenses (as is the case for a micro- or telescope) but by detecting diffracted radiation in the far field and employing Fourier transform techniques to reconstruct the object. This is especially useful in applications where lenses are difficult to fabricate (as is the case for XUV and X-ray radiation). The experimental geometry of a general lensless imaging setup is simple: an electromagnetic wave interacts with an object, propagates, and is typically recorded in the far-field. Theoretically, an inverse Fourier transform would suffice to reconstruct the object from the recorded far field radiation. The central problem to lensless imaging is that typical detectors (photographic film, a CCD camera, our eyes) detect photons, not waves. We therefore have access only to the amplitude (squared) of the far field, not the phase, and do not have sufficient information to perform the inverse Fourier transform. To deal with this missing phase information, three main techniques of lensless imaging can be distinguished: holography, ptychography and phase retrieval.

Holography

In holography[1] the wave leaving the object is made to interfere with a known reference wave [4]. This reference wave can either be the source wave itself (in-line holography) or a wave emanating from a second (point-) source (off-axis holography). The phase information of the object wave is now imprinted in the far field diffraction pattern (called a hologram) and can be retrieved by using the same reference wave (either experimentally or numerically). Since its invention in 1948 the technique has been awarded the Nobel Prize in Physics in 1971 and has found widespread applications in optics [5], data storage and art. The main limitation of the technique is the required high quality of the reference beam, the main advantage is the deterministic retrieval of the phase.

[1] The word holography comes from the Greek words ὅλος (holos; “whole") and γραφή (graphē; “writing" or “drawing"). The technique was originally invented by Dennis Gabor in 1948 to improve the resolution of electron microscopes, which were limited by lens aberrations.

Ptychography

In ptychography[2] the incident beam (usually focused or apertured) is scanned over an extended sample, while the diffraction pattern at each probe position is recorded. The probe positions are made to overlap, such that there is a high degree of redundancy in the data allowing iterative algorithms to retrieve the phase (and more recently even the probe). Originally developed by the electron microscopy community half a decade ago [6, 7], the advent of third generation synchrotron sources has seen a plethora of impressive applications of X-ray ptychography in e.g. life and materials science (see [8] for a recent review). The main advantages of ptychography are its robustness (thanks to the redundancy in the data) and the ability to image extended samples. The main disadvantage is the fact that no (fast) dynamics can be imaged as the technique requires many exposures while scanning the probe position on the sample.

Phase retrieval

Finally, it is also possible to numerically retrieve the phase of a recorded diffraction pattern directly, without the need of a reference wave or scanning of the probe beam. An algorithm iterates between real and Fourier space, updating its guess of the phase. A constraint on the object (typically the fact that it is isolated in space) forces the algorithm to converge to the solution. This principle was developed by Gerchberg and Saxton in 1972 [9] and further optimized by Fienup [10] and Marchesini [11]. The experimental work was pushed mainly by David Sayre in the 80's and 90's [12–14] on synchrotron sources, with the first experimentally reconstructed object published in 1999 with his colleagues Jianwei Miao and Henry Chapman [15]. Since then, the field of CDI on synchrotron sources has grown into a mature field of its own, with unique applications such as Bragg CDI (phase retrieval of the patterns surrounding Bragg peaks of a crystal lattice sample, allowing to image imperfections and strain in the lattice). The advent of the Free Electron Laser (FEL) holds the promise of what is arguably the most exciting application of phase retrieval; single particle imaging, allowing structure determination of proteins that are impossible to grow into crystals (e.g. membrane proteins), even in a time-resolved manner. Compared to the other two techniques, the advantage of using phase retrieval is that in principle it can be used in single shot, so ultrafast dynamics can be recorded, while no reference beam is needed. The disadvantage is the constraint it places on the sample (such as it being isolated in space).

As all three techniques are lensless, the attainable resolution is not limited by optical aberrations but ideally only by the wavelength of the used radiation (Abbe limit[3]). In practice however, the diffracted signal drops drastically for large scattering angles, so the experimentally accessible numerical aperture is limited by noise, thus limiting the attainable resolution. Although technically all above techniques fall under the principle of coherent diffractive imaging (CDI), in practice the term CDI is used to indicate the latter (phase retrieval). Of these three techniques this thesis focuses on CDI through phase retrieval. However, the main principles are similar and the method of broadband imaging proposed in the remainder of this thesis could also be applied to holography and ptychography, thanks to its generality.

[2] πτυχο means "to fold", to indicate that the illuminating function and sample function "fold into each other" as they propagate and interfere. In fact, the seminal paper on ptychography [6] was written in German, where the term "folding" is used interchangeably with convolution.

[3] The Abbe limit on the minimum resolvable distance d using light with a wavelength λ and a numerical aperture NA is given by $d = \frac{\lambda}{2\mathrm{NA}} = \frac{\lambda}{2n\sin\theta}$

The main development of CDI has been performed by the (coherent) X-ray imaging community, which has traditionally used synchrotron and more recently FEL radiation for their experiments. In addition, in the past decade CDI has also found its way to high-harmonic sources [16–18], which are highly suitable to CDI thanks to their excellent spatial coherence. As mentioned in the Introduction of this thesis, HHG sources are unique in the sense that they can provide light pulses with durations on the attosecond time scale. Making use of these sources to track attosecond dynamics using CDI is however currently impossible. A pulse that is so short in the time domain, at photon energies currently attainable by HHG, inevitably has a large spectrum, where CDI (as well as holography and ptychography) assumes a monochromatic illumination. This chapter first describes the state of the art of monochromatic CDI, then explains the challenge and state of the art of broadband CDI. Next, the method for broadband CDI as proposed in this thesis (method of numerical monochromatization) is explained, thus setting the stage for the next chapters. For more information on Fourier transforms and (Fraunhofer) diffraction, see Appendices A and B.

2.2 Narrowband Coherent Diffractive Imaging

2.2.1 Principle and state of the art

Figure 2.1 shows the main principle of CDI through phase retrieval. A sample (typically isolated in space) is illuminated by a monochromatic, plane wave. The exiting wave-field is left to propagate to the far-field where the resulting diffraction pattern is recorded. As explained in Appendix B, the recorded far-field diffraction pattern is the amplitude squared of the Fourier transform of the wave-field as it exits the sample. To reconstruct the sample, the phase information needs to be retrieved. This phase is guessed by an iterative algorithm, which under suitable constraints converges to the correct phase, thus reconstructing an amplitude and phase representation of the sample (the next paragraph elaborates on phase retrieval algorithms). As explained in the previous section, the technique was developed on synchrotron sources, then adopted for applications on Free Electron Lasers. The famous first result of CDI on an FEL was obtained in 2006 by Chapman *et. al.* [19], in which an aperture in a membrane was imaged on the soft X-ray laser FLASH. Since then the field has developed enormously [20–24] with as recent examples the imaging of the Giant Mimivirus [25] or live cyanobacteria [26]. Although these results are still far from the promise of atomic structure determination, the transition from membrane test samples to actual biological samples is an impressive feat. On HHG sources the photon flux is many orders of magnitude lower, hence the typical membrane samples of Chapman's initial demonstration are still in use. An example of a recent result of a high-flux HHG source is of Tadesse *et. al.* [27], where a record high 13.6 nm resolution at 18 nm wavelength was reported. When acquiring for only 3 seconds (at a repetition rate of 30 kHz) 20 nm resolution was obtained. Although this is rather quick compared to other HHG sources, it is far from single shot, as opposed to e.g. [17].

2.2.2 Phase Retrieval Algorithms

The foundation for the most successful and widely applied phase retrieval algorithms was laid by Gerchberg and Saxton in 1972 [9]. Their principle was to start with a random guess for the phase, then iteratively transform between real and Fourier space applying constraints in each of the spaces. The typical constraints in use nowadays come from Fienup's adaptation [10]: the sample should be contained within a support (isolated) in

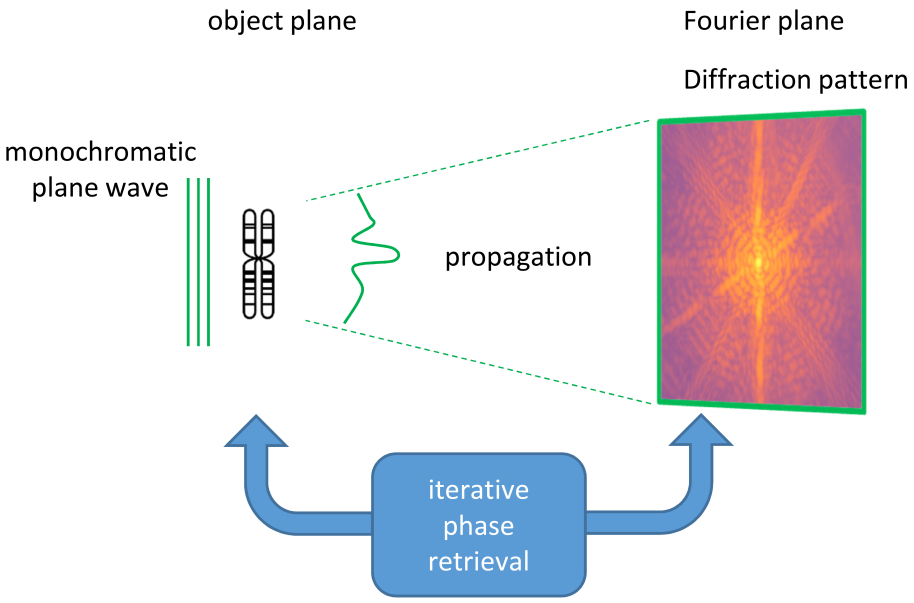

FIGURE 2.1: The principle of Coherent Diffractive Imaging (CDI) through phase retrieval. The sample is illuminated by a plane wave. The diffraction pattern is recorded in the far-field. An iterative algorithm repeatedly transforms between real and Fourier space, updating its guess of the phase. In real space, a typical constraint is that the sample is isolated (zero outside a support). In Fourier space, the constraint is the measured diffraction pattern. By retrieving the phase the sample is reconstructed.

real space and the pattern in Fourier space should correspond to the measured intensities of the diffraction pattern. At each iteration the guess of the phase is updated, and if the data is of sufficient quality the algorithm converges to the correct phase, thus reconstructing a complex image representation of sample[4]. The original algorithm, technically a steepest-descent gradient search method, monotonously decreased the error in every step and was thus dubbed the error-reduction algorithm (ER). Denoting $\mathbf{P_s}$ as the projection onto the support (application of real-space constraint) and $\mathbf{P_m}$ as the projection onto the measured modulus in Fourier space, one iteration of ER can be written as:

$$\rho^{(n+1)} = \mathbf{P_s}\mathbf{P_m}\rho^{(n)} \tag{2.1}$$

where $\rho^{(n+1)}$ is the updated estimate of the reconstructed sample. It is however prone to getting trapped in local minima[5]. As an alternative Fienup proposed the hybrid input-output algorithm (HIO)[10], which minimizes the error inside the support while simultaneously maximizing the error in the space perpendicular to the support. Although convergence is not guaranteed, the algorithm is robust against local minima. Finally Elser in 2003 proposed the more general difference map algorithm (DM) [28], of which HIO is a special case. A comparison of the different phase retrieval algorithms is given in [29]. Another important improvement is the concept of a dynamic support, which becomes tighter as the algorithm converges. This so-called "shrink-wrap" algorithm [11] speeds up convergence and helps to avoid the problem of twin-image formation [30]. In the work of this thesis, a difference map algorithm is used unless stated otherwise. Using the

[4]Technically the wave as it exits the sample is reconstructed. In the projection approximation this is equivalent to the sample density, see Appendix D.

[5]Although the real space constraint is a convex set, the Fourier space constraint is not, so local minima exist.

same operator notation, phase retrieval algorithm used in our group can be described as:

$$\rho^{(n+1)} = [\mathbf{I} - \mathbf{P_s} - \mathbf{P_m} + 2\mathbf{P_m}\mathbf{P_s}]\,\rho^{(n)}, \tag{2.2}$$

corresponding to DM with $(\gamma_s, \gamma_m, \beta) = (-1, 1, -1)$ in the expressions given in [28, 29].

2.2.3 Resolution and sampling requirements

An important factor for any imaging technique is the resolution. High spatial frequencies in the sample correspond to diffraction at large scattering angles, low spatial frequencies in the sample correspond to small scattering angles. More formally, if we denote q as the resolution in half-cycles per meter[6], for a scattering angle θ at wavelength λ it is given by:

$$q = 2\frac{\sin\theta}{\lambda}. \tag{2.3}$$

The pixel size of the reconstructed sample is determined by the largest angle θ_{max}, corresponding to the most outward pixel on the diffraction pattern, as the inverse of q:

$$\Delta_s = \frac{1}{q_{max}} = \frac{\lambda}{2\sin\theta_{max}}. \tag{2.4}$$

For example, if a diffraction pattern is 2 cm wide, and it is obtained at 1m distance from the sample, $\sin\theta_{max} \approx 10^{-2}$ and $\Delta_s \approx 50\lambda$. Note that the reconstructed pixel size Δ_s is not equal to the resolution, but it represents the minimum feature that can theoretically be resolved. If the signal on the diffraction pattern at θ_{max} is zero, or covered by noise, the information at spatial frequency q_{max} is lost and will not be present in the reconstructed sample. In practice, the resolution will also depend on how reliably the phase retrieval algorithm has retrieved the phase. Therefore the Phase Retrieval Transfer Function (PRTF) is often reported as a measure for the resolution, although technically it is a measure for the reliability of the phase retrieval process. It is given by [20]:

$$\mathrm{PRTF} = \frac{|\mathscr{F}\{\bar{\rho}\}|}{\sqrt{M}}, \tag{2.5}$$

being the ratio between the modulus of the retrieved diffraction pattern, averaged over many independent reconstructions, and the modulus of the measured diffraction pattern M. It should be close to 1 for low spatial frequencies and drop for higher q. A more empirical way of determining the resolution is through performing a line-out on a sharp edge of the sample.

[6] So the inverse resolution is equal to the Abbe criterion.

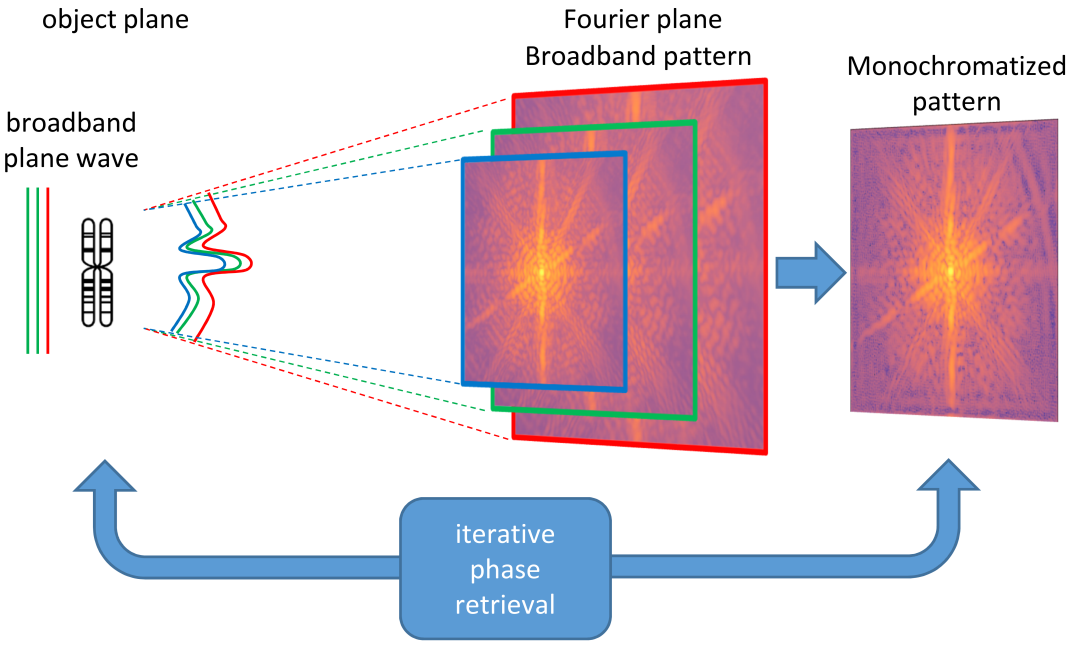

FIGURE 2.2: In broadband coherent diffractive imaging the broadband diffraction pattern is an incoherent sum of all patterns corresponding to the wavelengths of the source spectrum. The interference fringes appear "smeared out" and standard phase retrieval algorithms do not work. By adding a numerical step (depending only on the spectrum of the diffracted radiation) the broadband pattern is monochromatized and using a standard phase retrieval algorithm the sample is reconstructed.

Finally a remark on the sampling of the diffraction pattern: after the inverse Fourier transform, the number of pixels in sample space will be the same as the number of pixels in Fourier space. The sample pixel size is set by equation 2.4. For each sample pixel two values need to be reconstructed: the amplitude and phase of the wave leaving the sample. So, to reconstruct a sample in a support of size a, at least $2a/\Delta_s$ measurement points per dimension are needed in the diffraction pattern (this is a manifestation of the Nyquist-Shannon sampling theorem). Then, because of the presence of noise in any realistic measurement, it is better to oversample the diffraction pattern. For $2a/\Delta_s$ points the oversampling ratio is 1, typically a ratio of 2-3 (per dimension) is recommended. These considerations determine the geometry of an experiment. The wavelength and desired resolution determine the NA of the setup as described above, the sample size, oversampling ratio R_o and detector pixel size Δ_d determine the sample-detector distance z:

$$z = \frac{a\Delta_d}{\Delta_s NA} R_o. \tag{2.6}$$

2.3 Broadband Coherent Diffractive Imaging

2.3.1 Coherent Diffractive Imaging with attosecond resolution

As mentioned in the Introduction, attosecond sources are being developed to follow matter on the shortest timescales. The most successful examples at the moment are based

on absorption spectroscopy (e.g. [31, 32]) or ionization dynamics (e.g. [33]). It is currently impossible to do CDI with attosecond resolution on table-top sources. The two main challenges are:

Low photon flux

Compared to synchrotron and FEL sources, HHG sources suffer from low photon flux. A setup optimized for single shot imaging ([17]) managed to produce up to 10 μJ per shot. These were however no isolated attosecond pulses, but pulse trains on a femtosecond timescale. Setups that generate isolated attosecond pulses can be on the order of 10 nJ per shot [34] , corresponding to about 10^9 photons per shot in the XUV. In Chapman's original FEL experiment ([19]) they had 10^{12} photons per shot, which allowed single shot CDI. This suggests HHG sources need to gain 3 orders of magnitude in pulse energy in order to allow attosecond CDI. In the soft X-ray regime the HHG flux drops even further. Although it is not entirely fair to compare the 25 fs pulse of FLASH with an HHG pulse that is two orders of magnitude shorter at a similar photon energy, it does illustrate that for attosecond CDI the pulse energy, needs to be improved by orders of magnitude. One extremely high flux isolated attosecond pulse has been reported in [35] of 1 μJ per shot, showing that although it is very challenging, it is possible to attain the necessary number of photons in a single attosecond pulse.

CDI with broad spectra

The 10^9 photons per shot on a HHG source mentioned above are spread over a wide spectrum, from 30 to 100 eV, whereas the 10^{12} photons per shot of FLASH are quasi-monochromatic (0.2 nm at 32 nm). Cutting a similarly narrow band out of the HHG spectrum would reduce the number of photons by two orders of magnitude, even three or more taking the typical reflectivity of a multi-layer optic into account (e.g. [36]). So to preserve the photon flux, it is important to make use of the entire spectral bandwidth of the pulse. Secondly, cutting the spectrum means losing the attosecond nature of the pulses. It is thus important to develop a way to perform CDI using a broad spectrum.

If these two issues are solved, it will be possible to see ultrafast structural changes in materials, with nanometer-scale spatial resolution and sub-femtosecond temporal resolution, on a table-top setup. Examples of interesting samples are ultrafast switching of magnetic materials [37, 38] or phase transitions in nanoparticles [39, 40]. See Chapter 9 for more details. Attosecond CDI will probably remain a dream for years to come, because of above-mentioned challenges. The argument of using broadband CDI to preserve photon flux is however of immediate importance. Static imaging applications (such as verification of lithography steps in the semiconductor industry) on table-top sources can benefit immediately from a broadband CDI technique that can make use of the complete spectrum of these sources. Besides HHG sources, inverse-Compton Scattering sources (ICS) are another example of laser-based, table-top sources that can be used for CDI, typically at higher energies than HHG sources, and that also feature large spectra [41–43], as explored in Chapter 4.

2.3.2 Role of the coherence length

An important fundamental limit for broadband CDI is imposed by the temporal coherence of the source (see Appendix C). The temporal coherence of a realistic source is limited by random phase variations and by, more relevant to this thesis, the bandwidth of the radiation. The coherence length is derived from the coherence time, which is the maximum time delay at which a wave can interfere with itself. As shown in figure 2.3, even

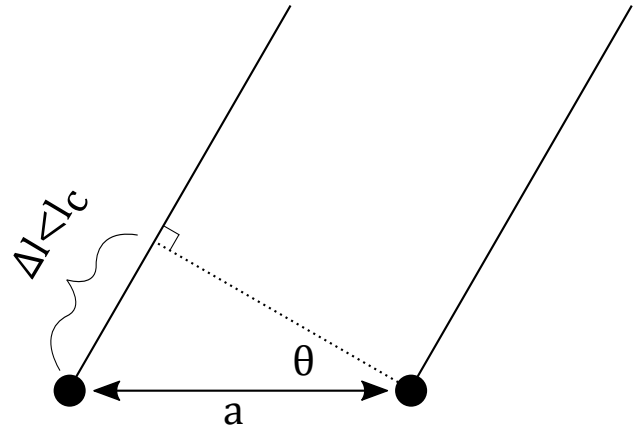

FIGURE 2.3: Interference from two points in a sample a distance is limited to a path length difference smaller than the coherence length. The finite coherence length of a broadband source thus poses a fundamental limit on the attainable resolution for a give sample size.

if a source is perfectly spatially coherent, two points in a sample cannot interfere if the difference in path length is larger than the coherence length l_c. If these two points are a distance a apart, the maximum diffraction angle is limited as $\sin\theta_{max} = l_c/a$, thus limiting the resolution to:

$$q_{max,l_c} = 2\frac{l_c}{\lambda a}. \tag{2.7}$$

For continuous broadband radiation, the coherence length can be estimated by (see Appendix C for a more rigorous treatment of the coherence length):

$$l_c = \frac{\lambda^2}{\Delta\lambda}. \tag{2.8}$$

For pulsed radiation, the coherence length roughly equals the Fourier limited pulse length. This places a more stringent limit on the coherence length (see appendix C). For a 1 fs, Fourier limited, Gaussian pulse this means a coherence length of 0.25 μm. Imaging a sample down to a 5λ resolution means that the sample can be no larger than $10l_c$ or 2.5 μm.

2.3.3 State of the art

Previous work on broadband CDI has mainly been performed by the (former) group at the Centre for Coherent X-ray Science of the University of Melbourne. The main principle of their work is an extension of Gerchberg-Saxton algorithm with a constraint on the spectrum to perform the spectral deconvolution in parallel to the phase retrieval [44–48]. Their test experiments on synchrotron sources show convergence up to 3% bandwidth. The work in this thesis performs the monochromatization as an independent step, before starting the phase retrieval process. Other work in the area of broadband lensless imaging has been performed for different experimental setups, including ptychography with an overlapped red, green and blue laser [49], ptychography with 1.5 % bandwidth at 17 keV [50], two-pulse imaging with three harmonics from 47 to 62 nm [51], and two-pulse HERALDO [52] with 8 harmonics spanning 12 to 33 eV [53]. Another interesting example is [54], in which single helium nanodroplets were “imaged” by fitting Mie scattering parameters to polychromatic diffraction data, obtained using 4 harmonics of a HHG source.

2.4 Numerical Monochromatization

Under certain conditions the broadband diffraction pattern is simply an incoherent sum of monochromatic patterns which are identical up to a scaling. This is represented schematically in figure 2.2. The method presented here numerically inverts this scaling operation, to extract the monochromatic pattern out of the broadband pattern, making use only of the spectrum of the diffracted radiation. This monochromatized pattern is then used as input for a regular phase retrieval process.

2.4.1 Broadband Fraunhofer diffraction

Consider a sample at $z = 0$, irradiated by a monochromatic plane wave with angular frequency ω. In the paraxial approximation, the far-field diffraction pattern at $z = \Delta$ is given by the Fraunhofer diffraction formula (see Appendix B and [2] for a derivation):

$$\psi_\omega(x,y,z=\Delta) = -\frac{ik\mathrm{e}^{ik\Delta}}{\Delta}\mathrm{e}^{i\frac{k}{2\Delta}(x^2+y^2)}\tilde{\psi}_\omega\left(k_x=\frac{kx}{\Delta},k_y=\frac{ky}{\Delta},z=0\right) \tag{2.9}$$

with the tilde indicating a 2-dimensional (spatial) Fourier transform. To describe the diffraction of a sample by a broadband source, we write the broadband diffracted field Φ as:

$$\Phi(\omega) = s(\omega)\psi_\omega(x,y,z=\Delta), \tag{2.10}$$

with $s(\omega)$ being the square root of the power spectral density of the diffracted radiation. The spatial coordinates $(x,y,z=\Delta)$ will be omitted for sake of brevity. To obtain the broadband diffraction pattern as seen by the detector it is convenient to pass to the time domain through an inverse Fourier transform:

$$\Phi(t) = \frac{1}{\sqrt{2\pi}}\int_{-\infty}^{\infty}\Phi(\omega)\mathrm{e}^{\mathrm{i}\omega t}\mathrm{d}\omega. \tag{2.11}$$

The detector will integrate over time to produce the broadband pattern $B(x,y,z=\Delta)$:

$$B = \int |\Phi(t)|^2\,\mathrm{d}t \tag{2.12}$$

$$= \frac{1}{2\pi}\int |\Phi(\omega)|^2\,\mathrm{d}\omega \tag{2.13}$$

$$= \frac{1}{2\pi\Delta^2}\int s(\omega)^2\,|\psi_\omega|^2\,\mathrm{d}\omega \tag{2.14}$$

where in the second step use is made of Parseval's theorem (Appendix A).

Writing the central angular frequency of the spectrum as ω_c, we will now assume that

Assumption 1 *We assume that* $\psi_\omega(x,y,z=0) \approx C(\omega)\psi_{\omega_c}(x,y,z=0), \quad C(\omega)\in\mathbb{C}$

meaning that the sample is spatially non-dispersive over the source bandwidth (C does not depend on x,y). Introducing the scaling factor $\alpha \equiv \frac{\lambda}{\lambda_c} = \frac{\omega_c}{\omega}$, then

$$B(x,y) = \left(\frac{k_c}{\Delta}\right)^2\int\left(\frac{s(\alpha)}{\alpha}\right)^2\left|\tilde{\psi}_{\omega_c}\left(k_x=\frac{k_c x}{\alpha\Delta},k_y=\frac{k_c y}{\alpha\Delta},z=0\right)\right|^2\mathrm{d}\omega, \tag{2.15}$$

where $C(\omega)$ has been absorbed into $s(\alpha)$. Hence the broadband diffraction pattern is now just a spectrally weighted sum of homothetically scaled copies of the monochromatic pattern $|\psi_{\omega_c}(x,y,z=\Delta)|^2$. By measuring the broadband diffraction pattern and the spectrum of the diffracted radiation, the monochromatic pattern can be retrieved using linear algebra, as explained in the next section.

2.4.2 Monochromatization through regularized matrix inversion

First we will rewrite equation 2.15 in a linear algebra formulation. The measured intensity of the broadband diffraction pattern $B(x,y)$ is given by the sum of scaled copies of the monochromatic diffraction pattern $M_{\lambda_c}(x,y)$, weighted by the normalized spectral density $S(\alpha)$:

$$B(x,y) = \int M_{\lambda_c}\left(\frac{x}{\alpha},\frac{y}{\alpha}\right)\frac{S(\alpha)}{\alpha^2}\mathrm{d}\alpha \tag{2.16}$$

$S(\alpha)$ is normalized such that $\int S(\alpha)/\alpha^2\mathrm{d}\alpha = 1$.

The scaling and weighting of copies of the monochromatic pattern is perfectly suited for a matrix-vector product. Writing the monochromatic pattern as vector **m**, the broadband pattern as vector **b** and the scaling matrix as **C**, the broadband diffraction can be written simply as:

$$\mathbf{b} = \mathbf{C}\mathbf{m}. \tag{2.17}$$

Matrix **C** can be regarded as containing the radially dependent point-spread function (PSF) of the convolution in Eq. 2.16. It maps a point in **m** to the shape of the spectrum in **b**. For a 2-dimensional diffraction pattern **C** becomes a 4-dimensional tensor, although in the numerical implementation the diffraction patterns are rearranged in a 1-dimensional vector, so **C** is kept 2-dimensional. Matrix **C** is fully determined by the spectrum and the size of the diffraction pattern. In one dimension **C** is formed as follows:

$$C_{nj} = \sum_L \underbrace{[\min\{j\,,\,\alpha_l n\} - \max\{j-1\,,\,\alpha_l(n-1)\}]}_{\text{part of scaled pixel } n \text{ falling onto pixel } j}\frac{S_l}{\alpha_l} \tag{2.18}$$

where

$$N = \left\{n : \frac{j-1}{\alpha_{max}} < n < \frac{j}{\alpha_{min}+1}\right\},$$
$$L = \left\{l : \frac{j-1}{n} < \alpha_l < \frac{j}{n-1}\right\}.$$

Here l, n, j are the indices that run over $\alpha, \mathbf{m}, \mathbf{b}$ respectively. This expression can be understood as: "The contribution of pixel n of **m** to pixel j of **b** is given by the part of pixel n that falls onto pixel j for the scaled pattern l times the spectral weight, summed over all L. " This principle is illustrated in figure 2.4. The flow of the numerical implementation of the method is depicted in Fig. 2.5. In the experiment the broadband pattern and the spectrum are measured (this is either a corrected source spectrum or the spectrum of the diffracted radiation, and both should be corrected for the response of the camera). The measured pattern is centered and binned to obtain pattern **b**. The spectrum is normalized to obtain $S(\alpha)$ which, combined with the size of **b**, is all the information needed to compute matrix **C**. The monochromatization of a broadband diffraction pattern is now reduced to the inversion of matrix **C**. For a diffraction pattern **b** of 480×480 pixels, **C** has 240^4 values (the scaling is the same for each quadrant). However, **C** is a sparse matrix: depending on the spectrum only a few percent of the values is non-zero. **C** is now built

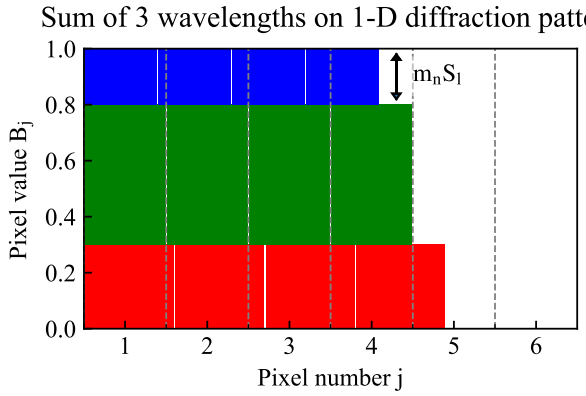

FIGURE 2.4: Schematic illustration of the way matrix C is built up, for a spectrum consisting of three wavelengths ($l = 1, 2, 3$ or red, green, blue) with spectral weights $S_l = 0.3, 0.5, 0.2$. The contribution of pixel n of $\mathbf{m}$ to pixel j of $\mathbf{b}$ is given by the part of pixel n that falls onto pixel j for the scaled pattern l times the spectral weight S_l, summed over all L.

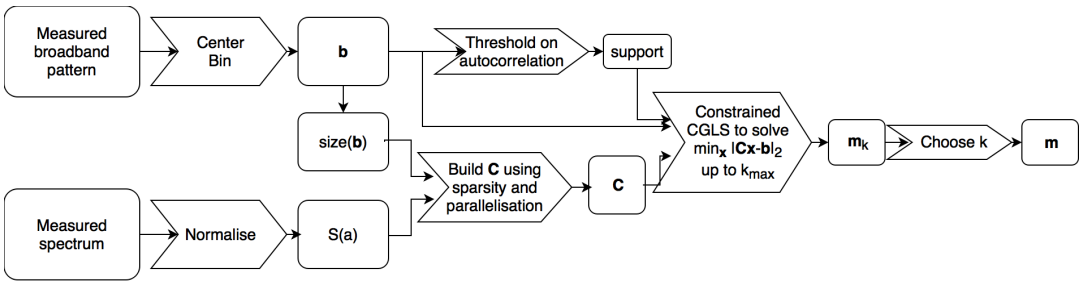

FIGURE 2.5: The information flow of the numerical monochromatization.

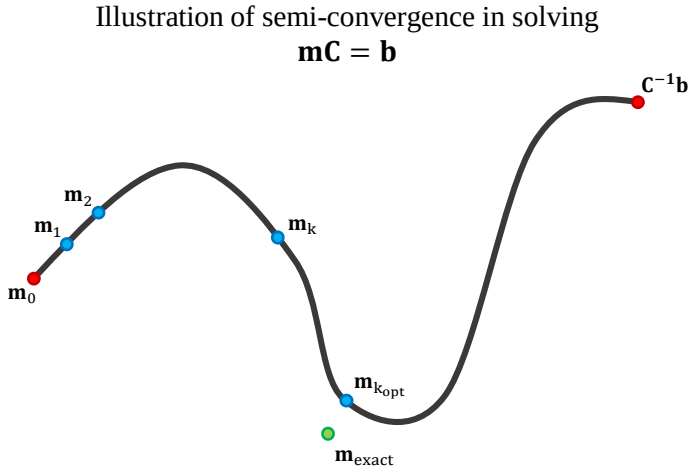

FIGURE 2.6: In ill-conditioned problems, such as the numerical monochromatization problem considered here, direct inversion $\mathbf{C}^{-1}\mathbf{b}$ will be dominated by inverted noise, and thus far from the exact solution $\mathbf{m}_{exact}$. Regularization methods allow to perform the inversion gradually, ideally by inverting the signal first, thus getting close to $\mathbf{m}_{exact}$.

by evaluating Eq. 2.18 in a set of parallel for-loops running only over the non-zero part of **C**. Note that **C** only has to be built once per spectrum (and size of **b**). As **C** is highly ill-conditioned (meaning its inverse exists, but the inversion is extremely sensitive to noise), inversion of the problem is performed using a regularization method called Conjugate Gradient Least Squares (CGLS, see e.g. [55]). It consists of minimizing the least squares problem

$$\min_x \|Cx - b\|_2 \qquad \text{subject to} \quad x \in \mathscr{K}_k \tag{2.19}$$

where $\mathscr{K}$ denotes the so-called Krylov subspace:

$$\mathscr{K}_k \equiv \text{span}\{C^T b, C^T C C^T b, \ldots, (C^T C)^{k-1} C^T b\}. \tag{2.20}$$

The power of this method is its behavior of semi-convergence: for increasing k, first the signal is inverted so x comes close to the exact solution, then the noise starts being inverted as well and x diverges. This is illustrated in figure 2.6: the direct inverse $\mathbf{C}^{-1}\mathbf{b}$ is dominated by inverted noise, but by regularizing the inversion (in our case by building up the Krylov subspace) one can come close to the exact solution $\mathbf{m}_{exact}$. Typically the inverted patterns $\mathbf{m}_k$ are computed up to $k_{max} = 40$. The optimum value for k is then chosen either manually by visual inspection of $\mathbf{m}_k$ (choose k_{opt} just before inverted noise starts to dominate), or automatically by maximizing the variance in the autocorrelation (a measure for sharp edges in real space) (typically $k_{opt} \approx 25$). The monochromatized pattern $\mathbf{m}_{k_{opt}}$ now serves as input for a conventional phase retrieval algorithm. The numerical implementation is based on a Matlab function [55] which was translated to Python with the addition of two constraints: positivity of x_k (photon counts should not be negative) and a support constraint on the Fourier transform of x_k. The latter is justified as we are dealing with isolated samples, so the sample's autocorrelation is isolated as well. These constraints help to further improve the regularizing power of the method. The developed Python code is available on github.com/jhuijts under the BSD license.

2.4.3 An example

Figure 2.7 shows a 1-dimensional example to illustrate the workings of the method. A spectrum with a bandwidth of 5 % ($\Delta\lambda/\lambda$) is sampled at 100 points. Matrix C is calculated using this spectrum for a diffraction pattern of 256 pixels. A cosine is taken as an example of a monochromatic pattern $\mathbf{m}$. The broadband pattern $\mathbf{b}$ is also plotted. The pixel number on the x-axis can be seen as the radial axis for a 2-D pattern: the further away from the center, the stronger the blurring due to the spectral bandwidth. A naive, direct inversion of $\mathbf{b} = \mathbf{Cm}$ leads to the pattern plotted in blue in the top panel of figure 2.8 (note the logarithmic y-scale). The reason for this behavior is the so-called condition number of $\mathbf{C}$. Although the determinant of $\mathbf{C}$ is non-zero (so its inverse exists), it has a condition number on the order of 10^7. The condition number of a matrix is the ratio between the largest and the smallest singular value, and it estimates the (worst case) loss of precision in solving a linear system with that matrix. If it is infinite, the matrix is singular and the determinant is zero (no inverse). In our example, the expected precision loss through inversion is 7 orders of magnitude. Using the regularization method, the inversion can be performed in a controlled way. The bottom panel of figure 2.8 shows the monochromatized pattern for $k = 0$ (so using just the first basis vector of the Krylov subspace) and for $k = 14$ (using the first 14 basis vectors). For $k \to \infty$ the monochromatized pattern will tend to the direct inversion, corresponding the behavior of semiconvergence as indicated in figure 2.6. To show this, the monochromatized pattern for $k = 700$ is also plotted in the top panel of figure 2.8. Figure 2.9 quantifies the introduced monochromatization error, as

$$\epsilon = |\hat{\mathbf{m}} - \mathbf{m}|. \tag{2.21}$$

The top panel of the figure plots ϵ for $k = 14$ and shows how the error increases towards the edge of the diffraction pattern. The bottom panel shows the semi-convergence behavior: the error is minimal for $k = 14$, after which the inversion diverges. For this example, building matrix $\mathbf{C}$ took 290 ms on an average PC, calculating $\hat{\mathbf{m}}$ up to $k = 700$ took about 1 second.

2.4.4 Limits

Assumption 1 in practice means that the refractive indices of the materials in the sample do not change significantly over the source spectrum, or that these changes are spatially homogeneous at the reconstructed length scales. This means that masks and apertures are perfect samples, but for more complex samples, constituted of different materials with different refractive indices, the monochromatization step introduces errors as the assumption is no longer valid. The magnitude of this error will depend not only on the difference in refractive index and the spectral bandwidth, but also on the spatial frequencies in the object and the sampling of the experimental diffraction pattern.

Matrix C is invertible as the determinant is non-zero. This is however only the case for a spectrum that does not contain any zeros. For a discrete spectrum (as is the case for many XUV HHG spectra), the determinant is zero and the algorithm will fail (the inverted pattern will tend to infinity). Hence, the method is also limited to continuous spectra.

As a final remark, the spectrum should be finely sampled to avoid that the pattern expected by the algorithm contain discontinuities. These discontinuities first appear at large diffraction angles, or high spatial frequencies. The wavelengths λ_l and λ_{l+1}, diffracted onto the outer edge of the captured diffraction pattern will be separated by a fraction of a pixel ϵ. The spectrum should thus be sampled finely enough[7] that $\epsilon \ll 1$. For a

[7] Theoretically, for a detector with infinitely small pixels, the limit would be determined by the integration time of the detector, i.e. $\Delta\omega < 1/T_{int}$

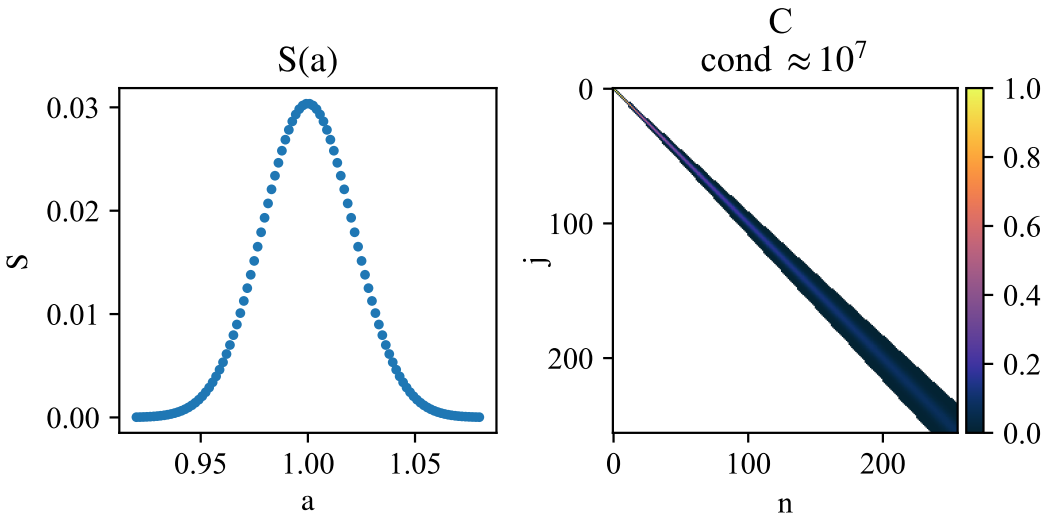

(A) A Gaussian spectrum with a 5 % bandwidth ($\Delta\lambda/\lambda$) sampled at 100 points, and the corresponding matrix **C** for a diffraction pattern of 256 pixels.

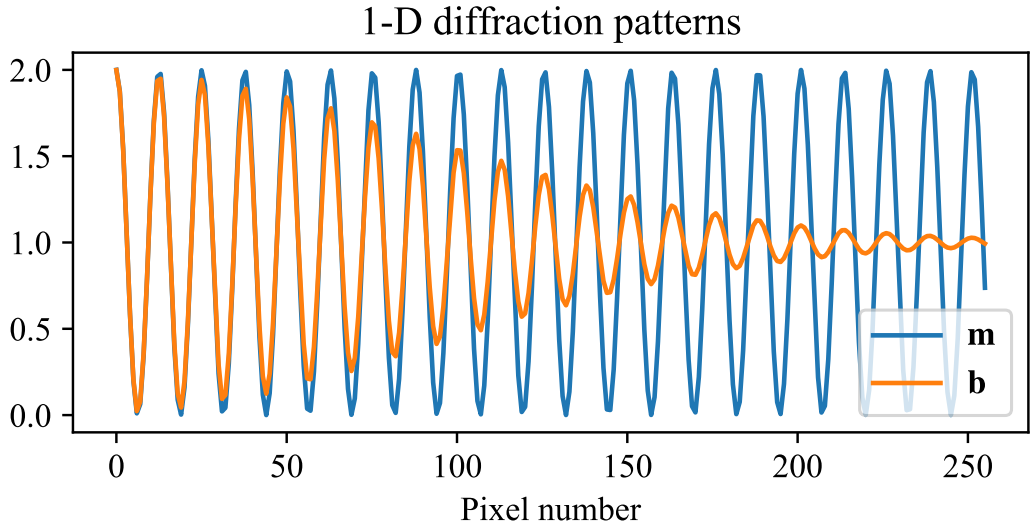

(B) A simple one-dimensional "diffraction pattern" **m** (a cosine), and the corresponding broadband pattern **b** at 5 % bandwidth.

FIGURE 2.7: One-dimensional example to illustrate the workings of the monochromatization method.

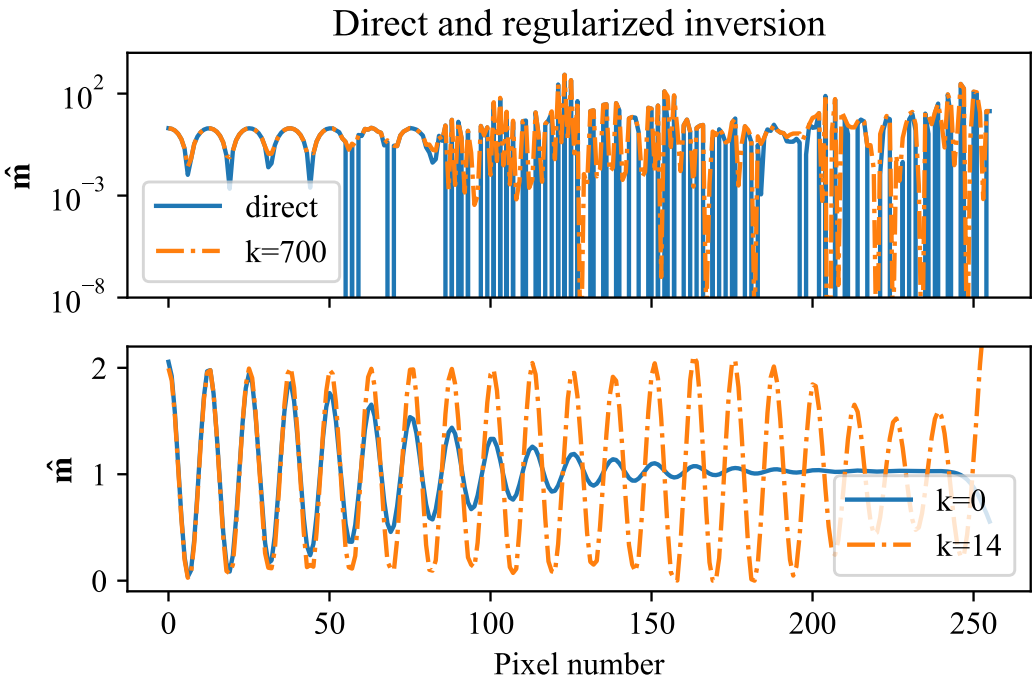

FIGURE 2.8: In the top panel, the "monochromatized" pattern obtained through direct inversion of $\mathbf{b}$ (note the logarithmic y-scale). In the bottom panel, the monochromatized patterns obtained through regularized inversion as described in the main text, for $k = 0$ and $k = 14$. As $k \to \infty$ $\hat{\mathbf{m}}$ will tend to the solution obtained by direct inversion (see $k = 700$ plotted in the top panel).

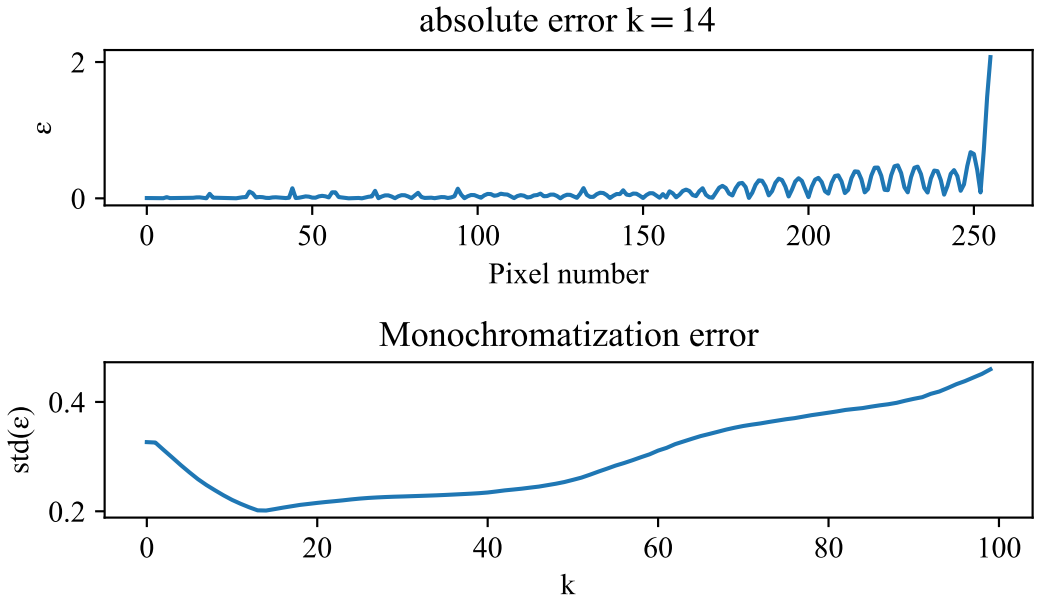

FIGURE 2.9: Error introduced by the monochromatization procedure, as $\epsilon = |\hat{\mathbf{m}} - \mathbf{m}|$. Top panel: the absolute error for optimum k ($k = 14$). Clearly the error is larger towards the edge of this 'diffraction pattern'. Bottom panel: the error as a function of k shows the characteristic semi-convergence behavior.

diffraction pattern of $N \times N$ pixels

$$\epsilon = \frac{N(\lambda_{l+1} - \lambda_l)}{2\lambda} \ll 1 \tag{2.22}$$

and thus

$$\frac{\Delta\lambda}{\lambda} \ll \frac{2}{N}. \tag{2.23}$$

2.5 Conclusions

CDI through phase retrieval is an important imaging technique that is gaining momentum on several sources (synchrotron, FEL, HHG) thanks to its ease of implementation (no lenses or reference wave needed). Traditional CDI however assumes a perfectly coherent, monochromatic wave. In order to make full use of the developed attosecond sources, and other sources that feature a broad spectrum, it is necessary to extend CDI methods to cope with broadband diffraction patterns. Some work has been performed in this direction, particularly by extending the iterative phase retrieval algorithm. In this thesis work, a method has been developed to perform a numerical monochromatization, directly on the broadband diffraction pattern, using only the spectrum of the diffracted radiation. It makes use of a regularized matrix inversion. An important limiting assumption is that the sample be non-dispersive over the source bandwidth. In the coming chapters, the method will be applied to experimental and simulated cases, to explore its applicability and limitations.

Bibliography

[1] Joseph W. Goodman. *Introduction to Fourier Optics*. Roberts and Company Publishers, 2005. ISBN 978-0-9747077-2-3.

[2] David M. Paganin. *Coherent X-Ray Optics*. Number 6 in Oxford Series on Synchrotron Radiation. Oxford University Press, Oxford, 2006. ISBN 978-0-19-856728-8.

[3] Max Born and Emil Wolf. *Principles of Optics: Electromagnetic Theory of Propagation, Interference and Diffraction of Light (7th Edition)*. Cambridge University Press, 7th edition, 1999. ISBN 978-0-521-64222-4.

[4] Dennis Gabor. A New Microscopic Principle. *Nature*, 161:777, May 1948.

[5] Tais Gorkhover, Anatoli Ulmer, Ken Ferguson, Max Bucher, Filipe R. N. C. Maia, Johan Bielecki, Tomas Ekeberg, Max F. Hantke, Benedikt J. Daurer, Carl Nettelblad, Jakob Andreasson, Anton Barty, Petr Bruza, Sebastian Carron, Dirk Hasse, Jacek Krzywinski, Daniel S. D. Larsson, Andrew Morgan, Kerstin Mühlig, Maria Müller, Kenta Okamoto, Alberto Pietrini, Daniela Rupp, Mario Sauppe, Gijs van der Schot, Marvin Seibert, Jonas A. Sellberg, Martin Svenda, Michelle Swiggers, Nicusor Timneanu, Daniel Westphal, Garth Williams, Alessandro Zani, Henry N. Chapman, Gyula Faigel, Thomas Möller, Janos Hajdu, and Christoph Bostedt. Femtosecond X-ray Fourier holography imaging of free-flying nanoparticles. *Nature Photonics*, 12(3):150–153, March 2018. ISSN 1749-4885, 1749-4893. doi: 10.1038/s41566-018-0110-y.

[6] R. Hegerl and W. Hoppe. Dynamische Theorie der Kristallstrukturanalyse durch Elektronenbeugung im inhomogenen Primärstrahlwellenfeld. *Berichte der Bunsengesellschaft für physikalische Chemie*, 74(11):1148–1154, November 1970. ISSN 0005-9021. doi: 10.1002/bbpc.19700741112.

[7] S. L. Friedman and J. M. Rodenburg. Optical demonstration of a new principle of far-field microscopy. *Journal of Physics D: Applied Physics*, 25(2):147–154, February 1992. ISSN 0022-3727. doi: 10.1088/0022-3727/25/2/003.

[8] Franz Pfeiffer. X-ray ptychography. *Nature Photonics*, 12(1):9, January 2018. ISSN 1749-4893. doi: 10.1038/s41566-017-0072-5.

[9] R. W. Gerchberg and W. O. Saxton. A Practical Algorithm for the Determination of Phase from Image and Diffraction Plane Pictures. *Optik*, 35(2):237–246, 1972.

[10] J. R. Fienup. Reconstruction of an object from the modulus of its Fourier transform. *Optics Letters*, 3(1):27, July 1978. ISSN 0146-9592, 1539-4794. doi: 10.1364/OL.3.000027.

[11] S. Marchesini, H. He, H. N. Chapman, S. P. Hau-Riege, A. Noy, M. R. Howells, U. Weierstall, and J. C. H. Spence. X-ray image reconstruction from a diffraction pattern alone. *Physical Review B*, 68(14), October 2003. ISSN 0163-1829, 1095-3795. doi: 10.1103/PhysRevB.68.140101.

[12] D. Sayre. Prospects for long-wavelenth x-ray microscopy and diffraction. In M. Schlenker, M. Fink, J. P. Goedgebuer, C. Malgrange, J. C. Viénot, and R. H. Wade, editors, *Imaging Processes and Coherence in Physics*, volume 112 of *Springer Lecture Notes in Physics*, pages 229–235. Springer-Verlag, Berlin, 1980.

[13] David Sayre, W. B. Yun, and Janos Kirz. Experimental Observation of Diffraction Patterns from Micro-Specimens. In *X-Ray Microscopy II Proceedings of the International Symposium, Brookhaven, NY, August 31-September 4, 1987*, volume 56, pages 272–275, Berlin, 1988. Springer Berlin. ISBN 978-3-662-14490-9. OCLC: 864591414.

[14] D. Sayre, H. N. Chapman, and J. Miao. On the Extendibility of X-ray Crystallography to Noncrystals. *Acta Crystallographica Section A Foundations of Crystallography*, 54 (2):232–239, March 1998. ISSN 01087673. doi: 10.1107/S0108767397015572.

[15] Jianwei Miao, Pambos Charalambous, Janos Kirz, and David Sayre. Extending the methodology of X-ray crystallography to allow imaging of micrometre-sized noncrystalline specimens. *Nature*, 400(6742):342–344, July 1999. ISSN 0028-0836, 1476-4687. doi: 10.1038/22498.

[16] Richard L. Sandberg, Ariel Paul, Daisy A. Raymondson, Steffen Hädrich, David M. Gaudiosi, Jim Holtsnider, Ra'anan I. Tobey, Oren Cohen, Margaret M. Murnane, Henry C. Kapteyn, Changyong Song, Jianwei Miao, Yanwei Liu, and Farhad Salmassi. Lensless Diffractive Imaging Using Tabletop Coherent High-Harmonic Soft-X-Ray Beams. *Physical Review Letters*, 99(9), August 2007. ISSN 0031-9007, 1079-7114. doi: 10.1103/PhysRevLett.99.098103.

[17] A. Ravasio, D. Gauthier, F. R. N. C. Maia, M. Billon, J-P. Caumes, D. Garzella, M. Géléoc, O. Gobert, J-F. Hergott, A-M. Pena, H. Perez, B. Carré, E. Bourhis, J. Gierak, A. Madouri, D. Mailly, B. Schiedt, M. Fajardo, J. Gautier, P. Zeitoun, P. H. Bucksbaum, J. Hajdu, and H. Merdji. Single-Shot Diffractive Imaging with

a Table-Top Femtosecond Soft X-Ray Laser-Harmonics Source. *Physical Review Letters*, 103(2), July 2009. ISSN 0031-9007, 1079-7114. doi: 10.1103/PhysRevLett.103.028104.

[18] Jan Rothhardt, Getnet K Tadesse, Wilhelm Eschen, and Jens Limpert. Table-top nanoscale coherent imaging with XUV light. *Journal of Optics*, 20(11):113001, November 2018. ISSN 2040-8978, 2040-8986. doi: 10.1088/2040-8986/aae2d8.

[19] Henry N. Chapman, Anton Barty, Michael J. Bogan, Sébastien Boutet, Matthias Frank, Stefan P. Hau-Riege, Stefano Marchesini, Bruce W. Woods, Saša Bajt, W. Henry Benner, Richard A. London, Elke Plönjes, Marion Kuhlmann, Rolf Treusch, Stefan Düsterer, Thomas Tschentscher, Jochen R. Schneider, Eberhard Spiller, Thomas Möller, Christoph Bostedt, Matthias Hoener, David A. Shapiro, Keith O. Hodgson, David van der Spoel, Florian Burmeister, Magnus Bergh, Carl Caleman, Gösta Huldt, M. Marvin Seibert, Filipe R. N. C. Maia, Richard W. Lee, Abraham Szöke, Nicusor Timneanu, and Janos Hajdu. Femtosecond diffractive imaging with a soft-X-ray free-electron laser. *Nature Physics*, 2(12):839–843, December 2006. ISSN 1745-2473, 1745-2481. doi: 10.1038/nphys461.

[20] Henry N. Chapman, Anton Barty, Stefano Marchesini, Aleksandr Noy, Stefan P. Hau-Riege, Congwu Cui, Malcolm R. Howells, Rachel Rosen, Haifeng He, John C. H. Spence, Uwe Weierstall, Tobias Beetz, Chris Jacobsen, and David Shapiro. High-resolution ab initio three-dimensional x-ray diffraction microscopy. *Journal of the Optical Society of America A*, 23(5):1179, May 2006. ISSN 1084-7529, 1520-8532. doi: 10.1364/JOSAA.23.001179.

[21] Henry N. Chapman and Keith A. Nugent. Coherent lensless X-ray imaging. *Nature Photonics*, 4(12):833–839, December 2010. ISSN 1749-4885, 1749-4893. doi: 10.1038/nphoton.2010.240.

[22] James R. Fienup. Phase retrieval algorithms: A personal tour [Invited]. *Applied Optics*, 52(1):45–56, January 2013. ISSN 2155-3165. doi: 10.1364/AO.52.000045.

[23] J. Miao, T. Ishikawa, I. K. Robinson, and M. M. Murnane. Beyond crystallography: Diffractive imaging using coherent x-ray light sources. *Science*, 348(6234):530–535, May 2015. ISSN 0036-8075, 1095-9203. doi: 10.1126/science.aaa1394.

[24] Anton Barty. Single molecule imaging using X-ray free electron lasers. *Current Opinion in Structural Biology*, 40:186–194, October 2016. ISSN 0959440X. doi: 10.1016/j.sbi.2016.11.017.

[25] Tomas Ekeberg, Martin Svenda, Chantal Abergel, Filipe R. N. C. Maia, Virginie Seltzer, Jean-Michel Claverie, Max Hantke, Olof Jönsson, Carl Nettelblad, Gijs van der Schot, Mengning Liang, Daniel P. DePonte, Anton Barty, M. Marvin Seibert, Bianca Iwan, Inger Andersson, N. Duane Loh, Andrew V. Martin, Henry Chapman, Christoph Bostedt, John D. Bozek, Ken R. Ferguson, Jacek Krzywinski, Sascha W. Epp, Daniel Rolles, Artem Rudenko, Robert Hartmann, Nils Kimmel, and Janos Hajdu. Three-Dimensional Reconstruction of the Giant Mimivirus Particle with an X-Ray Free-Electron Laser. *Physical Review Letters*, 114(9), March 2015. ISSN 0031-9007, 1079-7114. doi: 10.1103/PhysRevLett.114.098102.

[26] Gijs van der Schot, Martin Svenda, Filipe R. N. C. Maia, Max Hantke, Daniel P. DePonte, M. Marvin Seibert, Andrew Aquila, Joachim Schulz, Richard Kirian, Mengning Liang, Francesco Stellato, Bianca Iwan, Jakob Andreasson, Nicusor Timneanu,

Daniel Westphal, F. Nunes Almeida, Dusko Odic, Dirk Hasse, Gunilla H. Carlsson, Daniel S. D. Larsson, Anton Barty, Andrew V. Martin, Sebastian Schorb, Christoph Bostedt, John D. Bozek, Daniel Rolles, Artem Rudenko, Sascha Epp, Lutz Foucar, Benedikt Rudek, Robert Hartmann, Nils Kimmel, Peter Holl, Lars Englert, Ne-Te Duane Loh, Henry N. Chapman, Inger Andersson, Janos Hajdu, and Tomas Ekeberg. Imaging single cells in a beam of live cyanobacteria with an X-ray laser. *Nature Communications*, 6(1), December 2015. ISSN 2041-1723. doi: 10.1038/ncomms6704.

[27] G. K. Tadesse, R. Klas, S. Demmler, S. Hädrich, I. Wahyutama, M. Steinert, C. Spielmann, M. Zürch, T. Pertsch, A. Tünnermann, J. Limpert, and J. Rothhardt. High speed and high resolution table-top nanoscale imaging. *Optics Letters*, 41(22):5170, November 2016. ISSN 0146-9592, 1539-4794. doi: 10.1364/OL.41.005170.

[28] Veit Elser. Phase retrieval by iterated projections. *Journal of the Optical Society of America A*, 20(1):40, January 2003. ISSN 1084-7529, 1520-8532. doi: 10.1364/JOSAA.20.000040.

[29] S. Marchesini. Invited Article: A unified evaluation of iterative projection algorithms for phase retrieval. *Review of Scientific Instruments*, 78(1):011301, January 2007. ISSN 0034-6748, 1089-7623. doi: 10.1063/1.2403783.

[30] Manuel Guizar-Sicairos and James R. Fienup. Understanding the twin-image problem in phase retrieval. *Journal of the Optical Society of America A*, 29(11):2367, November 2012. ISSN 1084-7529, 1520-8532. doi: 10.1364/JOSAA.29.002367.

[31] Yoann Pertot, Cédric Schmidt, Mary Matthews, Adrien Chauvet, Martin Huppert, Vit Svoboda, Aaron von Conta, Andres Tehlar, Denitsa Baykusheva, Jean-Pierre Wolf, and Hans Jakob Wörner. Time-resolved x-ray absorption spectroscopy with a water window high-harmonic source. *Science*, 355(6322):264–267, January 2017. ISSN 0036-8075, 1095-9203. doi: 10.1126/science.aah6114.

[32] Bárbara Buades, Dooshaye Moonshiram, Themistoklis P. H. Sidiropoulos, Iker León, Peter Schmidt, Irina Pi, Nicola Di Palo, Seth L. Cousin, Antonio Picón, Frank Koppens, and Jens Biegert. Dispersive soft x-ray absorption fine-structure spectroscopy in graphite with an attosecond pulse. *Optica*, 5(5):502, May 2018. ISSN 2334-2536. doi: 10.1364/OPTICA.5.000502.

[33] V. Gruson, L. Barreau, Á. Jiménez-Galan, F. Risoud, J. Caillat, A. Maquet, B. Carré, F. Lepetit, J.-F. Hergott, T. Ruchon, L. Argenti, R. Taïeb, F. Martín, and P. Salières. Attosecond dynamics through a Fano resonance: Monitoring the birth of a photoelectron. *Science*, 354(6313):734–738, November 2016. ISSN 0036-8075, 1095-9203. doi: 10.1126/science.aah5188.

[34] E. Skantzakis, P. Tzallas, J. Kruse, C. Kalpouzos, and D. Charalambidis. Coherent continuum extreme ultraviolet radiation in the sub-100-nJ range generated by a high-power many-cycle laser field. *Optics Letters*, 34(11):1732, June 2009. ISSN 0146-9592, 1539-4794. doi: 10.1364/OL.34.001732.

[35] Eiji J. Takahashi, Pengfei Lan, Oliver D. Mücke, Yasuo Nabekawa, and Katsumi Midorikawa. Attosecond nonlinear optics using gigawatt-scale isolated attosecond pulses. *Nature Communications*, 4(1):2691, December 2013. ISSN 2041-1723. doi: 10.1038/ncomms3691.

[36] C. Burcklen, S. de Rossi, E. Meltchakov, D. Dennetière, B. Capitanio, F. Polack, and F. Delmotte. High-reflectance magnetron-sputtered scandium-based x-ray multilayer mirrors for the water window. *Optics Letters*, 42(10):1927, May 2017. ISSN 0146-9592, 1539-4794. doi: 10.1364/OL.42.001927.

[37] S. Eisebitt, J. Lüning, W. F. Schlotter, M. Lörgen, O. Hellwig, W. Eberhardt, and J. Stöhr. Lensless imaging of magnetic nanostructures by X-ray spectro-holography. *Nature*, 432(7019):885–888, December 2004. ISSN 0028-0836, 1476-4679. doi: 10.1038/nature03139.

[38] Jean-Yves Bigot and Mircea Vomir. Ultrafast magnetization dynamics of nanostructures: Ultrafast magnetization dynamics of nanostructures. *Annalen der Physik*, 525 (1-2):2–30, February 2013. ISSN 00033804. doi: 10.1002/andp.201200199.

[39] R. Lopez, T. E. Haynes, L. A. Boatner, L. C. Feldman, and R. F. Haglund. Size effects in the structural phase transition of VO 2 nanoparticles. *Physical Review B*, 65(22), June 2002. ISSN 0163-1829, 1095-3795. doi: 10.1103/PhysRevB.65.224113.

[40] D. Alloyeau, C. Ricolleau, C. Mottet, T. Oikawa, C. Langlois, Y. Le Bouar, N. Braidy, and A. Loiseau. Size and shape effects on the order–disorder phase transition in CoPt nanoparticles. *Nature Materials*, 8(12):940–946, December 2009. ISSN 1476-1122, 1476-4660. doi: 10.1038/nmat2574.

[41] A Variola, J Haissinski, A Loulergue, and F Zomer. ThomX Technical Design Report. Technical report, Laboratoire de l'Accélérateur Linéaire (LAL), Orsay, 2014.

[42] W. S. Graves, J. Bessuille, P. Brown, S. Carbajo, V. Dolgashev, K.-H. Hong, E. Ihloff, B. Khaykovich, H. Lin, K. Murari, E. A. Nanni, G. Resta, S. Tantawi, L. E. Zapata, F. X. Kärtner, and D. E. Moncton. Compact x-ray source based on burst-mode inverse Compton scattering at 100 kHz. *Physical Review Special Topics - Accelerators and Beams*, 17(12), December 2014. ISSN 1098-4402. doi: 10.1103/PhysRevSTAB.17.120701.

[43] Benedikt Günther, Martin Dierolf, Regine Gradl, Elena Eggl, Christoph Jud, Lorenz Hehn, Stephanie Kulpe, Bernhard Gleich, Madleen Busse, Kaye S. Morgan, Klaus Achterhold, and Franz Pfeiffer. The Munich Compact Light Source: Biomedical Research At a Laboratory-Scale Inverse-Compton Synchrotron X-ray Source. *Microscopy and Microanalysis*, 24(S1):984–985, August 2018. ISSN 1431-9276, 1435-8115. doi: 10.1017/S143192761800541X.

[44] Brian Abbey, Lachlan W. Whitehead, Harry M. Quiney, David J. Vine, Guido A. Cadenazzi, Clare A. Henderson, Keith A. Nugent, Eugeniu Balaur, Corey T. Putkunz, Andrew G. Peele, G. J. Williams, and I. McNulty. Lensless imaging using broadband X-ray sources. *Nature Photonics*, 5(7):420–424, July 2011. ISSN 1749-4885, 1749-4893. doi: 10.1038/nphoton.2011.125.

[45] Ruben A. Dilanian, Bo Chen, Garth J. Williams, Harry M. Quiney, Keith A. Nugent, Sven Teichmann, Peter Hannaford, Lap V. Dao, and Andrew G. Peele. Diffractive imaging using a polychromatic high-harmonic generation soft-x-ray source. *Journal of Applied Physics*, 106(2):023110, July 2009. ISSN 0021-8979, 1089-7550. doi: 10.1063/1.3176976.

[46] Bo Chen, Ruben A. Dilanian, Sven Teichmann, Brian Abbey, Andrew G. Peele, Garth J. Williams, Peter Hannaford, Lap Van Dao, Harry M. Quiney, and Keith A.

Nugent. Multiple wavelength diffractive imaging. *Physical Review A*, 79(2), February 2009. ISSN 1050-2947, 1094-1622. doi: 10.1103/PhysRevA.79.023809.

[47] Sven Teichmann, Bo Chen, Ruben A. Dilanian, Peter Hannaford, and Lap Van Dao. Experimental aspects of multiharmonic-order coherent diffractive imaging. *Journal of Applied Physics*, 108(2):023106, July 2010. ISSN 0021-8979, 1089-7550. doi: 10.1063/1.3462438.

[48] Bo Chen, Brian Abbey, Ruben Dilanian, Eugeniu Balaur, Grant van Riessen, Mark Junker, Chanh Q. Tran, Michael W. M. Jones, Andrew G. Peele, Ian McNulty, David J. Vine, Corey T. Putkunz, Harry M. Quiney, and Keith A. Nugent. Diffraction imaging: The limits of partial coherence. *Physical Review B*, 86(23), December 2012. ISSN 1098-0121, 1550-235X. doi: 10.1103/PhysRevB.86.235401.

[49] Darren J. Batey, Daniel Claus, and John M. Rodenburg. Information multiplexing in ptychography. *Ultramicroscopy*, 138:13–21, March 2014. ISSN 03043991. doi: 10.1016/j.ultramic.2013.12.003.

[50] B. Enders, M. Dierolf, P. Cloetens, M. Stockmar, F. Pfeiffer, and P. Thibault. Ptychography with broad-bandwidth radiation. *Applied Physics Letters*, 104(17):171104, April 2014. ISSN 0003-6951, 1077-3118. doi: 10.1063/1.4874304.

[51] Stefan Witte, Vasco T Tenner, Daniel WE Noom, and Kjeld SE Eikema. Lensless diffractive imaging with ultra-broadband table-top sources: From infrared to extreme-ultraviolet wavelengths. *Light: Science & Applications*, 3(3):e163–e163, March 2014. ISSN 2047-7538. doi: 10.1038/lsa.2014.44.

[52] Manuel Guizar-Sicairos and James R. Fienup. Holography with extended reference by autocorrelation linear differential operation. *Optics Express*, 15(26):17592–17612, December 2007. ISSN 1094-4087. doi: 10.1364/OE.15.017592.

[53] Yijian Meng, Chunmei Zhang, Claude Marceau, A. Yu. Naumov, P. B. Corkum, and D. M. Villeneuve. Octave-spanning hyperspectral coherent diffractive imaging in the extreme ultraviolet range. *Optics Express*, 23(22):28960, November 2015. ISSN 1094-4087. doi: 10.1364/OE.23.028960.

[54] Daniela Rupp, Nils Monserud, Bruno Langbehn, Mario Sauppe, Julian Zimmermann, Yevheniy Ovcharenko, Thomas Möller, Fabio Frassetto, Luca Poletto, Andrea Trabattoni, Francesca Calegari, Mauro Nisoli, Katharina Sander, Christian Peltz, Marc J. Vrakking, Thomas Fennel, and Arnaud Rouzée. Coherent diffractive imaging of single helium nanodroplets with a high harmonic generation source. *Nature Communications*, 8(1), December 2017. ISSN 2041-1723. doi: 10.1038/s41467-017-00287-z.

[55] Per Christian Hansen. REGULARIZATION TOOLS: A Matlab package for analysis and solution of discrete ill-posed problems. *Numerical Algorithms*, 6(1):1–35, March 1994. ISSN 1572-9265. doi: 10.1007/BF02149761.

Chapter 3

Experimental validation of the broadband CDI method on a supercontinuum source in the visible

3.1 Introduction

To validate the concepts put forward in the previous chapter (numerical monochromatization, behavior of semi-convergence), an experiment was performed in the visible. For this validation a source was needed with excellent spatial coherence and a tunable, broad bandwidth. This was found at the Laboratoire Charles Fabry (Institut d'Optique, Palaiseau, France) in the form of a supercontinuum generated in a photonic crystal fiber, as explained in the next section. This chapter describes the experimental setup and presents the obtained results, which will confirm the expectations raised in the previous chapter and illustrate the principle and power of the numerical monochromatization method.

3.2 Experimental Setup

To create spatially coherent light with a broad spectrum, pulses from an Yb:KGW oscillator (1030 nm, 240 fs, 1W average power - Mikan Amplitude Systèmes) were focused into a photonic crystal fiber (PCF). This PCF (T2270, Laboratoire PhLAM - Université Lille) was developed to generate a soliton at 1550 nm and a dispersive wave at 625 nm. Two short-pass filters (Thorlabs FES0850) were used to at the output of the PCF to block the soliton and the residual 1030 nm light, as illustrated in the schematic of the experimental setup, figure 3.1. Using these filters resulted in the broadband spectrum shown in Figure 3.2. For the narrowband case, a 10 nm bandpass filter at 800 nm (Thorlabs FB800-10) was inserted. The spectra were recorded using an Ocean Optics USB4000 VIS-NIR spectrometer. An off-axis parabola with an effective focal length of 75 mm was used to focus the beam onto the sample, which was mounted on a translation stage. A CCD (Illunis RMV 4022) was used to acquire the diffraction pattern, at distance sample-CCD of 16 mm. This corresponds to a numerical aperture of 0.39 for the diffraction patterns in Figure 3.4.

3.2.1 Sample

As test sample a micrometric, pure amplitude aperture was used, similar to the one in the original experiment at FLASH by Chapman [1]. It has been etched out of a gold-covered

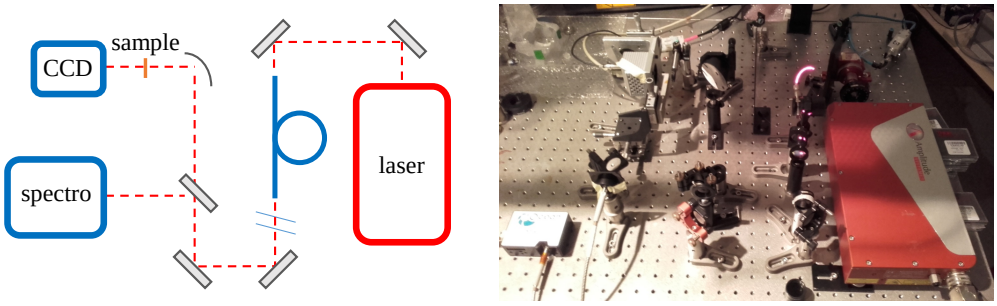

FIGURE 3.1: Setup used to verify the monochromatization method in the visible.

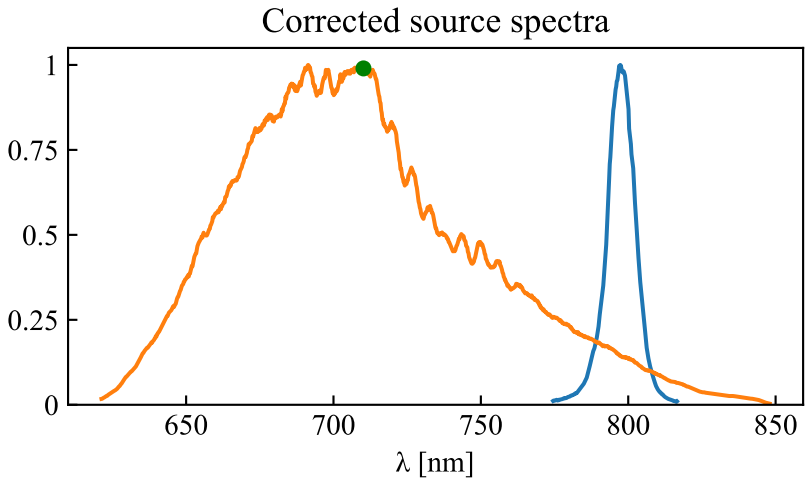

FIGURE 3.2: The broadband spectrum (orange) from a super-continuum generated in a PCF, with a bandwidth of $\Delta\lambda/\lambda = 11\%$ and the narrow-band spectrum (blue) with a bandwidth of $\Delta\lambda/\lambda = 1.2\%$. The green dot at 710 nm represents λ_c, which is taken at the center of mass of the spectrum.

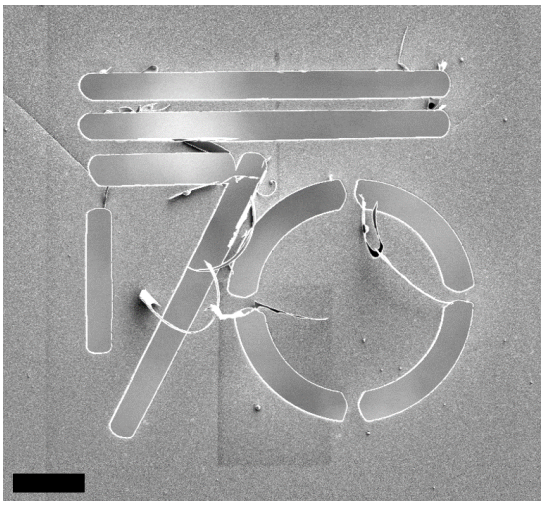

FIGURE 3.3: Sample as used in the experiment. It is an aperture etched out of a gold-covered silicon nitride membrane using a focused ion beam (FIB). The scalebar corresponds to 10 micron.

silicon nitride membrane using a Focused Ion Beam (FIB) at the Centre de Sciences Nucléaires et de Sciences de la Matière (CSNSM, Orsay). These test samples are ubiquitous in the field of diffractive imaging on HHG sources as they present a known, binary and two-dimensional object. An scanning electron microscopy (SEM) image of the sample used in this experiment is shown in figure 3.3.

3.3 Numerical processing

The first part of the data processing of the experiment follows the scheme shown in figure 2.5.

Spectrum

The spectrometer measures the spectrum at a sampling of $\Delta\lambda \approx 0.2$ nm. Equation 2.22 then evaluates to $\epsilon \approx 0.07$ for the broadband diffraction patterns ($N = 480$ pixels), which was considered sufficiently small, so no interpolation was used. The spectrum is normalized to yield $\mathbf{S}$.

High dynamic range acquisition

The diffraction patterns were obtained by using high-dynamic range (HDR) acquisitions, such that the effective bit-depth of the acquired diffraction patterns up to 24, when the bit-depth of the CCD is 14 bits. In HDR, acquisitions of different exposure times are combined to increase the effective bit-depth. The long-exposure acquisitions are saturated in the center of the diffraction pattern, but capture the low-signal wings of the pattern which contain the information about the high spatial frequencies in the sample. The values of the saturated pixels are taken from the short-exposure acquisition (with a multiplicative factor). This procedure is similar to that of [2, 3].

Center, crop, binning

The patterns are then cropped to 1440 x 1440 pixels, such that the direct beam is in the center of the diffraction pattern. Next, the patterns are binned 3 x 3 (software binning) to reduce computation time for the phase retrieval algorithm.

Numerical monochromatization The broadband patterns are monochromatized following the procedure explained in the previous chapter. Matrix **C** is built and the regularized inversion is computed up to $k_{max} = 40$. Phase retrieval was launched for different values of k, and an optimum value for k was determined.

Phase retrieval An erosion step was applied to the diffraction patterns to suppress noise in the low signal areas of the pattern, similar to [2–4]. The sample was then reconstructed using the difference map algorithm as described in the previous chapter, with a shrink-wrap-like support, within a maximum of 1000 iterations. To compute the PRTF 1024 independent reconstructions were launched with random starting points. The successful reconstructions were then hand-selected to be registered (using an adaptation from [5]) and averaged to enhance the signal on the final result.

A number of these procedures already existed in the group and were transposed from MATLAB to Python.

3.4 Results

This section subsequently shows the obtained diffraction patterns, the monochromatization process, the reconstructions of the sample and an assessment of the quality of these reconstructions.

3.4.1 Diffraction patterns

First a word on how the diffraction patterns are displayed in this thesis. Because of the large difference in signal level between the center and the outer regions of diffraction patterns, they are displayed using a logarithmic color scale. On the x-axis the spatial frequency in the sample plane is given in inverse micrometers (or sometimes simply the pixel number). The y-axis is always identical to the x-axis (all diffraction patterns in this thesis are square), so the label for the y-axis is omitted to allow more space on the page to the pattern itself. The narrowband diffraction patterns are shown in figure 3.4, for three different signal levels. It clearly shows the contribution of the circle and the different straight lines of the sample, with the strongest diffraction in the vertical direction from the three horizontal lines in the sample. The broadband diffraction patterns in the same figure were obtained to have similar signal levels (thus shorter acquisition times by about a factor of 10). Although they have the same shape as the narrowband patterns, the radial blurring due to the large bandwidth is clearly visible. The sharp fringes that are clear in the monochromatic case are “smeared out”.

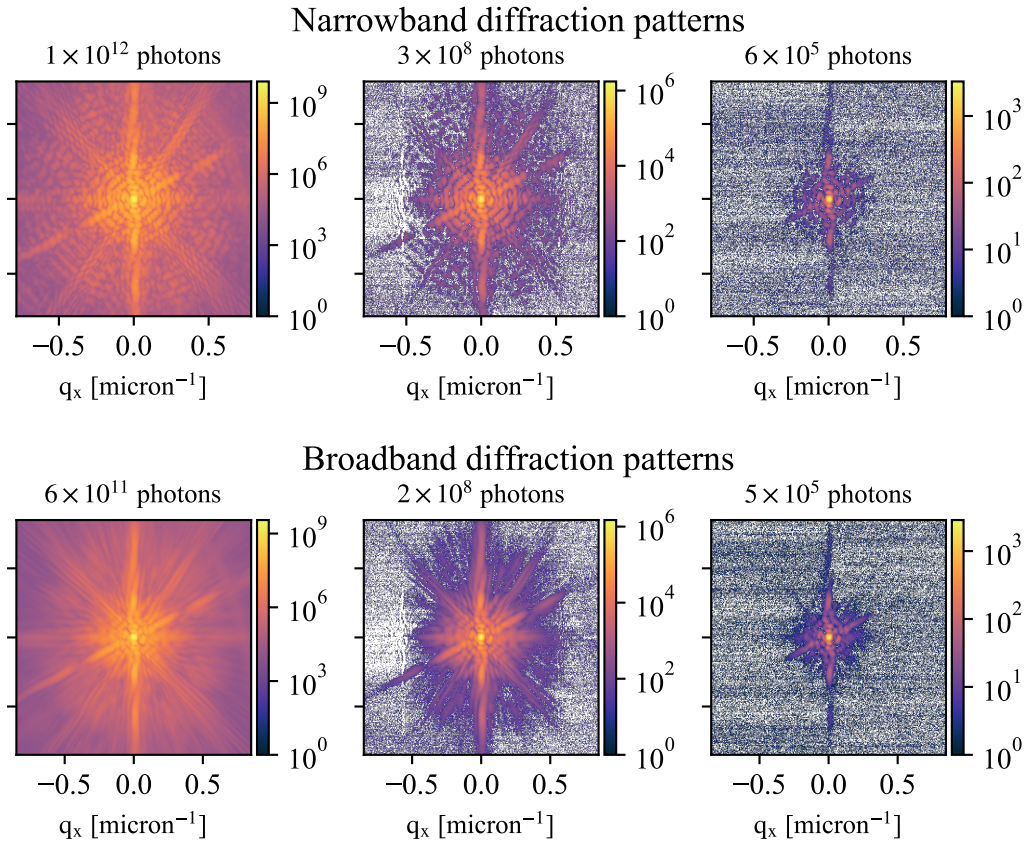

FIGURE 3.4: Narrowband diffraction patterns (upper panels) acquired using the narrow spectral cut (1.2%) of the supercontinuum source, for three different signal levels. Broadband diffraction patterns (lower panels) acquired using the full (11%) spectral bandwidth of the supercontinuum source, for three different signal levels similar to the narrowband case.

3.4.2 Monochromatization

As explained in the previous chapter, the monochromatization step is done in a gradual way, with the "degree of monochromatization" being controlled by the parameter k, the number of basis-vectors in the Krylov subspace. To demonstrate this gradual monochromatization and the behavior of semi-convergence, figure 3.5 shows the diffraction patterns at three stages of the monochromatization process. Comparing the patterns at $k = 3$ to the broadband patterns of figure 3.4 the onset of the monochromatization is clear, but the radial blurring due to the large bandwidth is still strongly present. At $k = k_{opt}$ the inverted patterns are as close as possible to the narrowband patterns, although they are not identical (semi-convergence). Also, the lower the signal level in the broadband pattern, the earlier the inverted noise starts to dominate, i.e. the lower the value for k_{opt}. Further increasing the value for k, the inverted noise dominates and the result of the matrix inversion moves away from the exact solution (which is again the behavior of semi-convergence). Interesting to note is the evolution of the band of stray light in the top right of the high signal level broadband pattern (indicated by a red arrow). This stray light is not part of the physical diffraction pattern and thus does not follow the spectral convolution expected by the inversion method. In the monochromatized patterns the inversion of this stray light causes unphysical oscillations. Another unphysical feature is the square structure that appears near the edges of the monochromatized patterns, especially in the low signal case. These regions are dominated by noise (outside the red square indicated in the figure), which does not follow the expected spectral convolution either. These are examples of sources of artifacts, the inversion of which would render the diffraction pattern unusable for phase retrieval if they were not controlled by the regularization method (CGLS).

Broadband diffraction patterns were obtained for 9 different signal levels. The value of k_{opt} as a function of signal level is shown in figure 3.6. The tendency is clear: higher signal levels allow a higher degree of monochromatization of the diffraction pattern.

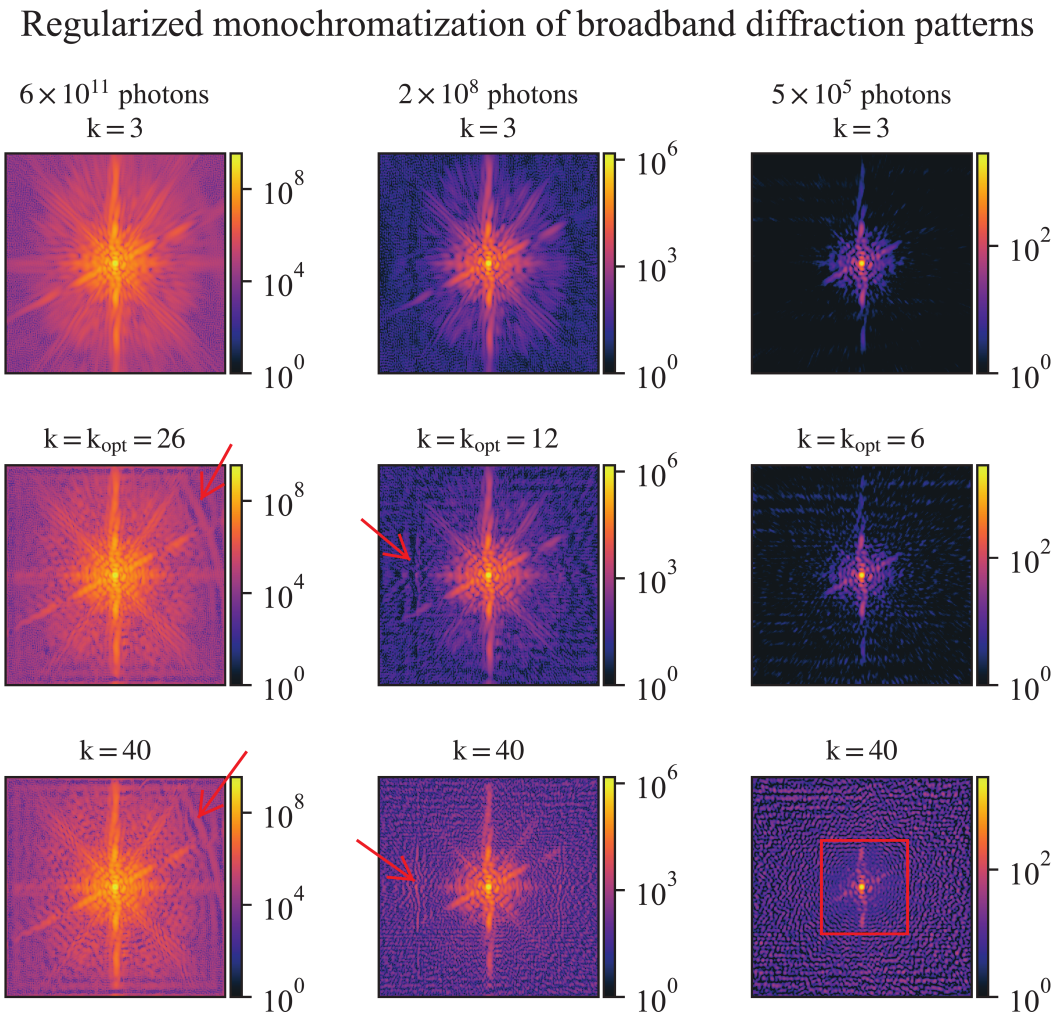

FIGURE 3.5: The regularized monochromatization process. For a too low value of k, strong blurring is still visible. As k increases, the diffraction pattern is monochromatized, but artefacts are also introduced, as indicated by red arrows. The higher the signal, the further the pattern can be monochromatized until the inverted noise starts to dominate. Here the optimal value of k, k_{opt} was chosen manually and verified through successful phase retrieval.

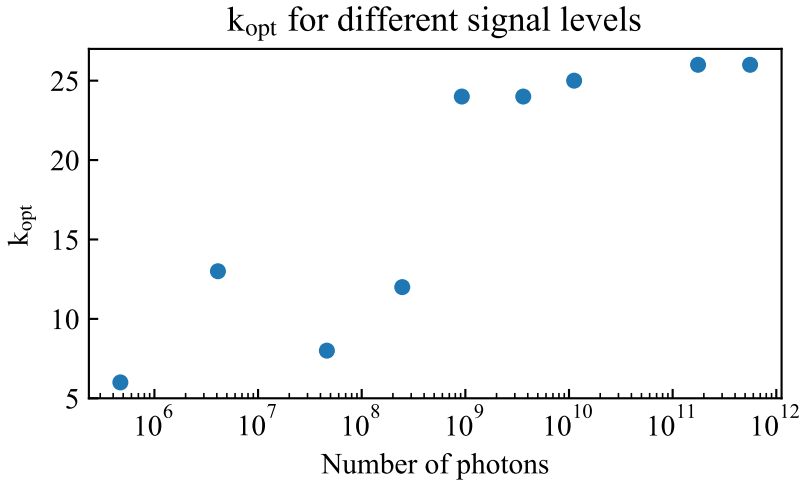

FIGURE 3.6: The optimal degree of monochromatization for different signal levels. The higher the signal, the further a diffraction pattern can be monochromatized before inverted noise starts to dominate.

3.4.3 Reconstructions

As a benchmark for the reconstructions, consider the reconstructed sample of the high-signal narrowband pattern, shown in the top panels of figure 3.7. The sample aperture is perfectly reconstructed, even showing the cracks in the membrane in the top left and top right of the image (compare with the SEM image, figure 3.3). The phase is flat where the sample transmission is non-zero, as expected for a plane wave incident on the sample. Now feeding the exact same phase retrieval algorithm with the monochromatized pattern of figure 3.5 (6×10^{11} photons, $k = k_{opt}$), results in the reconstruction shown in the center panels. Again, even the small cracks in the membrane are reconstructed, and the phase is flat across the transmissive region of the sample. Only the lower right corner of the figure is not reconstructed as well as in the narrowband case. As a cross-check the broadband pattern was also directly fed into the phase retrieval algorithm (so without any monochromatization) and across 100 independent launches no convergence was reached. The lower panels show such a failed reconstruction. Although some features of the sample are vaguely recognizable, it is by no means a satisfying reconstruction of the sample.

At lower signal levels, the monochromatization is stopped earlier to prevent inverted noise from dominating the signal. To see the effect of this lower degree of monochromatization on the sample reconstruction, consider figures 3.8 and 3.9, which are the broadband and narrowband reconstructions of the medium and low signal level cases (3×10^8 and 6×10^5 for the narrowband case, 2×10^8 and 5×10^5 photons for the broadband case).

The medium signal level reconstructions are practically identical to the high signal level reconstructions, but the low signal level reconstructions are significantly worse. The narrowband reconstruction has downright failed. The reconstruction of the broadband case is still successful, albeit with a clear loss in resolution. This is remarkable, considering that the raw broadband diffraction pattern contains about the same number of photons as the narrowband pattern. The monochromatization process introduces some artefacts, but apparently its noise-suppressing behavior more than compensates for these artefacts, producing a pattern that is of sufficient quality for its phase to be retrieved.

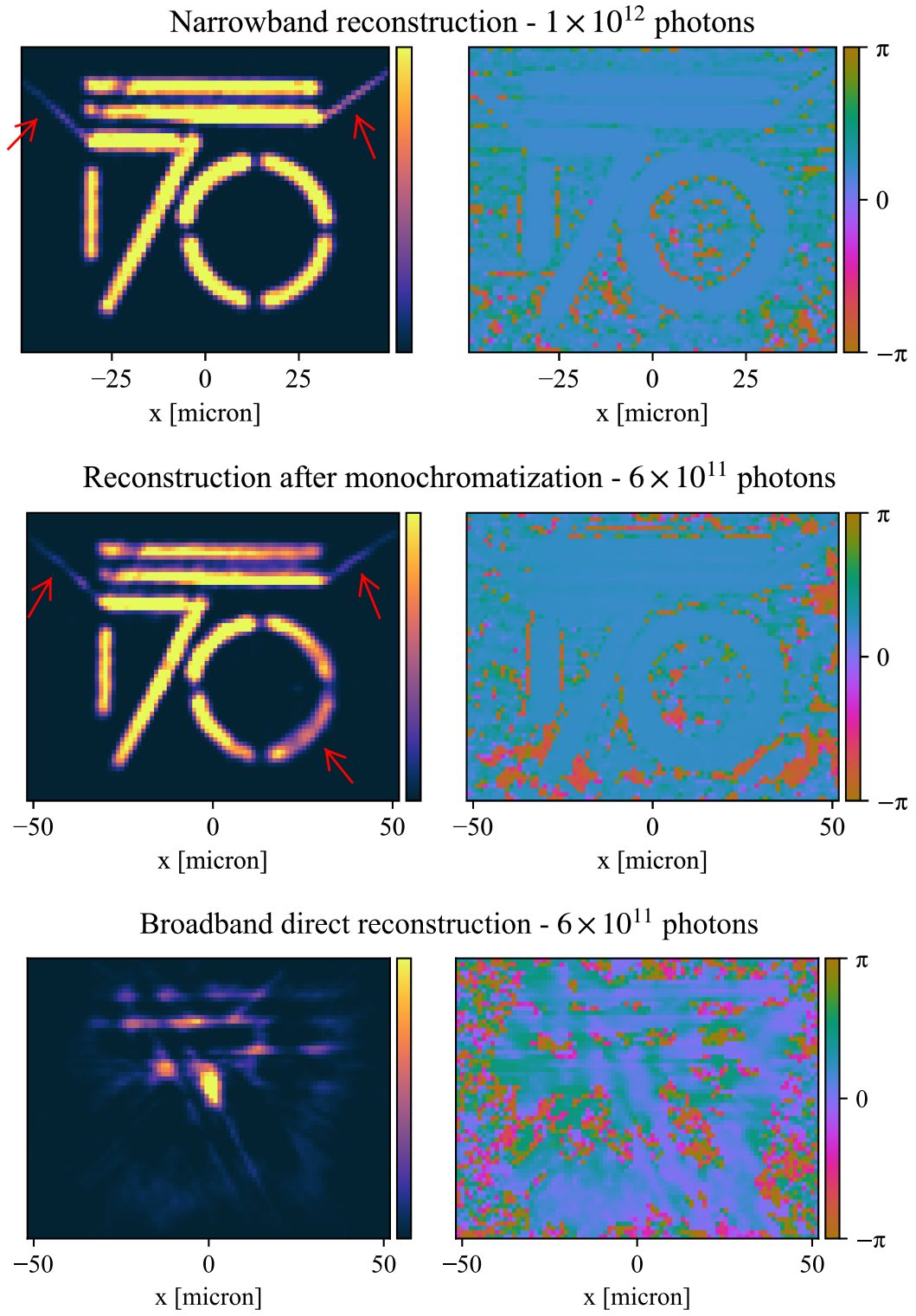

FIGURE 3.7: In the narrowband case (upper panels) the sample is readily reconstructed. The phase (right panel) is flat across the transmissive area of the sample. As the center panels show, feeding the monochromatized pattern (highest signal level) into the phase retrieval algorithm properly reconstructs the sample, with even the membrane cracks being visible (red arrows). On the bottom right of the circle a loss of signal is visible. The phase is again correct. As is clear from the lower panels, trying to reconstruct the sample directly from the highest signal broadband diffraction pattern fails. Although some features from the sample are vaguely recognizable, the blurring in the diffraction pattern is too strong for the phase retrieval algorithm to converge.

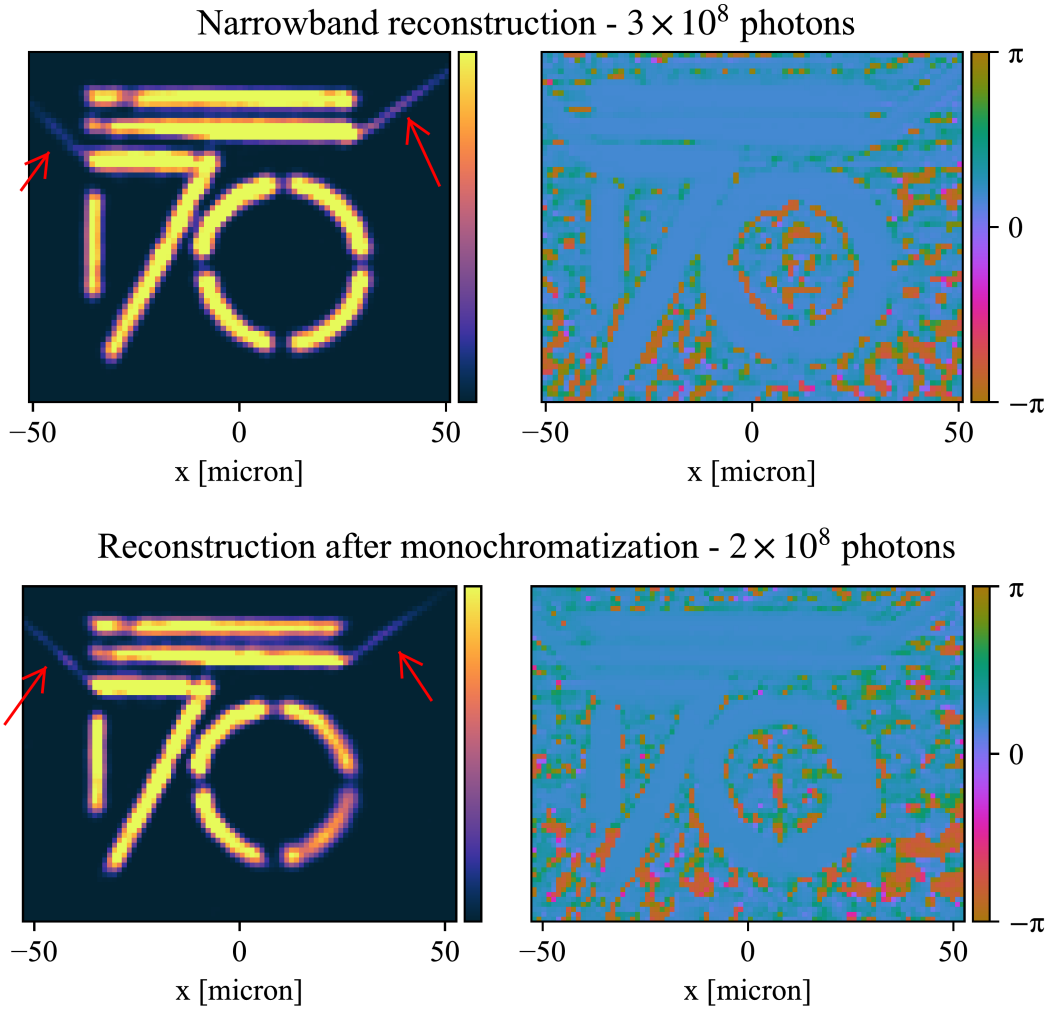

FIGURE 3.8: Reconstructions of the signal at medium signal levels. The reconstructions are practically identical to the high signal level case.

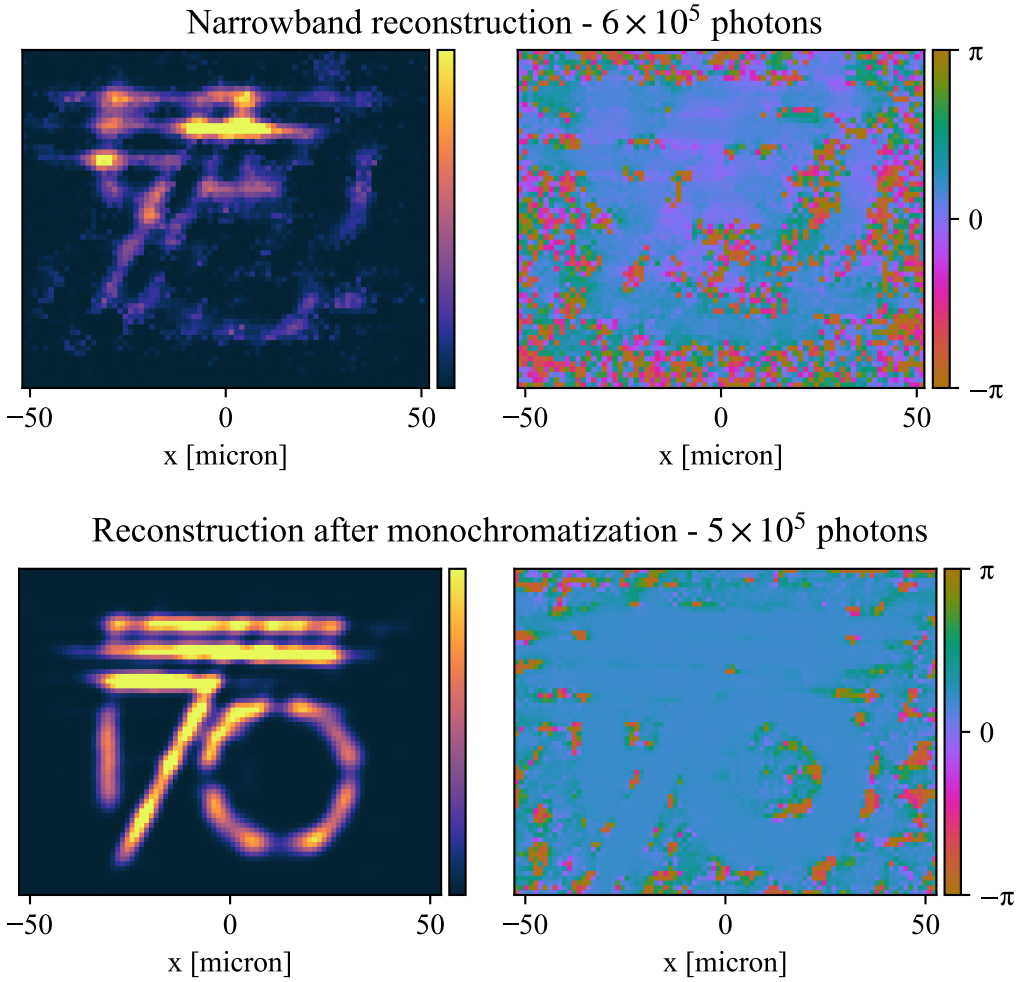

FIGURE 3.9: Reconstruction of the sample at low signal levels. For the narrowband case, no successful reconstruction could be obtained. The reconstruction of the broadband case is still successful, albeit with a clear loss in resolution.

3.4.4 Quality of the reconstructions - Resolution considerations

As explained in the previous chapter, to assess the quality of the reconstruction after phase retrieval it is useful to look at the phase retrieval transfer function (PRTF). It is computed by launching many independent reconstructions and then taking the ratio between the mean retrieved amplitude of the far-field and the amplitude of the measured diffraction pattern. This procedure was followed for all six cases (narrowband and broadband, 3 signal levels), launching the phase retrieval from 1024 independent, random starting points. The results are shown in figure 3.10. Although in practice the PRTF is used to determine the resolution of a reconstruction, it technically is a measure of the reliability of the phase retrieval process. The PRTF is close to one in the center of the diffraction patterns, and drops in the radial direction. Hence the low spatial frequencies are reconstructed more reliably than the higher frequencies, as one would expect. What is clear from this figure is that the narrowband cases reconstruct more reliably than the broadband cases, indicating that the artifacts introduced by the monochromatization procedure are a source of uncertainty in the retrieval of the phase. Also, for the lowest signal level, the PRTF of the narrowband and broadband cases look similar. However, the narrowband case failed to reconstruct the sample, whereas the broadband case succeeded. For this failed, narrowband case the PRTF was calculated by taking into account all 1024 reconstructions, not just the successful ones (as there were none).

By azimuthally integrating the PRTF one obtains an average trace that quantifies how reliably different spatial frequencies are reconstructed. The spatial frequency for which this trace drops below e^{-1} is typically quoted as the obtained resolution [6]. Figure 3.11 shows these traces for our 6 cases, with the e^{-1}-value indicated by a dot. It is interesting to see the dependence of this PRTF-based resolution criterium as a function of signal level, to compare the results of the monochromatization process to the narrowband case. Consider figure 3.12, which plots this value for 9 different signal levels, for the broadband and narrowband case. For high signal levels, the monochromatized case performs similar to the narrowband case (but for an acquisition time shorter by about a factor of 10). For low signal levels, the broadband case even outperforms the narrowband case, thanks to the noise-suppressing behavior introduced by the monochromatization step. The cross indicates the failed reconstruction of the lowest-signal narrowband case. The dotted lines at the bottom of the figure indicate the theoretical limit on the resolution. For the narrowband case, this limit is given by the Abbe limit for this numerical aperture, corresponding to a limit of 1.3 micron. For the broadband case the theoretical limit is imposed by the limited coherence length, as described by equation 2.7, corresponding to a limit of 3.3 micron. Instead of the PRTF, one can also look at the mean residual error after reconstruction (MRE), which takes the average distance between the retrieved and measured farfield amplitude, a slightly different way of quantifying the quality of the phase retrieval process. Here, the narrowband case clearly performs better for high signal levels, meaning that the monochromatization artifacts refrain the phase retrieval from reaching the same level of convergence as the narrowband case. Again for the low signal levels the noise-suppressing effect of the monochromatization comes into play and the broadband case outperforms the narrowband case for an equal signal level. Finally, as a more empirical and direct way of determining the resolution of the reconstructed sample, one can look at the size of the cracks in the membrane. They are visible in all high-signal reconstructions and disappear only below a signal level of 10^7 photons. Figure 3.14 shows the FWHM size of the reconstructed cracks in the sample membrane as a function of signal level. The behavior is similar to that of the other indicators, and because the reconstructed pixel size is about one micron, the error bars are large. Within error bars, the broadband and narrowband case yield similar results for the reconstructed

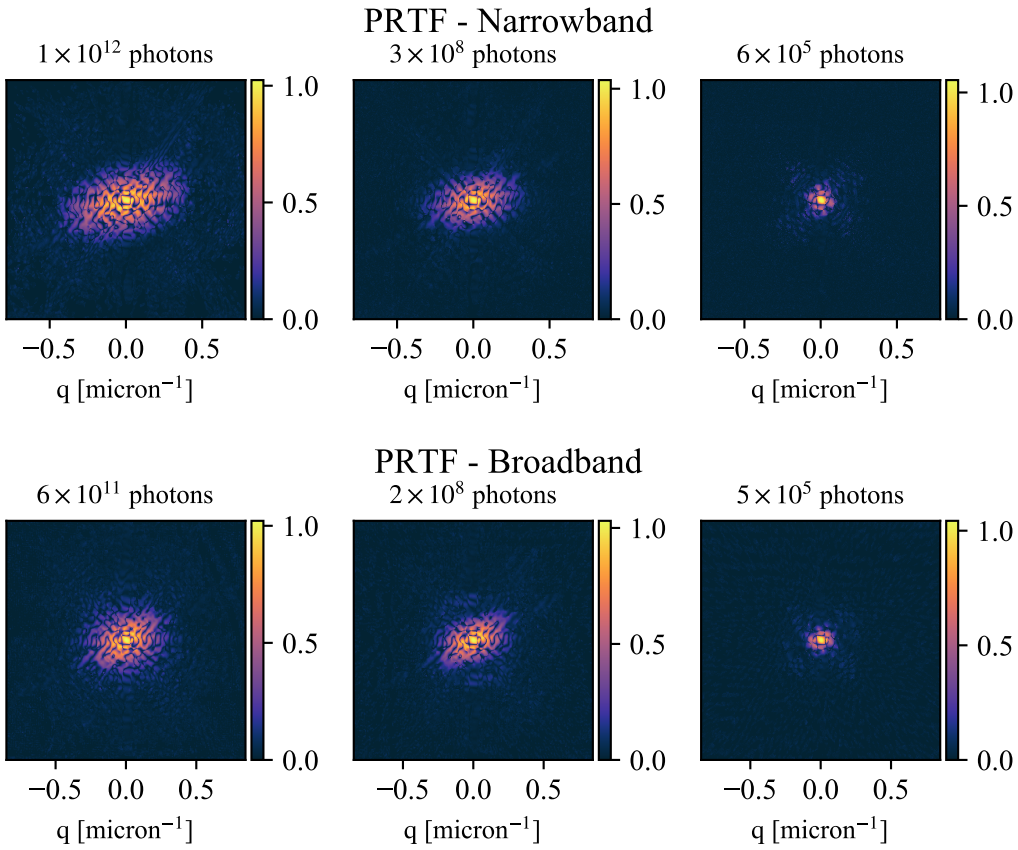

FIGURE 3.10: The phase retrieval transfer function (PRTF), calculated from 1024 independent reconstructions, for all six cases. Note that for the lowest signal level the narrowband and broadband PRTF look similar, but the broadband case could be reconstructed successfully, whereas the narrowband case could not.

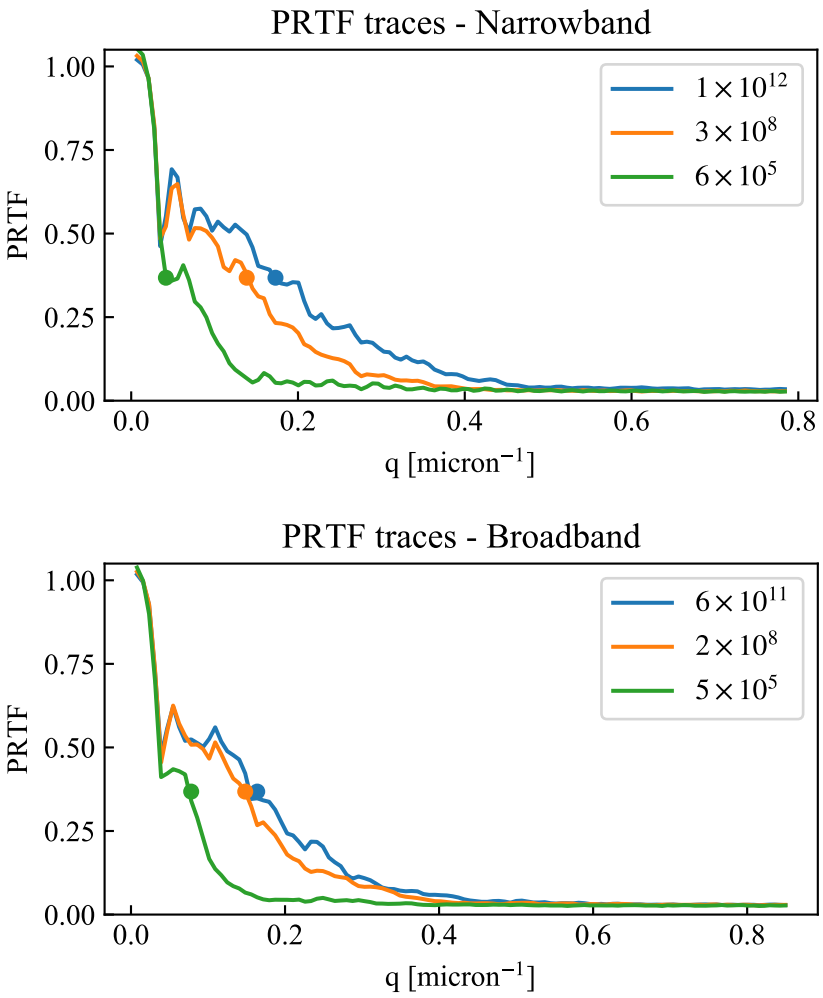

FIGURE 3.11: Traces of the PRTFs in figure 3.10, obtained by azimuthal integration. The dots mark the point where the PRTF drops below e^{-1}.

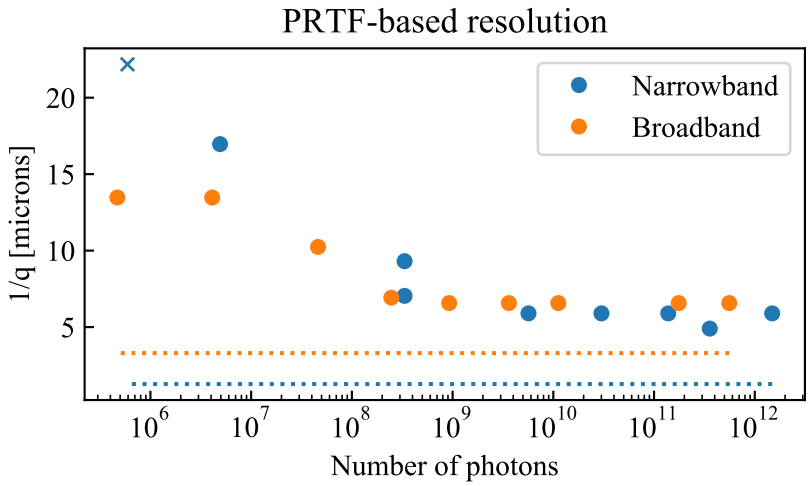

FIGURE 3.12: Comparison between the obtained "resolution" of the broadband and narrowband cases, determined as the value of q^{-1} for which the PRTF drops below e^{-1}. Thanks to the noise-suppressing properties of the monochromatization procedure, the broadband case even outperforms the narrowband case for low signal levels. The cross indicates that no successful reconstruction could be obtained. The dotted lines indicate the theoretical limits on the resolution, posed by the limited coherence length for the broadband case and by the Abbe limit for this NA for the narrowband case.

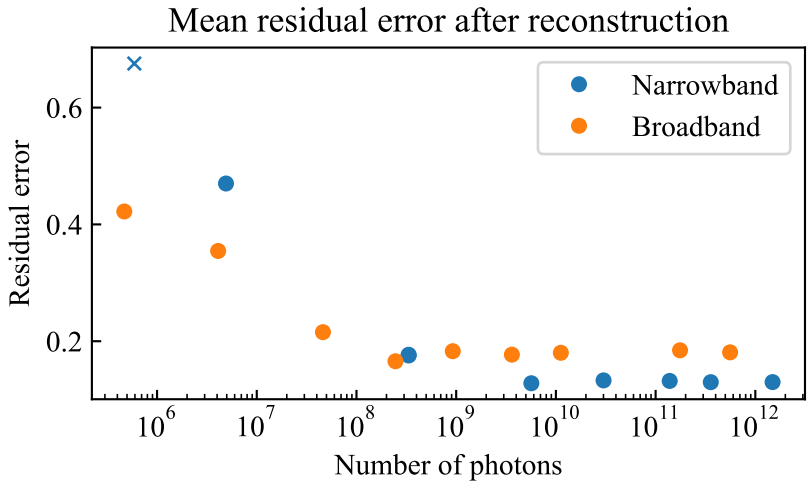

FIGURE 3.13: The mean residual error after phase retrieval, comparison between broadband and narrowband cases for different signal levels. Again, the broadband case outperforms the narrowband case for low signal levels. The cross indicates that no successful reconstruction could be obtained.

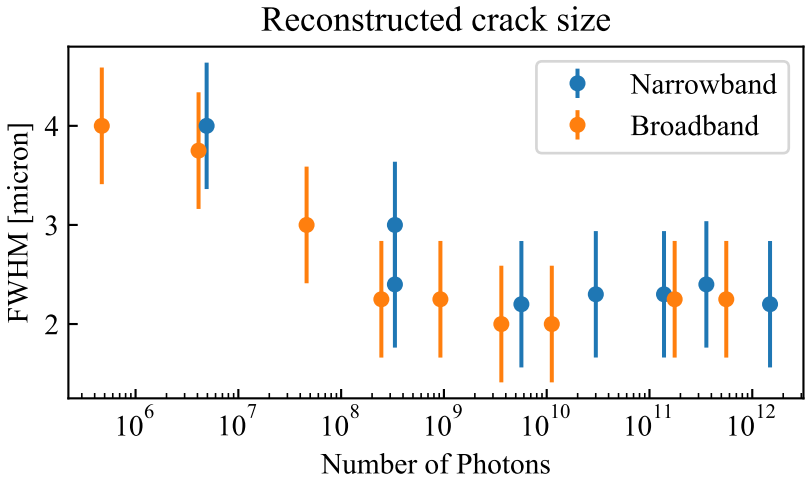

FIGURE 3.14: As a more empirical way of determining the resolution, the size of the reconstructed crack in the sample has been measured. As the reconstructed crack size is only 2-3 pixels, the measurement error is large. Within errorbars, the broadband and narrowband case yield similar results.

crack size.

3.5 Discussion

The binary sample and the relatively simple setup allow the monochromatization method itself to be investigated. The monochromatization procedure works as it is supposed to, but also has its limitations. It does indeed monochromatize the broadband pattern to an extent at which the phase retrieval algorithm readily reaches convergence and properly reconstructs the sample. It has a noise-suppressing effect that is beneficial at low signal levels. It does however also introduce artifacts in the monochromatized pattern, which reduce the reliability of the phase retrieval process. The behavior of semi-convergence is clear and easily controlled by the parameter k. The resolution limit posed by the limited coherence length of 3.3 micron has unfortunately not been reached (at least based on the PRTF-criterium), but neither did the reconstruction of the narrowband case. Other factors such as noise detection limit the resolution of these reconstructions to about 5 micron (PRTF-based).

3.6 Conclusions

In this experiment where the sample was binary and thus within the limits posed by the fundamental assumption of the monochromatization method, the method performed according to expectation. For similar signal levels the result of the broadband case were similar to that of the narrowband case, thus effectively allowing for a reduction in measurement time of an order of magnitude. It must be noted that the sample has a rather simple geometry, and thus a limited number of spatial frequencies need to be reconstructed. The promising result of this chapter encourages a validation of the method using X-ray radiation, on a more challenging sample geometry, as will first be explored through simulations in the next chapter.

Bibliography

[1] Henry N. Chapman, Anton Barty, Michael J. Bogan, Sébastien Boutet, Matthias Frank, Stefan P. Hau-Riege, Stefano Marchesini, Bruce W. Woods, Saša Bajt, W. Henry Benner, Richard A. London, Elke Plönjes, Marion Kuhlmann, Rolf Treusch, Stefan Düsterer, Thomas Tschentscher, Jochen R. Schneider, Eberhard Spiller, Thomas Möller, Christoph Bostedt, Matthias Hoener, David A. Shapiro, Keith O. Hodgson, David van der Spoel, Florian Burmeister, Magnus Bergh, Carl Caleman, Gösta Huldt, M. Marvin Seibert, Filipe R. N. C. Maia, Richard W. Lee, Abraham Szöke, Nicusor Timneanu, and Janos Hajdu. Femtosecond diffractive imaging with a soft-X-ray free-electron laser. *Nature Physics*, 2(12):839–843, December 2006. ISSN 1745-2473, 1745-2481. doi: 10.1038/nphys461.

[2] Julien Samaan. *Étude et Applications de l'imagerie sans Lentille Par Diffraction Cohérente*. Thesis, Paris Saclay, December 2016.

[3] Rémy Cassin. *Imagerie Nanométrique Ultra-Rapide Par Diffraction Cohérente de Rayonnement XUV Produit Par Génération d'harmoniques d'ordre Élevés*. Thesis, Paris Saclay, December 2017.

[4] David Gauthier. *Imagerie Nanométrique Ultra-Rapide Par Diffraction Cohérente de Rayonnement Extrême-UV Produit Par Génération d'harmoniques d'ordre Élevé*. Thesis, Paris 11, February 2012.

[5] Manuel Guizar-Sicairos, Samuel T. Thurman, and James R. Fienup. Efficient subpixel image registration algorithms. *Optics Letters*, 33(2):156, January 2008. ISSN 0146-9592, 1539-4794. doi: 10.1364/OL.33.000156.

[6] Henry N. Chapman, Anton Barty, Stefano Marchesini, Aleksandr Noy, Stefan P. Hau-Riege, Congwu Cui, Malcolm R. Howells, Rachel Rosen, Haifeng He, John C. H. Spence, Uwe Weierstall, Tobias Beetz, Chris Jacobsen, and David Shapiro. High-resolution ab initio three-dimensional x-ray diffraction microscopy. *Journal of the Optical Society of America A*, 23(5):1179, May 2006. ISSN 1084-7529, 1520-8532. doi: 10.1364/JOSAA.23.001179.

Chapter 4

X-ray simulations on broadband CDI and ptychography - applied to lithography mask inspection

4.1 Introduction

After the successful validation of the numerical monochromatization method in the visible we will apply the method using X-rays. As explained in Appendix D, X-rays have a number of peculiar properties that make them interesting for e.g. scientific imaging, notably their penetration power owing to a weak interaction with matter. In the hard x-ray regime, away from any absorption edges, the refractive index is close to constant and it is thus easier to find a realistic application that corresponds to the limit of a non-dispersive sample (Assumption 1). This chapter deals with simulated cases of broadband CDI and ptychography, the next chapter with an experimental validation.

4.2 Sample: EUV lithography mask

As explained in chapter 2 the monochromatization method works best with mask-like samples, as they are non-trivial but not constituted of different materials, which would introduce errors in the monochromatization process. An important example of the imaging of masks is in the semiconductor industry, where lithography masks are used to imprint patterns on an integrated circuit. Inspection of these masks is of utmost importance, as any appreciable error in a mask translates into a defect on the chip each time the mask is used. In the race of keeping up with Moore's law [1] (describing how miniaturization of integrated circuits doubles every two years) the lithography industry has been moving to sources of smaller wavelength, leading to machines currently being developed at a source wavelength of 13.5 nm, so-called EUV lithography. One of the major hurdles for the adoption of EUV lithography by the semiconductor industry is the inspection of the lithography masks [2, 3]. These masks work in reflection off a multilayer mirror, and the EUV is sensitive to defects not only on the surface, but also within the multilayer. One of the options is to use hard X-rays, as explored in this chapter. EUV lithography masks consist of a patterned absorber (typically TaBN) deposited on a multilayer mirror on a quartz substrate, as schematically depicted in figure 4.1. Provided the substrate is sufficiently thin and homogeneous, the absorber pattern can be imaged in transmission geometry through coherent diffractive imaging using hard X-rays, greatly simplifying the experimental setup. It can in principle offer single nanometer resolution and even be sensitive to defects in the multilayer mirror. Note that there is a magnification factor of 4 between the mask and the wafer, which is advantageous for inspection. For this simulation the sample was assumed to have a perfectly flat substrate and multi-layer mirror, such that

FIGURE 4.1: Schematic representation of Ta-based EUV photomasks. Adapted from [4].

only the absorber needs to be taken into account. The reason for this simplification is that the simulation procedure assumes a weakly interacting sample (see below), which is no longer the case for a significant substrate.

4.3 Inverse Compton Scattering sources

Synchrotron sources (see also next chapter) are the work-horses of science when it comes to X-rays. However as they are large-scale facilities their access is limited. As an in-house alternative to synchrotron sources one could use the emerging Inverse Compton Scattering (ICS) sources [5–7]. These compact, 'table-top' sources offer high flux (10^{10}-10^{14} photons/s) X-ray radiation from a compact setup, but with a large bandwidth (typically 3-10%). The physical mechanism behind the X-ray generation is the inverse Compton scattering of laser photons off a relativistic electron bunch. The scattered photons gain energy from the electrons and are emitted in the X-ray regime, with a maximum energy of

$$E_{max} = 2\gamma^2 E_L(1+\cos\theta_c), \tag{4.1}$$

where θ_c is the collision angle between the electrons and the laser (typically close to π, so head-on), E_L is the laser photon energy and γ is the Lorentz factor for the relativistic electrons ($\gamma = (1-v^2/c^2)^{-1/2}$). This maximum energy is emitted on axis; it corresponds to perfectly back-scattered photons. Off-axis the emitted energy slowly drops off, following

$$E_X = \frac{E_{max}}{1+\gamma^2\theta_X^2}, \tag{4.2}$$

where θ_X is the angle between the emitted X-rays and the electron beam axis (see e.g. [8]). Two schemes exist, as depicted in figure 4.2a. In the linac scheme (*bottom*) the inverse Compton scattering takes place directly after the linear accelerator; the electron bunches are used only once for X-ray generation. In the storage ring scheme (*top*) an electron bunch is recycled many times before it is dumped. A storage ring can therefore operate at high repetition rates (MHz-scale) without the need for superconducting accelerating structures, but the quality of the electron bunch (the emittance) degrades as the bunch circulates in the storage ring. Several initiatives to build ICS sources exist all over the world: one is ThomX at the Laboratoire de l'accélérateur linéaire (LAL) in Orsay, France. Figure 4.2b shows a drawing of the machine. The electron bunches are created at 50 Hz by an RF photogun (1), accelerated to 50 MeV in the linac (3), to then circulate at 17.84 MHz in the storage ring. Each 20 ms, the bunch is dumped (11) and a new bunch enters the ring. This storage ring has a circumference of 16.8 m (compact compared to the 345 m of synchrotron Soleil mentioned in the next chapter). On the left of the setup an Ytterbium-doped fiber laser system with an output of 50-100 W is coupled to a Fabry-Perot cavity. Inside the cavity the 5 ps pulses resonate and the power increases until the losses equal the input power. Thanks to the very high quality of the cavity the power

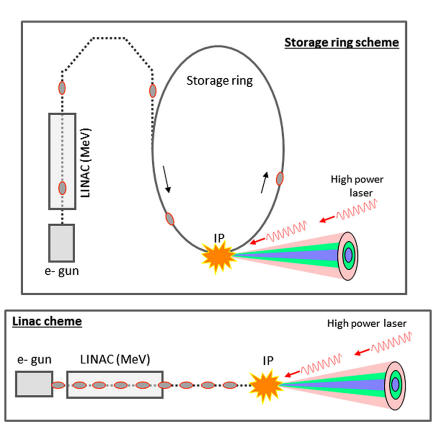

(A) Two main schemes exist for ICS sources. In the linac scheme (*bottom*) the electron bunches are used only once for X-ray generation, in the storage ring scheme (*top*) an electron bunch is reused many times before it is dumped. Taken from [9].

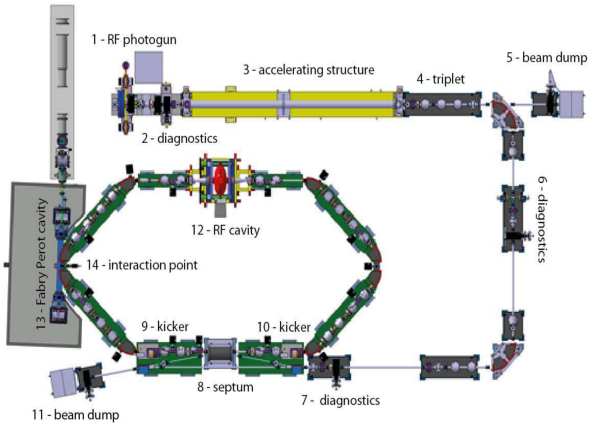

(B) The setup of ThomX, the inverse Compton scattering source being built at LAL, Orsay, implementing the storage ring scheme. Explanation in the main text. Taken from [5]

FIGURE 4.2: Inverse Compton scattering source layout.

inside the cavity is on the order of 100 kW. At the interaction point (14) the electron beam collides with the laser beam, generating hard X-rays at 17.84 MHz repetition rate. Following equations 4.1 and 4.2 the emitted X-ray pulse inherits the spectral bandwidth of the laser pulse. A Fourier limited ps-scale pulse at 1 micron wavelength has a bandwidth of less than a percent. However, the electron bunch has an energy spread itself, and both the electron bunch and the laser pulse have a finite divergence, contributing to the X-ray bandwidth on the percent, ten percent and percent level respectively (see [8]). To make this more concrete, consider the result of the Monte Carlo simulation performed by Dr. C. Bruni *et. al.* using the parameters for ThomX, displayed in figure 4.3a. The figure shows a 2D histogram of the spectral intensity (emitted X-ray photons per second per steradian per eV bandwidth), in X-ray energy bins of 33.8 eV and emission angle θ_X bins of 0.2 mrad. The marginal plots show the spectrum obtained after integration over all emission angles (photons per second per eV bandwidth, left), and the radiant intensity (spectral intensity integrated over all energies), as a function of emission angle (photons per second per steradian in a 0.2 mrad bin, bottom). The data shown is an average over the 20 ms that an electron bunch spends in the storage ring (and thus an average over the expected emittance degradation during that storage time). The figure shows how the X-ray energy and intensity is highest on-axis (corresponding to a head-on collision and thus the highest energy transfer from the electron to the photon) and decreases for increasing angle θ_X, as described by equations 4.1 and 4.2. It also shows the finite bandwidth of the source, mainly as a result of a finite energy spread and divergence of the electron bunch [8]. Figure 4.3b shows the spectral intensity on axis, which features a $\Delta E/E$ bandwidth of 5 % (FWHM). Judging from the results of the previous chapter, this is exactly the kind of bandwidth where the numerical monochromatization method can be applied.

4.3.1 Spatial coherence of ICS sources

The ICS process is treated incoherently: photons scatter off electrons, in the physical picture no wave information is used. It has not yet been studied whether the emitted X-rays inherit some coherence from the laser pulse, so for the moment the source should be regarded as a spatially incoherent source as described in Appendix C. This is detrimental

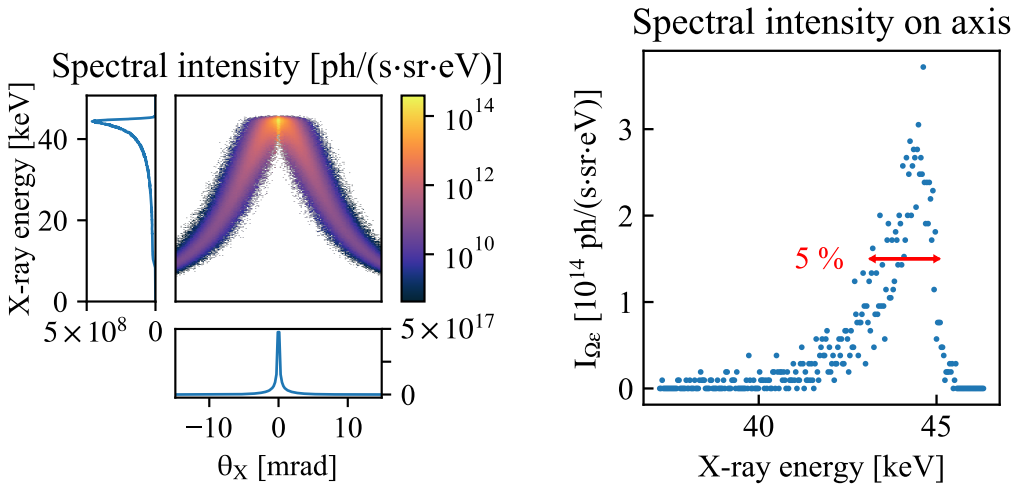

(A) Histogram of the radiant intensity in X-ray energy bins of 2.67 eV and emission angle θ_X bins of 0.2 mrad. The marginal plots show the spectrum obtained after integration over all emission angles (photons per second in a 2.67 eV bin, left), and the radiant intensity integrated over all energies, as a function of emission angle (photons per second per steradian in a 0.2 mrad bin, bottom).

(B) On-axis spectral intensity, showing a FWHM bandwidth of 5 %. This bandwidth is mainly the result of a finite energy spread and divergence of the electron bunch.

FIGURE 4.3: ThomX spectrum obtained from Monte Carlo simulations using CAIN [10]. Data courtesy of Dr. C. Bruni, Laboratoire de l'accélérateur linéaire, Orsay.

to the usable flux for coherent imaging applications. With a source size on the order of tens of microns, and an X-ray energy on the order of tens of keV, the spatial coherence is on the order of a micron at 1 m distance from the source (Appendix C). Hence in order to produce coherent diffraction patterns, the angle subtended by the sample from the source should be on a microradian-scale. Of course, this comes at a cost of flux: integrating the curve of figure 4.3b gives about 5×10^{17} ph/(s·sr), meaning about 5×10^5 ph/s in a μrad^2 solid angle. At the moment this source is not sufficiently bright for a realistic CDI experiment. The emittance of the electron beam would have to be reduced. As the flux is roughly proportional to the density of photons and electrons in the interaction region [8], the flux could be kept constant for a smaller source, thus increasing the coherent part of the flux. An ICS source with a source size on the order of 2 microns is under development at MIT [11], and a source using microbunching is proposed [12], increasing its coherence. It could also be beneficial to lower the X-ray energy to have a stronger interaction at the sample.

4.4 Simulation tool: Condor

For this validation broadband diffraction patterns are generated. The quickest way to do so would be starting from a monochromatic pattern and multiplying it by the matrix **C** introduced in the previous chapters. The goal of this simulation is however to validate the method, so it is best to make use of an external, already validated code to generate the diffraction patterns. For this purpose use was made of *Condor* [13, 14], a simulation tool used by the VUV and XFEL community for (flash) X-ray imaging. This code makes use of the first Born approximation (weak interaction with the sample, see Appendix D)

Variable	Value	Unit
X-ray central energy	8	keV
total number of photons	10^{14}	photons
sample dx	10	nm
mask thickness	60	nm
distance sample-detector	2 (2.25)	m
detector size	512×512	pixels
detector pixel size	30	μm
reconstructed pixel size	20.2 (22.7)	nm

TABLE 4.1: Values used for the broadband X-ray CDI simulations.

to calculate the farfield diffraction pattern from a 3-dimensional sample, for a certain X-ray energy, photon number and as a function of detector specifications. The sample is uploaded as a 3-dimensional array of refractive index values, from which the monochromatic diffraction pattern is computed. To obtain the broadband pattern, this function was called in a loop while scanning the X-ray energy. The monochromatic patterns were then summed incoherently to obtain the broadband pattern. These calculations were performed on the *Davinci* computer cluster of the Laboratory of Molecular Biophysics (Collaboration with F. Maia, Uppsala University, Sweden).

4.5 Results in CDI

The "experimental" conditions used in these simulations are indicated in table 4.1. The sample mask used for the simulation is shown in figure 4.4a. In the simulation the mask was made of TaBN, at a thickness of 60 nm. The voxels of the sample array are 10 nm in each dimension. Figure 4.4b shows the monochromatic diffraction pattern of a single energy slice, at the central energy of 8 keV. In the simulation a monochromatic pattern was calculated for each of the energy points in the spectrum. The three gaussian spectra used for the CDI simulation, with bandwidths of 5, 10 and 15 % are plotted in figure 4.5, with a dot for each energy slice. The total number of photons was kept constant during the simulations, i.e. the total scan always consisted of 10^{14} photons at the source, spread out over different bandwidths. The simulation also returns the phase for one of the monochromatic patterns. Through the inverse Fourier transform of this pattern we have the ideal reconstruction, with which the results obtained after monochromatization and phase retrieval can be compared and an error can be estimated.

The broadband pattern at 5 % bandwidth is shown in the left panel of figure 4.6a. This pattern is the sum of 101 monochromatic patterns, and the radial blurring is obvious. The monochromatized pattern (same figure, right panel) regains the sharp features of the monochromatic pattern. Its reconstruction through CDI shows all features of the mask (left panel of figure 4.6b). The reconstruction is however not perfect, as shown in the panel on the right. This panel shows the difference between the obtained reconstruction and the ideal reconstruction as explained above. To quantify this error, the reconstructions are normalized to a scale from 0 to 1 and the standard deviation of the error image is computed, 0.12 for the case of 5 % bandwidth. The same procedure was applied to the case with 10 % bandwidth, the results of which are shown in figure 4.7a and 4.7b. The quality of the reconstruction is similar to that of the 5 % bandwidth case, judging from the error and the reconstruction itself. Finally, at 15 % bandwidth the method starts to break

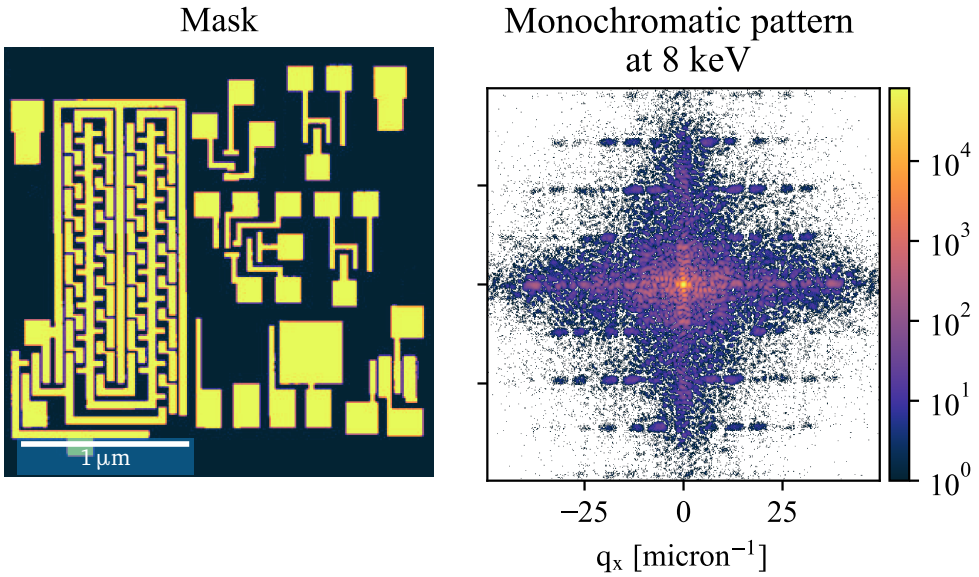

(A) The mask used for the broadband X-ray CDI simulations. Only the absorber layer is taken into account.

(B) Monochromatic diffraction pattern of the lithography mask at 8 keV.

FIGURE 4.4: Sample and its monochromatic diffraction pattern, calculated using *Condor*.

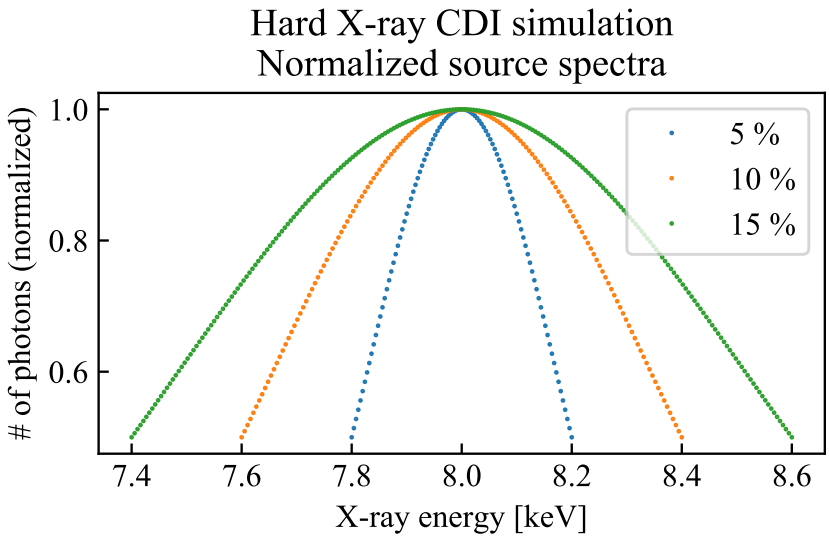

FIGURE 4.5: Normalized source spectra as used in the hard X-ray simulation, all Gaussian with bandwidths of 5, 10 and 15 %.

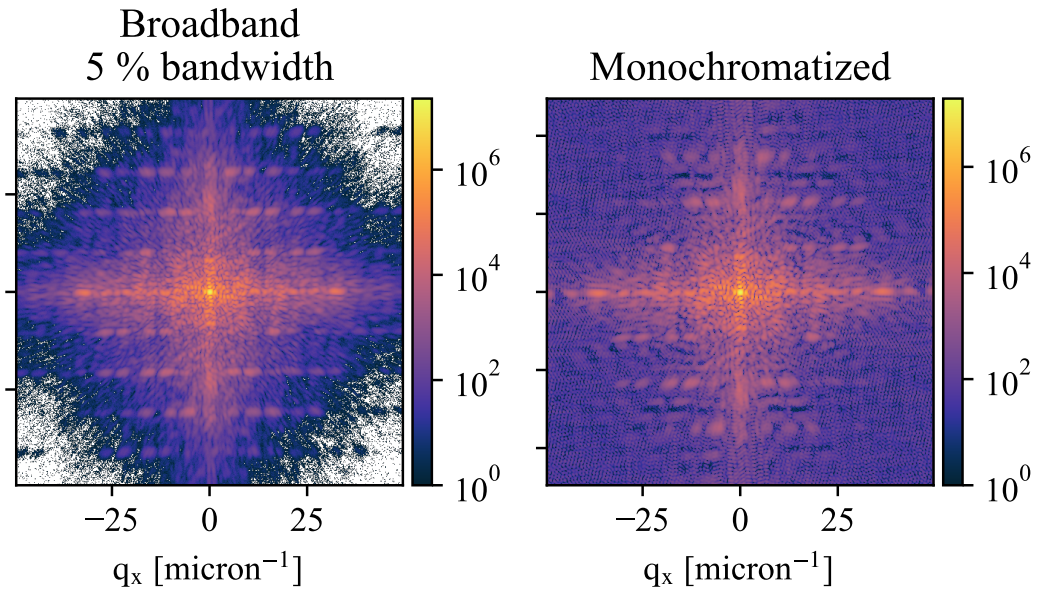

(A) The broadband pattern (*left*) is the sum of 101 monochromatic patters at 5 % bandwidth at 8 keV. The monochromatized pattern (*right*) shows some artifacts.

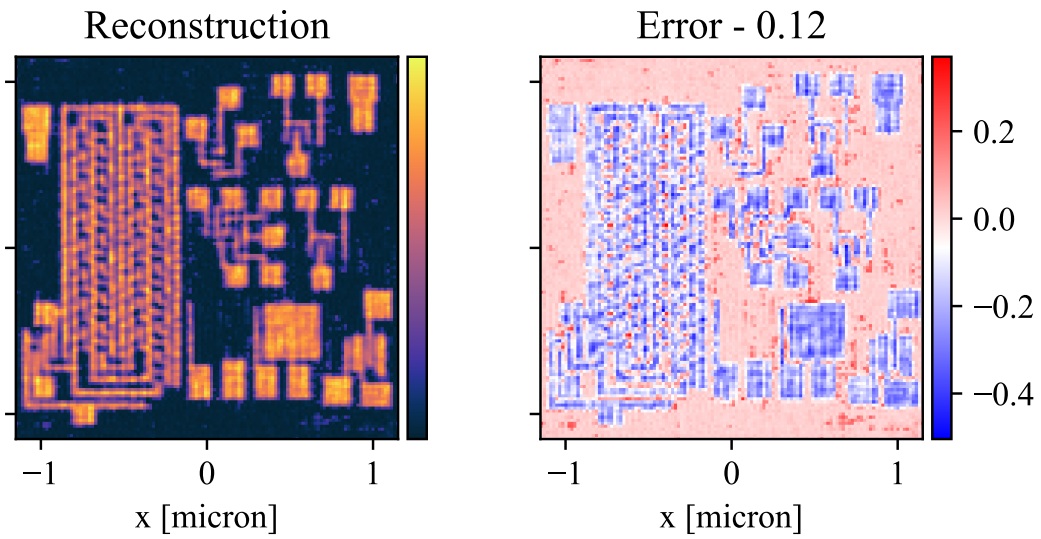

(B) Amplitude of the reconstructed sample at 5 % bandwidth (*left*). Its error is calculated through comparison with the inverse Fourier transform of the simulated pattern.

FIGURE 4.6: Simulation results at 5 % bandwidth

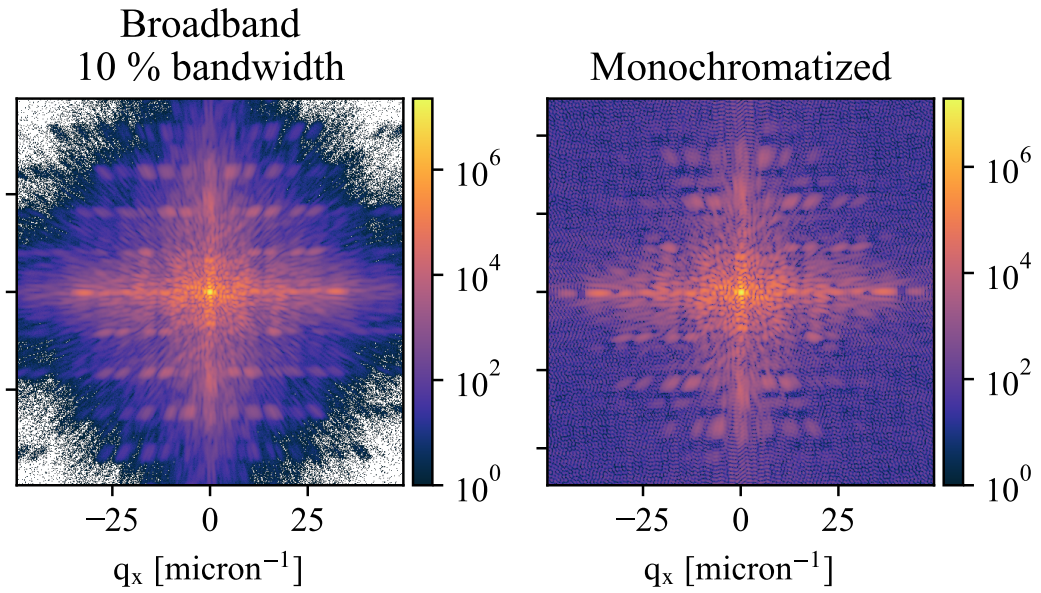

(A) The broadband pattern (*left*) is the sum of 151 monochromatic patters at 10 % bandwidth at 8 keV and shows strong radial blurring. The monochromatized pattern (*right*) shows some artifacts.

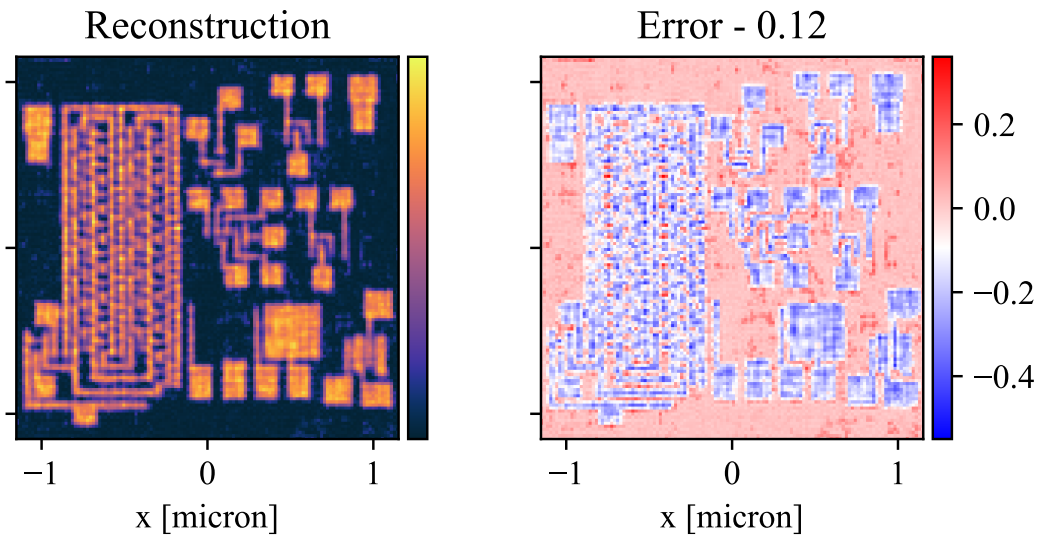

(B) Amplitude of the reconstructed sample at 10 % bandwidth (*left*). Its error (*right*) is calculated through comparison with the inverse Fourier transform of the simulated pattern.

FIGURE 4.7: Simulation results at 10 % bandwidth

down. Initially no successful reconstruction was obtained, despite launching 10 independent phase retrievals for all monochromatized patterns ranging from $k = 10 - 35$. Apparently the errors in the monochromatized patterns grew too large and inhibited proper phase retrieval. By increasing the sample-detector distance from 2 m to 2.25 m (in parentheses in table 4.1), keeping all other variables constant, thus effectively improving the sampling of the broadband pattern by sacrificing the maximally obtainable resolution, these errors could be reduced and a reasonable reconstruction was achieved, as shown in figure 4.8b, with an increased error of 0.19.

4.6 Results in ptychography

Real lithography masks are a lot larger that the sample shown in the previous section. It could therefore be desirable to extend the monochromatization method to ptychography (lensless imaging technique where a probe is scanned over an extended sample, see Chapter 2). Using the same parameters as in the previous section (table 4.1), but with a sample that is 4 times as large in each direction, a ptychography experiment was simulated for three cases: monochromatic, 5% bandwidth, and 10 % bandwidth. A supergaussian probe beam with a diameter of 2.4 micron ($1/e^2$) scanned the sample at 32×32 positions. At each position the monochromatic patterns were accumulated at different energies to obtain a broadband pattern. These broadband patterns were then monochromatized and the set of monochromatized patterns and probe locations were used as input for a ptychographic reconstruction, in collaboration with Dr. S. Fernandez (CEA, former Paul Scherrer Institute, Switzerland) [3, 15]. Figure 4.9 shows the result of the monochromatic case at 8 keV, obtained after 130 iterations, showing all sample details. The reconstruction at 5 % bandwidth as shown in figure 4.10 is of similar quality as the monochromatic case, maybe even slightly better (which could indicate that the monochromatic reconstruction was stopped preliminarily). This result was obtained after 300 iterations of the ptychography algorithm. The error image is calculated with respect to the monochromatic reconstruction, in the same way as for the CDI case described in the previous section. At 10 % bandwidth the reconstruction has clearly lost in resolution. It was also more difficult to reach convergence, as the reconstruction needed 1000 iterations, and multiple modes were used for the probe (meaning that for the reconstruction not just a single coherent probe was assumed but a sum of mutually incoherent probes) [16]. This indicates that the errors introduced by the monochromatization process have become more significant, introducing non-physical features that change from one pattern to the next. The constraint of a single probe thus prevents convergence, while having a multi-mode probe allows for some extra degrees of freedom to cope with these errors, leading to convergence at the expense of a higher computation time.

4.7 Conclusions

This chapter shows that according to simulations the numerical monochromatization method can be applied to X-ray imaging of samples which comply with Assumption 1 of a spatially non-dispersive sample, with bandwidths up to 15 %. A case of societal relevance was presented, namely that of lithography mask inspection with inverse Compton scattering sources. Although the coherent fraction of the flux of these sources is insufficient at the moment for a practical realization, simulations show that the monochromatization method can cope very well with the large spectral bandwidth of these sources. Successful combination of the method with an external ptychography code shows the versatility of the method. Ptychography allows imaging extended samples, and is more robust to

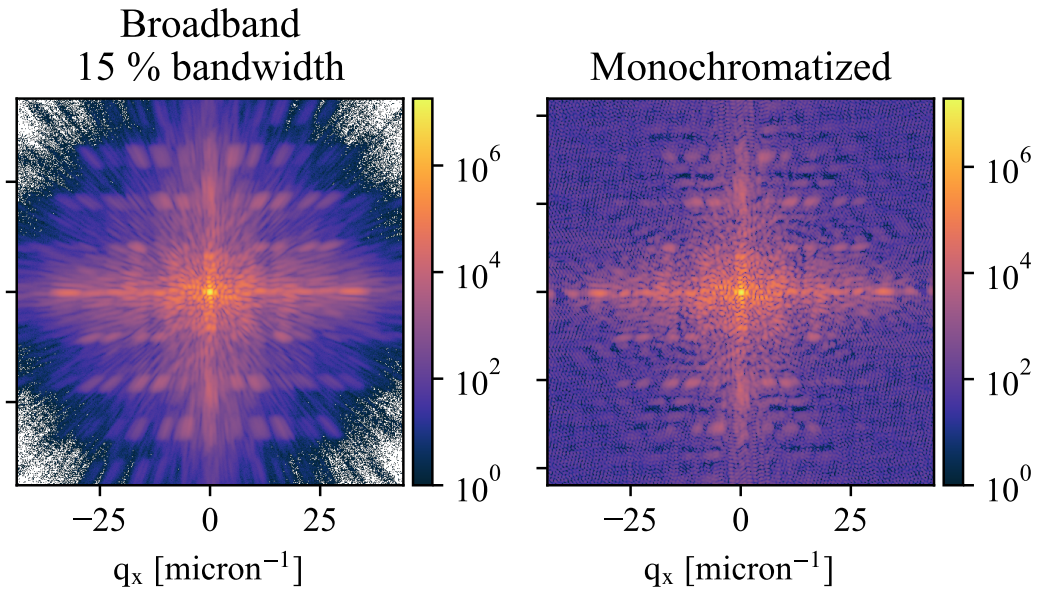

(A) The broadband pattern (*left*) is the sum of 225 monochromatic patters at 15 % bandwidth at 8 keV and shows strong radial blurring. The artifacts in the monochromatized pattern (*right*) have become stronger.

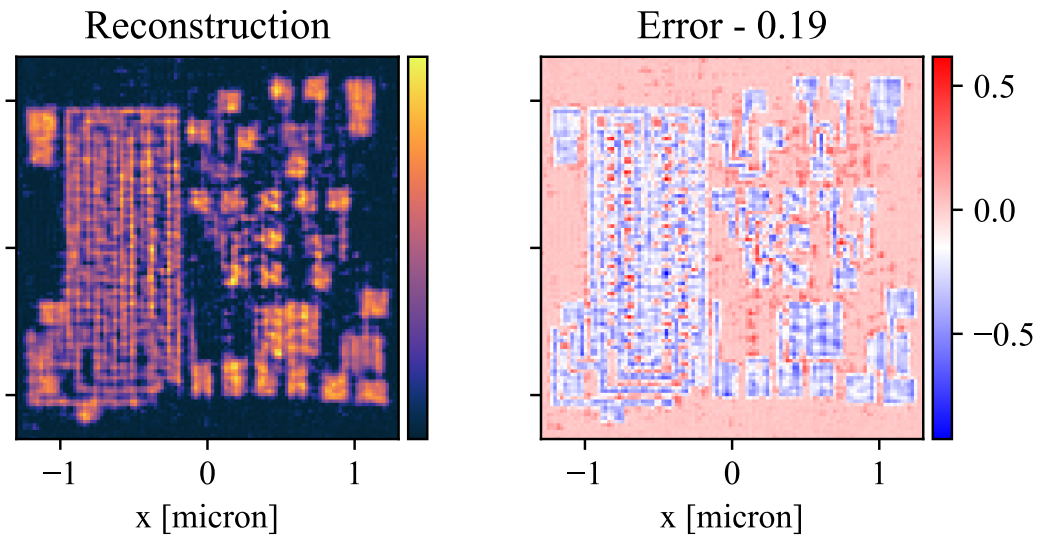

(B) Amplitude of the reconstructed sample at 15 % bandwidth (*left*), which is getting significantly worse. Its error (*right*) is calculated through comparison with the inverse Fourier transform of the simulated pattern.

FIGURE 4.8: Simulation results at 15 % bandwidth

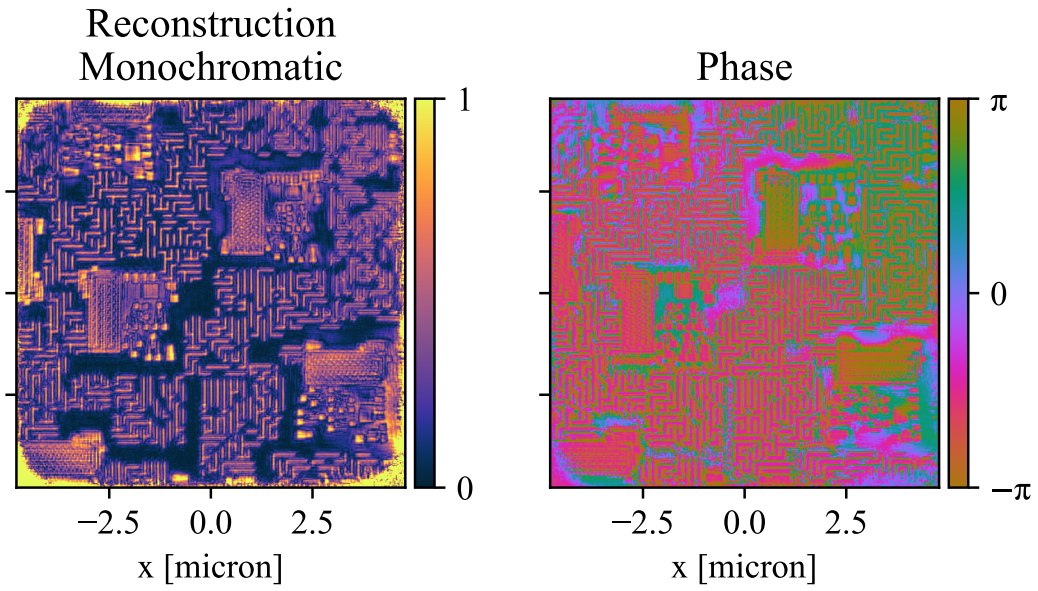

FIGURE 4.9: Ptychographic reconstruction of the extended mask sample, monochromatic case at 8 keV. This reconstruction acts as a reference for the broadband reconstructions.

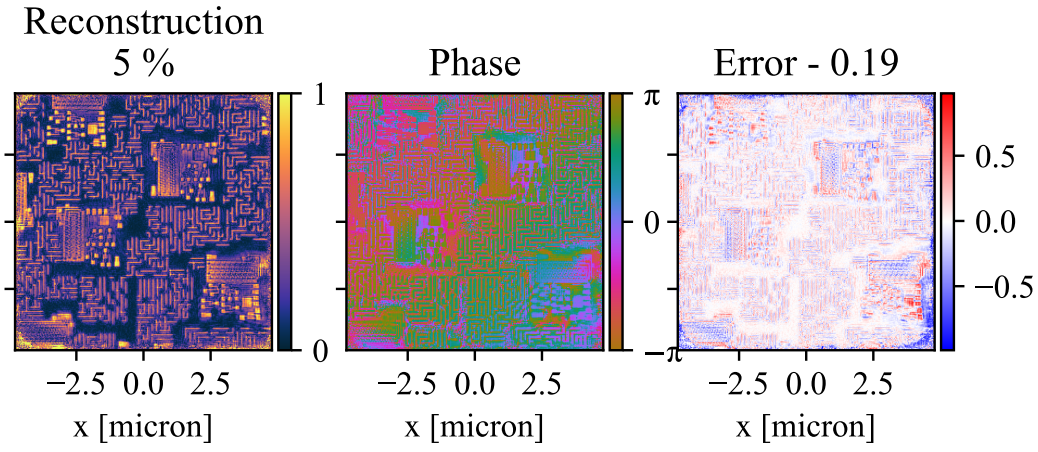

FIGURE 4.10: Ptychographic reconstruction of the extended mask sample at 5 % bandwidth. The quality of the reconstruction is similar to the monochromatic reconstruction. The error is computed with respect to the monochromatic reconstruction.

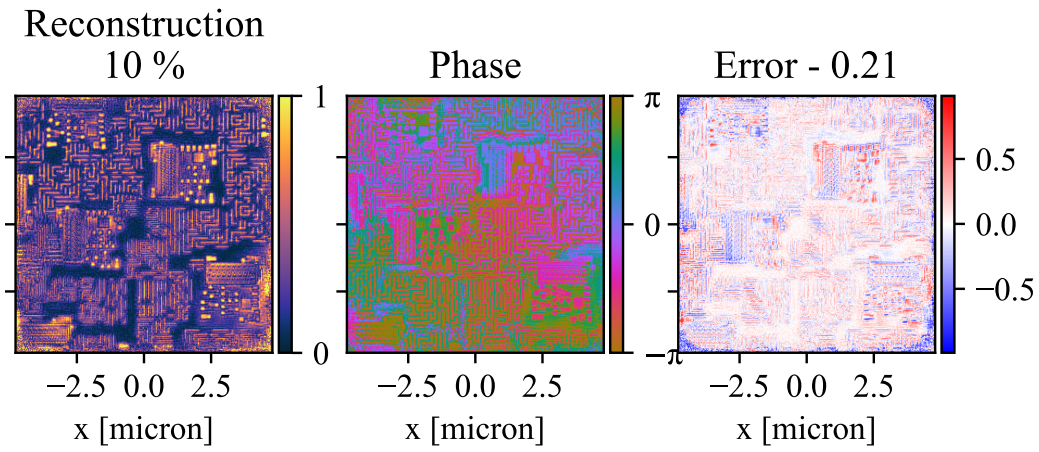

FIGURE 4.11: Ptychographic reconstruction of the extended mask sample at 10 % bandwidth. The quality of the reconstruction is getting worse, as indicated by the increased error.

noise thanks to the redundancy of the method. There is also room for improvement, as the resolution of the presented results is not yet at the scale needed for the semiconductor industry (a few nm), but the principle of the application of the numerical monochromatization method using hard X-rays on broadband sources is shown to be viable.

Bibliography

[1] Gordon E. Moore. Lithography and the future of Moore's law. In *Integrated Circuit Metrology, Inspection, and Process Control IX*, volume 2439, pages 2–18. International Society for Optics and Photonics, May 1995. doi: 10.1117/12.209195.

[2] Markus R. Weiss, Dirk Hellweg, Markus Koch, Jan Hendrik Peters, Sascha Perlitz, Anthony Garetto, Krister Magnusson, Renzo Capelli, and Vibhu Jindal. Actinic review of EUV masks: Status and recent results of the AIMS EUV system. In Obert R. Wood and Eric M. Panning, editors, *SPIE Advanced Lithography*, page 942219, San Jose, California, United States, March 2015. doi: 10.1117/12.2086265.

[3] Patrick Helfenstein, Iacopo Mochi, Rajendran Rajeev, Sara Fernandez, and Yasin Ekinci. Coherent diffractive imaging methods for semiconductor manufacturing. *Advanced Optical Technologies*, 6(6), December 2017. ISSN 2192-8584, 2192-8576. doi: 10.1515/aot-2017-0052.

[4] Sara Fernandez, Dimitrios Kazazis, Rajeev Rajendran, Iacopo Mochi, Patrick Helfenstein, Shusuke Yoshitake, and Yasin Ekinci. Comparative study of extreme ultraviolet absorber materials using lensless actinic imaging. *Journal of Micro/Nanolithography, MEMS, and MOEMS*, 18(01):1, March 2019. ISSN 1932-5150. doi: 10.1117/1.JMM.18.1.013506.

[5] A Variola, J Haissinski, A Loulergue, and F Zomer. ThomX Technical Design Report. Technical report, Laboratoire de l'Accélérateur Linéaire (LAL), Orsay, 2014.

[6] W. S. Graves, J. Bessuille, P. Brown, S. Carbajo, V. Dolgashev, K.-H. Hong, E. Ihloff, B. Khaykovich, H. Lin, K. Murari, E. A. Nanni, G. Resta, S. Tantawi, L. E. Zapata, F. X. Kärtner, and D. E. Moncton. Compact x-ray source based on burst-mode inverse

Compton scattering at 100 kHz. *Physical Review Special Topics - Accelerators and Beams*, 17(12), December 2014. ISSN 1098-4402. doi: 10.1103/PhysRevSTAB.17.120701.

[7] Benedikt Günther, Martin Dierolf, Regine Gradl, Elena Eggl, Christoph Jud, Lorenz Hehn, Stephanie Kulpe, Bernhard Gleich, Madleen Busse, Kaye S. Morgan, Klaus Achterhold, and Franz Pfeiffer. The Munich Compact Light Source: Biomedical Research At a Laboratory-Scale Inverse-Compton Synchrotron X-ray Source. *Microscopy and Microanalysis*, 24(S1):984–985, August 2018. ISSN 1431-9276, 1435-8115. doi: 10.1017/S143192761800541X.

[8] M. Jacquet and C. Bruni. Analytic expressions for the angular and the spectral fluxes at Compton X-ray sources. *Journal of Synchrotron Radiation*, 24(1):312–322, January 2017. ISSN 1600-5775. doi: 10.1107/S1600577516017227.

[9] M. Jacquet. High intensity compact Compton X-ray sources: Challenges and potential of applications. *Nuclear Instruments and Methods in Physics Research Section B: Beam Interactions with Materials and Atoms*, 331:1–5, July 2014. ISSN 0168583X. doi: 10.1016/j.nimb.2013.10.078.

[10] P. Chen, G. Horton-Smith, T. Ohgaki, A. W. Weidemann, and K. Yokoya. CAIN: Conglomérat d'ABEL et d'Interactions Non-linéaires. *Nuclear Instruments and Methods in Physics Research Section A: Accelerators, Spectrometers, Detectors and Associated Equipment*, 355(1):107–110, February 1995. ISSN 0168-9002. doi: 10.1016/0168-9002(94)01186-9.

[11] W. S. Graves, W. Brown, F. X. Kaertner, and D. E. Moncton. MIT inverse Compton source concept. *Nuclear Instruments and Methods in Physics Research Section A: Accelerators, Spectrometers, Detectors and Associated Equipment*, 608(1, Supplement): S103–S105, September 2009. ISSN 0168-9002. doi: 10.1016/j.nima.2009.05.042.

[12] W. S. Graves, F. X. Kärtner, D. E. Moncton, and P. Piot. Intense Superradiant X Rays from a Compact Source Using a Nanocathode Array and Emittance Exchange. *Physical Review Letters*, 108(26):263904, June 2012. doi: 10.1103/PhysRevLett.108.263904.

[13] Max F. Hantke, Tomas Ekeberg, and Filipe R. N. C. Maia. *Condor* : A simulation tool for flash X-ray imaging. *Journal of Applied Crystallography*, 49(4):1356–1362, August 2016. ISSN 1600-5767. doi: 10.1107/S1600576716009213.

[14] Max Felix Hantke. *Coherent Diffractive Imaging with X-Ray Lasers*. PhD thesis, Uppsala University, 2016.

[15] Patrick Helfenstein, Rajendran Rajeev, Iacopo Mochi, Armin Kleibert, C. a. F. Vaz, and Yasin Ekinci. Beam drift and partial probe coherence effects in EUV reflective-mode coherent diffractive imaging. *Optics Express*, 26(9):12242–12256, April 2018. ISSN 1094-4087. doi: 10.1364/OE.26.012242.

[16] Pierre Thibault and Andreas Menzel. Reconstructing state mixtures from diffraction measurements. *Nature*, 494(7435):68–71, February 2013. ISSN 1476-4687. doi: 10.1038/nature11806.

Chapter 5

Hard X-ray broadband CDI experiments using synchrotron radiation

5.1 Introduction

The simulations of the previous chapter validate the step towards the experimental demonstration. To test the method for broadband CDI with hard X-rays, campaigns at different synchrotrons were performed. Ideally one would use a broadband (white) spectrum, out of which to cut spectra with different bandwidths by using a combination of filters and mirrors at grazing incidence. This was however not accessible. An alternative is to perform the experiment using an approach similar to the simulation detailed in previous chapter: taking monochromatic diffraction patterns at finely spaced discrete energy levels, a quasi-continuous dataset is obtained from which broadband patterns can be made with the desired spectral bandwidth. The first experiment was performed at B16, a bending magnet beamline at the Diamond Light Source at Didcot, UK. The 48-hour time-slot we were given was not sufficient to align, characterize and solve a number of issues with the setup. It was however a good exercise for the second synchrotron beamtime, at the Nanoscopium beamline at Soleil, Saint-Aubin, France, the results of which are the main body of this chapter.

5.2 Synchrotron sources

A charge moving along a curved trajectory emits radiation. Synchrotrons are large scale installations that use this effect to produce X-rays, by accelerating electrons to relativistic velocities and sending them through magnetic fields thus bending their trajectory and emitting radiation in a forward-pointing cone of half-angle [1, 2].

$$\theta \approx \frac{1}{\gamma} \tag{5.1}$$

where $\gamma = 1/\sqrt{1-(v/c)^2}$ is the relativistic Lorentz factor. The emitted radiation is characterized by a critical wavelength[1]

$$\lambda = \frac{4\pi R}{3}\frac{1}{\gamma^3} \tag{5.2}$$

with R the radius of curvature of the electrons trajectory. In a synchrotron, electron bunches circle in a large storage ring (typical diameter several hundreds of m), where

[1] Half of the power is emitted at wavelengths below the critical wavelength.

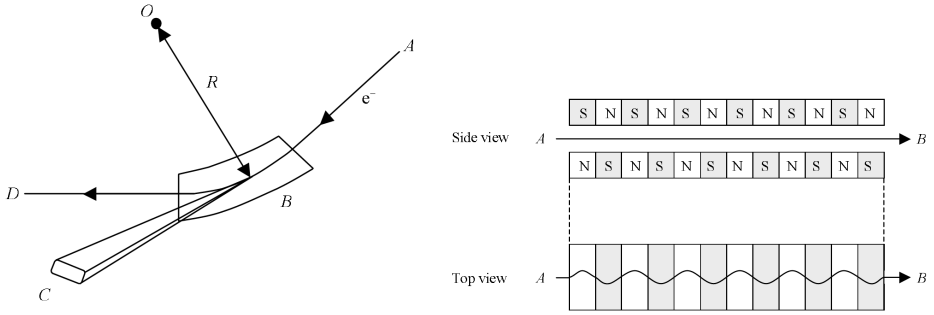

(A) A bending magnet (B) An insertion device (wiggler or undulator)

FIGURE 5.1: Schematic representations of the two radiation sources in a synchrotron. Images taken from [1].

their path is deflected inward each time they pass a so-called bending magnet. At each bending magnet radiation is emitted as depicted in figure 5.1a. This radiation has a broad spectrum and is only spatially coherent through propagation (as with the ICS source in the previous chapter). In addition to these bending magnets, modern synchrotrons (so-called 'third generation') use 'insertion devices' to generate X-rays with a higher brightness. This device is schematically depicted in figure 5.1b. It is like having a sequence of small bending magnets with opposite magnetic fields, and at each curve a burst of radiation is emitted. This is called a 'wiggler'. The magnet period can be made so short that on-axis emission combines coherently - in that case one speaks of an undulator. The spatially coherent fraction of undulator radiation is given by [2]

$$\eta_{sc} = \frac{\lambda^2}{(4\pi)^2 \epsilon_x \epsilon_y} \tag{5.3}$$

where $\epsilon = \sigma\sigma'$ is the electron beam emittance (product of source size and divergence). The spectrum of an undulator consists of harmonic peaks at those wavelengths for which the emitted X-rays interfere constructively. Its coherence length is given by [2]

$$l_c = qN\lambda \tag{5.4}$$

where N is the number of magnet periods and q is the harmonic order.

5.3 Sample preparation

At photon energies ranging from 7 to 8 keV available at these synchrotron beamlines, the sample used for the experimental verification in the visible (Chapter 3) becomes almost transparent: the attenuation length of gold at these energies is around 2 μm [3]. Thus thicker membranes were designed (from Silson Ltd, Southam, UK) with a gold layer of 3 μm and 6 μm thickness. This thickness renders the sample preparation more challenging: for a given sample size the aspect ratio of the holes to be etched with the focused ion beam has increased by over a tenfold. To cope with this high aspect ratio a test was performed with a He-FIB at ICFO (Institut de Ciències Fotòniques, Castelldefels, Spain). Where a normal FIB uses gallium ions, this FIB uses helium ions and is optimized to etch samples with an extremely high aspect ratio, as the lateral scatter of He-ions is considerably lower. It is however also considerably slower, and was found to be incompatible with our thick sample membranes. Hence the samples that were used in these synchrotron experiments were made using the Ga-FIB at CSNSM, Orsay, France (like the sample in

Chapter 3), with necessary precautions concerning the sample thickness. Where for the thin membranes on the order of a few hundred nanometers it is for example possible to just etch out the edges of an aperture, for these thicknesses the amount of material re-deposited during etching is so significant that the edge cannot be made to traverse the membrane. One thus needs to fully edge out the surface of the aperture (which dramatically increases the etching time).

5.4 Beamtime at Diamond synchrotron

5.4.1 Setup at B16

B16 [4] is a bending magnet beamline at the Diamond synchrotron, designed to be a flexible, versatile setup to test X-ray optics and experimental imaging techniques. The bending magnet radiation is monochromatized in a double-crystal monochromator before arriving to the experimental hutch. There a CRL (Compound Refractive Lens) was used to focus the X-rays onto the sample, to increase intensity on the sample and thus the signal on the detector. This lens is chromatic, meaning that the sample needed to be moved downstream when increasing the X-ray energy. Unfortunately the beamtime was not long enough to properly perform the necessary alignment and calibration procedure. Additionally the obtained diffraction patterns did not correspond to what was expected from the simulations, and no successful reconstruction was achieved (see next paragraph).

5.4.2 Results from beamtime at B16

Figure 5.2a shows the sample used in the experiment. Based on this SEM image, the expected diffraction pattern can be calculated, as shown in figure 5.2b. This pattern contains 5×10^7 photons, to obtain a signal level similar to the experimental pattern shown next to it. The experimental pattern is rather different from the simulated pattern, and no successful reconstruction was obtained. This is attributed to a low spatial coherence of the bending magnet beam. A trial to further close the pair of slits upstream to improve the spatial coherence did not succeed. Hence no successful results were obtained from this (short) beamtime, but it helped in preparing the next.

5.5 Beamtime at Soleil synchrotron

5.5.1 Setup at the Nanoscopium beamline

Nanoscopium is an undulator beamline which, with a distance of about 150 m between the undulator and the experimental hutch, has been developed specifically for applications requiring excellent spatial coherence ([5]). Figure 5.3a shows a schematic of the layout of the beamline. Also specific care has been taken for the stability of the beam, a crucial parameter to the requirements of our experiment: In order to scan the energy over a large (10 %) range, the undulator separation and monochromator position will need to be varied. During these movements it is of paramount importance that the beam does not move on our sample, otherwise the diffraction patterns at different energy will differ by more than just a homothetic scaling which will introduce errors in the monochromatization procedure. Prior to the experiment, beamline scientists Dr. Medjoubi and Dr. Somogyi calibrated the undulator and monochromator over the 7-8 keV energy range to ensure the stability of the beam. Figure 5.3b shows a simple schematic of the setup used in the experiment. Monochromatic X-rays (starting at 7.1 keV) enter the experimental

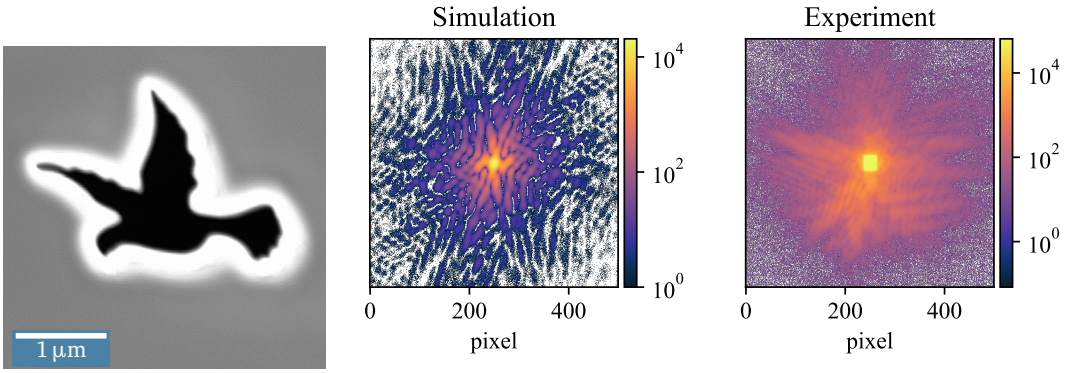

(A) SEM image of the sample, etched out of a membrane with a gold layer of 3 micron thickness.

(B) Monochromatic diffraction pattern as simulated based on the SEM image, at 8 keV. The pattern contains 10^7 photons, to obtain a signal level similar to the experimental pattern.

(C) Experimental monochromatic diffraction pattern at 8 keV.

FIGURE 5.2: A comparison between the simulated and experimental monochromatic patterns already shows that there is a problem in the setup.

hutch of the Nanoscopium beamline and are apertured by a pair of slits set to 1×1 mm^2. After passing through a tungsten pinhole of 24 µm diameter the X-rays hit the sample. 331 cm downstream the diffraction pattern is recorded using a scintillator and a CMOS camera fitted with a microscope objective (of ×5 or ×10 magnification depending on the experiment). The X-ray intensity is monitored using a 8 µm thick Si diode, the X-ray energy is measured through the X-ray fluorescence spectra acquired by a silicon drift detector (SDD), see figure 5.3d. During the experiment, diffraction patterns were acquired using High Dynamic Range (HDR): each pattern consisted of a long (10 s) and a short (1 s) acquisition. The long acquisition contains information at high scattering angles, the information at the saturated center is obtained from the short acquisition (with a multiplicative factor of 10).

5.5.2 Results at the Nanoscopium beamline

After some accurate calibration and optimisation clear diffraction patterns were obtained from the sample shown in figure 5.4. The slits of the second point source (SPS) were open at 200 µm × 200 µm. A test at 100 µm × 100 µm did not show appreciably higher fringe contrast, so the slits were left at 200x200 to preserve flux. A short and a long energy scan was launched. Figure 5.5a shows the patterns obtained for different energies. The homothetic scaling is clearly visible. Unfortunately no successful reconstruction was obtained from these monochromatic patterns. We tried using our own code based on a Difference Map algorithm (DM) and one based on Hybrid-Input-Output (HIO) (see e.g. [6, 7]), and a Shrinkwrap algorithm [8] for evolution of the support. As this did not give a proper reconstruction, we also tried Hawk [9], but without success. Nevertheless, the broadband pattern was computed as the incoherent sum of the acquired monochromatic patterns, and subsequently monochromatized, as shown in figure 5.6. This monochromatized pattern did not yield any successful reconstruction either (figure 5.7). It was upon closer inspection of the a later scan that we noticed an instability in the beam, present in practically all acquisitions. This instability caused a movement of speckles on the order

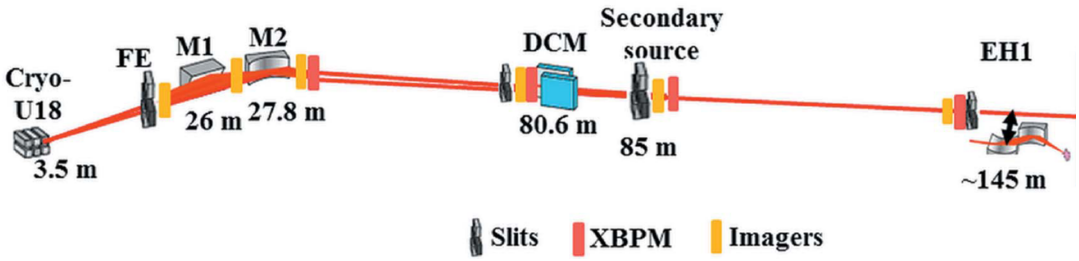

(A) Beamline layout. X-rays between 5 - 20 keV are generated in the undulator (U18) and apertured by pair of slits (Front End, FE). The X-ray energy is selected by the double crystal monochromator (DCM). The beam can be apertured further to create a secondary point source (SPS) and eventually arrives at the experimental hutch EH1. The vertical red lines are X-ray beam position monitors (XBPM), the yellow lines beam imagers. Image from [5]

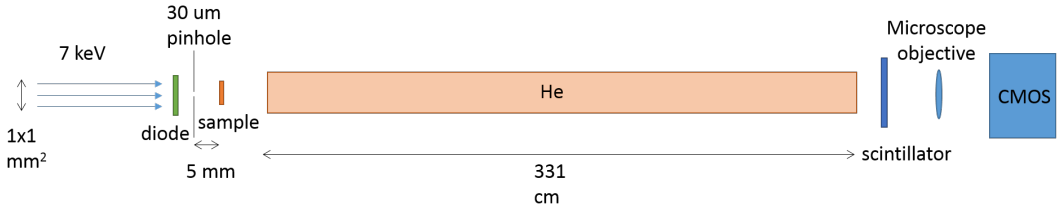

(B) Schematic of the setup in the experimental hutch. The X-ray beam is apertured to 1×1 mm^2. The flux is measured through a silicon diode. A 24 μm pinhole defines the beam onto the sample. The diffracted beam propagates through a 331 cm long flight tube filled with helium to reduce scattering. The diffraction pattern is imaged using a scintillator, microscope objective and CMOS camera.

(C) Picture of the setup in the experimental hutch.

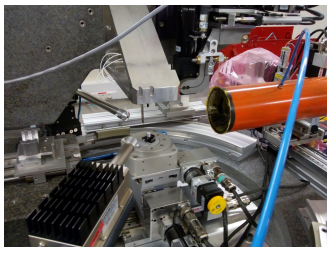

(D) Picture of the pinhole, sample stage and silicon drift detector (SDD), which measures X-ray fluorescence from the sample allowing accurate measurement of the X-ray energy.

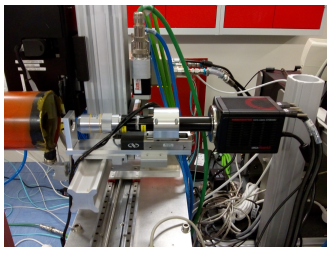

(E) Picture of the scintillator, microscope objective and CMOS detector.

FIGURE 5.3: The experiment setup at the Nanoscopium beamline.

of a pixel from one pattern to the next, but on longer timescales amounted to speckles moving more than their own size. Upon summing the monochromatic patterns, this instability thus causes additional blurring, on top of the expected wavelength scaling.

The next sample was a Siemens star, see figure 5.8. This SEM image shows only the central part (diameter 9.2 μm), the Siemens star itself extends to a 200 μm diameter. This central part has details down to 50 nm, whereas our reconstructed pixel size is 560 nm. We thus do not expect to reconstruct the center of the sample. The diffraction pattern is well defined, and in the post-experiment analysis a reasonable reconstruction was achieved (figure 5.11). On this same sample an energy scan was launched (figure 5.9a). The broadband and monochromatized patterns show the expected behavior. The reconstruction of the monochromatic case is reasonable considering that the central part cannot be resolved. The broadband case after monochromatization is also reconstructed, although the artifacts from the monochromatization seem to have a detrimental effect on the quality of the reconstruction.

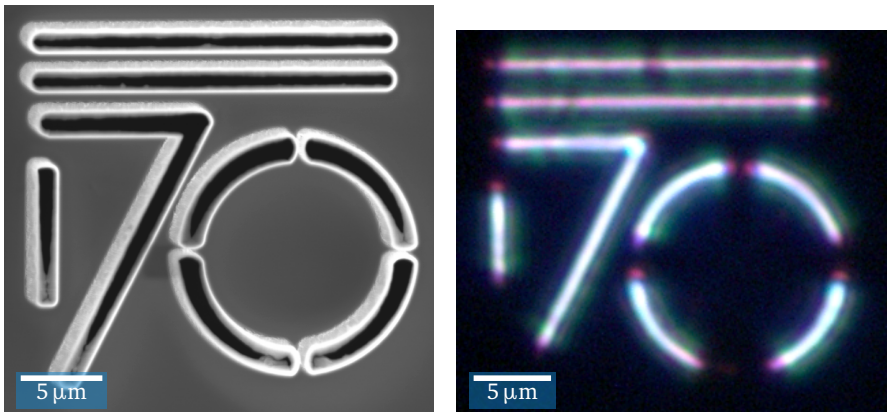

(A) SEM image of the first sample, seen from the SiN-side.

(B) Optical microscopy image of the same sample, seen from the gold-covered side.

FIGURE 5.4: The newly prepared sample is larger and with a clearer aperture, thus giving more diffraction signal.

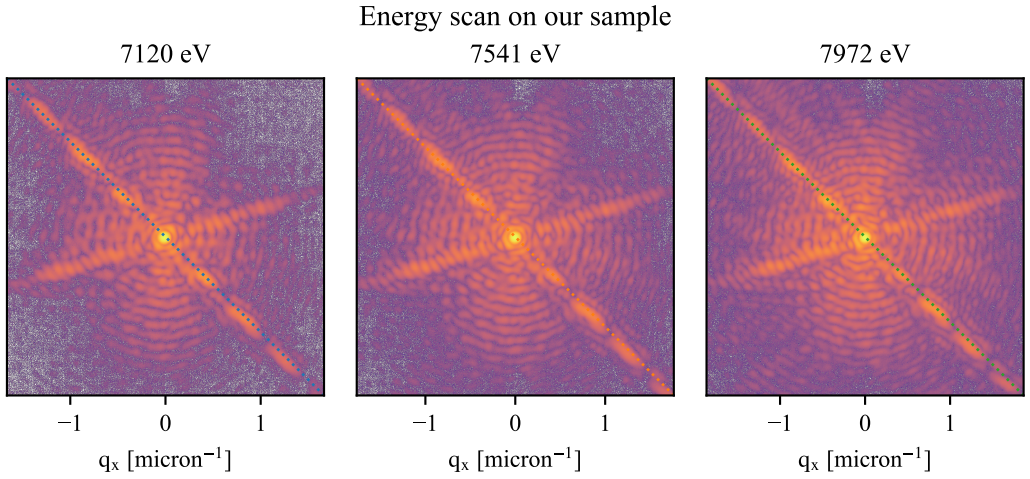

(A) Diffraction patterns of the energy scan, for three different X-ray energies. The full scan consists of 108 acquisitions from 7120 to 7972 eV.

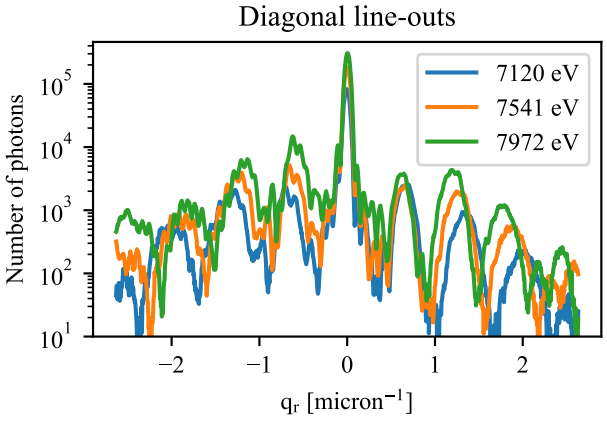

(B) Line-outs on the diagonal of the diffraction patters for three different X-ray energies, showing the expected scaling.

FIGURE 5.5: Results of the first energy scan.

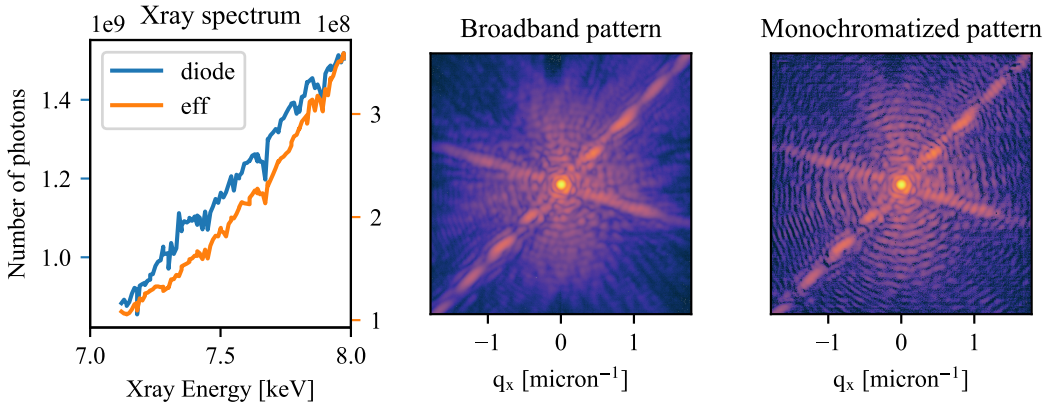

FIGURE 5.6: (*left*) The spectrum of the energy scan, as the number of photons in a 10 second acquisition at each X-ray energy. The blue line (left y-axis) shows the spectrum as measured by the Si diode before the pinhole, the orange line (right y-axis) the effective spectrum as seen by the CMOS camera, obtained by counting the photons in each monochromatic pattern. (*center*) The broadband pattern obtained by summing the 108 acquired monochromatic diffraction patterns. The blurring effect of a bandwidth of 11 % is clear. (*right*) The diffraction pattern obtained after numerical monochromatization. It has regained most of the interference fringes present in the monochromatic patterns.

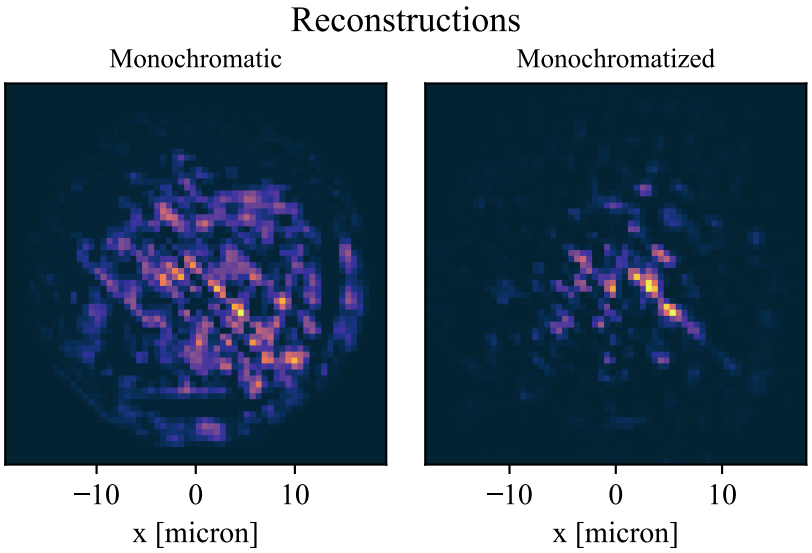

FIGURE 5.7: (*left*) An example of a failed reconstruction of the monochromatic pattern. (*right*) An example of a failed reconstruction of the monochromatized pattern.

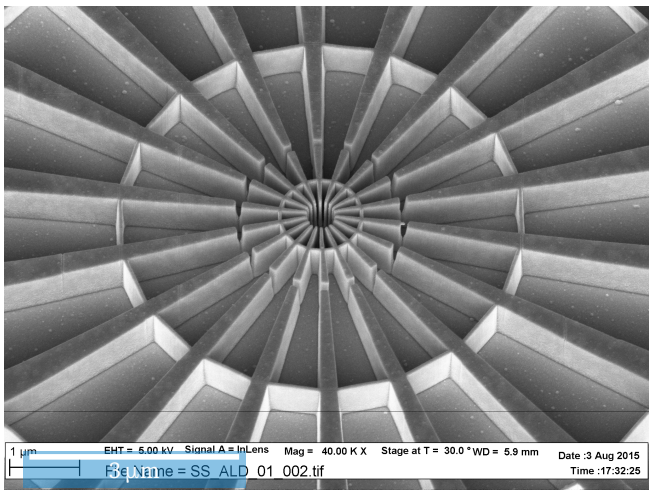

FIGURE 5.8: SEM image of the Siemens star sample, consisting of a patterned (through EBL) layer of Au of about 1 micron thick deposited on a Si membrane. This image only shows the center of the sample (a diameter of 9.2 µm), the sample extends to a 200 µm diameter.

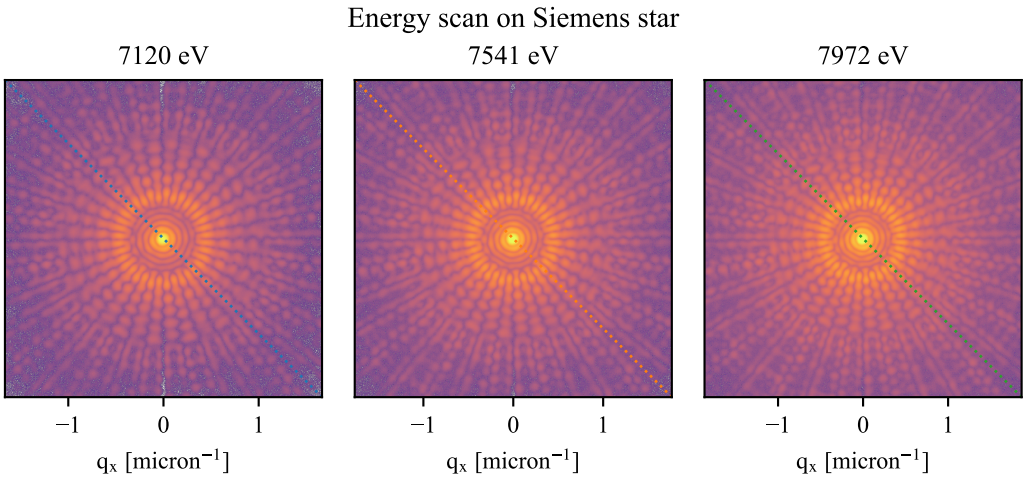

(A) Diffraction patterns of the energy scan, for three different X-ray energies. The full scan consists of 108 acquisitions from 7120 to 7972 eV.

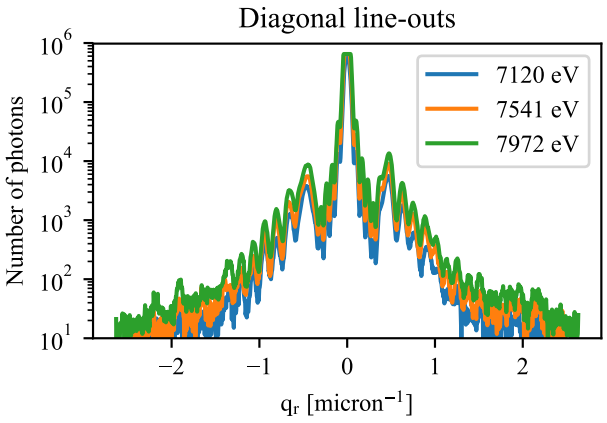

(B) Line-outs on the diagonal of the diffraction patters for three different X-ray energies.

FIGURE 5.9: Results of the energy scan on the Siemens star sample.

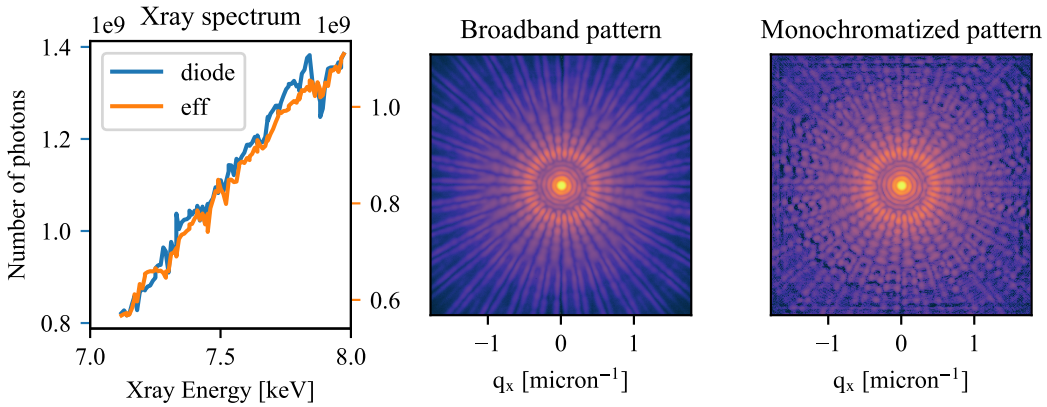

FIGURE 5.10: (*left*) The spectrum of the energy scan, as the number of photons in a 10 second acquisition at each X-ray energy. The blue line (left y-axis) shows the spectrum as measured by the Si diode before the pinhole, the orange line (right y-axis) the effective spectrum as seen by the CMOS camera, obtained by counting the photons in each monochromatic pattern. (*center*) The broadband pattern obtained by summing the 108 acquired monochromatic diffraction patterns. The blurring effect of a bandwidth of 11 % is clear. (*right*) The diffraction pattern obtained after numerical monochromatization. It has regained most of the interference fringes present in the monochromatic patterns. It also shows the appearance of artifacts near the borders.

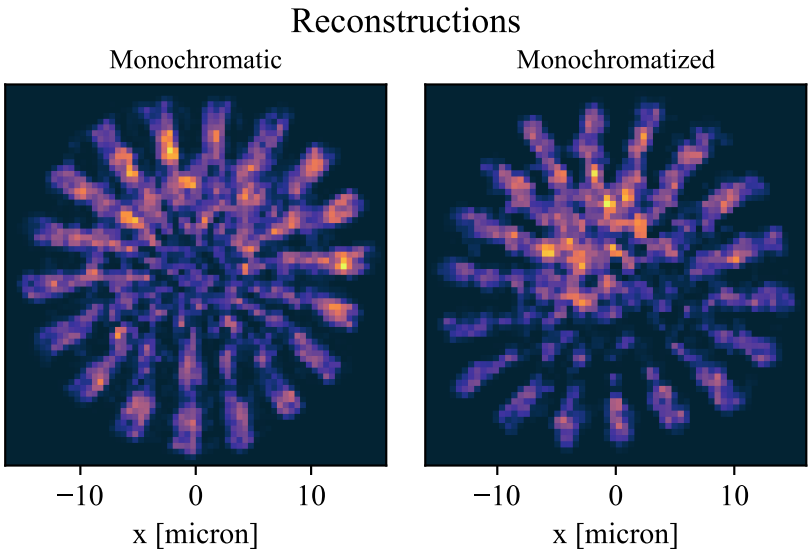

FIGURE 5.11: Reconstructions of the first Siemens star sample. (*left*) A reconstruction of the monochromatic pattern at 7120 eV of reasonable quality. (*right*) A reconstruction of the monochromatized pattern.

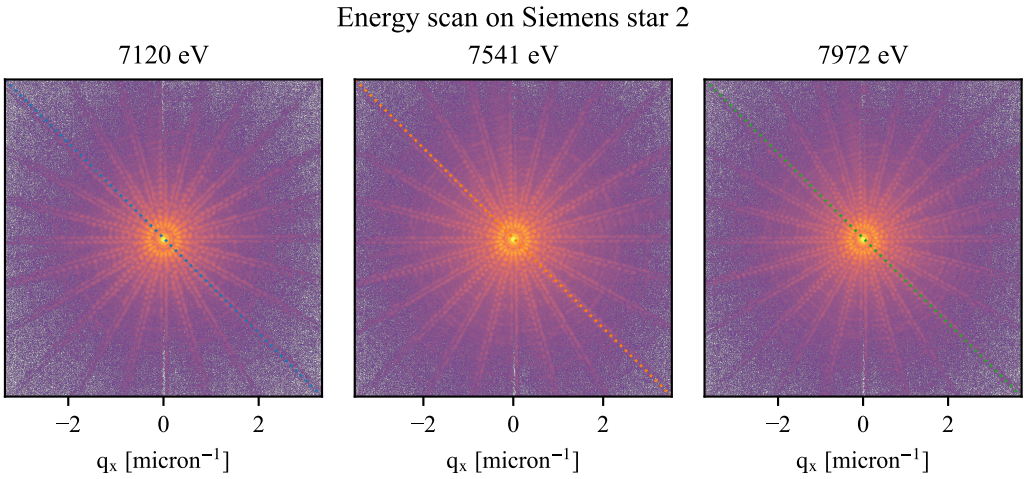

(A) Diffraction patterns of the energy scan, for three different X-ray energies. The full scan consists of 108 acquisitions from 7120 to 7972 eV.

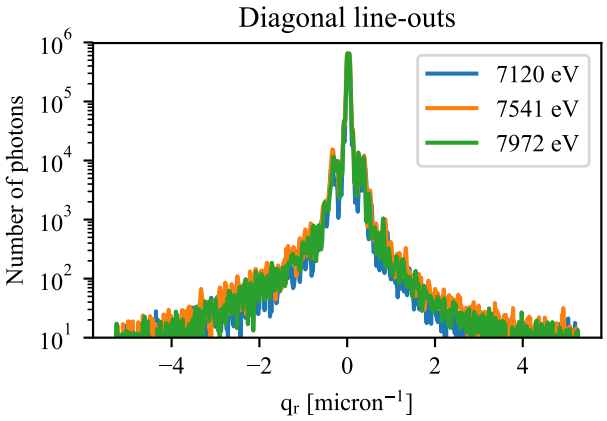

(B) Line-outs on the diagonal of the diffraction patters for three different X-ray energies.

FIGURE 5.12: Results of the energy scan on the second Siemens star sample.

Next, the microscope objective was changed from a x10 to a x5, to increase the maximum scattering angle, and as such the reconstructed pixel size is reduced to 280 µm. Tests were performed at different configurations of slit separation and hardware binning, but we decided to stay at 200 µm × 200 µm for the SPS and at 2x2 hardware binning. A new energy scan was launched on a slightly different Siemens star sample (on the same sample membrane). The results are shown in figure 5.12a. Again, the patterns nicely show the wavelength scaling and the monochromatized pattern looks reasonable (figure 5.13), but reconstruction with neither our codes nor with Hawk yielded acceptable results. The effective spectrum (as seen by the CMOS camera) shows a drop after about 7.6 keV. This scan was performed during the night, and the helium supply to the tube between the sample and detector ran out, causing the effective flux to drop.

5.5.3 Correction of instabilities

An analysis of the experienced instabilities is ongoing. An idea is to track the movement of a number of speckels and try to decouple the movement due to instabilities and that due

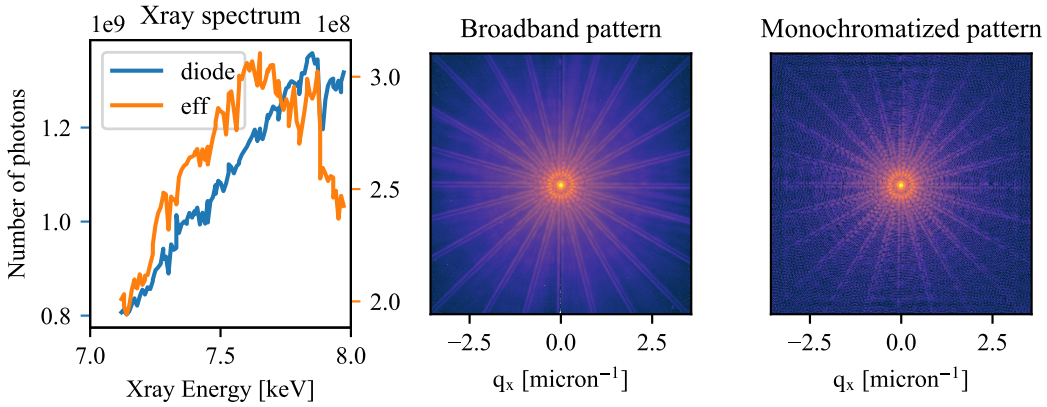

FIGURE 5.13: (*left*) The spectrum of the energy scan, as the number of photons in a 10 second acquisition at each X-ray energy. The blue line (left y-axis) shows the spectrum as measured by the Si diode before the pinhole, the orange line (right y-axis) the effective spectrum as seen by the CMOS camera, obtained by counting the photons in each monochromatic pattern. (*center*) The broadband pattern obtained by summing the 108 acquired monochromatic diffraction patterns. The blurring effect of a bandwidth of 11 % is clear. (*right*) The diffraction pattern obtained after numerical monochromatization. It has regained most of the interference fringes present in the monochromatic patterns. It also shows the appearance of artifacts near the borders.

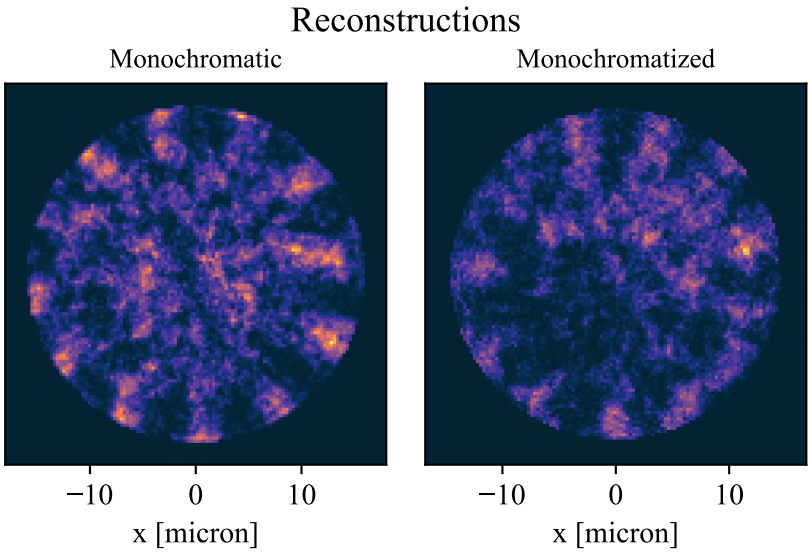

FIGURE 5.14: Reconstructions of Siemens star 2. (*left*) A reconstruction of the monochromatic pattern at 7972 eV, only hinting at the star-shaped structure of the sample. (*right*) A reconstruction of the monochromatized pattern, similar to the monochromatic reconstruction though of slightly lower quality.

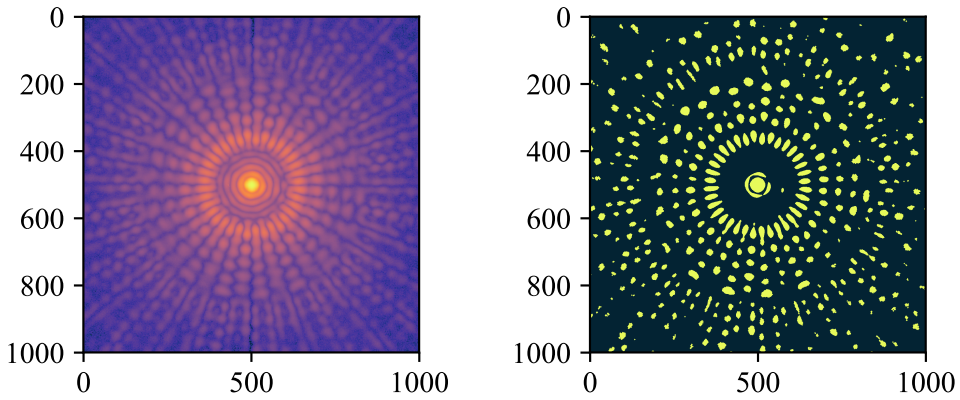

(A) A monochromatic pattern, of which we want to track the speckle movement.

(B) Binary image of the speckles to be tracked.

FIGURE 5.15: The speckles of the monochromatic diffraction pattern are identified using a high-pass filter on the logarithm of the diffraction pattern, and thresholding the result. This is repeated for different patterns in a scan.

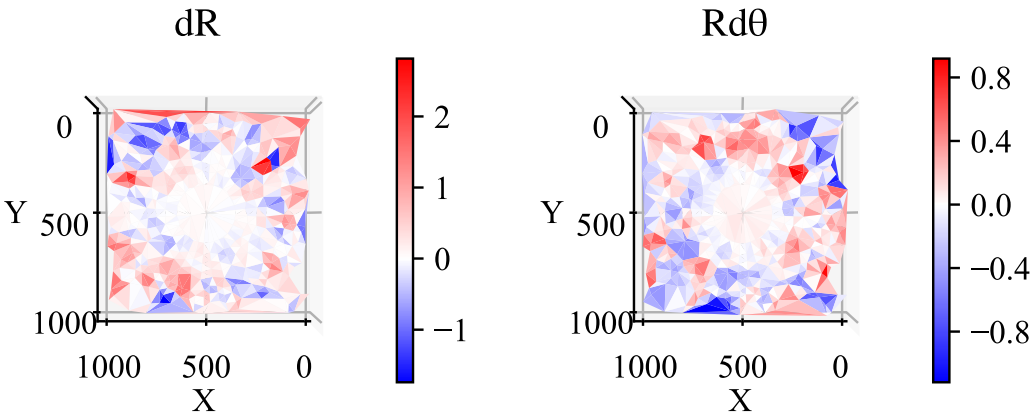

FIGURE 5.16: Radial and azimuthal speckle displacement in pixels, from one diffraction pattern to the next, at the same energy.

to the expected wavelength scaling. An example is shown in figure 5.15. The speckles of the diffraction pattern are identified through a high-pass filter on the logarithm of the diffraction pattern (5.15a), and subsequent thresholding to yield the binary image in 5.15b. This is repeated for all patterns in a scan, and as such the speckle movement is identified. Figure 5.16 shows this speckle displacement decomposed in the radial and azimuthal direction, in units of pixels, for two subsequently acquired diffraction patterns at the same X-ray energy. The procedure needs to be made more robust and may then be used to disentangle beam instability and the sought-after wavelength scaling.

5.5.4 Monochromatic ptychographic reconstruction

Ptychography is more robust to sources of noise (and thus to instabilities) thanks to the redundancy in the procedure. During the beamtime, the beamline scientist Dr. Medjoubi tested his ptychography routine on yet another Siemens star sample, to see to what extent the instabilities would affect the ptychographic reconstruction. As shown in figure 5.17,

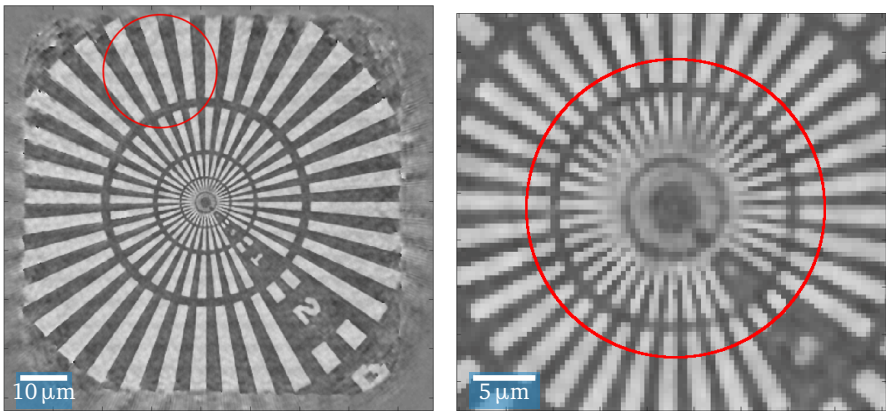

(A) Monochromatic ptychographic reconstruction.

(B) Zoom on the central part of the ptychographic reconstruction.

FIGURE 5.17: Monochromatic ptychographic reconstruction, by Dr. Medjoubi, Nanoscopium. The red circle indicates the beam size (24 µm diameter), equal to the size of the CDI reconstructions.

the sample was reconstructed correctly. Also here, the reconstructed pixel size (217 nm) is not sufficient to resolve the features in the center. Due to limited time a broadband ptychography scan was not attempted, but this could be the subject of a future beamtime proposal.

5.6 Conclusions

Thanks to the outstanding spatial coherence of the Nanoscopium beamline well-defined diffraction patterns were obtained. The homothetic scaling at different energies is clearly shown. This chapter also shows how the reality of the experiment is always more challenging than the simulation. The technological feat of scanning an energy range of over 11 % while keeping the beam stable is a real challenge which was well met by the beamline scientists. Unfortunately, some unexpected instabilities were still present, to which CDI, in general, is extremely sensitive. Of over twenty acquired datasets, one dataset gave a reasonable reconstruction in both the monochromatic and the broadband case (figure 5.11), especially considering the central features of the sample are smaller than can be resolved for this experimental setup. So although the validation by a converging phase retrieval of a broadband pattern is complicated by experimental difficulties, one could conclude that the monochromatization method itself also works with hard X-rays. An analysis to quantify the instabilities to correct for them is still ongoing and may allow a significant improvement of the results shown in this chapter.

Bibliography

[1] David M. Paganin. *Coherent X-Ray Optics*. Number 6 in Oxford Series on Synchrotron Radiation. Oxford University Press, Oxford, 2006. ISBN 978-0-19-856728-8.

[2] K.-J. Kim. Characteristics of synchrotron radiation. In *X-Ray Data Booklet*, pages 2.1–2.16. Lawrence Berkeley National Laboratory, Berkeley, 2006.

[3] B. L. Henke, E. M. Gullikson, and J. C. Davis. X-Ray Interactions: Photoabsorption, Scattering, Transmission, and Reflection at E = 50-30,000 eV, Z = 1-92. *Atomic*

Data and Nuclear Data Tables, 54(2):181–342, July 1993. ISSN 0092-640X. doi: 10.1006/adnd.1993.1013.

[4] K. J. S. Sawhney, I. P. Dolbnya, M. K. Tiwari, L. Alianelli, S. M. Scott, G. M. Preece, U. K. Pedersen, R. D. Walton, R. Garrett, I. Gentle, K. Nugent, and S. Wilkins. A Test Beamline on Diamond Light Source. In *SRI 2009, 10TH INTERNATIONAL CONFERENCE ON RADIATION INSTRUMENTATION*, pages 387–390, Melbourne (Australia), 2010. doi: 10.1063/1.3463220.

[5] Andrea Somogyi, Kadda Medjoubi, Gil Baranton, Vincent Le Roux, Marc Ribbens, François Polack, Pascal Philippot, and Jean-Pierre Samama. Optical design and multi-length-scale scanning spectro-microscopy possibilities at the Nanoscopium beamline of Synchrotron Soleil. *Journal of Synchrotron Radiation*, 22(4):1118–1129, July 2015. ISSN 1600-5775. doi: 10.1107/S1600577515009364.

[6] Veit Elser. Phase retrieval by iterated projections. *Journal of the Optical Society of America A*, 20(1):40, January 2003. ISSN 1084-7529, 1520-8532. doi: 10.1364/JOSAA.20.000040.

[7] S. Marchesini. Invited Article: A unified evaluation of iterative projection algorithms for phase retrieval. *Review of Scientific Instruments*, 78(1):011301, January 2007. ISSN 0034-6748, 1089-7623. doi: 10.1063/1.2403783.

[8] S. Marchesini, H. He, H. N. Chapman, S. P. Hau-Riege, A. Noy, M. R. Howells, U. Weierstall, and J. C. H. Spence. X-ray image reconstruction from a diffraction pattern alone. *Physical Review B*, 68(14), October 2003. ISSN 0163-1829, 1095-3795. doi: 10.1103/PhysRevB.68.140101.

[9] Filipe R. N. C. Maia, Tomas Ekeberg, David van der Spoel, and Janos Hajdu. *Hawk* : The image reconstruction package for coherent X-ray diffractive imaging. *Journal of Applied Crystallography*, 43(6):1535–1539, December 2010. ISSN 0021-8898. doi: 10.1107/S0021889810036083.

Chapter 6

Towards a high repetition rate, keV high harmonic source

6.1 Introduction

The advent of the laser [1], enabled the birth and quick development of the field of non-linear optics, marked by the observation of second harmonic generation (SHG) in 1961 by P. A. Franken [2]. The laser is one of the favorite items in the physicist's toolbox as it is a coherent, intense and precise tool to explore Nature's intricate machinery. It is also the basis for a number of other compact and precise (but not always intense) sources of radiation and particles (of which the previous chapter already gave an example). The first two sentences of Franken's paper read:

"The development of pulsed ruby optical masers has made possible the production of monochromatic (6943 A) light beams which, when focussed, exhibit electric fields of the order of 10^5 *volts/cm. The possibility of exploiting this extraordinary intensity for the production of optical harmonics from suitable nonlinear materials is most appealing."*

Almost 60 years have passed, but the principle of (high) harmonic generation stays the same: focus laser light in a material (solid like Franken's quartz, or a gas, sometimes even a liquid), and make use of its excellent coherence and high intensity to generate harmonic radiation through the materials non-linearity. As explained in this chapter, generation of high harmonics starting at the end of the eighties has led to sources of radiation with pulses of attosecond-scale duration. The past years these sources have yielded impressive results, by tracing directly in the time domain with femto- to attosecond resolution: time resolved Auger decay [3]; charge migration [4], ionization [5], photodissociation[6] and electrocyclic ring-opening [7] in different molecules; the 'birth of a photoelectron' through a Fano resonance [8]; condensed phase spin dynamics [9] and phonon excitation [10], to name but a few.

The major challenges in the field are to extend the energy of coherent radiation towards keV X-rays, decrease the pulse duration, and to increase the repetition rate and overall flux of these sources. An important part of this thesis work was performed towards this goal, the experimental results of which are presented in the next chapter. This chapter introduces the necessary concepts with a focus on HHG using high repetition rate, mid-IR driver lasers and solitonic compression, and calculations performed in preparation of the experiments. Some of the basics of non-linear optics are described in Appendix E, for more details the reader is referred to the references therein.

6.2 Theory of High Harmonic Generation

One important difference should be noted between perturbative harmonic generation as described by Franken, and that of *high* harmonic generation: the generation of low order harmonics can be described in a perturbative fashion (expanding the materials non-linear susceptibility as in Appendix E), whereas HHG is a non-perturbative process. In the eighties, as the maximally attainable electric field strength became comparable to the electric field of a bound electron (around 10^{14} W/cm^2), three important phenomena were observed [11]:

Above-threshold ionization (ATI)
Electrons are ionized through instantaneous absorption of multiple photons (multi-photon ionization), more than necessary to overcome the atoms binding potential. Electrons were thus observed with an excess energy of multiples of the photon energy [12].

High (order) harmonic generation (HHG)
Electrons are ionized through tunnel ionization, accelerated in the laser field and then recombine with the parent ion upon emitting a photon with an energy that is a multiple of the laser photon energy (three-step model, see below). It was first observed by McPherson *et al.* in Chicago in 1987 [13] and practically simultaneously by Ferray *et al.* in Saclay [14].

Non-sequential double ionization (NSDI)
Tunnel ionization, acceleration and recombination as in HHG, but where a second electron is ejected from the core upon recollision of the first.

The harmonic emission observed by McPherson and Ferray did not exhibit the exponential decay with harmonic number as expected for a perturbative process. Rather the spectrum featured a 'plateau'-region extending several harmonic orders, and then a sudden drop dubbed the 'cut-off'. Figure 6.1a shows one of the original spectra reported by Ferray *et al.*, clearly showing this behavior. An intuitive explanation called the 'Three-step model' was put forward in 1993 by Corkum [15] and Lewenstein [16], presented in the next paragraph. In subsequent years the harmonic emission was found to inherit the coherence of the laser, as the phase of the harmonic emission is locked to the laser phase [17]. Moreover, the observed spectra support extremely short pulses, currently down to tens of attoseconds, as measured through reconstruction of the relative phase of the harmonics [18] and through streaking of photoelectrons produced by the attosecond pulse [19]. Although the first results were on attosecond pulse trains (one pulse emitted at each half-cycle of the laser, the interference of which give a harmonic spectrum in the spectral domain), isolated attosecond pulses (corresponding to a broad, continuous spectrum) have also been produced, either through intensity gating [19], polarization gating [20, 21], two-color gating [22–24] or ionization gating [25]. Many review articles on high harmonic generation and attosecond science are available, e.g. [11, 26–30].

6.2.1 Three-step model and the cut-off energy

Many of the properties of HHG can be explained by a semi-classical model called the three-step model, put forward by Corkum [15] and Lewenstein [16]. In this model, schematically depicted in figure 6.1b, the first step is tunnel ionization: the strong electric field of the laser bends the effective atomic potential seen by the bound electron - there is now a

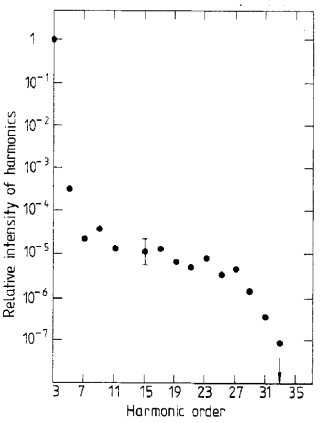

(A) High harmonic spectrum in the original experiment by Ferray *et al.*, showing the relative intensity of the harmonics generated in Ar at a laser intensity of approximately 3×10^{13} W/cm2, a laser wavelength of 1064 nm and a pulse length of 30 ps. It clearly shows the behavior of a plateau and a cut-off at the 33st harmonic. Taken from [14].

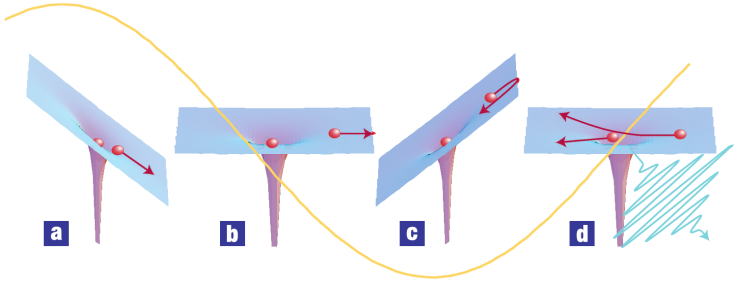

(B) Schematic of the three-step model: ionization, acceleration, recombination. The yellow line indicates the electric field of the driver laser. Near the peak of the field (a) the atomic potential is strongly deformed, allowing the electron wavepacket to (partially) escape through tunnel ionization. The electron wavepacket is driven away from the parent ion until the laser field is reversed (b). The wave packet is now accelerated back to the ionic remnant (c) where it may recombine (d). Image taken from [31].

FIGURE 6.1: Original high harmonic spectrum from Ferray (1988) and the three-step model by Corkum (1993).

reasonable probability that the electron tunnels out of the atomic potential.[1] This probability is highest near the peak of the laser field. Next, the ionized fraction is driven away in the continuum by the laser field. This can be described in a classical manner, as just an electron accelerated by an electric field, although quantum-mechanically part of the electron's wave function stays bound to the atom. As the laser field reverses the electron wave packet is accelerated back onto the ion. When it recollides there is a probability that the electron recombines to the ground state, emitting the energy it has gained in the laser field in the form of an XUV or soft X-ray burst of light (or, quantum-mechanically, the returning wave packet interferes with the ionic remnant of the wave function).

The moment in the laser cycle at which the electron tunnels through the atomic potential barrier determines its trajectory and the moment and energy of recollision, as depicted in figure 6.2. The trajectory corresponding to maximum recollision energy is plotted in black; for lower recollision energies two trajectories are possible, known as the 'long' and 'short' trajectories. The maximum collision energy corresponds to the cut-off shown by the spectrum above, and it is given by:

$$U_{co} = 3.17U_P + I_P. \quad \text{(high harmonic cut-off energy)} \tag{6.1}$$

[1] To differentiate between MPI and tunneling, the keldysh or adiabaticity parameter $\gamma = \sqrt{\frac{I_p}{2Up}} = \frac{2\tau_T}{\tau_L}$ should be evaluated. $\gamma \gg 1$ is the MPI regime, $\gamma \ll 1$ is the tunneling or quasi-static regime, where the tunneling time τ_T is short compared to the laser period τ_L. See Appendix E.

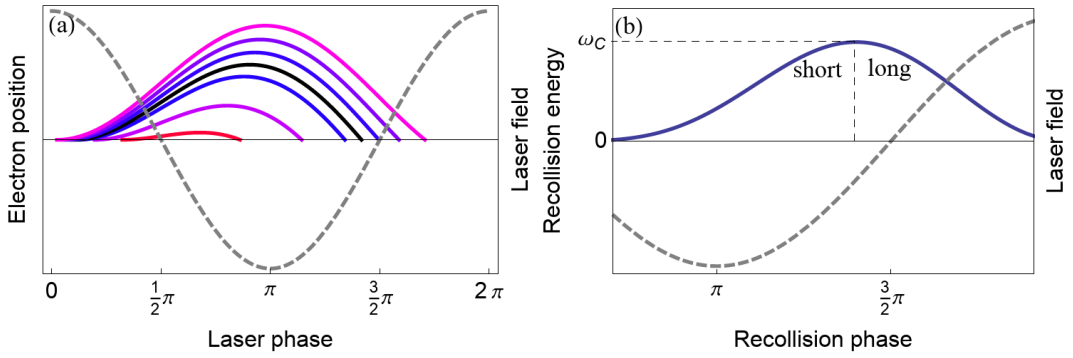

FIGURE 6.2: Electron trajectories and their recollision energies. The gray dashed line indicates the laser field. Panel (a) shows the short and long electron trajectories, the trajectory in black corresponding to the electron with maximum energy on recollision. Panel (b) shows the recollision energies of the electrons as a function of the recollision time. Taken from [11].

with

$$U_P = \frac{e^2\mathscr{E}^2}{4m_e\omega^2} \quad \text{(ponderomotive potential)} \tag{6.2}$$

$$= \left(\frac{e^2}{8\pi^2\epsilon_0 m_e c^3}\right) I\lambda^2 \tag{6.3}$$

and I_P the ionization potential (see also Appendix E).

To obtain an attosecond pulse, or pulse train, typically only the short trajectories are selected by placing the laser focus up to about one Rayleigh length before the gas jet (this causes the short trajectories to be phase matched, see next paragraph). The harmonics corresponding to a family of trajectories are phase locked [32, 33]. However, as can be inferred from figure 6.2, harmonic emissions of different energies are emitted at different times. This causes attosecond pulses to have an intrinsic chirp, the so-called attochirp, as first measured by Mairesse *et al.* [34]. For the short trajectories, high energy harmonics are emitted later, corresponding to a positive chirp. This makes attosecond pulses far from fourier limited, although the chirp can be partially compensated in the XUV using thin metallic filters (such as in [35] using an Al filter around 30 eV), or using chirped multilayer mirrors [36, 37].

6.2.2 Phase Matching

The three-step model describes the generation of high harmonics from a single atom. As with perturbative harmonic generation, in the macroscopic picture the radiation from different emitters has to be in phase in order to get coherent build-up and an appreciable harmonic signal [38, 39]. Four main contributions to the phase mismatch can be identified (e.g. [40, 41]):

$$\Delta k = k_{HH} - q_k L \tag{6.4}$$

$$= \Delta k_{dip} + \Delta k_{geo} + \Delta k_{atom} + \Delta k_{elec} \tag{6.5}$$

Δk_{dip}
: The dipole phase of the single-atom response depends on the intensity gradient as $\Delta k_{dip} = \alpha_q \partial I/\partial z$, where I and z are the intensity and longitudinal coordinate

respectively, and α_q is a proportionality constant for harmonic number q [17]. α is positive and small for short trajectories, large for long trajectories (which is why short trajectories have a smaller chirp and are typically easier to phase-match, at least on-axis). Because Δk_{dip} is determined by the intensity gradient, it varies in both time and space.

Δk_{geo}

The geometry of the experiment contributes to the phase of the laser. If the HHG takes place near the focus of a Gaussian beam this phase is the Gouy phase,

$$\Phi_{Gouy} = -\tan^{-1}\frac{z}{z_R}, \tag{6.6}$$

with z_R the Rayleigh range. The corresponding wave-vector is

$$k_{Gouy} = \frac{\mathrm{d}\Phi_{\mathrm{Gouy}}}{\mathrm{d}z} \tag{6.7}$$

$$= -\frac{1}{1-\left(\frac{z}{z_R}\right)^2}\frac{1}{z_R} \tag{6.8}$$

The low order harmonics can be assumed to have the same Rayleigh length, such that

$$\Delta k_{Gouy} = k_{Gouy}(q\omega_L) - qk_{Gouy}(\omega_L) = \frac{1}{1-\left(\frac{z}{z_R}\right)^2}\frac{q-1}{z_R}. \tag{6.9}$$

The higher order harmonics are generated mainly on axis, so $z_{R,q} \to \infty$ and

$$\Delta k_{Gouy} = \frac{1}{1-\left(\frac{z}{z_R}\right)^2}\frac{q}{z_R}. \tag{6.10}$$

Instead of the focus of a Gaussian beam, harmonics can also be generated in a waveguide. The dispersion relation of a waveguide is given by $k_{wg} = \frac{u_{ml}^2 c}{2a^2\omega}$, where u_{ml} and a are the l^{th} zero of the Bessel function $J_{m-1}(u_{ml}) = 0$ and the waveguide radius respectively [42–45]. For the fundamental mode $u_{11} = 2.405$. Thus

$$\Delta k_{wg} = \frac{u_{ml}^2 q\lambda_L}{4\pi a^2}. \tag{6.11}$$

Δk_{atom}

The dispersion by neutral atoms is simply the difference in refractive index n of the generation medium at the driver wavelength λ_L and the generated harmonic λ_L/q. It is given by

$$\Delta k_{atom} = -q\frac{p}{p_0}(1-\eta)\frac{2\pi}{\lambda_L}(\Delta\delta + n_2), \tag{6.12}$$

where p, p_0, η, $\Delta\delta$ and n_2 are the gas pressure, standard pressure, ionization fraction, difference in refractive index and the nonlinear index of refraction (see Appendix E), respectively.

Δk_{elec}

The generation medium becomes ionized as it is traversed by the laser pulse (only a tiny fraction of the ionized atoms actually generates harmonics, the vast majority is just ionized and takes nanoseconds to recombine). These free electrons form a

plasma with a resonance frequency

$$\omega_p = \sqrt{\frac{e^2\rho_n}{\epsilon_0 m_e}}, \tag{6.13}$$

with ρ_n the electron number density. ω_p is the frequency below which the plasma is completely opaque. The refractive index of the plasma is then given by

$$n_{plasma} = \sqrt{1-\left(\frac{\rho_n}{\rho_{n,cr}}\right)} \tag{6.14}$$

where $\rho_{n,cr}$ is the critical electron number density, i.e. the density for which the resonance frequency equals the frequency of the radiation. Typically, $\rho_n \ll \rho_{n,cr}$, so that

$$\Delta k_{elec} = \frac{\omega_p^2(q^2-1)}{(2qc\omega_L)} \tag{6.15}$$

$$= \rho_n r_e \frac{q^2-1}{q}\lambda_L \tag{6.16}$$

$$= \frac{p}{k_B T}\eta r_e \frac{q^2-1}{q}\lambda_L \tag{6.17}$$

where r_e is the classical electron radius:

$$r_e = \frac{1}{4\pi\epsilon_0}\frac{e^2}{m_e c^2} \tag{6.18}$$

We can now describe the total wave-vector mismatch for the case of free-focusing:

$$\Delta k = \alpha_q \partial I/\partial z + \frac{1}{1-\left(\frac{z}{z_R}\right)^2}\frac{q}{z_R} - q\frac{p}{p_0}(1-\eta)\frac{2\pi}{\lambda_L}(\Delta\delta + n_2) + \frac{p}{k_B T}\eta r_e \frac{q^2-1}{q}\lambda_L, \tag{6.19}$$

and for the case of a waveguide:

$$\Delta k = \alpha_q \partial I/\partial z + \frac{u_{ml}^2 q\lambda_L}{4\pi a^2} - q\frac{p}{p_0}(1-\eta)\frac{2\pi}{\lambda_L}(\Delta\delta + n_2) + \frac{p}{k_B T}\eta r_e \frac{q^2-1}{q}\lambda_L. \tag{6.20}$$

For the free-focusing geometry phase matching is obtained by adjusting the gas pressure and gas jet position such that the negative dispersion of the atoms is balanced with the positive dispersion of the geometry, the free electrons and the dipole. In the case of a waveguide, the same terms need to be balanced just by adjusting the pressure (and potentially the waveguide geometry).

For high laser intensities (for example in an attempt to extend the cut-off energy) the ionization fraction becomes too large and the terms described above can no longer be balanced. The critical ionization fraction is reached when the atom dispersion (the only negative contribution to the phase mismatch) equals the free electron dispersion (e.g. [43, 46–48]):

$$\eta_c = \left[\frac{p_0\lambda_L^2 r_e}{k_B T 2\pi\Delta\delta} + 1\right]^{-1} \tag{6.21}$$

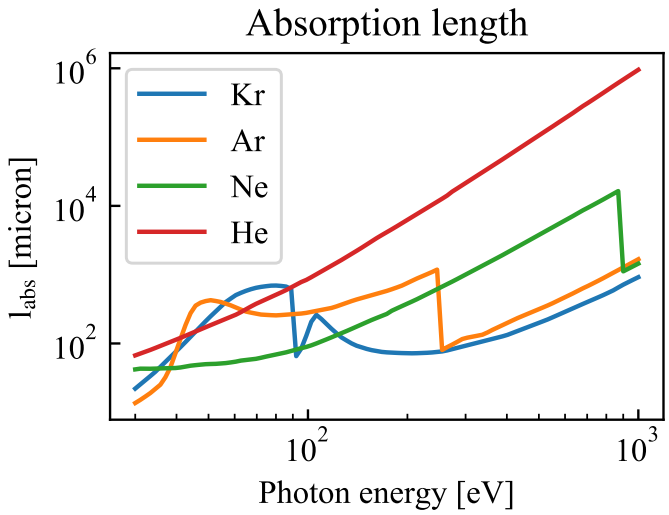

FIGURE 6.3: Absorption length as a function of energy for a number of noble gases.

A number of schemes has been put forward to circumvent this problem. The generation process can be periodically suppressed or enhanced, which is called Quasi-Phase Matching (QPM). The wave-vector mismatch Δk defines a coherence length $l_{coh} = \pi/\Delta k$ over which the harmonics build up in a coherent way. By suppressing the generation process every other l_{coh} by use of a counterpropagating beam [49–51], through modulation of the inner wall of the waveguide [52, 53] or through the beating of waveguide modes [54], coherent build-up can be extended beyond l_{coh}. Another option is to use very short, intense pulses, such that generation can take place before the medium ionization has surpassed the critical level. This is called non-adiabatic phase matching [55–58] and has been shown to generate up to 3.5 keV (but at a flux of 10^2 photons/s at 2 keV, using a 12 fs 3 mJ pulse at 800 nm).

6.2.3 Reabsorption

Depending on the harmonic wavelength and the generation medium, the generated harmonics are reabsorbed by the same medium. So even for perfectly phase-matched HHG, in which case $l_{coh} = \infty$, the effective generation will be limited to the last approximately $3l_{abs}$ of the medium [59], where l_{abs} is the absorption length. Figure 6.3 shows the absorption length for some noble gases, at atmospheric pressure p_0.

6.2.4 Ponderomotive scaling of the cut-off

In order to push the high-harmonic cut-off to higher energies, so as to cover the water window, relevant X-ray absorption edges, and/or to increase imaging resolution or even to support zeptosecond pulses [60], the ponderomotive potential U_p of the laser field needs to be increased (see equation 6.2.1). As explained in Appendix E $U_p \propto I\lambda^2$. As we have seen in the previous paragraph, increasing the intensity causes an increase in the ionization fraction, which at some point prevents phase matching. It is thus interesting to consider increasing the wavelength. The well-spread work horse in ultrafast science is the Ti:Sapph laser, which has a center wavelength around 800 nm, and features a typical cut-off between 100-200 eV. By increasing the wavelength, the cut-off can be extended to the keV-range, while maintaing a moderate intensity and thus a low ionization fraction.

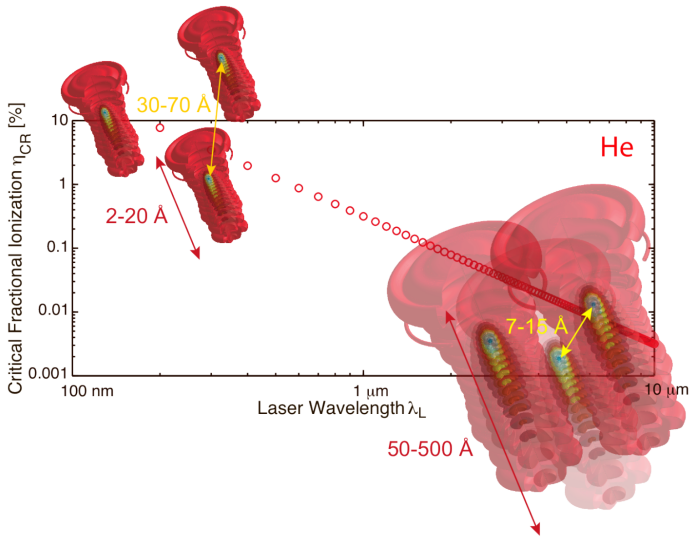

FIGURE 6.4: In the quest for a high cut-off energy, longer wavelength driver lasers are used, lowering the critical ionization fraction as described by equation 6.22 and necessitating higher gas pressures. As the pressure and thus the atom density increases, and the wavepacket excursion increases as well, at some point the electron wave packet will encounter neighboring atoms, causing a loss of coherence. Figure taken from [67].

This wavelength scaling has been demonstrated experimentally [44, 47, 61]. An important disadvantage to using longer driver wavelengths is the unfavourable scaling of the recombination probability. Going back to the three-step model, during the excursion of the electron in the laser field, the electron wave function expands. The longer the driver wavelength, the longer the excursion time and larger the expansion of the electron wave function. At the moment of recollision the overlap between the electron wave function with that of the parent ion is reduced, thus reducing the recombination probability. Theoretical estimates for the scaling give a proportionality of $\sim \lambda^{-5.5\pm0.5}$ [15, 62–65], thus indicating that it is highly unfavourable to use longer driving wavelengths. This reduced single-atom response can however be compensated for by increasing the pressure of the generation medium by orders of magnitude (thus increasing the number of emitters in the macroscopic picture). Nevertheless, two fundamental limits are expected to extending the cut-off through ponderomotive scaling. First, at very long excursion lengths of the electron wave packet, and high generation pressures, the wave packet risks to encounter neighboring atoms, causing a loss of coherence, as indicated in figure 6.4. The classical quiver amplitude of the electron is $\frac{2}{\omega_L}\sqrt{\frac{U_p}{m_e}}$ (see Appendix E). At $U_p = 50$ eV, and $\lambda = 800$ nm, this amplitude is about 2.5 nm. Keeping the same intensity, but at $\lambda = 3$ micron, $U_p = 700$ eV, and the classical quiver amplitude is 35 nm. For comparison, the average intermolecular distance of a gas at atmospheric pressure is about 3.5 nm. Secondly, as explained in Appendix E, U_p needs to be negligibly small compared to the electron rest mass energy (511 keV) for the magnetic component of the laser field to be neglectable. If U_p becomes a reasonable fraction of 511 keV, the electrons velocity becomes relativistic and will experience a drift, thus missing the parent ion upon recollision.

Finally, going to longer wavelengths poses another, more concrete challenge: it means changing the laser architecture from the common Ti-Sapph technology, typically to systems based on optical parametric amplification (OPA). For a review on ultrafast mid-IR lasers see e.g. [66] or section 5.2 of [26].

6.3 High Harmonic Generation at High Repetition Rate

Solid state, femtosecond lasers typically have an average power output on the order of a few up to a few tens of Watts. This means (roughly) that one can get pulse energies on the order of a Joule only at a few Hz repetition rate, or μJ pulses at MHz repetition rates. For time-resolved imaging, it is important to have a high number of photons in a single pulse, so it makes sense to choose a system with low repetition rate and a high pulse energy (and a loose focusing geometry). Other experiments would however greatly benefit from attosecond pulses at a higher repetition rate: photo-electron spectroscopy [68–70], low cross-section processes or experiments relying on coincidence detection [71, 72]. In order to generate high harmonic radiation in spite of a low pulse energy, the peak intensity must somehow be pushed to the order of 10^{14} W/cm^2. This can be through spatial confinement (focusing tightly) and/or temporal confinement (compressing temporally).

6.3.1 Tight focusing

To generate high harmonics at a high repetition rate and low pulse energy the driving laser should be focused to a small focal spot. Several publications investigate the scaling of the generation parameters with pulse energy [40, 48, 73]. They state that the phase matching pressure is inversely proportional to the pulse energy, and moreover the conversion efficiency should remain constant, so that in principle harmonic generation can be generated efficiently even at high repetition rates. Following [40] and [48], the phase matching pressure p_{pm} at focus can be calculated from equation 6.19 as the pressure for which dispersion by atoms and free electrons equals the Gouy phase. To simplify, the analysis is done at focus ($z = 0$) so $\Delta k_{dip} \approx 0$ and $\Delta k_{geo} \approx q/z_R$. Then

$$p_{pm} = p_0 \frac{\lambda^2}{2\pi^2 w_0^2 \Delta\delta \left(1 - \frac{\eta}{\eta_c}\right)}. \tag{6.22}$$

It is instructive to see the behavior of the phase-matching pressure as a function of the focal spot size. This is plotted in figure 6.5, for a driving laser centered at 3.1 μm, a pulse length of 95 fs and a pulse energy of 65 μJ, corresponding to the parameters of the OPCPA used in this thesis (see next chapter for a description). As the pulse energy and pulse length are fixed, the focal waist w_0 determines the peak intensity and thus the high-harmonic cut-off energy, as plotted with a solid line (scale on the left y-axis). For a waist below 11 μm the cut-off energy is expected to be over a keV. However, for this radiation to be phase-matched with the driver laser, high pressures are needed. This phase matching pressure depends on the degree of ionization η, as indicated by the thin, straight lines. They are the phase matching pressures for $\eta = 0, 0.1, 0.2, \ldots, 0.9\eta_c$. Finally, instead of just giving a region, the expected ionization fraction can be estimated using the ADK model [74, 75]. Using this model, the ionization fraction at the peak of the pulse is calculated, thus giving the curve for the expected phase-matching pressure plotted by the dashed-dotted lines in figure 6.5. This procedure was performed for generation in argon, neon and helium. The 'sweet spot' for the experiment are in the bend of the ADK curve: to the right of it, the tunneling probability drops, so the expected flux drops as well. To the left of it, the phase matching is very sensitive to variations in the pressure, before becoming impossible. The critical ionization fractions are around $\eta_c = 2.6 \times 10^{-3}$ (Ar), 6.4×10^{-4} (Ne), 3.3×10^{-4} (He) and vary by only a few percent over the plotted range.

This analysis shows how a low pulse energy requires tight focusing, which in turn requires high phase-matching pressures. Such high pressures are beneficial to compensate

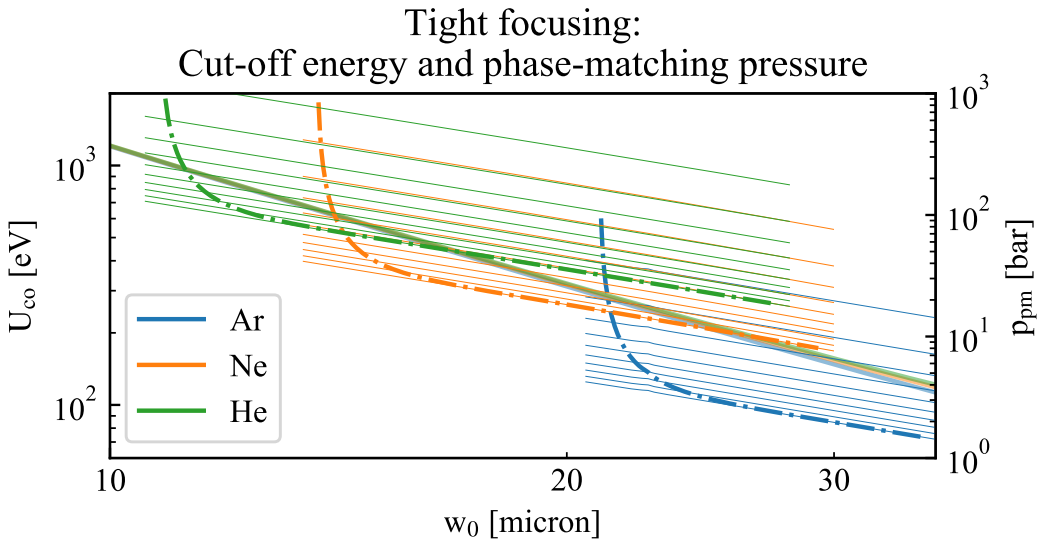

FIGURE 6.5: Cut-off energy (solid line) and expected phase matching pressure (dash-dotted line) as a function of focal spot size for the laser parameters under concern ($\lambda_L = 3.1$ µm, $\tau_{FWHM} = 95$ fs, $E_{pulse} = 65$ µJ) and for various gases. The thin lines indicate phase matching pressures for ionization fractions of $\eta = 0, 0.1, 0.2, \ldots, 0.9\eta_c$. The dash-dotted line indicates the phase-matching pressure for the ionization fraction expected from calculation using the ADK model.

for the low single-atom response due to the long driver wavelength, and for the small generation volume due to the tight focusing geometry.

6.3.2 Generation in a waveguide: combining pulse compression and HHG

In addition to spatial confinement of the pulse energy to obtain the necessary peak intensity, one can compress the pulse in the time domain. To compress a pulse that is already close to its Fourier limit, the spectral bandwidth of the pulse needs to be increased. The typical way to do so [76–78] is to send the femtosecond pulse in a gas-filled, hollow-core fiber (HCF) to increase the spectral bandwidth through self-phase modulation (SPM, see Appendix E), which redshifts the leading edge of the pulse and blueshifts the trailing edge of the pulse. After SPM, the spectrum is thus broadened but the pulse has actually become longer, as it is now chirped (positively). Hence, it then needs to be compressed, which is typically done using prisms, gratings or chirped mirrors. Although this scheme works well and its use is widespread, a considerable amount of energy is lost (50-60 % transmission through the HCF). An alternative solution is to combine spectral broadening, compression *and* high-harmonic generation in one device, thus minimizing the energy losses between the steps. This 'device' can be a special type of wave-guide, the details of the scheme are explained in the next section. For now, we will focus on the phase-matching characteristics of such a waveguide. From equation 6.2.2, we can derive the expression for the phase matching pressure in a waveguide. As in the case for the free-focusing geometry, we will constrain ourselves to the peak of the pulse and thus $\partial I/\partial z \approx 0$. However, this time the geometrical contribution cannot be neglected. Keeping the same expression for the critical ionization fraction η_c, the phase matching pressure for HHG in a waveguide is:

$$p_{pm} = \frac{p_0}{(\eta_c - \eta)} \frac{u_{lm}^2 \lambda_L}{4\pi a^2} \left(\frac{2\pi\Delta\delta}{\lambda_L} + \frac{p_0 r_e \lambda_L}{k_B T} \right)^{-1}. \tag{6.23}$$

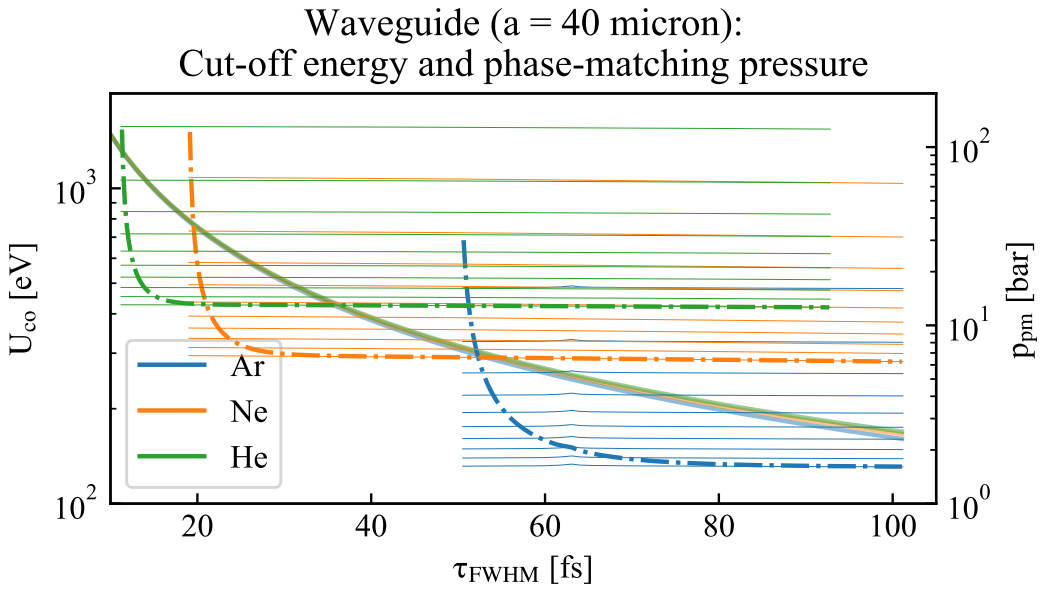

FIGURE 6.6: Cut-off energy (solid line) and expected phase matching pressure (dash-dotted line) as a function of pulse length, for a waveguide radius of $a = 40$ μm ($\lambda_L = 3.1$ μm, $E_{pulse} = 55$ μJ) and for various gases. The thin lines indicate phase matching pressures for ionization fractions of $\eta = 0, 0.1, 0.2, \ldots, 0.9\eta_c$. The dash-dotted line indicates the phase-matching pressure for the ionization fraction expected from calculation using the ADK model.

As before, we can now see the effect of temporal compression on the cut-off energy and the necessary phase-matching pressure. This is shown in figure 6.6 for a waveguide with radius $a = 40$ μm, assuming a coupling efficiency of 85 %, i.e. a pulse energy of 55 μJ (85 % is too high for a normal waveguide, however for a PCF it is reasonable, see next section). We also assume all energy is in the fundamental mode u_{11}, and that no energy is lost during compression (which is an approximation, but it serves to illustrate the principle). The principle of the figure is the same as for figure 6.5: as the pulse length decreases, the cut-off energy U_{co} increases, from about 105 eV at 100 fs to over a keV below 15 fs. The gas pressure for which this radiation can be phase-matched with the driver laser depends on the ionization level. The thin lines indicate ionization levels from $\eta = 0, 0.1, 0.2, \ldots, 0.9\eta_c$, the dash-dotted line is the phase-matching pressure for the ionization level as calculated using the ADK model, at the peak of the pulse. Again, the 'sweet spot' for the experiment is in the bend of the ADK-curve, for the same reasons as mentioned above. Hence, if we can compress the pulse to 60 fs, 25 fs, or 15 fs we can generate phase-matched high harmonics at a pressure of 2, 8, or 15 bar of argon, neon or helium, respectively. Because of the strong reabsorption of argon and neon (figure 6.3) it is preferable to generate with helium, but a pulse length of 15 fs is extremely challenging at 3 micron wavelength (one optical cycle corresponds to 10 fs). Figure 6.7 shows the same procedure but for a waveguide with a smaller radius, of $a = 30$ μm. Now the 'sweet spot' for generation in helium is shifted to around 23 fs and 30 bar.

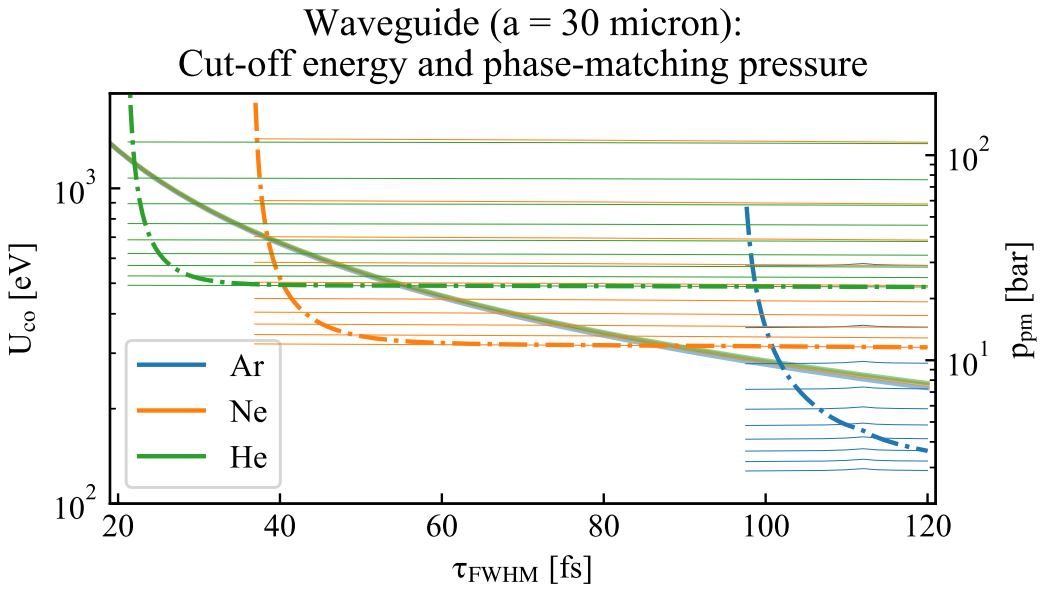

FIGURE 6.7: Cut-off energy (solid line) and expected phase matching pressure (dash-dotted line) as a function of pulse length, for a waveguide radius of $a = 30$ µm ($\lambda_L = 3.1$ µm, $E_{pulse} = 55$ µJ) and for various gases. The thin lines indicate phase matching pressures for ionization fractions of $\eta = 0, 0.1, 0.2, \ldots, 0.9\eta_c$. The dash-dotted line indicates the phase-matching pressure for the ionization fraction expected from calculation using the ADK model.

6.4 Soliton compression in a photonic crystal fiber for high-harmonic generation

In order to combine spectral broadening, temporal compression and high-harmonic generation, soliton compression in a photonic crystal fiber is proposed. The two main elements are explained in this section, and promising simulation results are presented.

6.4.1 Soliton compression

When an intense pulse propagates in a fiber and the chirp caused by self-phase modulation (SPM) is exactly balanced by the dispersion of the fiber, the pulse shape and spectrum remain invariant under propagation. This is a fundamental soliton. If the peak power of the input pulse is close to N^2 times that of a fundamental soliton, a higher order soliton is formed with order N. This higher order soliton is not invariant under propagation, but changes shape periodically with a so-called soliton period z_0. The initial part of this period consist of a considerable spectral broadening through SPM and a subsequent temporal compression as the chirp from SPM gets compensated by the (anomalous) dispersion of the fiber. This is the principle of soliton compression. More detail can be found in Appendix E and the references mentioned therein.

Already in the eighties, soliton compression in solid-core fibers was used to compress picosecond pulses by orders of magnitude [79–81]. More recently, the use of photonic crystal fibers (next paragraph) has allowed soliton compression to much higher peak intensities.

6.4.2 Photonic crystal fibers

In solid core fibers, such as the ones used for soliton compression in [79–81], the damage threshold of the material limits the use to (nowadays) fairly low peak intensities. Also, the nonlinearity of the medium cannot be adjusted to the experimental conditions. Hollow-core fibers filled with gas do sustain high peak intensities, and the non-linearity of the process under concern (soliton compression in our case) can be adjusted by adjusting the gas pressure. However the refractive index of the gas is close to unity, lower than that of the dielectric material that constitutes the fiber cladding. These fibers thus do not support bound modes, although for large diameter fibers all energy can be coupled into the fundamental mode with low losses to the cladding. However, for such large diameters the anomalous dispersion from these HCFs becomes very weak and with the addition of high pressure gas the dispersion turns normal. They are thus not ideal for soliton compression (which needs anomalous dispersion)[2]. The solution is given by hollow-core photonic crystal fibers (HC-PCF) [83–85]. They consist of a configuration of microchannels forming a two-dimensional photonic crystal. This photonic crystal forms a bandgap that confines the light within the hollow (gas-filled) core, through a mechanism called anti-resonant reflection (ARR). These come in two main varieties: Kagomé PCFs [86] and single-ring PCFs[3] [87–90], which are typically easier to make and have less absorption (and thus a higher damage threshold) in the infra-red spectral region. This thesis work uses the latter, through a collaboration with the Russel group at the Max Planck Institute for the Science of Light (Erlangen, Germany). Figure 6.8 shows the dispersion curve and a cross-section of one of the SR-PCFs used in this thesis. The wall thickness of the hollow capillaries inside the PCF defines a resonant condition for the laser wavelength (inside the capillary wall). At these resonances, the SR-PCF absorbs, at 2.0 μm for this particular PCF, as is clear from the dispersion curve. Away from these resonances the PCF guides the fundamental mode, with very low losses (tens of dB km^{-1}). The position of these resonances can be tailored through the wall thickness [91].

6.4.3 Simulation on soliton compression in a SR-PCF for high-harmonic generation

From the previous section on phase-matching of high-harmonics in a waveguide we can conclude that reasonably high gas pressures (several bar to several tens of bar) are needed. Although this is good to compensate the low single-atom response, it introduces strong reabsorption by all gases except helium. We would however need to compress the pulse by a factor 4 or 6 depending on the inner diameter of the PCF. To see if this is feasible, consider the results of a simulation performed by Dr. F. Tani from MPL, shown in figure 6.9. The code used for the simulation is described in [92] and solves the multimode full-field equation (using the propagation modes of the PCF) including linear dispersion, Kerr effects and ionization. The simulation was performed for soliton compression in the SR-PCF described above, in helium at 100 bar and at a pulse energy of 100 μJ (consistent with the plan at an earlier stage of the project). As the compression factor is proportional to the soliton order, which is proportional to the square root of the peak power, the compressed pulse length is expected to be about 1.3 times longer than the simulation result.

[2]Even though, very recently, impressive soliton compression has been achieved in a HCF [82].

[3]One might argue that SR-PCFs are not photonic crystal fibers as their guiding principle is not based on a photonic band gap as in the case of the Kagomé-type fiber (band gap in the radial direction). Indeed, technically these fibers should be called negative curvature hollow core fibers. However, as noted in [87], one can consider the cladding as a photonic crystal with a modulation of the curvature of the core-cladding boundary in the azimuthal direction. Following [88, 89], the term SR-PCF is used in this thesis.

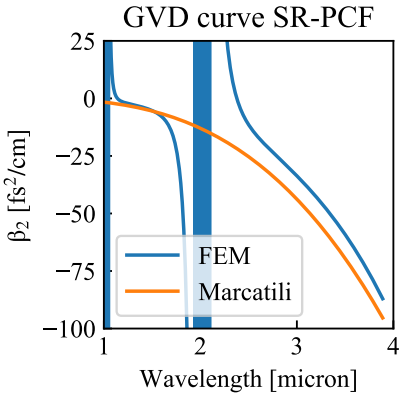

(A) Dispersion curve for the single-ring photonic crystal fiber (SR-PCF) used in this thesis. The blue line is the result of a finite elements calculation performed by MPL, the orange line is the dispersion from a waveguide with radius $a = 40$ µm using the Marcatili model [42].

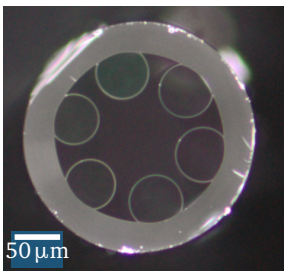

(B) Cross-section of the SR-PCF. The inner capillaries are hollow, their wall thickness determines the resonances of the SR-PCF.

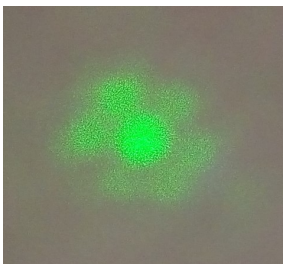

(C) Pattern formed by the green alignment laser as it exits the PCF.

FIGURE 6.8: The single-ring photonic crystal fiber, developed by the Russel group at MPL (Max Planck Institute for the Science of Light, Erlangen, Germany).

Alternatively, a PCF with a smaller core size ($a = 30$ instead of $a = 40$) would yield the same peak power, and thus a similar compression factor.

The simulation assumes a pressure profile as depicted in figure 6.9a: it is constant at 100 bar for the first 18 cm of PCF; then over the last 10 mm the pressure drops to a low vacuum (see next chapter for the technical implementation). The soliton compression takes place over the 18 cm length at constant pressure. Then, as the pulse is short and the peak intensity high enough to generate harmonics, it propagates through a pressure gradient, where the harmonics are efficiently generated over a length of about 1 mm, where the pressure equals the phase matching pressure. Next, the pressure drops to low vacuum levels to prevent reabsorption.

The bottom panels show the spectral and temporal evolution of the high-order soliton as it propagates through the fiber, showing a strong spectral broadening and temporal narrowing, leading to an output pulse with a pulse length of 8.6 fs (FWHM)[4], hence a compression factor of more than an order of magnitude. The compressed part of the pulse contains 51 % of the input pulse energy, increasing the peak intensity by a factor of 5.4.

6.5 Conclusions

High harmonic generation is a technique that has opened the field of attosecond science: laser-based sources generate light pulses in the XUV and soft X-ray regime with durations as short as tens of attoseconds. The mechanism is based on tunnel ionization, acceleration and recombination of electrons by a strong laser field. Phase matching of the laser with the harmonic radiation allows for efficient generation. To extend the cut-off energy of phase-matched harmonics to a keV and beyond, long wavelength driver lasers are needed. In addition, high repetition rates are beneficial for many experiments. High

[4]Although 8.6 fs is shorter than a single optical cycle, note that this value is the FWHM of the intensity profile (as is customary in laser physics) and that this intensity profile is far from gaussian. The electric field does thus consist of more than one optical cycle.

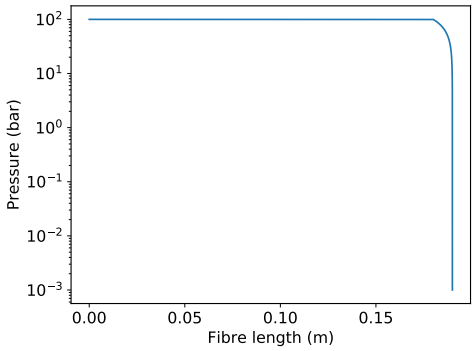

(A) The pressure profile of the helium inside the fiber. The first 18 cm are at 100 bar, this is where the soliton compression takes place. The last 10 mm of PCF the pressure drops to a low vacuum. In this pressure drop harmonics are generated.

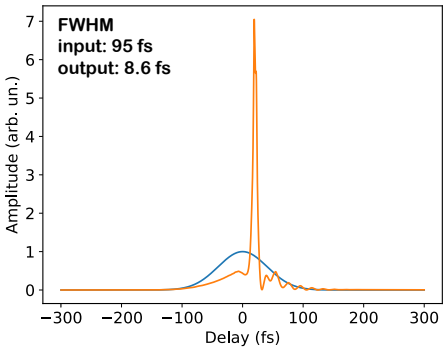

(B) The input and output pulse, showing a compression of more than a factor 10.

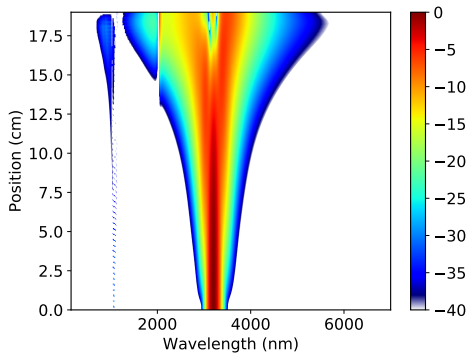

(C) Spectral evolution of the soliton. Note the resonance at 2 micron.

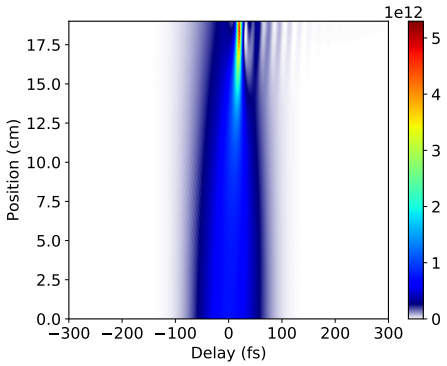

(D) Temporal evolution of the soliton.

FIGURE 6.9: Simulation results for soliton compression in He at 100, and an input pulse energy of 100 μJ. Simulation performed by Dr. F. Tani (MPL).

harmonic generation using a high rep-rate, mid-IR OPCPA can be done in a tight focusing geometry, for which the scaling with focal spot size is investigated. It shows that high phase-matching pressures are needed, which are beneficial to compensate for the low single-atom response and the small generation volume, but which can be hard to realize experimentally. An alternative scheme is proposed, where the pulses are temporally compressed in a single-ring photonic crystal fiber through soliton compression, and where the harmonics are generated at the end of the fiber. Both schemes could provide a way towards a high repetition rate, keV high harmonic source. The next chapter explores these schemes experimentally.

Bibliography

[1] T. H. Maiman. Stimulated Optical Radiation in Ruby. *Nature*, 187(4736):493, August 1960. ISSN 1476-4687. doi: 10.1038/187493a0.

[2] P. A. Franken, A. E. Hill, C. W. Peters, and G. Weinreich. Generation of Optical Harmonics. *Physical Review Letters*, 7(4):118–119, August 1961. doi: 10.1103/PhysRevLett.7.118.

[3] M. Drescher, M. Hentschel, R. Kienberger, M. Uiberacker, V. Yakovlev, A. Scrinzi, Th Westerwalbesloh, U. Kleineberg, U. Heinzmann, and F. Krausz. Time-resolved atomic inner-shell spectroscopy. *Nature*, 419(6909):803, October 2002. ISSN 1476-4687. doi: 10.1038/nature01143.

[4] F. Calegari, D. Ayuso, A. Trabattoni, L. Belshaw, S. De Camillis, S. Anumula, F. Frassetto, L. Poletto, A. Palacios, P. Decleva, J. B. Greenwood, F. Martín, and M. Nisoli. Ultrafast electron dynamics in phenylalanine initiated by attosecond pulses. *Science*, 346(6207):336–339, October 2014. ISSN 0036-8075, 1095-9203. doi: 10.1126/science.1254061.

[5] Yoann Pertot, Cédric Schmidt, Mary Matthews, Adrien Chauvet, Martin Huppert, Vit Svoboda, Aaron von Conta, Andres Tehlar, Denitsa Baykusheva, Jean-Pierre Wolf, and Hans Jakob Wörner. Time-resolved x-ray absorption spectroscopy with a water window high-harmonic source. *Science*, 355(6322):264–267, January 2017. ISSN 0036-8075, 1095-9203. doi: 10.1126/science.aah6114.

[6] L. Drescher, M. C. E. Galbraith, G. Reitsma, J. Dura, N. Zhavoronkov, S. Patchkovskii, M. J. J. Vrakking, and J. Mikosch. Communication: XUV transient absorption spectroscopy of iodomethane and iodobenzene photodissociation. *The Journal of Chemical Physics*, 145(1):011101, July 2016. ISSN 0021-9606. doi: 10.1063/1.4955212.

[7] Andrew R. Attar, Aditi Bhattacherjee, C. D. Pemmaraju, Kirsten Schnorr, Kristina D. Closser, David Prendergast, and Stephen R. Leone. Femtosecond x-ray spectroscopy of an electrocyclic ring-opening reaction. *Science*, 356(6333):54–59, April 2017. ISSN 0036-8075, 1095-9203. doi: 10.1126/science.aaj2198.

[8] V. Gruson, L. Barreau, Á. Jiménez-Galan, F. Risoud, J. Caillat, A. Maquet, B. Carré, F. Lepetit, J.-F. Hergott, T. Ruchon, L. Argenti, R. Taïeb, F. Martín, and P. Salières. Attosecond dynamics through a Fano resonance: Monitoring the birth of a photoelectron. *Science*, 354(6313):734–738, November 2016. ISSN 0036-8075, 1095-9203. doi: 10.1126/science.aah5188.

[9] F. Willems, C. T. L. Smeenk, N. Zhavoronkov, O. Kornilov, I. Radu, M. Schmidbauer, M. Hanke, C. von Korff Schmising, M. J. J. Vrakking, and S. Eisebitt. Probing ultrafast spin dynamics with high-harmonic magnetic circular dichroism spectroscopy. *Physical Review B*, 92(22):220405, December 2015. doi: 10.1103/PhysRevB.92.220405.

[10] J. Weisshaupt, A. Rouzée, M. Woerner, M. J. J. Vrakking, T. Elsaesser, E. L. Shirley, and A. Borgschulte. Ultrafast modulation of electronic structure by coherent phonon excitations. *Physical Review B*, 95(8):081101, February 2017. doi: 10.1103/PhysRevB.95.081101.

[11] M. C. Kohler, T. Pfeifer, K. Z. Hatsagortsyan, and C. H. Keitel. Chapter 4 - Frontiers of Atomic High-Harmonic Generation. In Paul Berman, Ennio Arimondo, and Chun Lin, editors, *Advances In Atomic, Molecular, and Optical Physics*, volume 61 of *Advances in Atomic, Molecular, and Optical Physics*, pages 159–208. Academic Press, July 2012. doi: 10.1016/B978-0-12-396482-3.00004-1.

[12] P. Agostini, F. Fabre, G. Mainfray, G. Petite, and N. K. Rahman. Free-Free Transitions Following Six-Photon Ionization of Xenon Atoms. *Physical Review Letters*, 42(17):1127–1130, April 1979. doi: 10.1103/PhysRevLett.42.1127.

[13] A. McPherson, G. Gibson, H. Jara, U. Johann, T. S. Luk, I. A. McIntyre, K. Boyer, and C. K. Rhodes. Studies of multiphoton production of vacuum-ultraviolet radiation in the rare gases. *JOSA B*, 4(4):595–601, April 1987. ISSN 1520-8540. doi: 10.1364/JOSAB.4.000595.

[14] M. Ferray, A. L'Huillier, X. F. Li, L. A. Lompre, G. Mainfray, and C. Manus. Multiple-harmonic conversion of 1064 nm radiation in rare gases. *Journal of Physics B: Atomic, Molecular and Optical Physics*, 21(3):L31–L35, February 1988. ISSN 0953-4075. doi: 10.1088/0953-4075/21/3/001.

[15] P. B. Corkum. Plasma perspective on strong field multiphoton ionization. *Physical Review Letters*, 71(13):1994–1997, September 1993. doi: 10.1103/PhysRevLett.71.1994.

[16] M. Lewenstein, Ph. Balcou, M. Yu. Ivanov, Anne L'Huillier, and P. B. Corkum. Theory of high-harmonic generation by low-frequency laser fields. *Physical Review A*, 49(3):2117–2132, March 1994. doi: 10.1103/PhysRevA.49.2117.

[17] Maciej Lewenstein, Pascal Salières, and Anne L'Huillier. Phase of the atomic polarization in high-order harmonic generation. *Physical Review A*, 52(6):4747–4754, December 1995. doi: 10.1103/PhysRevA.52.4747.

[18] P. M. Paul, E. S. Toma, P. Breger, G. Mullot, F. Augé, Ph Balcou, H. G. Muller, and P. Agostini. Observation of a Train of Attosecond Pulses from High Harmonic Generation. *Science*, 292(5522):1689–1692, June 2001. ISSN 0036-8075, 1095-9203. doi: 10.1126/science.1059413.

[19] M. Hentschel, R. Kienberger, Ch Spielmann, G. A. Reider, N. Milosevic, T. Brabec, P. Corkum, U. Heinzmann, M. Drescher, and F. Krausz. Attosecond metrology. *Nature*, 414(6863):509, November 2001. ISSN 1476-4687. doi: 10.1038/35107000.

[20] I. J. Sola, E. Mével, L. Elouga, E. Constant, V. Strelkov, L. Poletto, P. Villoresi, E. Benedetti, J.-P. Caumes, S. Stagira, C. Vozzi, G. Sansone, and M. Nisoli. Controlling attosecond electron dynamics by phase-stabilized polarization gating. *Nature Physics*, 2(5):319–322, May 2006. ISSN 1745-2481. doi: 10.1038/nphys281.

[21] G. Sansone, E. Benedetti, F. Calegari, C. Vozzi, L. Avaldi, R. Flammini, L. Poletto, P. Villoresi, C. Altucci, R. Velotta, S. Stagira, S. De Silvestri, and M. Nisoli. Isolated Single-Cycle Attosecond Pulses. *Science*, 314(5798):443–446, October 2006. ISSN 0036-8075, 1095-9203. doi: 10.1126/science.1132838.

[22] Thomas Pfeifer, Lukas Gallmann, Mark J. Abel, Daniel M. Neumark, and Stephen R. Leone. Single attosecond pulse generation in the multicycle-driver regime by adding a weak second-harmonic field. *Optics Letters*, 31(7):975–977, April 2006. ISSN 1539-4794. doi: 10.1364/OL.31.000975.

[23] Hamed Merdji, Thierry Auguste, Willem Boutu, J.-Pascal Caumes, Bertrand Carré, Thomas Pfeifer, Aurélie Jullien, Daniel M. Neumark, and Stephen R. Leone. Isolated attosecond pulses using a detuned second-harmonic field. *Optics Letters*, 32(21): 3134–3136, November 2007. ISSN 1539-4794. doi: 10.1364/OL.32.003134.

[24] C. Vozzi, F. Calegari, F. Frassetto, L. Poletto, G. Sansone, P. Villoresi, M. Nisoli, S. De Silvestri, and S. Stagira. Coherent continuum generation above 100 eV driven by an ir parametric source in a two-color scheme. *Physical Review A*, 79(3):033842, March 2009. doi: 10.1103/PhysRevA.79.033842.

[25] Thomas Pfeifer, Aurélie Jullien, Mark J. Abel, Phillip M. Nagel, Lukas Gallmann, Daniel M. Neumark, and Stephen R. Leone. Generating coherent broadband continuum soft-x-ray radiation by attosecond ionization gating. *Optics Express*, 15(25): 17120–17128, December 2007. ISSN 1094-4087. doi: 10.1364/OE.15.017120.

[26] Linda Young, Kiyoshi Ueda, Markus Gühr, Philip H. Bucksbaum, Marc Simon, Shaul Mukamel, Nina Rohringer, Kevin C. Prince, Claudio Masciovecchio, Michael Meyer, Artem Rudenko, Daniel Rolles, Christoph Bostedt, Matthias Fuchs, David A. Reis, Robin Santra, Henry Kapteyn, Margaret Murnane, Heide Ibrahim, François Légaré, Marc Vrakking, Marcus Isinger, David Kroon, Mathieu Gisselbrecht, Anne L'Huillier, Hans Jakob Wörner, and Stephen R. Leone. Roadmap of ultrafast x-ray atomic and molecular physics. *Journal of Physics B: Atomic, Molecular and Optical Physics*, 51 (3):032003, January 2018. ISSN 0953-4075. doi: 10.1088/1361-6455/aa9735.

[27] Giuseppe Sansone, Luca Poletto, and Mauro Nisoli. High-energy attosecond light sources. *Nature Photonics*, 5(11):655–663, November 2011. ISSN 1749-4893. doi: 10.1038/nphoton.2011.167.

[28] Zenghu Chang and P. Corkum. Attosecond photon sources: The first decade and beyond [Invited]. *JOSA B*, 27(11):B9–B17, November 2010. ISSN 1520-8540. doi: 10.1364/JOSAB.27.0000B9.

[29] Ferenc Krausz and Misha Ivanov. Attosecond physics. *Reviews of Modern Physics*, 81 (1):163–234, February 2009. doi: 10.1103/RevModPhys.81.163.

[30] M. Nisoli and G. Sansone. New frontiers in attosecond science. *Progress in Quantum Electronics*, 33(1):17–59, January 2009. ISSN 0079-6727. doi: 10.1016/j.pquantelec.2008.10.004.

[31] P. B. Corkum and Ferenc Krausz. Attosecond science. *Nature Physics*, 3(6):381–387, June 2007. ISSN 1745-2481. doi: 10.1038/nphys620.

[32] Philippe Antoine, Anne L'Huillier, and Maciej Lewenstein. Attosecond Pulse Trains Using High–Order Harmonics. *Physical Review Letters*, 77(7):1234–1237, August 1996. doi: 10.1103/PhysRevLett.77.1234.

[33] Mette B. Gaarde and Kenneth J. Schafer. Space-Time Considerations in the Phase Locking of High Harmonics. *Physical Review Letters*, 89(21):213901, October 2002. doi: 10.1103/PhysRevLett.89.213901.

[34] Y. Mairesse, A. de Bohan, L. J. Frasinski, H. Merdji, L. C. Dinu, P. Monchicourt, P. Breger, M. Kovačev, R. Taïeb, B. Carré, H. G. Muller, P. Agostini, and P. Salières. Attosecond Synchronization of High-Harmonic Soft X-rays. *Science*, 302(5650): 1540–1543, November 2003. ISSN 0036-8075, 1095-9203. doi: 10.1126/science.1090277.

[35] Rodrigo López-Martens, Katalin Varjú, Per Johnsson, Johan Mauritsson, Yann Mairesse, Pascal Salières, Mette B. Gaarde, Kenneth J. Schafer, Anders Persson, Sune Svanberg, Claes-Göran Wahlström, and Anne L'Huillier. Amplitude and Phase Control of Attosecond Light Pulses. *Physical Review Letters*, 94(3):033001, January 2005. doi: 10.1103/PhysRevLett.94.033001.

[36] Anne-Sophie Morlens, Philippe Balcou, Philippe Zeitoun, Constance Valentin, Vincent Laude, and Sophie Kazamias. Compression of attosecond harmonic pulses by extreme-ultraviolet chirped mirrors. *Optics Letters*, 30(12):1554–1556, June 2005. ISSN 1539-4794. doi: 10.1364/OL.30.001554.

[37] Michael Hofstetter, Martin Schultze, Markus Fieß, Benjamin Dennhardt, Alexander Guggenmos, Justin Gagnon, Vladislav S. Yakovlev, Eleftherios Goulielmakis, Reinhard Kienberger, Eric M. Gullikson, Ferenc Krausz, and Ulf Kleineberg. Attosecond dispersion control by extreme ultraviolet multilayer mirrors. *Optics Express*, 19(3): 1767–1776, January 2011. ISSN 1094-4087. doi: 10.1364/OE.19.001767.

[38] Ph. Balcou and Anne L'Huillier. Phase-matching effects in strong-field harmonic generation. *Physical Review A*, 47(2):1447–1459, February 1993. doi: 10.1103/PhysRevA.47.1447.

[39] Philippe Balcou, Pascal Sali'eres, Anne L'Huillier, and Maciej Lewenstein. Generalized phase-matching conditions for high harmonics: The role of field-gradient forces. *Physical Review A*, 55(4):3204–3210, April 1997. doi: 10.1103/PhysRevA.55.3204.

[40] C. M. Heyl, J. Güdde, A. L'Huillier, and U. Höfer. High-order harmonic generation with micro-Joule laser pulses at high repetition rates. *Journal of Physics B: Atomic, Molecular and Optical Physics*, 45(7):074020, March 2012. ISSN 0953-4075. doi: 10.1088/0953-4075/45/7/074020.

[41] Mette B. Gaarde, Jennifer L. Tate, and Kenneth J. Schafer. Macroscopic aspects of attosecond pulse generation. *Journal of Physics B: Atomic, Molecular and Optical Physics*, 41(13):132001, June 2008. ISSN 0953-4075. doi: 10.1088/0953-4075/41/13/132001.

[42] E. a. J. Marcatili and R. A. Schmeltzer. Hollow Metallic and Dielectric Waveguides for Long Distance Optical Transmission and Lasers. *Bell System Technical Journal*, 43(4):1783–1809, July 1964. ISSN 1538-7305. doi: 10.1002/j.1538-7305.1964.tb04108.x.

[43] Charles G. Durfee, Andy R. Rundquist, Sterling Backus, Catherine Herne, Margaret M. Murnane, and Henry C. Kapteyn. Phase Matching of High-Order Harmonics in Hollow Waveguides. *Physical Review Letters*, 83(11):2187–2190, September 1999. doi: 10.1103/PhysRevLett.83.2187.

[44] Tenio Popmintchev, Ming-Chang Chen, Alon Bahabad, Michael Gerrity, Pavel Sidorenko, Oren Cohen, Ivan P. Christov, Margaret M. Murnane, and Henry C. Kapteyn. Phase matching of high harmonic generation in the soft and hard X-ray regions of the spectrum. *Proceedings of the National Academy of Sciences*, 106 (26):10516–10521, June 2009. ISSN 0027-8424, 1091-6490. doi: 10.1073/pnas.0903748106.

[45] Tenio Popmintchev. *Tunable Ultrafast Coherent Light in the Soft and Hard X-Ray Regions of the Spectrum: Phase Matching of Extreme High-Order Harmonic Generation*. PhD thesis, University of Colorado, 2010.

[46] Andy Rundquist, Charles G. Durfee, Zenghu Chang, Catherine Herne, Sterling Backus, Margaret M. Murnane, and Henry C. Kapteyn. Phase-Matched Generation of Coherent Soft X-rays. *Science*, 280(5368):1412–1415, May 1998. ISSN 0036-8075, 1095-9203. doi: 10.1126/science.280.5368.1412.

[47] M.-C. Chen, P. Arpin, T. Popmintchev, M. Gerrity, B. Zhang, M. Seaberg, D. Popmintchev, M. M. Murnane, and H. C. Kapteyn. Bright, Coherent, Ultrafast Soft X-Ray Harmonics Spanning the Water Window from a Tabletop Light Source. *Physical Review Letters*, 105(17):173901, October 2010. doi: 10.1103/PhysRevLett.105.173901.

[48] Jan Rothhardt, Manuel Krebs, Steffen Hädrich, Stefan Demmler, Jens Limpert, and Andreas Tünnermann. Absorption-limited and phase-matched high harmonic generation in the tight focusing regime. *New Journal of Physics*, 16(3):033022, March 2014. ISSN 1367-2630. doi: 10.1088/1367-2630/16/3/033022.

[49] J. Peatross, M. V. Fedorov, and K. C. Kulander. Intensity-dependent phase-matching effects in harmonic generation. *JOSA B*, 12(5):863–870, May 1995. ISSN 1520-8540. doi: 10.1364/JOSAB.12.000863.

[50] Xiaoshi Zhang, Amy L. Lytle, Tenio Popmintchev, Xibin Zhou, Henry C. Kapteyn, Margaret M. Murnane, and Oren Cohen. Quasi-phase-matching and quantum-path control of high-harmonic generation using counterpropagating light. *Nature Physics*, 3(4):270–275, April 2007. ISSN 1745-2481. doi: 10.1038/nphys541.

[51] Oren Cohen, Xiaoshi Zhang, Amy L. Lytle, Tenio Popmintchev, Margaret M. Murnane, and Henry C. Kapteyn. Grating-Assisted Phase Matching in Extreme Nonlinear Optics. *Physical Review Letters*, 99(5):053902, July 2007. doi: 10.1103/PhysRevLett.99.053902.

[52] A. Paul, R. A. Bartels, R. Tobey, H. Green, S. Weiman, I. P. Christov, M. M. Murnane, H. C. Kapteyn, and S. Backus. Quasi-phase-matched generation of coherent extreme-ultraviolet light. *Nature*, 421(6918):51, January 2003. ISSN 1476-4687. doi: 10.1038/nature01222.

[53] Emily A. Gibson, Ariel Paul, Nick Wagner, Ra'anan Tobey, David Gaudiosi, Sterling Backus, Ivan P. Christov, Andy Aquila, Eric M. Gullikson, David T. Attwood, Margaret M. Murnane, and Henry C. Kapteyn. Coherent Soft X-ray Generation in the Water Window with Quasi-Phase Matching. *Science*, 302(5642):95–98, October 2003. ISSN 0036-8075, 1095-9203. doi: 10.1126/science.1088654.

[54] M. Zepf, B. Dromey, M. Landreman, P. Foster, and S. M. Hooker. Bright Quasi-Phase-Matched Soft-X-Ray Harmonic Radiation from Argon Ions. *Physical Review Letters*, 99(14):143901, October 2007. doi: 10.1103/PhysRevLett.99.143901.

[55] Ch Spielmann, N. H. Burnett, S. Sartania, R. Koppitsch, M. Schnürer, C. Kan, M. Lenzner, P. Wobrauschek, and F. Krausz. Generation of Coherent X-rays in the Water Window Using 5-Femtosecond Laser Pulses. *Science*, 278(5338):661–664, October 1997. ISSN 0036-8075, 1095-9203. doi: 10.1126/science.278.5338.661.

[56] Gabriel Tempea, Michael Geissler, Matthias Schnürer, and Thomas Brabec. Self-Phase-Matched High Harmonic Generation. *Physical Review Letters*, 84(19):4329–4332, May 2000. doi: 10.1103/PhysRevLett.84.4329.

[57] M. Geissler, G. Tempea, and T. Brabec. Phase-matched high-order harmonic generation in the nonadiabatic limit. *Physical Review A*, 62(3):033817, August 2000. doi: 10.1103/PhysRevA.62.033817.

[58] J. Seres, P. Wobrauschek, Ch Streli, V. S. Yakovlev, E. Seres, F. Krausz, and Ch Spielmann. Generation of coherent keV x-rays with intense femtosecond laser pulses. *New Journal of Physics*, 8(10):251–251, October 2006. ISSN 1367-2630. doi: 10.1088/1367-2630/8/10/251.

[59] E. Constant, D. Garzella, P. Breger, E. Mével, Ch. Dorrer, C. Le Blanc, F. Salin, and P. Agostini. Optimizing High Harmonic Generation in Absorbing Gases: Model and Experiment. *Physical Review Letters*, 82(8):1668–1671, February 1999. doi: 10.1103/PhysRevLett.82.1668.

[60] C. Hernández-García, J. A. Pérez-Hernández, T. Popmintchev, M. M. Murnane, H. C. Kapteyn, A. Jaron-Becker, A. Becker, and L. Plaja. Zeptosecond High Harmonic keV X-Ray Waveforms Driven by Midinfrared Laser Pulses. *Physical Review Letters*, 111 (3):033002, July 2013. doi: 10.1103/PhysRevLett.111.033002.

[61] Tenio Popmintchev, Ming-Chang Chen, Oren Cohen, Michael E. Grisham, Jorge J. Rocca, Margaret M. Murnane, and Henry C. Kapteyn. Extended phase matching of high harmonics driven by mid-infrared light. *Optics Letters*, 33(18):2128–2130, September 2008. ISSN 1539-4794. doi: 10.1364/OL.33.002128.

[62] Ariel Gordon and Franz X. Kärtner. Scaling of keV HHG photon yield with drive wavelength. *Optics Express*, 13(8):2941–2947, April 2005. ISSN 1094-4087. doi: 10.1364/OPEX.13.002941.

[63] J. Tate, T. Auguste, H. G. Muller, P. Salières, P. Agostini, and L. F. DiMauro. Scaling of Wave-Packet Dynamics in an Intense Midinfrared Field. *Physical Review Letters*, 98(1):013901, January 2007. doi: 10.1103/PhysRevLett.98.013901.

[64] P. Colosimo, G. Doumy, C. I. Blaga, J. Wheeler, C. Hauri, F. Catoire, J. Tate, R. Chirla, A. M. March, G. G. Paulus, H. G. Muller, P. Agostini, and L. F. DiMauro. Scaling strong-field interactions towards the classical limit. *Nature Physics*, 4(5):386–389, May 2008. ISSN 1745-2481. doi: 10.1038/nphys914.

[65] M. V. Frolov, N. L. Manakov, and Anthony F. Starace. Wavelength Scaling of High-Harmonic Yield: Threshold Phenomena and Bound State Symmetry Dependence. *Physical Review Letters*, 100(17):173001, May 2008. doi: 10.1103/PhysRevLett.100.173001.

[66] Giulio Cerullo and Sandro De Silvestri. Ultrafast optical parametric amplifiers. *Review of Scientific Instruments*, 74(1):1–18, January 2003. ISSN 0034-6748. doi: 10.1063/1.1523642.

[67] T. Popmintchev, M.-C. Chen, D. Popmintchev, P. Arpin, S. Brown, S. Alisauskas, G. Andriukaitis, T. Balciunas, O. D. Mucke, A. Pugzlys, A. Baltuska, B. Shim, S. E. Schrauth, A. Gaeta, C. Hernandez-Garcia, L. Plaja, A. Becker, A. Jaron-Becker, M. M. Murnane, and H. C. Kapteyn. Bright Coherent Ultrahigh Harmonics in the keV X-ray Regime from Mid-Infrared Femtosecond Lasers. *Science*, 336(6086):1287–1291, June 2012. ISSN 0036-8075, 1095-9203. doi: 10.1126/science.1218497.

[68] Stefan Mathias, Michael Bauer, Martin Aeschlimann, Luis Miaja-Avila, Henry C. Kapteyn, and Margaret M. Murnane. Time-Resolved Photoelectron Spectroscopy at Surfaces Using Femtosecond XUV Pulses. In *Dynamics at Solid State Surfaces and Interfaces*, pages 499–535. John Wiley & Sons, Ltd, 2010. ISBN 978-3-527-63341-8. doi: 10.1002/9783527633418.ch21.

[69] T. Südmeyer, S. V. Marchese, S. Hashimoto, C. R. E. Baer, G. Gingras, B. Witzel, and U. Keller. Femtosecond laser oscillators for high-field science. *Nature Photonics*, 2 (10):599–604, October 2008. ISSN 1749-4893. doi: 10.1038/nphoton.2008.194.

[70] T. Haarlammert and H. Zacharias. Application of high harmonic radiation in surface science. *Current Opinion in Solid State and Materials Science*, 13(1):13–27, February 2009. ISSN 1359-0286. doi: 10.1016/j.cossms.2008.12.003.

[71] P. Billaud, M. Géléoc, Y. J. Picard, K. Veyrinas, J. F. Hergott, S. Marggi Poullain, P. Breger, T. Ruchon, M. Roulliay, F. Delmotte, F. Lepetit, A. Huetz, B. Carré, and D. Dowek. Molecular frame photoemission in dissociative ionization of H2and D2induced by high harmonic generation femtosecond XUV pulses. *Journal of Physics B: Atomic, Molecular and Optical Physics*, 45(19):194013, September 2012. ISSN 0953-4075. doi: 10.1088/0953-4075/45/19/194013.

[72] Giuseppe Sansone. New perspectives in attosecond physics. *Journal of Physics: Conference Series*, 388(1):012028, November 2012. ISSN 1742-6596. doi: 10.1088/1742-6596/388/1/012028.

[73] C. M. Heyl, H. Coudert-Alteirac, M. Miranda, M. Louisy, K. Kovacs, V. Tosa, E. Balogh, K. Varjú, A. L'Huillier, A. Couairon, and C. L. Arnold. Scale-invariant nonlinear optics in gases. *Optica*, 3(1):75–81, January 2016. ISSN 2334-2536. doi: 10.1364/OPTICA.3.000075.

[74] Maxim V. Ammosov, Nikolai B. Delone, and Vladimir P. Krainov. Tunnel Ionization Of Complex Atoms And Atomic Ions In Electromagnetic Field. In *High Intensity Laser Processes*, volume 664, pages 138–141, October 1986. doi: 10.1117/12.938695.

[75] Zenghu Chang. *Fundamentals of Attosecond Optics*. CRC Press, Boca Raton, Fla., 2011. ISBN 978-1-4200-8938-7. OCLC: 798923668.

[76] M. Nisoli, S. De Silvestri, and O. Svelto. Generation of high energy 10 fs pulses by a new pulse compression technique. *Applied Physics Letters*, 68(20):2793–2795, May 1996. ISSN 0003-6951. doi: 10.1063/1.116609.

[77] M. Nisoli, S. Stagira, S. De Silvestri, O. Svelto, S. Sartania, Z. Cheng, M. Lenzner, C. Spielmann, and F. Krausz. A novel-high energy pulse compression system: Generation of multigigawatt sub-5-fs pulses. *Applied Physics B*, 65(2):189–196, August 1997. ISSN 1432-0649. doi: 10.1007/s003400050263.

[78] Bruno E. Schmidt, Andrew D. Shiner, Mathieu Giguère, Philippe Lassonde, Carlos A. Trallero-Herrero, J.-C. Kieffer, P. B. Corkum, D. M. Villeneuve, and François Légaré.

High harmonic generation with long-wavelength few-cycle laser pulses. *Journal of Physics B: Atomic, Molecular and Optical Physics*, 45(7):074008, March 2012. ISSN 0953-4075. doi: 10.1088/0953-4075/45/7/074008.

[79] L. F. Mollenauer, R. H. Stolen, J. P. Gordon, and W. J. Tomlinson. Extreme picosecond pulse narrowing by means of soliton effect in single-mode optical fibers. *Optics Letters*, 8(5):289–291, May 1983. ISSN 1539-4794. doi: 10.1364/OL.8.000289.

[80] K. Tai and A. Tomita. 1100x optical fiber pulse compression using grating pair and soliton effect at 1.319 Mm. *Applied Physics Letters*, 48(16):1033–1035, April 1986. ISSN 0003-6951. doi: 10.1063/1.96639.

[81] A. S. Gouveia-Neto, A. S. L. Gomes, and J. R. Taylor. Generation of 33-fsec pulses at 1.32 Mm through a high-order soliton effect in a single-mode optical fiber. *Optics Letters*, 12(6):395–397, June 1987. ISSN 1539-4794. doi: 10.1364/OL.12.000395.

[82] John C. Travers, Teodora F. Grigorova, Christian Brahms, and Federico Belli. High-energy pulse self-compression and ultraviolet generation through soliton dynamics in hollow capillary fibres. *Nature Photonics*, page 1, April 2019. ISSN 1749-4893. doi: 10.1038/s41566-019-0416-4.

[83] John M. Dudley and J. Roy Taylor. Ten years of nonlinear optics in photonic crystal fibre. *Nature Photonics*, 3(2):85–90, February 2009. ISSN 1749-4893. doi: 10.1038/nphoton.2008.285.

[84] John C. Travers, Wonkeun Chang, Johannes Nold, Nicolas Y. Joly, and Philip St J. Russell. Ultrafast nonlinear optics in gas-filled hollow-core photonic crystal fibers [Invited]. *JOSA B*, 28(12):A11–A26, December 2011. ISSN 1520-8540. doi: 10.1364/JOSAB.28.000A11.

[85] P. St J. Russell, P. Hölzer, W. Chang, A. Abdolvand, and J. C. Travers. Hollow-core photonic crystal fibres for gas-based nonlinear optics. *Nature Photonics*, 8(4):278–286, April 2014. ISSN 1749-4893. doi: 10.1038/nphoton.2013.312.

[86] F. Benabid, J. C. Knight, G. Antonopoulos, and P. St J. Russell. Stimulated Raman Scattering in Hydrogen-Filled Hollow-Core Photonic Crystal Fiber. *Science*, 298(5592):399–402, October 2002. ISSN 0036-8075, 1095-9203. doi: 10.1126/science.1076408.

[87] Andrey Pryamikov. Negative curvature hollow core fibers: Design, fabrication, and applications. In *Proceedings of SPIE - The International Society for Optical Engineering*, volume 8961, February 2014. doi: 10.1117/12.2041653.

[88] Fei Yu, William J. Wadsworth, and Jonathan C. Knight. Low loss silica hollow core fibers for 3–4 Mm spectral region. *Optics Express*, 20(10):11153–11158, May 2012. ISSN 1094-4087. doi: 10.1364/OE.20.011153.

[89] Patrick Uebel, Mehmet C. Günendi, Michael H. Frosz, Goran Ahmed, Nitin N. Edavalath, Jean-Michel Ménard, and Philip St J. Russell. Broadband robustly single-mode hollow-core PCF by resonant filtering of higher-order modes. *Optics Letters*, 41(9):1961–1964, May 2016. ISSN 1539-4794. doi: 10.1364/OL.41.001961.

[90] Andrey D. Pryamikov, Alexander S. Biriukov, Alexey F. Kosolapov, Victor G. Plotnichenko, Sergei L. Semjonov, and Evgeny M. Dianov. Demonstration of a waveguide regime for a silica hollow - core microstructured optical fiber with a negative

curvature of the core boundary in the spectral region > 3.5 micrometer. *Optics Express*, 19(2):1441–1448, January 2011. ISSN 1094-4087. doi: 10.1364/OE.19.001441.

[91] F. Tani, F. Köttig, D. Novoa, R. Keding, and P. St J. Russell. Effect of anti-crossings with cladding resonances on ultrafast nonlinear dynamics in gas-filled photonic crystal fibers. *Photonics Research*, 6(2):84–88, February 2018. ISSN 2327-9125. doi: 10.1364/PRJ.6.000084.

[92] Francesco Tani, John C. Travers, and Philip St J. Russell. Multimode ultrafast nonlinear optics in optical waveguides: Numerical modeling and experiments in kagomé photonic-crystal fiber. *JOSA B*, 31(2):311–320, February 2014. ISSN 1520-8540. doi: 10.1364/JOSAB.31.000311.

Chapter 7

Experiments towards a high repetition rate, mid-IR driven, high harmonic source

7.1 Introduction

This chapter summarizes the technical design and experimental works performed at ICFO (Institut de Ciències Fotòniques, Castelldefels, Spain) towards a high harmonic source with a high repetition rate (160 kHz) and a high cut-off energy, based on a mid-IR OPCPA laser system. First the laser system is described, as well as the high pressure gas and vacuum systems. Then the designs of the first attempts are presented, based on free focusing in a gas jet as well as in a high pressure gas cell. Next, the design of the integrated setup is explained, which combines soliton compression and high harmonic generation in one device (principles introduced in the previous chapter). Preliminary results as well as the technical challenges are specified. Finally, a setup which decoupled soliton compression and high harmonic generation was used, which also gave some preliminary results. The challenges are summarized at the end of the chapter.

7.2 The 3 micron OPCPA system

The 3 micron OPCPA laser system is schematically depicted in figure 7.1. The front-end consists of a commercial Er-fiber-based laser (Femtofiber Scientific from Toptica Photonics AG, Gräfelfing, Germany) and a difference frequency generation (DFG) stage. The output of the oscillator, operating at a wavelength of 1560 nm at 100 MHz, is split in two arms, which are both amplified and compressed (not shown here). One of these arms is then fed into a highly non-linear fiber to create a supercontinuum. From this supercontinuum a pulse is selected with a center wavelength of 1075 nm. These two pulses, at 1560 and 1075 nm, are then used for DFG in an MgO:PPLN crystal, to create an output at 3.1 micron with 7 pJ pulse energy. As the DFG input pulses originate from the same oscillator pulse, the 3 micron pulse is CEP stable.

The pump laser is a diode-pumped solid-state laser (Hyper-Rapid, Coherent Inc, Santa Clara, USA) at a center wavelength of 1064 nm at 160 kHz repetition rate and a pulse length of 9.5 ps. It has three outputs lines, designed to deliver 16, 40 and 160 W respectively. The synchronization between the pump and the oscillator is guaranteed by two feedback loops (fast and slow) acting on the oscillator cavity length.

The 3 micron pulse is stretched through propagation through a 50 mm long sapphire rod, stretching the seed from sub-100 fs to around 3.5 ps. After passing through 3 OPA stages (pumped by the first pump laser arm) the 3 micron pulse energy increases to 2.6 μJ by design, though about 1.9 μJ in practice during this thesis work. Next, the chirp of the

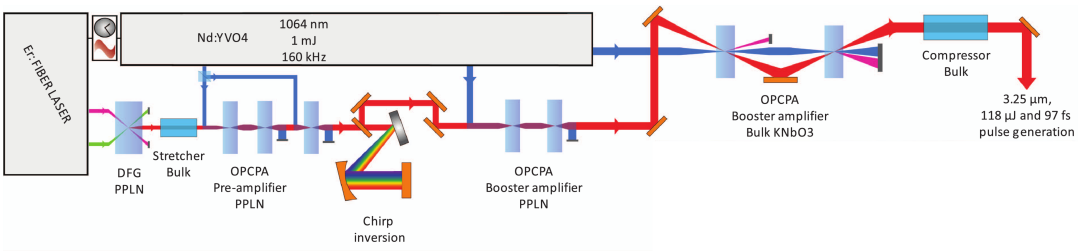

FIGURE 7.1: Schematic of the 3 micron OPCPA system, description in the main text. Figure adapted from [1].

pulse is inverted and increased through 4 bounces off a grating (Martinez configuration). This allows final compression to be obtained again with bulk sapphire, thus allowing for higher compression efficiency. The pulse duration is now 7 ps and negatively chirped. After OPA 4 and 5 the idler pulse energy is 18 µJ by design, 15 µJ in practice. For the last two OPA stages $KNbO_3$ crystals are used, and 100 W of pump power to obtain an output of 130 µJ by design. The pulses are then compressed by a double pass through a 5 cm long sapphire rod, to a pulse duration of around 97 fs. After transportation to the setup of this thesis work, the available pulse energy is about 65 µJ, corresponding to 10.5 W. For more information on the OPCPA system see [1–3].

7.3 Gas and vacuum systems

As the previous chapter has shown, gas pressures of several tens of bar are needed for soliton compression and high harmonic generation. To avoid reabsorption of the harmonics, and for much of the detection system to work, the pressure needs to drop to vacuum levels after generation. This requires a powerful vacuum pump and engineering of differential pumping apertures. For the first differential pumping step a combination of a rotary pump with a mechanical booster was used (Edwards E2M80 with an EH250 booster, see figure 7.2), with pumping speed of 274 m^3/h (between atmospheric pressure and a few 10^{-3} mbar). This value determines the design for the differential pumping apertures (for example the 10 mm pressure gradient in the integrated compression and generation design), through the vacuum conductance expressions:

$$C = 135\frac{d^4}{L}\bar{p} \qquad \bar{p} = \frac{p_h + p_l}{2} \qquad \text{(pipe)} \qquad (7.1)$$

$$C = 76.6\hat{p}^{0.712}\sqrt{1-\hat{p}^{0.288}}\frac{A}{(1-\hat{p})} \qquad \hat{p} = \frac{p_h}{p_l} \qquad \text{(orifice)} \qquad (7.2)$$

where d, L, A, p_h, p_l are the diameter, pipe length, orifice area, high pressure and low pressure respectively, and all units are in centimeters, millibars, liters and seconds (so the conductance C is in l/s). Both expressions are for the regime of viscous flow ($d\bar{p} >$ 0.6 cm·mbar for a pipe), which is appropriate for these high pressures (as opposed to molecular flow).

An important conclusion to draw is that the conductance through a pipe scales with the diameter to the fourth power, whereas the orifice scales with the square of the diameter. A small pipe is thus much more effective in reducing the gas conductance than an orifice of the same diameter. To put in some numbers, consider a waveguide (pipe) with an inner diameter of 90 µm and a length of 10 mm (as proposed at the end of the previous chapter). Setting $p_h = 100$ bar[1], p_l can be down to 40 mbar with our pumping

[1]For pumping helium an extra factor of 0.92 needs to be applied to the conductance.

FIGURE 7.2: The roughing pump is a combination of an E2M80 rotary pump with an EH250 mechanical booster (both from Edwards Vacuum Ltd), yielding a pumping speed of 274 m^3/h.

speed (giving $C = 0.04$ l/s). Reducing the waveguide diameter to 60 μm, a pressure of 12 mbar should be attainable (whereas an orifice of 60 μm would give).

7.4 The detection systems

A variety of instruments was used to detect the harmonics. As depicted in figure 7.3, the high harmonics are dispersed by a transmission grating, pass through a pair of filters (aluminium, 100 nm) and fall onto the X-ray CCD (PI-MTE 2048, Princeton Instruments). The transmission grating is a free-standing silicon-nitride grating with a 100 nm period, duty cycle of 0.5 and 160 nm bar depth [4], for which the theoretical diffraction efficiency is plotted in figure 7.4 for diffraction orders $m = 1$ and $m = 3$ following the expressions in [5] (a symmetrical grating - with duty cycle 0.5 only has odd diffraction orders).

The X-ray CCD used to detect the harmonics uses a back-illuminated 2048 × 2048 pixel array of 13.5 μm pixels, is vacuum compatible and can cool down to -40 ° C. Its quantum efficiency is shown in figure 7.5. At the beginning of the experiment a micro-channel plate (MCP) was used instead of the CCD, but the X-ray CCD was preferred to relax the vacuum requirements (10^{-6} mbar for the MCP versus 10^{-3} mbar for the CCD).

To look for lower harmonic orders (in the visible), the grating was moved out and the reflection of the first filter was collected using a spectrometer (Maya 2000, Ocean Optics), as indicated in figure 7.3a.

7.5 Free-focusing attempts: gas-jet and gas-cell based

The first attempt of this thesis project to generate high-harmonics with the 3 micron OPCPA system described above was through free-focusing in a gas jet. Figure 7.6 shows a CAD drawing and the realized chamber (machined by X. Menino and his team at the mechanical workshop of ICFO). The design is compact (the vacuum connections in the CAD drawing are KF40) and features a continuous jet with a design similar to that of [6]. The jet is mounted at the end of a gas tube which itself is mounted on an xyz-translation stage. The chamber operates with a removable differential pumping aperture (green in the CAD drawing) of a 300 μm opening. The laser beam was first aligned to be on axis with the differential pumping aperture, then the jet was moved into the laser beam. Finally the z-position (in the direction of propagation) was adjusted to look for signal on the spectrometer. As indicated by the phase-matching parameters of figure 6.5, argon was

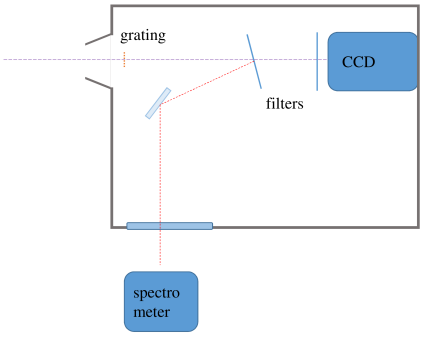

(A) Schematic representation of the detection system: the high harmonics are dispersed by a transmission grating and imaged by an X-ray CCD, after passing through a set of aluminium filters. With the grating out, the reflection of the first filter is used to measure low harmonics.

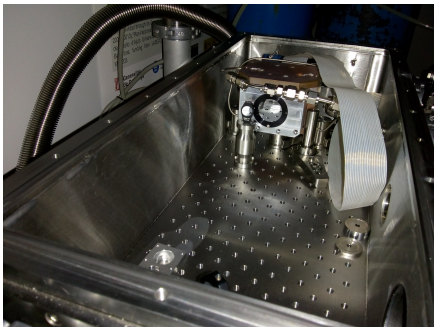

(B) A picture of the detection chamber, showing the X-ray CCD.

FIGURE 7.3: The detection setup.

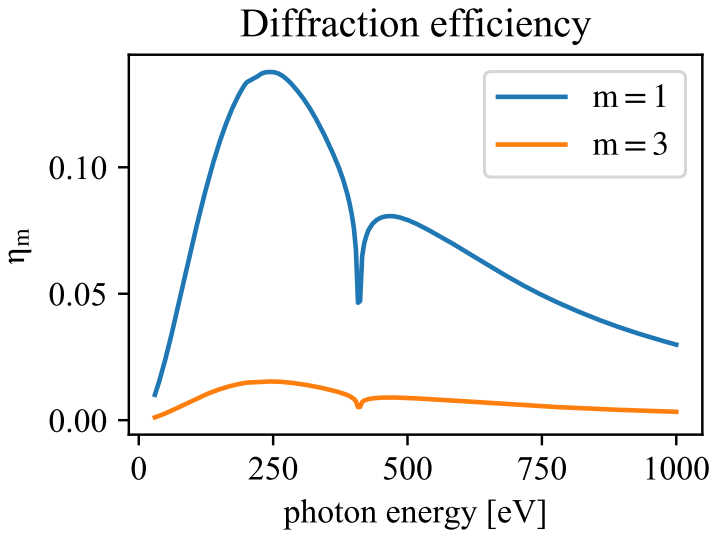

FIGURE 7.4: Theoretical diffraction efficiency η_m for orders $m = 1$ and $m = 3$, calculation based on [5].

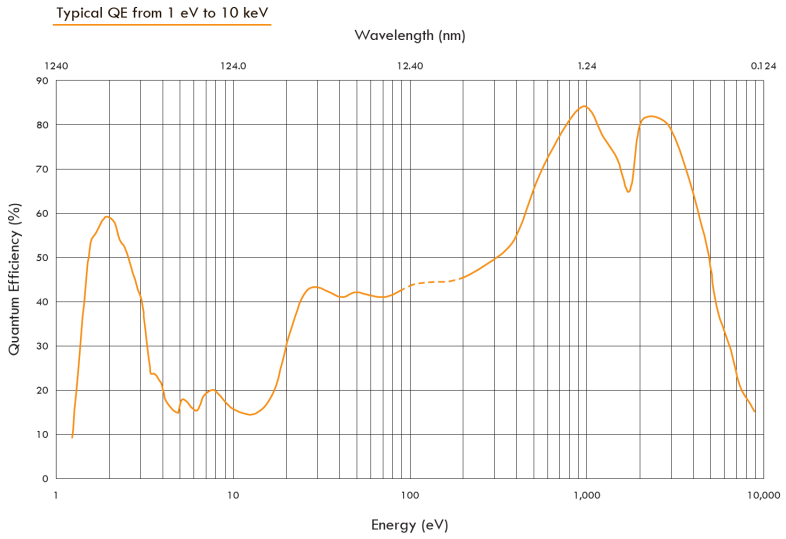

FIGURE 7.5: Quantum efficiency curve for the PI-MTE X-ray CCD.

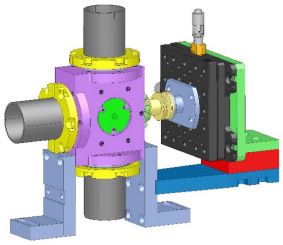

(A) CAD drawing of the generation chamber for generation in a gas-jet. Drawing by X. Menino (ICFO).

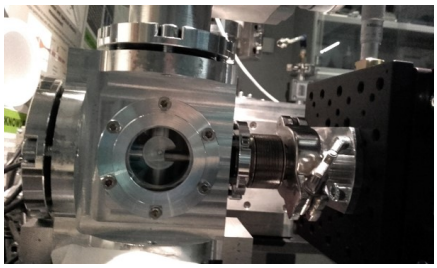

(B) Picture of the jet-based chamber.

FIGURE 7.6: First attempt: a small chamber at low vacuum with a gas jet. The pressure in the interaction region is estimated to be only about 1 bar, and the jet suffered from mechanical instabilities.

used at a pressure of several bar, and the beam was focused down to an initial waist of $w_0 \approx 22$ µm using an off-axis parabola. A faint signal at the third harmonic was observed on the spectrometer. Focusing more tightly, eventually to $w_0 \approx 15$ µm, the third and fifth harmonic appeared on the spectrometer, the fifth being just above the noise level. The fact that no higher harmonics were observed was attributed to an insufficient pressure in the interaction region of about 1 bar. The jet also suffered from mechanical instabilities.

For the second attempt, a gas cell geometry was chosen, the design of which is shown in figure 7.7. It was designed by the author and machined by R. Gall at the mechanical workshop at MPL. It features two glass capillaries for differential pumping, allowing a drop from 40 bar to 5×10^{-6} mbar over 8 cm. The laser is focused in the high-pressure compartment on the left, about 3 mm in front of the first capillary (in order not to burn the capillary), with special care taken to ensure proper alignment with the axis defined by the differential pumping capillaries. Although this setup was significantly more stable and could reach a static pressure of up to 40 bar, only a third, a fifth and very weak seventh harmonic were observed. A possible explanation could be because of reabsorption, as any generated harmonics need to travel through about a cm of argon at high pressure.

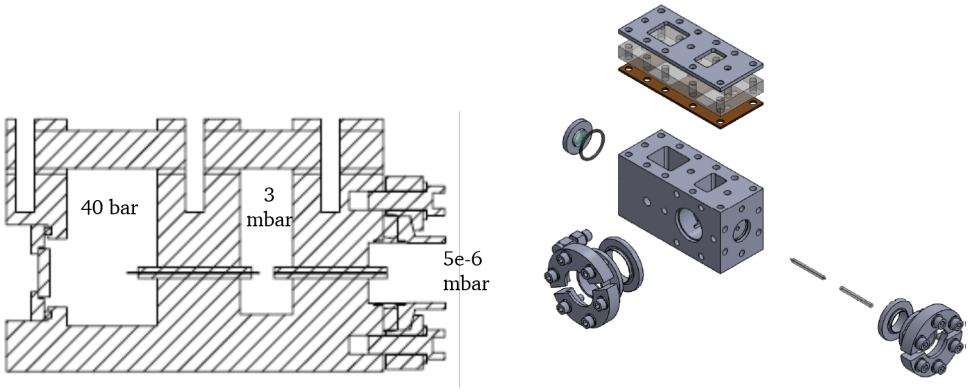

(A) Cross-sectional drawing of the chamber for the second attempt.

(B) Exploded view of the assembly of the chamber for the second attempt.

FIGURE 7.7: Second attempt: a small chamber with a first compartment designed to go up to 40 bar, a differential pumping section kept at 3 mbar and the connection to the high-vacuum environment of the spectrograph.

7.6 Integrated setup

The integrated design - soliton compression in a photonic crystal fiber followed by high harmonic generation - is a challenging design as it requires the PCF to be at a constant pressure of up to 100 bar of helium, with the pressure gradient confined to only the last centimeter of the fiber. Also, a second differential pumping aperture is needed to separate the low-vacuum from the high-vacuum part of the setup, which needs to be on axis with the (last part of the) PCF. A first design, realized in collaboration with MPL and machined at their workshop, fulfilled the requirements only partially. The above-mentioned coaxiality was met, but the separation between the high-pressure and the low vacuum part of the setup was done using an automotive gasket sealant, which 'only' held up to about 40 bar and complicated replacement of the fiber. An improved design was developed and drawn by the author, in collaboration with M. Bougeard (CEA) and machined by S. Foucquart and A. Fillon (mechanical workshop CEA). The result is shown in figure 7.8. The laser is focused into the entry chamber, where it is coupled into the PCF. This PCF is inside a glass capillary which in turn is lying inside a precisely machined V-groove, to insure coaxiality with the differential pumping aperture downstream. If a single, long piece of PCF is used, the entry is at high pressure, where the fiber exit is at low vacuum. There is thus a pressure gradient along the entire length of the PCF, which means that the amount of SPM reduces along the fiber length. In order to have a constant pressure along the first 18 cm of PCF, and the gradient only over the last 10 mm as described in the previous chapter, the PCF was split in a long (18 cm) and short (10 mm) part and the glass capillary holding the PCF was prepared as shown in figure 7.9. In the region where the two PCFs meet, the capillary is tapered to the outside diameter of the PCF (0.3 mm) such that the PCFs are forced exactly on axis and a good coupling efficiency (> 95 %) is obtained. A slot is machined in the glass capillary so gas can enter, thus maintaining a constant pressure over the long PCF, and a gradient over the short PCF. It must be noted that the technical implementation is rather challenging, as machining the gas slot makes the capillary fragile, then the capillary needs to be cleaned of glass debris, after which the two pieces of PCF need to be inserted (taking care not to damage or pollute the cleaved fiber end-facets).

With this setup, and a PCF with an inner diameter of 60 micron, a constant pressure profile for soliton compression of up to 110 bar can be reached, with the low-vacuum

chamber maintained at around 10-50 mbar and the detection chamber at around $10^{-4}-10^{-5}$ mbar. To verify the laser beam at the output of the PCF, as well as to measure lower harmonics, a pick-off mirror is installed on a small transfer rod. This mirror (consisting of a gold-covered silicon chip) sends the beam out through the window shown in figure 7.8d. It can be moved out to let the high harmonics pass to the detection chamber, through the differential pumping aperture. Part of the driver laser power is also transmitted, and blocked by the filters in front of the CCD.

7.6.1 Results from the integrated setup

Using this integrated setup, soliton compression was verified. The setup is shown in figure 7.10. A wire grid polarizer is used to ramp up the input power in a controlled way, while compensating any changes in beam pointing with the coupling lens (CaF_{22}, f=50 mm). The beam then enters the chamber through a 3 mm sapphire window and couples into the PCF. The input pulse is chirped (using the Martinez grating compressor mentioned in section 7.2) to compensate for the dispersion introduced by the polarizer, lens and entrance window (to about 116 fs at input, 105 fs after the polarizer and 97 fs after the entrance window). At the output of the PCF, the beam is sent out of the setup by the pick-off mirror, and its pulse length is measured through Frequency Resolved Optical Gating (FROG) [7], using FROG3 (Femtosoft Technologies). The input pulse energy arriving at the setup is about 65 μJ. After the losses on the mirrors, polarizer, lens and entrance window the pulse energy is about 47 μJ. With a coupling efficiency of about 85 % the energy of the pulse in the PCF is thus 42 μJ. At this rather low pulse energy, the optimum compression is expected to be at a later stage than with the original PCF length of 18 cm. Its length was thus increased to 26 cm. Figure 7.11 shows the FROG trace and retrieval for compression in helium at 110 bar. Although some compression is observed (down to 79 fs), it is far from sufficient and the spectrum does not show significant spectral broadening. This is attributed to the low pulse intensities. The polarizer could be removed to gain 17 % of energy, but at the expense of control. To see a stronger SPM, the experiment was repeated with up to 75 bar of neon (which has a higher n_2, see Appendix E). Now significant spectral broadening was observed, and a pulse of 61 fs was retrieved, as shown in figure 7.12. In these measurements the dispersion of the CaF_2 exit window was not compensated for, as it is not significant at these pulse lengths. Although this is a step in the right direction, it also shows that we are far from the parameters needed for efficient soliton compression in helium. Gaining 17 % by removing the polarizer will not be sufficient, the intensity needs to be increased significantly. As explained in the previous chapter, using argon is not an option as any generated harmonics are reabsorbed. So ideally one would use argon in the soliton compression stage, and helium in the HHG stage. As this is extremely challenging to achieve in this integrated setup, it was decided to decouple the compression and HHG stages, as described in the next section.

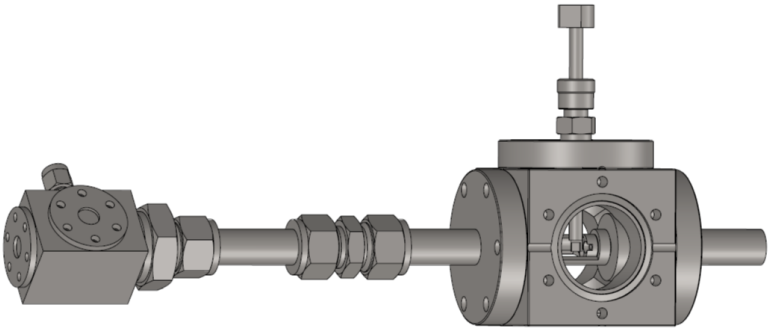

(A) CAD of the integrated compression and generation chamber.

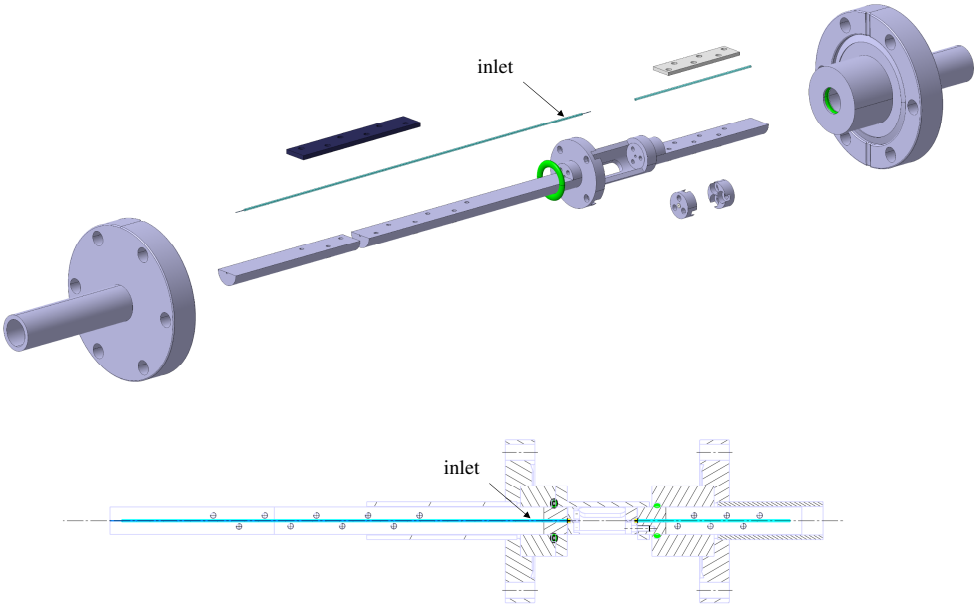

(B) Inner configuration of the compression and generation chamber, with the long glass capillary holding the two pieces of PCF, with the position of the gas inlet in the glass capillary as detailed in figure 7.9. Also shown is the second glass capillary that acts as differential pumping aperture between the low and high-vacuum sections.

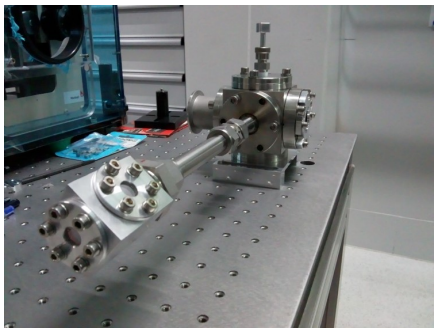

(C) Picture of the integrated compression and generation chamber.

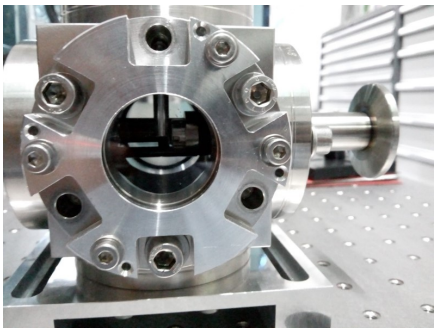

(D) With the pick-off mirror in place, the beam is sent out of this window to measure verify coupling, measure compression and look for low order harmonics.

FIGURE 7.8: Chamber of the integrated compression and generation design.

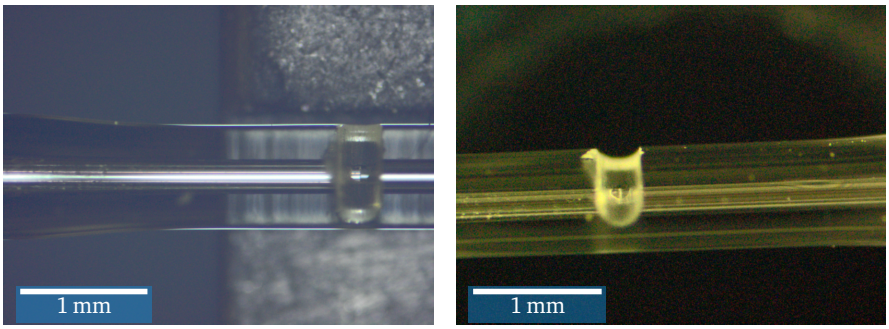

FIGURE 7.9: Using two pieces of PCF allows for a constant pressure along the first PCF, and thus better soliton compression. A slot is machined in the capillary to allow gas to flow in.Tapering of the capillary that holds the two PCFs ensures 95 % coupling efficiency.

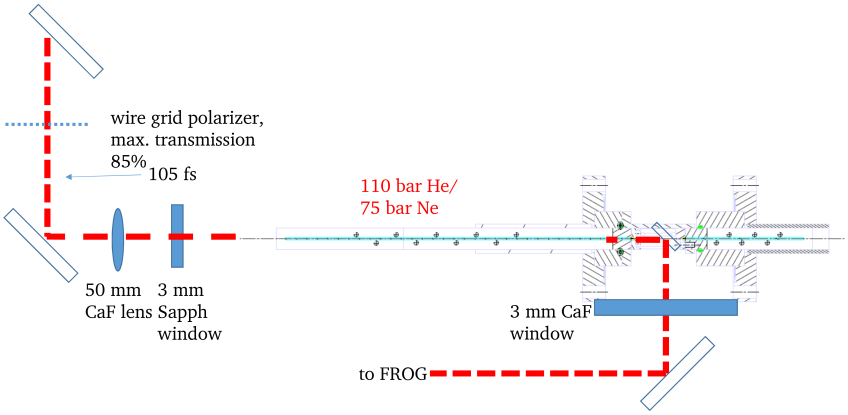

FIGURE 7.10: Schematic of the setup used to measure the pulse duration after soliton self-compression in the integrated compression and generation setup.

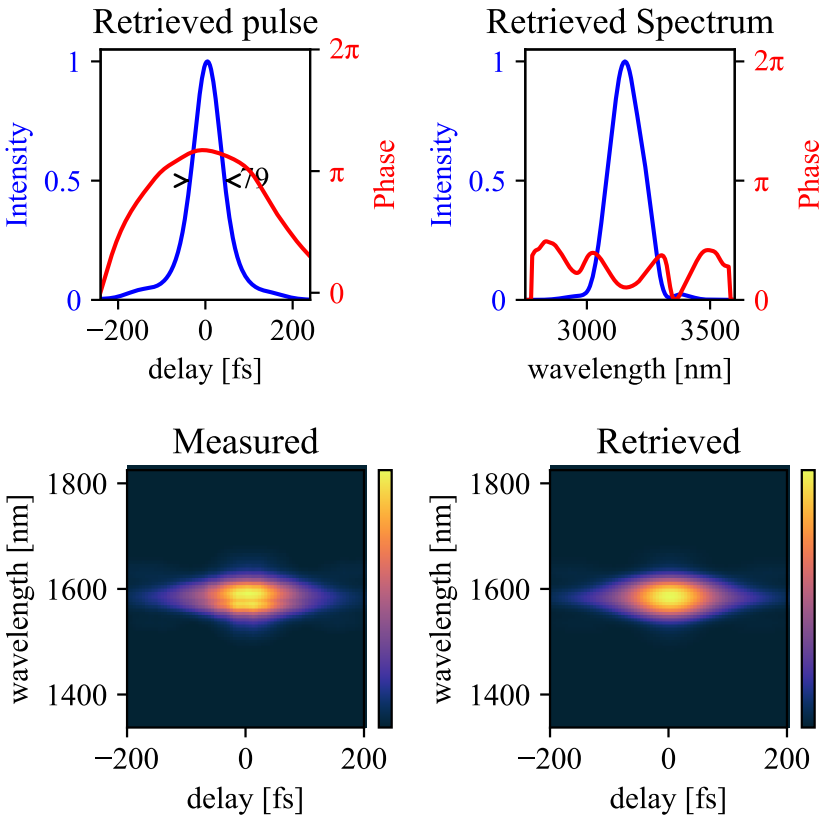

FIGURE 7.11: Soliton compression in helium at 110 bar gives a retrieved pulse length of 79 fs. The spectral phase shows some chirp (up to 4×10^3 fs^2).

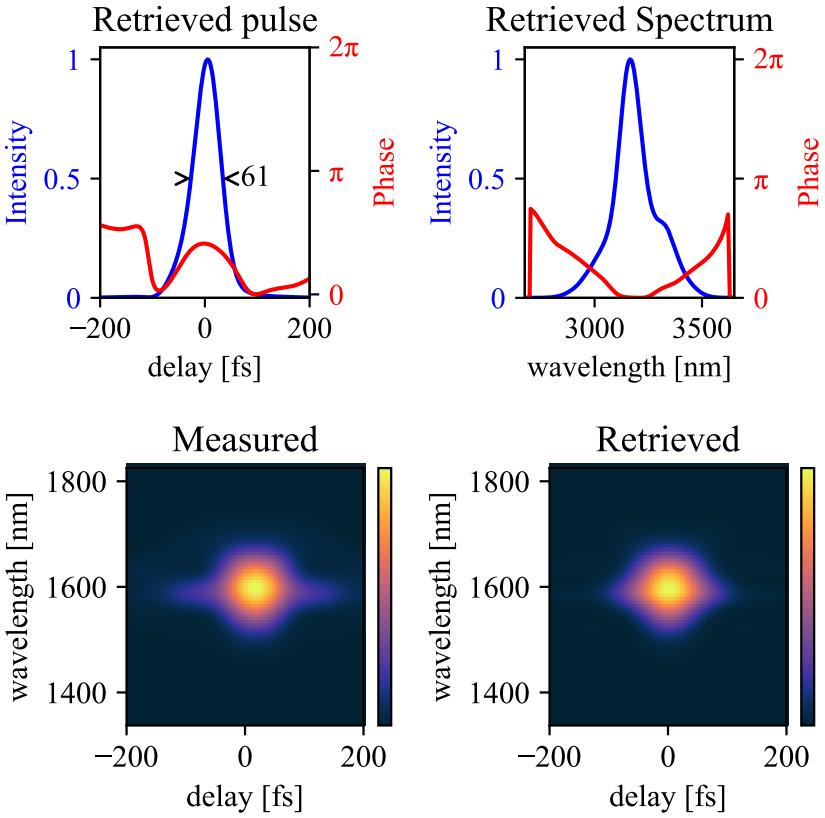

FIGURE 7.12: Soliton compression in neon at 75 bar gives gives a retrieved pulse length of 61 fs (also with some residual chirp, about 10^3 fs^2).

7.7 Decoupled setup

To decouple the parameters for soliton compression and high harmonic generation, the setup was modified to the one shown in figure 7.13.

7.7.1 Soliton self-compression results from the decoupled setup

The compression part could be based on earlier work [1], for the generation part the gas cell of section 7.5 was modified to handle up to 100 bar. Based on the results of [1], argon was used for the soliton compression part, and an optimum pressure of 10.5 bar was found for a PCF of 90 μm inner diameter and 22 cm length. This allowed compression down to 26 fs, as shown in figure 7.14, where the dispersion by the exit window is compensated for by a 1 mm thick silicon plate. The input pulse energy was 65 μJ, the output energy 40 μJ. The compression stage increased the peak power by a factor 1.5 to 0.96 GW, as can be seen in figure 7.15.

7.7.2 Harmonics generated from the decoupled setup

In the soliton compression stage harmonics up to the fifth order are generated. Figure 7.16a shows the spectrum of the fifth harmonic (the third harmonic being filtered out). The compressed beam is collimated using an off-axis parabola (f=150 mm), and focused into the generation chamber with another off-axis parabola (f=50 mm), to a focal spot with a waist of around $w_0 \approx 20$ μm. Taking the actual pulse shape as retrieved in figure 7.14, the peak intensity is expected to be 1.4×10^{14} W/cm^2. Following the analysis of the previous chapter, the cut-off energy would be at 430 eV, ADK theory predicts an ionization fraction of 5×10^{-9}, and the phase-matching pressure would be 35 bar of helium. In the experiment, the pressure was scanned from 20 to 100 bar, but no high harmonics were observed. Figure 7.16b shows harmonics 3 to 7, generated in the generation chamber. A possible explanation for not seeing higher harmonics could be that the alignment of the beam with the two glass capillaries (the differential pumping apertures) is not perfect, and that the high harmonics are absorbed whereas the low harmonics are partially transmitted through internal reflection. A repetition of the experiment after careful realignment however did not yield better results.

This chapter is concluded with two additional pictures of the experiment, shown in figure 7.17. The picture on the left shows the compression chamber with the PCF lighting up as a result of parasitic processes. The beam enters from the bottom of the picture. The intensity oscillations visible at the first few cm of the PCF are caused by poor mode matching (the picture should thus not be taken as an example). The focus of the incoming beam is too tight, exciting multiple modes which interfere as they propagate, until they extinct and only the fundamental mode is left. Going to high power with this poor mode matching would cause the fiber entry to burn, but it does make for an interesting and aesthetically pleasing image. The picture on the right shows the generation chamber of the decoupled setup, with the focus lit up as a result of ionization and/or fluorescence.

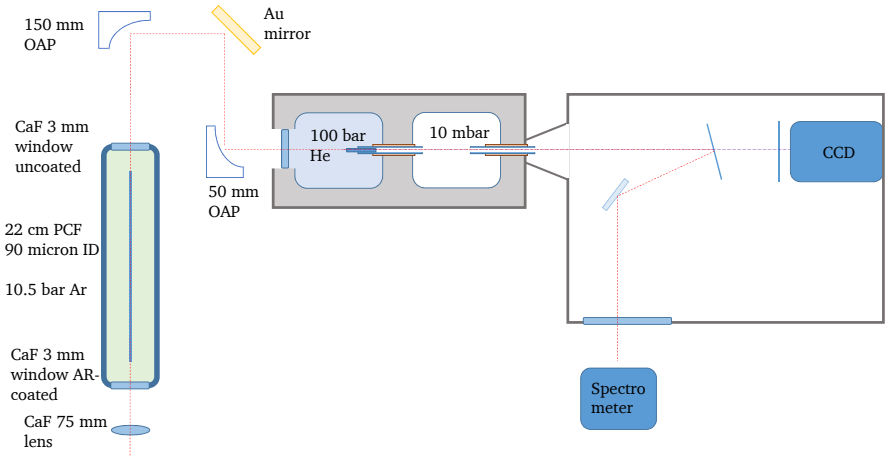

(A) Schematic of the decoupled setup.

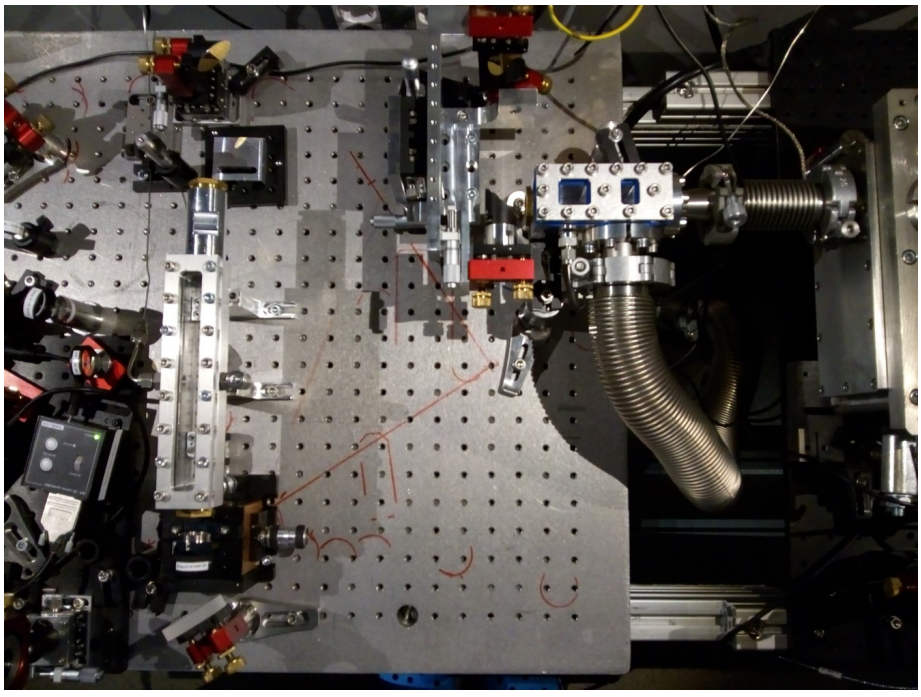

(B) Picture of the decoupled setup.

FIGURE 7.13: Decoupling the soliton compression and high harmonic generation finally gives more control over the experiment.

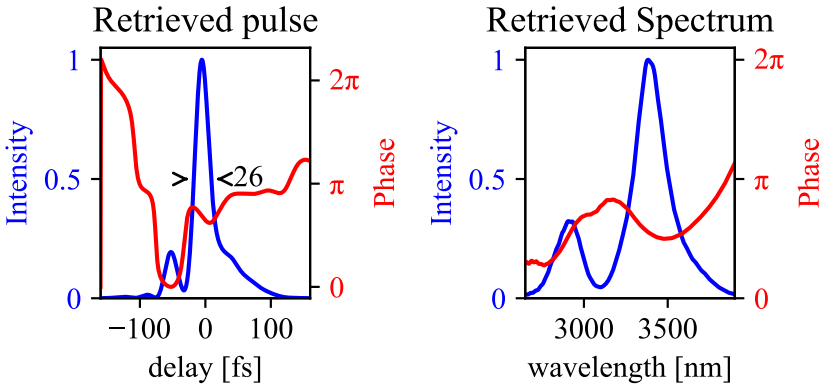

(A) Temporal and spectral envelope and phase of the retrieved pulse.

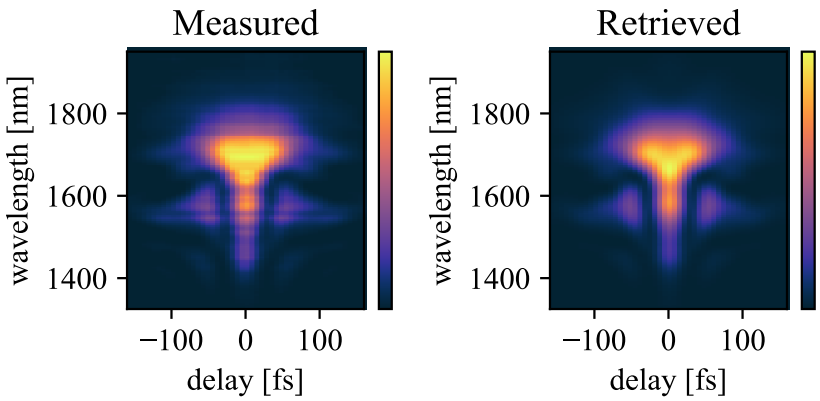

(B) Measured and retrieved FROG trace.

FIGURE 7.14: FROG measurement of the pulse after soliton self-compression in Argon, showing a pulse length of 26 fs FWHM at an optimum pressure of 10.5 bar. Input energy was 65 µJ, output energy 40 µJ. Measured with 1 mm of Si to compensate for the CaF_2 exit window of the soliton compression chamber.

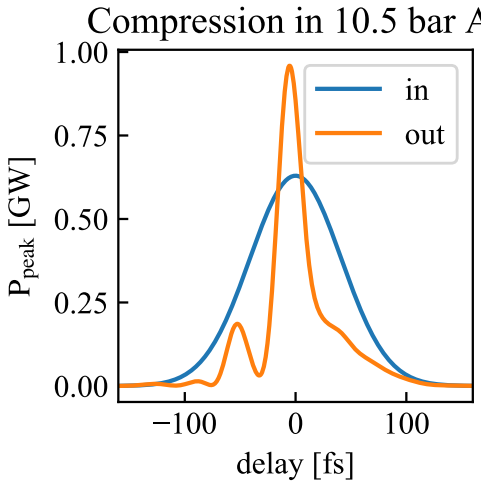

FIGURE 7.15: Peak power of the input and output pulse of the soliton compression stage, showing a gain of a factor 1.5.

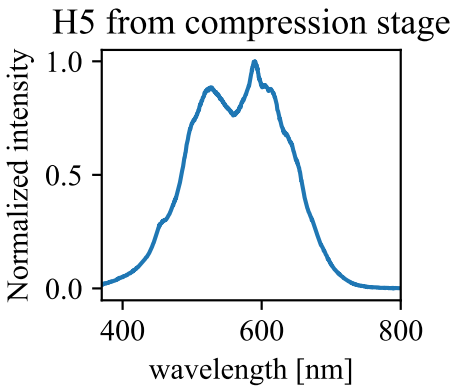

(A) Harmonic 5 generated during soliton compression in argon (harmonic 3 filtered out).

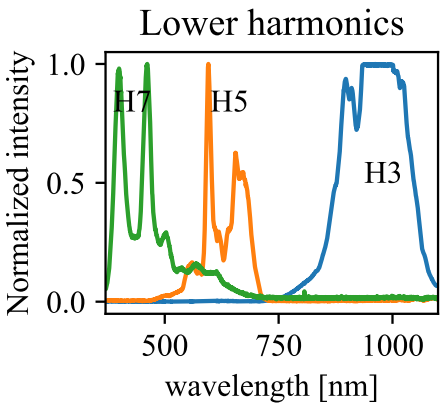

(B) Harmonic 3 to 7 generated in helium.

FIGURE 7.16: Lower harmonics generated in the self-compression stage (left) and in the HHG stage (right).

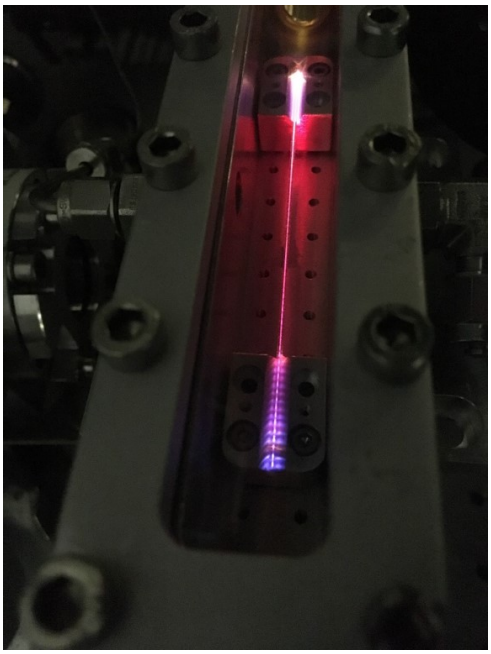

(A) Picture of the soliton compression stage. The intensity oscillations near the fiber entry are caused by poor mode matching.

(B) Picture of ionization (or fluorescence?) at focus in the HHG stage.

FIGURE 7.17

7.8 Conclusions

Through several design iterations, high harmonic generation was attempted using a 160 kHz 3-micron OPCPA laser system. Different schemes were tried: free-focusing in a gas jet; free-focusing in a gas cell; soliton compression and HHG in a PCF; and separated soliton compression and HHG.

The gas jet experiment did not yield results mainly because of the technical implementation: it was unstable and did not sustain high enough pressures. This could be improved upon, but priority was given to trying the next scheme. Free-focusing in the gas cell was stable, but the scheme inherently suffers from high reabsorption. It can thus only work with helium as the generation medium, but for this the peak intensity was insufficient. The scheme that integrates soliton compression and HHG in a PCF tested here could be an elegant solution, as it is compact, stable, and minimizes the losses between the compression and HHG stages. But the downside is that the parameters determining the HHG process and those determining the compression process are coupled (gas type, pressure, mode field diameter). For the parameters of this setup, it proved not feasible, notably due to a too low pulse energy. The decoupled setup came closest to generating high harmonics - it is even possible they were generated, but could not be observed.

All schemes could in principle lead to a high repetition rate, keV high harmonic source, using a significantly higher pulse energy.

Bibliography

[1] Ugaitz Elu, Matthias Baudisch, Hugo Pires, Francesco Tani, Michael H. Frosz, Felix Köttig, Alexey Ermolov, Philip St.J. Russell, and Jens Biegert. High average power and single-cycle pulses from a mid-IR optical parametric chirped pulse amplifier. *Optica*, 4(9):1024, September 2017. ISSN 2334-2536. doi: 10.1364/OPTICA.4.001024.

[2] M. Baudisch, B. Wolter, M. Pullen, M. Hemmer, and J. Biegert. High power multi-color OPCPA source with simultaneous femtosecond deep-UV to mid-IR outputs. *Optics Letters*, 41(15):3583, August 2016. ISSN 0146-9592, 1539-4794. doi: 10.1364/OL.41.003583.

[3] Matthias Baudisch. *High Power, High Intensity Few-Cycle Pulses in the Mid-IR for Strong-Field Experiments*. Ph.D. Thesis, Universitat Politècnica de Catalunya, July 2017.

[4] Glen Gronniger, Brett Barwick, Herman Batelaan, Tim Savas, Dave Pritchard, and Alex Cronin. Electron diffraction from free-standing, metal-coated transmission gratings. *Applied Physics Letters*, 87(12):124104, September 2005. ISSN 0003-6951. doi: 10.1063/1.2053347.

[5] G. Hurvitz, Y. Ehrlich, G. Strum, Z. Shpilman, I. Levy, and M. Fraenkel. Advanced experimental applications for x-ray transmission gratings spectroscopy using a novel grating fabrication method. *Review of Scientific Instruments*, 83(8):083109, August 2012. ISSN 0034-6748. doi: 10.1063/1.4746771.

[6] Seth Lucien Cousin. *Towards the Generation of Isolated Attosecond Pulses in the Water Window*. Ph.D. Thesis, Universitat Politècnica de Catalunya, September 2016.

[7] Rick Trebino and Daniel J. Kane. Using phase retrieval to measure the intensity and phase of ultrashort pulses: Frequency-resolved optical gating. *JOSA A*, 10(5):1101–1111, May 1993. ISSN 1520-8532. doi: 10.1364/JOSAA.10.001101.

Chapter 8

Conclusions

8.1 Conclusions on Broadband Coherent Diffractive Imaging

Coherent diffractive imaging through phase retrieval is an important imaging technique that is gaining momentum on several sources thanks to its ease of implementation. It traditionally assumes a perfectly coherent, monochromatic incident wave, and reconstructs an amplitude and phase representation of the sample from its diffraction pattern through an iterative phase retrieval process. In order to make full use of the developed attosecond sources, and other sources that feature a broad spectrum, it is necessary to extend CDI methods to cope with broadband diffraction patterns. Some work has been performed in this direction, particularly by extending the iterative phase retrieval algorithm. In this thesis work, a method has been developed to perform a numerical monochromatization.

The method

The monochromatization works directly on the broadband diffraction pattern, using only the spectrum of the diffracted radiation. It makes use of a regularized matrix inversion which controls the inverted noise and allows to optimize the degree of monochromatization, depending on the signal-to-noise ratio of the acquired diffraction patterns. An important limiting assumption is that the sample be non-dispersive over the source bandwidth, as only then can the broadband pattern be considered a sum of monochromatic patterns which are identical except for a geometrical scaling and a spectral weight.

Experimental validation in the visible

A CDI experiment was performed on a supercontinuum source in the visible, such as to have spatially coherent, broadband radiation. The sample - an aperture etched out of a membrane - was readily reconstructed even at 11 % bandwidth. A noise analysis shows that the broadband case performs comparably to the narrowband case for the same number of photons in the diffraction pattern. At low signal levels, the broadband case even performs slightly better thanks to the noise-suppressing behavior of the monochromatization method.

X-ray simulations

A possible application for hard X-ray broadband CDI is explored through simulation: the verification of lithography masks for the semiconductor industry. A possible source is also explored: inverse Compton scattering source ThomX. The monochromatization method is well suited to the source bandwidth of 5 %, but the brightness of the source lacks orders of magnitude for a realistic CDI experiment. Simulations with a sufficient number of photons yield good CDI reconstructions for 5 and 10 % bandwidth at 8 keV, whereas at 15 % bandwidth the reconstruction degrades significantly. Finally, combination of the monochromatization method with an external ptychography code yielded good results, showing the versatility of the

methods implementation. Ptychography can image extended samples and is more robust to noise than CDI.

X-ray experiments on synchrotron sources
Two experiments were performed at synchrotron sources to collect monochromatic diffraction patterns over a closely sampled energy range, to then constitute a broadband diffraction pattern at hard X-ray energies between 7 and 8 keV. The first experiment, at a bending magnet beamline at Diamond, did not yield usable results due to a too low spatial coherence of the source (in combination with limited beamtime). In the second experiment, at a highly spatially coherent undulator beamline at Soleil, several energy scans on different samples were obtained. The patterns are highly coherent, and a monochromatic ptychography scan was reconstructed successfully. In CDI only mediocre reconstructions were obtained, which could be linked to a stability problem. As this beamtime took place near the end of thesis project and was rather short, further analysis and follow-up experiments can yield improved results.

Overall the proposed monochromatization method was explored both through simulations and experiments, and yielded encouraging results. It may have brought attosecond CDI and efficient use of broadband sources of radiation one step closer, although the assumption on the sample limits its scope of application.

8.2 Conclusions on the development of a high repetition rate, mid-IR driven keV harmonic source

Generating high harmonic radiation with a high repetition rate means one has to deal with a low pulse energy. By focusing tightly, and/or compressing temporally, the peak intensity can be made sufficiently high to generate high harmonic radiation. Additionally, the cut-off energy can be pushed by using a long wavelength driver laser (mid-IR). However, as shown in Chapter 6, high phase matching pressures ranging from several bar to hundreds of bars are needed, posing a technical challenge. At these high pressures strong reabsorption of the harmonic radiation by the generation medium often leaves helium as the only option. Different schemes were explored theoretically and experimentally:

Free-focusing in a gas-jet
This scheme is probably easiest to implement, and if more time is spent designing (or buying) a stable gas-jet that can sustain high pressures, it could yield good results. Also, if the gas jet can be made such that the pressure down-ramp is steep, reabsorption is limited and other gases besides helium could be used. In this project, no results beyond a weak third and fifth harmonic were obtained, as preference was given to exploring the other schemes

Free-focusing in a gas-cell
Compared to a gas-jet, high pressures are much easier to reach in a gas-cell. In this project, a system of glass capillaries was used as differential pumping apertures to separate high pressure, low vacuum and high vacuum regions of the setup. These apertures keep the setup compact, but complicate alignment. Low harmonics were observed up to the seventh order. Reabsorption is significant in this scheme, so one is limited to generation in helium.

Integrated soliton compression and HHG in a photonic crystal fiber
PCFs are a great means of confining high power laser pulses and have it interact

over extended distances. They are thus ideal for soliton compression, and in principle also for phase-matched harmonic generation. Additionally, they can serve as a differential pumping aperture. To maintain a constant pressure for good soliton compression, a long PCF is coupled to a short PCF, with a gas slot in the capillary holding the two PCFs, at the point where they meet. The capillary is tapered to the outside diameter of the PCF, such that good ($>$ 95 %) coupling is reached. Compression from 97 to 79 fs was obtained in helium, and to 61 fs in neon. The downside of this integrated setup is that the parameters for compression and those for HHG are coupled. For example, depending on the laser parameters one would ideally generate in helium because of low reabsorption, but compress using e.g. argon because of the high n_2. The technical implementation is also challenging. For the correct parameters however, this could be a very compact and efficient solution.

Decoupled soliton compression and HHG in a gas-cell

Decoupling the compression stage and generation stage allows compression using argon, and a compressed pulse duration of 26 fs was obtained, with a gain in peak power of a factor 1.5. Focusing this pulse into a gas cell filled with helium, harmonics up to the seventh order were observed. The fact that no higher orders were observed could be a question of alignment through the differential pumping apertures. This scheme allows the highest degree of freedom for the experiment.

Each of the schemes could work to generate up to keV-scale, phase-matched harmonic radiation, but in this work all tried schemes lacked pulse energy to be feasible.

A 'recipe' was used to determine the experimental parameters: based on the available pulse energy and maximum gas pressure, how strongly should one focus and/or compress temporally to obtain phase-matched radiation at the highest cut-off? As more research groups move towards higher repetition rates and longer driver wavelengths, this recipe can be applied to similar cases.

Chapter 9

Outlook

9.1 Outlook on Broadband Coherent Diffractive Imaging

In the near future it would be interesting to go back to the Nanoscopium beamline at Soleil and try a broadband ptychography scan. As shown, it is more robust and would thus be a way to experimentally validate the monochromatization method with hard X-rays, unhindered by sources of noise that proved detrimental for the CDI experiment.

On the side of algorithm development, a good next step would be to couple the monochromatization method to the PolyCDI algorithm of the former group at the Centre for Coherent X-ray Science of the University of Melbourne [1–5], as mentioned in Chapter 2. As described in [1], step 3-6 of their modified iterative phase retrieval algorithm is to scale the updated guess of the farfield pattern to all wavelengths in the sample - exactly what matrix C does. The resulting method should be able to handle larger bandwidths than PolyCDI alone, and yield more reliable reconstructions than the numerical monochromatization method alone. The relevant authors have been contacted to initiate a merging of the two codes, but the group has been dissolved and their developments on PolyCDI are discontinued.

Another exciting development would be to loosen the constraint on the sample. As a first step, a sample consisting of two different, known indices of refraction could be considered. One of them could even have an absorption edge. These indices could then be used as additional constraint in the sample space. For this to work the dispersion function of the sample will need to be guessed iteratively, so it is probably best to implement this as an extension to the above-mentioned combination with PolyCDI.

In a more distant future, with robust, mature algorithms and with bright high harmonic sources delivering intense pulses on an attosecond timescale, it would be exciting to perform attosecond CDI on the type of samples mentioned in the Introduction: all-optical switching of magnetic domains [6, 7] and electron dynamics in candidate devices for petahertz electronics [8–12].

9.2 Outlook on high repetition rate, mid-IR driven keV harmonic source development

First, an outlook regarding experimental aspects and the immediate future. The decoupled setup gave the most promising results. It is advisable to work on a way to make the alignment less critical. One way this could be done is by adding the possibility to adjust the angle of the generation chamber up to a few millirad, so it can compensate for misalignment. In parallel, the pump laser should be upgraded so that the pulse energy can be increased.

If one is just starting to attempt HHG on a similar source and wants to start with the gas-jet design, some time should be spent optimizing the gas jet to obtain a high pressure

jet that is sharply localized to limit reabsorption. Suitable jets sustaining well over 10 bars of pressure have been developed in the context of near-critical density laser-plasma experiments [13, 14], and are even commercially available (e.g. Sourcelab, Palaiseau, France). Such jets are pulsed at Hz-scale repetition rates, and thus harmonics will be generated only when the jet valve is open (a few % of the time) but it serves to demonstrate the principle. Also Even-Lavie valves [15, 16] could be used for this purpose. If the pulse energy of the idler is low, as a first step HHG could be attempted using the signal [17], which has double the energy and with which it should be easier to generate because of the higher dipole emission. Once this works, and the detection system is proven, generation with the idler can be attempted.

For the mid-term future, it would be interesting to develop a way to implement a barrier in the PCFs that can withstand large pressure differences but is transparent to the driver laser, in order to separate the soliton compression section from the HHG section. One could imagine a transmission window at Brewster angle (on a tens-of-micron scale), or perhaps a layer of graphene [18].

Exciting long-term developments are to investigate the relativistic effects and decoherence induced by neighboring wavepackets as driver wavelengths become longer. Intense, ultrashort pulses at longer wavelengths are thus needed. More than 30 years ago, CO_2 laser pulses (at 10 μm) were compressed to 600 fs [19] and work is currently underway to go further in this direction [20].

Bibliography

[1] Brian Abbey, Lachlan W. Whitehead, Harry M. Quiney, David J. Vine, Guido A. Cadenazzi, Clare A. Henderson, Keith A. Nugent, Eugeniu Balaur, Corey T. Putkunz, Andrew G. Peele, G. J. Williams, and I. McNulty. Lensless imaging using broadband X-ray sources. *Nature Photonics*, 5(7):420–424, July 2011. ISSN 1749-4885, 1749-4893. doi: 10.1038/nphoton.2011.125.

[2] Ruben A. Dilanian, Bo Chen, Garth J. Williams, Harry M. Quiney, Keith A. Nugent, Sven Teichmann, Peter Hannaford, Lap V. Dao, and Andrew G. Peele. Diffractive imaging using a polychromatic high-harmonic generation soft-x-ray source. *Journal of Applied Physics*, 106(2):023110, July 2009. ISSN 0021-8979, 1089-7550. doi: 10.1063/1.3176976.

[3] Bo Chen, Ruben A. Dilanian, Sven Teichmann, Brian Abbey, Andrew G. Peele, Garth J. Williams, Peter Hannaford, Lap Van Dao, Harry M. Quiney, and Keith A. Nugent. Multiple wavelength diffractive imaging. *Physical Review A*, 79(2), February 2009. ISSN 1050-2947, 1094-1622. doi: 10.1103/PhysRevA.79.023809.

[4] Sven Teichmann, Bo Chen, Ruben A. Dilanian, Peter Hannaford, and Lap Van Dao. Experimental aspects of multiharmonic-order coherent diffractive imaging. *Journal of Applied Physics*, 108(2):023106, July 2010. ISSN 0021-8979, 1089-7550. doi: 10.1063/1.3462438.

[5] Bo Chen, Brian Abbey, Ruben Dilanian, Eugeniu Balaur, Grant van Riessen, Mark Junker, Chanh Q. Tran, Michael W. M. Jones, Andrew G. Peele, Ian McNulty, David J. Vine, Corey T. Putkunz, Harry M. Quiney, and Keith A. Nugent. Diffraction imaging: The limits of partial coherence. *Physical Review B*, 86(23), December 2012. ISSN 1098-0121, 1550-235X. doi: 10.1103/PhysRevB.86.235401.

[6] Jean-Yves Bigot and Mircea Vomir. Ultrafast magnetization dynamics of nanostructures. *Annalen der Physik*, 525(1-2):2–30, 2013. ISSN 1521-3889. doi: 10.1002/andp.201200199.

[7] Alexey V. Kimel and Mo Li. Writing magnetic memory with ultrashort light pulses. *Nature Reviews Materials*, 4(3):189, March 2019. ISSN 2058-8437. doi: 10.1038/s41578-019-0086-3.

[8] Ferenc Krausz and Mark I. Stockman. Attosecond metrology: From electron capture to future signal processing. *Nature Photonics*, 8(3):205–213, March 2014. ISSN 1749-4893. doi: 10.1038/nphoton.2014.28.

[9] Takuya Higuchi, Christian Heide, Konrad Ullmann, Heiko B. Weber, and Peter Hommelhoff. Light-field-driven currents in graphene. *Nature*, 550(7675):224–228, October 2017. ISSN 1476-4687. doi: 10.1038/nature23900.

[10] Hiroki Mashiko, Yuta Chisuga, Ikufumi Katayama, Katsuya Oguri, Hiroyuki Masuda, Jun Takeda, and Hideki Gotoh. Multi-petahertz electron interference in Cr:Al 2 O 3 solid-state material. *Nature Communications*, 9(1):1468, April 2018. ISSN 2041-1723. doi: 10.1038/s41467-018-03885-7.

[11] F. Langer, C. P. Schmid, S. Schlauderer, M. Gmitra, J. Fabian, P. Nagler, C. Schüller, T. Korn, P. G. Hawkins, J. T. Steiner, U. Huttner, S. W. Koch, M. Kira, and R. Huber. Lightwave valleytronics in a monolayer of tungsten diselenide. *Nature*, 557(7703):76, May 2018. ISSN 1476-4687. doi: 10.1038/s41586-018-0013-6.

[12] F. Schlaepfer, M. Lucchini, S. A. Sato, M. Volkov, L. Kasmi, N. Hartmann, A. Rubio, L. Gallmann, and U. Keller. Attosecond optical-field-enhanced carrier injection into the GaAs conduction band. *Nature Physics*, 14:560–564, March 2018. ISSN 1745-2473. doi: 10.1038/s41567-018-0069-0.

[13] F. Sylla, M. Veltcheva, S. Kahaly, A. Flacco, and V. Malka. Development and characterization of very dense submillimetric gas jets for laser-plasma interaction. *Review of Scientific Instruments*, 83(3):033507, March 2012. ISSN 0034-6748. doi: 10.1063/1.3697859.

[14] I. Prencipe, J. Fuchs, S. Pascarelli, D. W. Schumacher, R. B. Stephens, N. B. Alexander, R. Briggs, M. Büscher, M. O. Cernaianu, A. Choukourov, M. De Marco, A. Erbe, J. Fassbender, G. Fiquet, P. Fitzsimmons, C. Gheorghiu, J. Hund, L. G. Huang, M. Harmand, N. J. Hartley, A. Irman, T. Kluge, Z. Konopkova, S. Kraft, D. Kraus, V. Leca, D. Margarone, J. Metzkes, K. Nagai, W. Nazarov, P. Lutoslawski, D. Papp, M. Passoni, A. Pelka, J. P. Perin, J. Schulz, M. Smid, C. Spindloe, S. Steinke, R. Torchio, C. Vass, T. Wiste, R. Zaffino, K. Zeil, T. Tschentscher, U. Schramm, and T. E. Cowan. Targets for high repetition rate laser facilities: Needs, challenges and perspectives. *High Power Laser Science and Engineering*, 5, 2017/ed. ISSN 2095-4719, 2052-3289. doi: 10.1017/hpl.2017.18.

[15] U. Even. Pulsed Supersonic Beams from High Pressure Source: Simulation Results and Experimental Measurements. https://www.hindawi.com/journals/ac/2014/636042/abs/, 2014.

[16] U. Even. "The Even-Lavie valve as a source for high intensity supersonic beam". *EPJ Techniques and Instrumentation*, 2(1):17, December 2015. ISSN 2195-7045. doi: 10.1140/epjti/s40485-015-0027-5.

[17] Aura Inés Gonzalez, Gaëtan Jargot, Philippe Rigaud, Loïc Lavenu, Florent Guichard, Antoine Comby, Thierry Auguste, Olivier Sublemontier, Michel Bougeard, Yoann Zaouter, Patrick Georges, Marc Hanna, and Thierry Ruchon. Spatio-spectral structures in high harmonic generation driven by tightly focused high repetition rate lasers. *JOSA B*, 35(4):A6–A14, April 2018. ISSN 1520-8540. doi: 10.1364/JOSAB.35.0000A6.

[18] Shou-En Zhu, Shengjun Yuan, and G. C. A. M. Janssen. Optical transmittance of multilayer graphene. *EPL (Europhysics Letters)*, 108(1):17007, September 2014. ISSN 0295-5075. doi: 10.1209/0295-5075/108/17007.

[19] P. Corkum. Amplification of picosecond 10 *M*m pulses in multiatmosphere CO2lasers. *IEEE Journal of Quantum Electronics*, 21(3):216–232, March 1985. ISSN 0018-9197. doi: 10.1109/JQE.1985.1072638.

[20] Mikhail N. Polyanskiy, Marcus Babzien, and Igor V. Pogorelsky. BESTIA (Brookhaven Experimental Supra-Terawatt Infrared at ATF) laser: A status report. *AIP Conference Proceedings*, 1812(1):110007, March 2017. ISSN 0094-243X. doi: 10.1063/1.4975920.

Appendix A

The Fourier transform

The Fourier transform is an extremely important mathematical tool in physics, as it allows to switch between the spaces of a pair of conjugate variables. Pairs of conjugate variables are for example time and frequency (or energy), or distance and momentum. What this means in practice is that for example the Fourier transform of a signal in time shows the decomposition of this signal in frequency (in amplitude and phase), or the 2-dimensional Fourier transform of a light wave leaving a sample describes the observed interference pattern in the far field (again in amplitude and phase). See also Appendix B. The goal of this appendix is to give the definition of the Fourier transform, and explain why short pulses require broad spectra. It is by no means meant to be a complete introduction to Fourier analysis (for which plenty of undergraduate textbooks and online resources are available).

A.1 Definition of the Fourier transform

Taking as example the variables time (t) and angular frequency (ω), the Fourier transform is defined as:

$$H(\omega) = \frac{1}{\sqrt{2\pi}} \int_{-\infty}^{\infty} h(t) \mathrm{e}^{-\mathrm{i}\omega t} \mathrm{d}t \quad \text{(forward transform)} \tag{A.1}$$

$$h(t) = \frac{1}{\sqrt{2\pi}} \int_{-\infty}^{\infty} H(\omega) \mathrm{e}^{\mathrm{i}\omega t} \mathrm{d}\omega \quad \text{(inverse transform).} \tag{A.2}$$

Sometimes however it can be more convenient to use for example:

$$H(f) = \int_{-\infty}^{\infty} h(t) \mathrm{e}^{-\mathrm{i}2\pi f t} \mathrm{d}t \quad \text{(forward transform)} \tag{A.3}$$

$$h(t) = \int_{-\infty}^{\infty} H(f) \mathrm{e}^{\mathrm{i}2\pi f t} \mathrm{d}f \quad \text{(inverse transform),} \tag{A.4}$$

using $f = \omega/2\pi$ as independent variable in Fourier space.

A.2 Basic Fourier transform properties

Property	Real Space	Fourier Space
Linearity	$ah(t)+bg(t)$	$aH(\omega)+bG(\omega)$
Translation	$h(t-\tau)$	$\mathrm{e}^{-\mathrm{i}\omega\tau}H(\omega)$
Scaling	$h(at)$	$\frac{1}{\lvert a\rvert}H\left(\frac{\omega}{a}\right)$
Convolution	$h(t)*g(t)$	$H(\omega)G(\omega)$
Differentiation	$\frac{\mathrm{d}}{\mathrm{d}t}h(t)$	$\mathrm{i}\omega H(\omega)$
Integration	$\int_{-\infty}^{t} h(\tau)\mathrm{d}\tau$	$\frac{H(\omega)}{\mathrm{i}\omega}+\pi H(0)\delta(\omega)$
Energy conservation (Parseval's theorem)	$\int_{-\infty}^{\infty} \lvert h(t)\rvert^2\mathrm{d}t = \frac{1}{2\pi}\int_{-\infty}^{\infty} \lvert H(\omega)\rvert^2\mathrm{d}\omega$	
Symmetry (for h(t) real)	$H(-\omega)=H^*(\omega)$ $\mathrm{Re}\{H(\omega)\}=\mathrm{Re}\{H(-\omega)\}$ $\mathrm{Im}\{H(\omega)\}=-\mathrm{Im}\{H(-\omega)\}$ $\lvert H(\omega)\rvert=\lvert H(-\omega)\rvert$ $\arg\{H(\omega)\}=-\arg\{H(-\omega)\}$	

A.3 Uncertainty relation and why short pulses require broad spectra

If we now consider a Gaussian function in time:

$$h(t)=\frac{1}{\sqrt{\sigma}}\mathrm{e}^{-\frac{t^2}{2\sigma^2}} \tag{A.5}$$

the Fourier transform is given by:

$$H(\omega)=\sqrt{\sigma}\mathrm{e}^{-\frac{\sigma^2\omega^2}{2}} \tag{A.6}$$

which is again a Gaussian, but now in frequency space, and with a width of $\sigma_\omega=1/\sigma_t$. This is an example of the general inequality of the variances of Fourier transform pairs. In general, if f is an arbitrary probability density distribution and F its Fourier transform, then

$$\mathrm{var}(f)\mathrm{var}(F)\geq 1. \tag{A.7}$$

A profound implication of this principle is the famous Heisenberg uncertainty principle, stating that it is impossible to determine the exact position and momentum of a particle simultaneously. More relevant for the field of ultrafast optics and this thesis work, it also means that a pulse that is short in time, needs to have a broad spectrum. If equation A.5 describes the envelope of the electric field of a pulse, we can define the time-bandwidth product for a Gaussian pulse as $\sigma_t\sigma_\omega=1$. Experimentally, it is more common to look at the intensity (i.e. the square of the electric field) so $\sigma_I=\sigma/\sqrt{2}$ and to use the Full Width at Half Maximum (FWHM) so $\tau_{FWHM}=2\sqrt{2\ln 2}\sigma_I=2\sqrt{\ln 2}\sigma$. Again experimentally, it is also more convenient to use the oscillation frequency $f=\omega/2\pi$, so we can finally

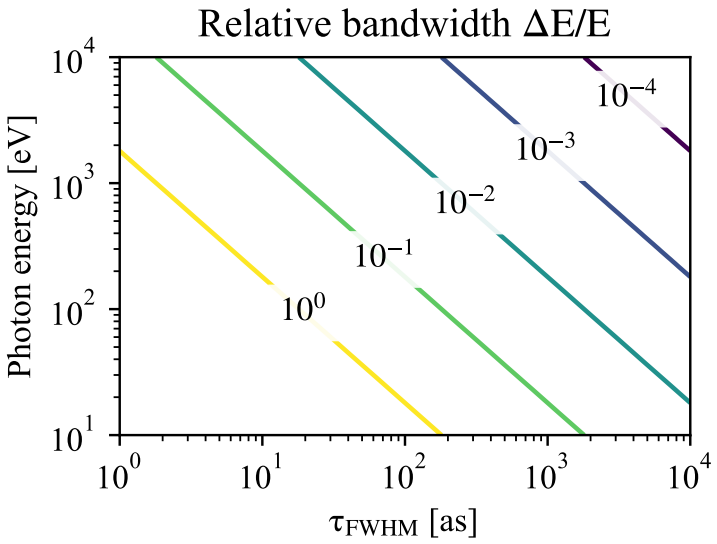

FIGURE A.1: Relative bandwidth of a gaussian pulse as a function of its Fourier-limited pulse length and the central photon energy of its spectrum. It shows how shorter pulses require broader spectra, and how this becomes easier for higher photon energies.

derive the time-bandwidth product for a gaussian pulse in experimental units:

$$\begin{aligned}\tau_{\text{FWHM}}(\Delta f)_{\text{FWHM}} &= 2\sqrt{\ln 2}\sigma_t 2\sqrt{\ln 2}\sigma_\omega/(2\pi) \\ &= 2\ln 2/\pi \approx 0.44\end{aligned} \tag{A.8}$$

which is a well-known fact in ultrafast laser physics. It is illustrative to see what this means for attoscience applications: if one wants to generate a pulse as short as 100 attoseconds (the world record is currently at 43 [1]), the bandwidth of this pulse has to be at least $0.44/10^{-16} = 4.4$ PHz or about 18 eV. In practice the spectra are much broader, as the High Harmonic Generation process inherently produces chirped pulses, and this chirp is difficult to compensate for. The higher the photon energy, the easier it is to make short pulses, as relative bandwidth decreases. This is quantified in figure A.1.

Bibliography

[1] Thomas Gaumnitz, Arohi Jain, Yoann Pertot, Martin Huppert, Inga Jordan, Fernando Ardana-Lamas, and Hans Jakob Wörner. Streaking of 43-attosecond soft-X-ray pulses generated by a passively CEP-stable mid-infrared driver. *Optics Express*, 25(22): 27506, October 2017. ISSN 1094-4087. doi: 10.1364/OE.25.027506.

Appendix B

Fraunhofer diffraction

This appendix shows the derivation of the expression for Fraunhofer diffraction starting from Maxwell's equations, based on [1].

B.1 From Maxwell to d'Alembert

The free-space Maxwell equations in SI units are given by:

$$\nabla \cdot \mathbf{E}(x,y,z,t) = 0, \tag{B.1}$$

$$\nabla \cdot \mathbf{B}(x,y,z,t) = 0, \tag{B.2}$$

$$\nabla \times \mathbf{E}(x,y,z,t) + \frac{\partial}{\partial t}\mathbf{B}(x,y,z,t) = \mathbf{0}, \tag{B.3}$$

$$\nabla \times \mathbf{B}(x,y,z,t) - \epsilon_0\mu_0\frac{\partial}{\partial t}\mathbf{E}(x,y,z,t) = \mathbf{0}, \tag{B.4}$$

where $\mathbf{E}, \mathbf{B}, \epsilon_0, \mu_0$ are the electric field, magnetic induction, electrical permittivity and magnetic permeability of free space respectively. Taking the curl of equation B.3 and making use of the vector identity:

$$\nabla \times [\nabla \times \mathbf{g}(x,y,z)] = \nabla[\nabla \cdot \mathbf{g}(x,y,z)] - \nabla^2\mathbf{g}(x,y,z), \tag{B.5}$$

we get:

$$\nabla[\nabla \cdot \mathbf{E}(x,y,z,t)] - \nabla^2\mathbf{E}(x,y,z,t) + \nabla \times \frac{\partial}{\partial t}\mathbf{B}(x,y,z,t) = \mathbf{0} \tag{B.6}$$

Applying equations B.1 and B.4 this equation reduces to:

$$\left(\epsilon_0\mu_0\frac{\partial^2}{\partial t^2} - \nabla^2\right)\mathbf{E}(x,y,z,t) = \mathbf{0} \tag{B.7}$$

which is the d'Alembert wave equation. The same can be done taking the curl of equation B.4 and applying equations B.2 and B.3 to obtain the vacuum field equation for the magnetic induction:

$$\left(\epsilon_0\mu_0\frac{\partial^2}{\partial t^2} - \nabla^2\right)\mathbf{B}(x,y,z,t) = \mathbf{0} \tag{B.8}$$

Injecting a plane wave solution $A(x,y)e^{i(kz-\omega t+\phi)}$ in d'Alembert's equation one obtains:

$$\epsilon_0\mu_0\omega^2 - k^2 = 0, \tag{B.9}$$

$$c = \frac{\omega}{k} = \frac{1}{\sqrt{\epsilon_0\omega_0}}, \tag{B.10}$$

where c is the speed of light. We can now write the d'Alembert vacuum field equations as:

$$\left(\frac{1}{c^2}\frac{\partial^2}{\partial t^2}-\nabla^2\right)\mathbf{E}(x,y,z,t)=\mathbf{0} \tag{B.11}$$

$$\left(\frac{1}{c^2}\frac{\partial^2}{\partial t^2}-\nabla^2\right)\mathbf{B}(x,y,z,t)=\mathbf{0} \tag{B.12}$$

From these equations we can conclude that each of the spatial components of the electric field and the magnetic field are uncoupled. Hence it is easy to pass from a vector description to a scalar description, in which the electromagnetic disturbance is characterized by a single scalar field $\Psi(x,y,z,t)$. Hence we can write a scalar d'Alembert equation:

$$\left(\frac{1}{c^2}\frac{\partial^2}{\partial t^2}-\nabla^2\right)\Psi(x,y,z,t)=0. \tag{B.13}$$

B.2 Helmholtz equation, free-space propagation and diffraction

By using a Fourier transform (appendix A) any scalar field $\Psi(x,y,z,t)$ can be decomposed into its spectral components $\psi_\omega(x,y,z)$:

$$\Psi(x,y,z,t)=\frac{1}{\sqrt{2\pi}}\int_{\infty}^{-\infty}\psi_\omega(x,y,z)\mathrm{e}^{\mathrm{i}\omega t}\mathrm{d}\omega. \tag{B.14}$$

Injecting this expression in the scalar d'Alembert equation yields:

$$\left(\frac{1}{c^2}\frac{\partial^2}{\partial t^2}-\nabla^2\right)\frac{1}{\sqrt{2\pi}}\int_{-\infty}^{\infty}\psi_\omega(x,y,z)\mathrm{e}^{\mathrm{i}\omega t}\mathrm{d}\omega=0 \tag{B.15}$$

$$\frac{1}{\sqrt{2\pi}}\int_{-\infty}^{\infty}\left(\nabla^2+\frac{\omega^2}{c^2}\right)\psi_\omega(x,y,z)\mathrm{e}^{\mathrm{i}\omega t}\mathrm{d}\omega=0 \tag{B.16}$$

$$\left(\nabla^2+\frac{\omega^2}{c^2}\right)\psi_\omega(x,y,z)=0 \tag{B.17}$$

$$\left(\nabla^2+k^2\right)\psi_\omega(x,y,z)=0, \tag{B.18}$$

a result which is known as the Helmholtz equation, central in scalar diffraction theory. In order to describe diffraction, we would like to consider a wave just after it has left a sample (say at $z=0$) and describe its propagation down stream (at $z=\Delta$). Between $z=0$ and $z=\Delta$ is a vacuum, such that Helmholtz' equation applies. The plane waves

$$\psi_\omega^{PW}(x,y,z)=\mathrm{e}^{\mathrm{i}(k_x x+k_y y+k_z z)} \tag{B.19}$$

are solutions to the Helmholtz equation, provided that:

$$k_x^2+k_y^2+k_z^2=k^2. \tag{B.20}$$

The elementary plane-wave solutions can now be written as:

$$\psi_\omega^{PW}(x,y,z) = e^{i(k_x x + k_y y)} e^{iz\sqrt{k^2-k_x^2-k_y^2}}. \tag{B.21}$$

This means that if $\psi_\omega^{PW}(x,y,z=0) = e^{i(k_x x+k_y y)}$, i.e. the value of the monochromatic plane wave at $z=0$ is known, the plane wave can be propagated to $z=\Delta$ by multiplication with $e^{iz\sqrt{k^2-k_x^2-k_y^2}}$. This last term is therefore also called the "free-space propagator". These plane waves can be used to synthesize any wave function ψ_ω through the inverse 2D spatial Fourier transform:

$$\psi_\omega(x,y,z=0) = \frac{1}{2\pi}\int\int \tilde{\psi}_\omega(k_x,k_y,z=0) e^{i(k_x x+k_y y)} dk_x dk_y, \tag{B.22}$$

where $\tilde{\psi}_\omega(k_x,k_y,z=0)$ is the 2D spatial Fourier transform of $\psi_\omega(x,y,z=0)$. The double integral constitutes a linear combination of plane waves $e^{i(k_x x+k_y y)}$, which is therefore itself also a solution of Helmholtz' equation. We can now propagate this wave function using the free-space propagator:

$$\psi_\omega(x,y,z=\Delta) = \frac{1}{2\pi}\int\int \tilde{\psi}_\omega(k_x,k_y,z=0) e^{i\Delta\sqrt{k^2-k_x^2-k_y^2}} e^{i(k_x x+k_y y)} dk_x dk_y. \tag{B.23}$$

This equation gives the recipe for free-space propagation and diffraction of any wave function $\Psi(x,y,z=0,t)$:

1. Decompose the wave function in its spectral components $\psi_\omega(x,y,z=0)$;
2. Compute the 2D spatial Fourier transform $\tilde{\psi}_\omega(k_x,k_y,z=0)$ for each spectral component;
3. Multiply by the free space propagator;
4. Fourier transform back;
5. Sum all spectral components $\psi_\omega(x,y,z=\Delta)$ to obtain $\Psi(x,y,z=\Delta,t)$.

B.3 Fresnel diffraction

For many applications one is only concerned with propagation of the field in the forward direction, at small scattering angles. In that case the paraxial approximation can be applied:[1]

$$\begin{aligned}\sqrt{k^2-k_x^{2-2}_y} &= k\left(1-\frac{k_x^2+k_y^2}{k^2}\right)^{\frac{1}{2}} \\ &\approx k - \frac{k_x^2+k_y^2}{2k} \qquad \text{if} \quad k_x^2+k_y^2 \ll k^2 \\ &\qquad\qquad\qquad\qquad \text{(paraxial approximation).}\end{aligned} \tag{B.24}$$

Thus the integral for Fresnel diffraction reads:

$$\psi_\omega(x,y,z=\Delta) = \frac{e^{ik\Delta}}{2\pi}\int\int \tilde{\psi}_\omega(k_x,k_y,z=0) e^{i\Delta\frac{k_x^2+k_y^2}{2k}} e^{i(k_x x+k_y y)} dk_x dk_y, \tag{B.25}$$

[1] This is a special case of the binomial approximation: $(1+x)^\alpha \approx 1+\alpha x$ for $x \ll 1$

with $e^{i\Delta\frac{k_x^2+k_y^2}{2k}}$ being the Fresnel propagator.

For the next section it is useful to change to a real-space formulation. For this, consider the following reformulation of equation B.25:

$$\psi_\omega(x,y,z=\Delta) = e^{ik\Delta}\mathscr{F}^{-1}\left\{\mathscr{F}\left[\psi_\omega(x,y,z=0)\right]e^{i\Delta\frac{k_x^2+k_y^2}{2k}}\right\} \tag{B.26}$$

$$= 2\pi\mathscr{F}^{-1}\left\{\mathscr{F}\left[\psi_\omega(x,y,z=0)\right]\frac{e^{ik\Delta}}{2\pi}e^{i\Delta\frac{k_x^2+k_y^2}{2k}}\right\} \tag{B.27}$$

where $\mathscr{F}$ denotes a 2D spatial Fourier transform and $\mathscr{F}^{-1}$ its inverse. The convolution property of the Fourier transform can be arranged in a similar way:

$$f(x,y) * g(x,y) = 2\pi\mathscr{F}^{-1}\left\{\mathscr{F}\left[f(x,y)\right]\ \mathscr{F}\left[g(x,y)\right]\right\}, \tag{B.28}$$

from which it is clear that:

$$\psi_\omega(x,y,z=\Delta) = \psi_\omega(x,y,z=0) * \frac{e^{ik\Delta}}{2\pi}\mathscr{F}^{-1}\left[e^{i\Delta\frac{k_x^2+k_y^2}{2k}}\right]. \tag{B.29}$$

To get the real-space form of the Fresnel propagator, $P(x,y,\Delta)$, the inverse Fourier transform can be performed independently for (k_x,x) and (k_y,y):

$$P(x,y,\Delta) = \frac{e^{ik\Delta}}{4\pi^2}\int_{-\infty}^{\infty} e^{i\left(k_x-\frac{\Delta}{2k}k_x^2\right)}dk_x \int_{-\infty}^{\infty} e^{i\left(k_y-\frac{\Delta}{2k}k_y^2\right)}dk_y \tag{B.30}$$

The trick in solving this integral is to use the following limit of the Fresnel integral: $\int_0^\infty e^{-i\pi x^2/2}dx = (1-i)/2 = e^{-i\pi/4}/\sqrt{2}$:

$$\int_{-\infty}^{\infty} e^{i\left(k_x x-\frac{\Delta}{2k}k_x^2\right)}dk_x = e^{i\frac{kx^2}{2\Delta}}\int_{-\infty}^{\infty} e^{-\frac{i\pi}{2}\left[\sqrt{\frac{\Delta}{\pi k}}\left(k_x-\frac{k}{\Delta}x\right)^2\right]} \tag{B.31}$$

$$= 2\sqrt{\frac{\pi k}{\Delta}}e^{i\frac{kx^2}{2\Delta}}\int_0^{\infty} e^{-\frac{i\pi}{2}\kappa^2}d\kappa, \quad \kappa = \sqrt{\frac{\Delta}{\pi k}}\left(k_x-\frac{k}{\Delta}x\right) \tag{B.32}$$

$$= \sqrt{\frac{2\pi k}{\Delta}}e^{i\left(\frac{kx^2}{2\Delta}-\frac{\pi}{4}\right)} \tag{B.33}$$

Now the Fresnel propagator can be written as:

$$P(x,y,\Delta) = \frac{e^{ik\Delta}}{4\pi^2}\frac{2\pi k}{\Delta}e^{\frac{i}{2\Delta}\left(kx^2+ky^2-\pi/2\right)} \tag{B.34}$$

$$= \frac{ike^{ik\Delta}}{2\pi}e^{\frac{ik}{2\Delta}\left(x^2+y^2\right)}. \tag{B.35}$$

Finally we arrive at the explicit, real-space formulation of Fresnel diffraction:

$$\psi_\omega(x,y,z=\Delta) = \psi_\omega(x,y,z=0) * P(x,y,\Delta) \tag{B.36}$$

$$= -\frac{\mathrm{i}k\mathrm{e}^{\mathrm{i}k\Delta}}{2\pi\Delta}\left[\psi_\omega(k_x,k_y,z=0) * \mathrm{e}^{\frac{\mathrm{i}k}{2\Delta}(x^2+y^2)}\right] \tag{B.37}$$

$$= -\frac{\mathrm{i}k\mathrm{e}^{\mathrm{i}k\Delta}}{2\pi\Delta}\int_{-\infty}^{\infty}\!\!\int \psi_\omega(x',y',z=0)\mathrm{e}^{\frac{\mathrm{i}k}{2\Delta}\left[(x-x')^2+(y-y')^2\right]}\mathrm{d}x'\mathrm{d}y' \tag{B.38}$$

$$= -\frac{\mathrm{i}k\mathrm{e}^{\mathrm{i}k\Delta}}{2\pi\Delta}\mathrm{e}^{\frac{\mathrm{i}k}{2\Delta}(x^2+y^2)}\int_{-\infty}^{\infty}\!\!\int \psi_\omega(x',y',z=0)\mathrm{e}^{\frac{\mathrm{i}k}{2\Delta}(x'^2+y'^2)}\mathrm{e}^{-i\frac{k}{\Delta}(xx'+yy')}\mathrm{d}x'\mathrm{d}y'. \tag{B.39}$$

B.4 Fraunhofer diffraction

If the detector is placed so far downstream that the diffraction pattern is completely developed we are in the so-called 'far field'. Then the expression for Fresnel diffraction can be further reduced to the case of Fraunhofer diffraction. The part of the wave field that diffracts the slowest is the part that corresponds to the largest length scale in the sample, say a. For far-field conditions to apply, the Fresnel number N_F:

$$N_F \equiv \frac{a^2}{\lambda\Delta} = \frac{ka^2}{2\pi\Delta} \tag{B.40}$$

should be well smaller than unity. x' and y' are non-zero only for values smaller than a, such that in the far-field the term $\mathrm{e}^{\frac{\mathrm{i}k}{2\Delta}(x'^2+y'^2)}$ can be neglected. The Fraunhofer diffraction integral is thus given as:

if $N_F \ll 1$:

$$\psi_\omega(x,y,z=\Delta) = -\frac{\mathrm{i}k\mathrm{e}^{\mathrm{i}k\Delta}}{2\pi\Delta}\mathrm{e}^{\frac{\mathrm{i}k}{2\Delta}(x^2+y^2)}\int_{-\infty}^{\infty}\!\!\int \psi_\omega(x',y',z=0)\mathrm{e}^{-i\frac{k}{\Delta}(xx'+yy')}\mathrm{d}x'\mathrm{d}y' \tag{B.41}$$

$$= -\frac{\mathrm{i}k\mathrm{e}^{\mathrm{i}k\Delta}}{\Delta}\mathrm{e}^{\frac{\mathrm{i}k}{2\Delta}(x^2+y^2)}\tilde{\psi}_\omega\left(k_x=\frac{kx}{\Delta},k_y=\frac{ky}{\Delta},z=0\right). \tag{B.42}$$

This can be interpreted as a (paraxial approximation to a) spherical wave originating in the sample, modulated by the 2D Fourier transform of the wave as it left the sample. When the diffraction pattern is recorded only the magnitude squared of the wave-field will be preserved, i.e. the product of the wave-field with its complex conjugate:

$$|\psi_\omega(x,y,z=\Delta)|^2 = \frac{k^2}{\Delta^2}\left|\tilde{\psi}_\omega(x,y,z=0)\right|^2 \tag{B.43}$$

Bibliography

[1] David M. Paganin. *Coherent X-Ray Optics*. Number 6 in Oxford Series on Synchrotron Radiation. Oxford University Press, Oxford, 2006. ISBN 978-0-19-856728-8.

Appendix C

Coherence

Two waves, or two parts of the same wave, are coherent if there exists a fixed phase relation between them. It is this phase relation that allows interference. Consider the addition of two general waves:

$$|\psi_1(\mathbf{r},t)+\psi_2(\mathbf{r},t)|^2 = |\psi_1(\mathbf{r},t)|^2 + |\psi_2(\mathbf{r},t)|^2 + 2\underbrace{|\psi_1(\mathbf{r},t)\psi_2(\mathbf{r},t)|}_{\text{interference term}}. \tag{C.1}$$

The cross-term, or interference term is what allows waves to interfere. If no phase relation exists between $\psi_1(\mathbf{r},t)$ and $\psi_2(\mathbf{r},t)$, the integral of this term over time drops to zero, and one is left with the incoherent sum of $\psi_1(\mathbf{r},t)$ and $\psi_2(\mathbf{r},t)$. It is coherence that makes interference possible, and giving rise to coherent diffraction. Coherence can be quantified by looking at the correlation between two waves, i.e.:

$$\Gamma_{12}(\mathbf{r_1},\mathbf{r_2},\tau) = \int_{-\infty}^{\infty} \psi_1(\mathbf{r_1},t+\tau)\psi_2^*(\mathbf{r_2},t)\mathrm{d}t \quad \text{for a pulse} \tag{C.2}$$

$$= \lim_{T\to\infty}\frac{1}{T}\int_0^T \psi_1(\mathbf{r_1},t+\tau)\psi_2^*(\mathbf{r_2},t)\mathrm{d}t \quad \text{for a continuous wave} \tag{C.3}$$

which is known as the mutual coherence function of ψ_1 and ψ_2. It can be normalized to yield the complex degree of coherence:

$$\gamma_{12}(\mathbf{r_1},\mathbf{r_2},\tau) = \frac{\Gamma_{12}(\mathbf{r_1},\mathbf{r_2},\tau)}{\sqrt{\Gamma_{11}(\mathbf{r_1},0)\Gamma_{22}(\mathbf{r_2},0)}}. \tag{C.4}$$

This allows to quantify interference in the case of partial coherence:

$$I_{tot}(\mathbf{r},\tau) = I_1 + I_2 + 2\sqrt{I_1 I_2}\Re\left\{\gamma_{12}(\mathbf{r},\tau)\right\}. \tag{C.5}$$

$|\gamma_{12}|$ can be inferred directly from the fringe visibility in an interferometer experiment. A distinction is generally made between temporal and spatial coherence, as explained in the coming sections. Common textbooks that treat coherence include [1–4].

C.1 Temporal coherence

An ideal monochromatic wave has infinite temporal coherence. In reality, perfectly coherent sources do not exist. Temporal coherence is spoiled by random jumps in phase, coming for example from spontaneous emission or thermal effects, and by changes in

the wavelength, i.e. the finite bandwidth of the source. To consider only temporal coherence is to consider the ability of a signal to interfere with itself over a time delay, i.e. $\Gamma_{11}(\mathbf{r},\tau)$ and $\gamma_{11}(\mathbf{r},\tau)$, which are also known as the first order autocorrelation and the temporal degree of coherence respectively. As an example, take a perfect plane wave $\psi(x,t) = \mathrm{e}^{\mathrm{i}(kx-\omega t)}$:

$$\Gamma_{11}(x,\tau) = \lim_{T\to\infty} \frac{1}{T} \int_0^T \mathrm{e}^{\mathrm{i}[kx-\omega(t+\tau)]} \mathrm{e}^{-\mathrm{i}(kx-\omega t)} \mathrm{d}t \tag{C.6}$$

$$= \lim_{T\to\infty} \frac{1}{T} \int_0^T \mathrm{e}^{-\mathrm{i}\omega\tau} \mathrm{d}t \tag{C.7}$$

$$= \mathrm{e}^{-\mathrm{i}\omega\tau}, \tag{C.8}$$

meaning that $|\gamma_{11}| = 1$ for all τ, so the plane wave is indeed perfectly coherent. If one takes however a pulse with a Gaussian envelope, it inherently has a certain bandwidth, and thus a limited temporal coherence. Consider the first order autocorrelation of $\psi(x,t) = \mathrm{e}^{\mathrm{i}(kx-\omega t)\mathrm{e}^{-\frac{t^2}{2\sigma_t^2}}}$:

$$\Gamma_{11}(x,\tau) = \int_{-\infty}^{\infty} \mathrm{e}^{-\mathrm{i}\omega\tau} \mathrm{e}^{-\frac{t^2+(t+\tau)^2}{2\sigma_t^2}} \tag{C.9}$$

$$= \mathrm{e}^{-\mathrm{i}\omega\tau} \mathrm{e}^{-\frac{-\tau^2}{4\sigma^2}} \int_{-\infty}^{\infty} \mathrm{e}^{-\frac{(t+\tau^2/2)^2}{\sigma_t^2}} \mathrm{d}t \tag{C.10}$$

$$= \sigma_t \sqrt{\pi} \mathrm{e}^{-\mathrm{i}\omega t - \frac{\tau^2}{4\sigma_t^2}}. \tag{C.11}$$

Hence $|\gamma_{11}(x,\tau)| = \mathrm{e}^{-\frac{\tau^2}{4\sigma_t^2}}$. The coherence function is thus also Gaussian, the wave is only partially coherent: as the time delay τ is increased, the coherence drops. The time delay for which $|\gamma_{11}(x,\tau)|$ drops below $1/\mathrm{e}$ is the coherence time, τ_{coh}. Comparing our result to the bandwidth of a Gaussian pulse (equation A.5 and onward), we see that $\tau_{coh} = \sqrt{2}\sigma_t = \sqrt{2}/\sigma_\omega$. The coherence length l_{coh} is then simply $c\tau_{coh}$. Often in literature, $l_{coh} \approx \frac{\lambda^2}{\Delta\lambda}$ is used, where $\Delta\lambda$ is the spectral bandwidth of the source in wavelength.

C.1.1 Wiener-Khinchin Theorem

The relation between the autocorrelation of a signal and its bandwidth that is illustrated in the previous section, is known as the Wiener-Khinchin Theorem. It states that the autocorrelation of a function equals the Fourier transform of the functions power spectrum:

$$\Gamma_{11}(\tau) = \int_{-\infty}^{\infty} \psi(t+\tau)\psi^*(t)\mathrm{d}t \tag{C.12}$$

$$= \int_{-\infty}^{\infty} \left[\int_{-\infty}^{\infty} \tilde{\psi}(f)\mathrm{e}^{\mathrm{i}2\pi f(t+\tau)}\mathrm{d}f\right]\left[\int_{-\infty}^{\infty} \tilde{\psi}^*(f')\mathrm{e}^{\mathrm{i}2\pi f' t}\mathrm{d}f'\right]\mathrm{d}t \tag{C.13}$$

$$= \int_{-\infty}^{\infty}\int_{-\infty}^{\infty}\int_{-\infty}^{\infty} \tilde{\psi}(f)\tilde{\psi}(f')\mathrm{e}^{\mathrm{i}2\pi(f-f')t}\mathrm{e}^{\mathrm{i}2\pi f\tau}\mathrm{d}t\mathrm{d}f'\mathrm{d}f \tag{C.14}$$

$$= \int_{-\infty}^{\infty}\int_{-\infty}^{\infty} \tilde{\psi}(f)\tilde{\psi}(f')\delta(f-f')\mathrm{e}^{\mathrm{i}2\pi f\tau}\mathrm{d}f'\mathrm{d}f \tag{C.15}$$

$$= \int_{-\infty}^{\infty} \left|\tilde{\psi}(f)\right|^2 \mathrm{e}^{\mathrm{i}2\pi f\tau}\mathrm{d}f \tag{C.16}$$

$$= \mathscr{F}^{-1}\left\{\left|\tilde{\psi}(f)\right|^2\right\}. \tag{C.17}$$

An important implication of this result is that, if random phase variations can be neglected, the coherence length depends only on the power spectrum. Adding a chirp to a Fourier limited pulse will increase its duration, but the coherence time is unaffected. The coherence time of a pulse is thus practically the same as its Fourier limited duration (up to a constant).

C.2 Spatial coherence

All practical light sources are of a finite size. Random variations in phase and wavelength between different parts of the source give rise to spatial incoherence. This is described by the mutual spatial coherence function, or mutual intensity $J(\mathbf{r_1}, \mathbf{r_2}) = \Gamma_{12}(\mathbf{r_1}, \mathbf{r_2}, 0)$. This quantity can be analyzed (on a source with good temporal coherence) by performing Young's slit experiment for different slit separations, or in more detail using a non-redundant array aperture (see e.g. [5]). Analogous to the case of temporal coherence, the slit separation for which the visibility of the interference fringes drops below 1/e corresponds to the transverse coherence length. As an example consider figure C.1: in orange it shows the interference pattern from a Young's slit experiment in the case of perfect spatial and temporal coherence. In blue the interference pattern is plotted of the same experiment, but now with limited spatial and temporal coherence. Because of limited spatial coherence of the wavefields at the two slits, the minima and maxima are reduced, even on-axis (i.e. zero path-length difference). The limited temporal coherence (in this case purely due to the finite bandwidth of the source) shows in the lateral direction, as a beating between different wavelengths.

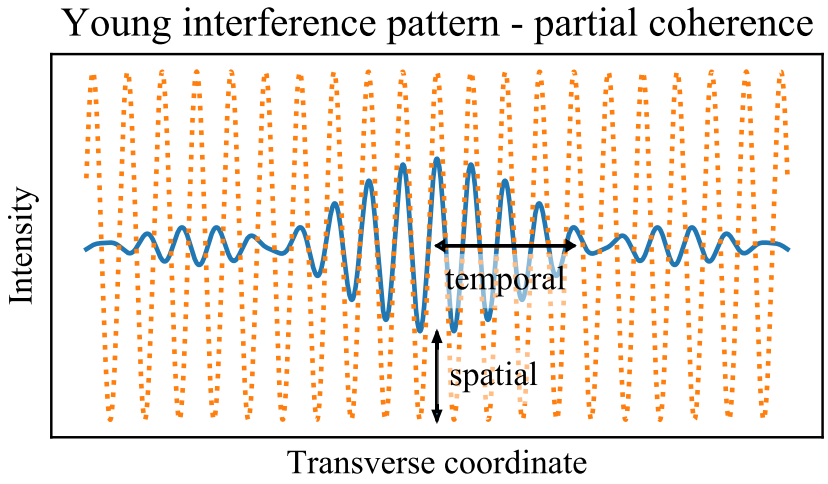

FIGURE C.1: Young's double slit experiment in the case of perfectly coherent source, plotted in orange. In blue the interference pattern in the case of limited spatial (fringe visibility) and temporal (fringe modulation) coherence.

C.2.1 Distant incoherent sources

Spatially incoherent sources can be rendered coherent by increasing the distance between the source and the sample, i.e. by decreasing the angle subtended by the finite source size and the sample. To explain this consider two mutually incoherent point sources, separated by a distance s. At large sample-detector distance z the angle between the wavevectors of the two waves incoming on the sample is s/z, see figureC.2a. Imagine the green and the red wave now hit a Young's double slit with separation d. The green wave, being itself perfectly coherent, will create a perfect cosine on the detector. Idem for the red wave. For small values of d (or small values of s/z), the green and red patterns will overlap, and the sum of the two sources will be close to that of a single coherent source. If however $d \to L$, the phase difference of the two cosines equals π (the case drawn here), the diffraction pattern is completely lost. Hence for spatially incoherent sources,

$$L \approx \frac{\lambda z}{s} \tag{C.18}$$

is often used as a measure for spatial coherence through propagation. It is a manifestation of the Van Cittert-Zernike theorem (for a formal treatment consider[1–4]). Note that although in this figure the two sources are drawn with equal wavelength, it is not necessary for the reasoning to hold.

C.3 CDI with partial coherence

These deviations from perfectly coherent radiation pose important limits on the applicability of coherent diffractive imaging techniques. CDI assumes perfect spatial and temporal coherence, which is a sometimes crude approximation to reality. For CDI with limited temporal coherence see Chapter 2. CDI with limited spatial coherence can be performed if the degree of coherence of the source has been characterized. The source radiation can then be decomposed in a number of independent spatial modes [6, 7], which themselves

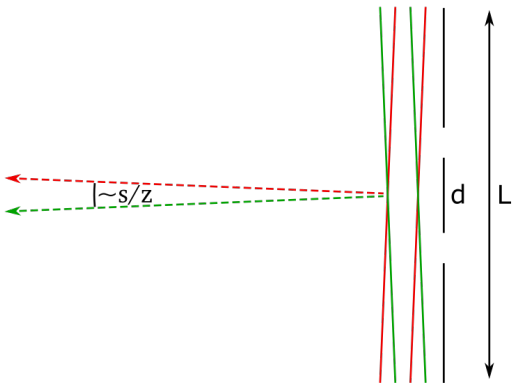

(A) Waves from two mutually incoherent point sources (green and red) separated by a distance s arrive with an angle s/z between each other. For transverse distances smaller than L they appear to be spatially coherent.

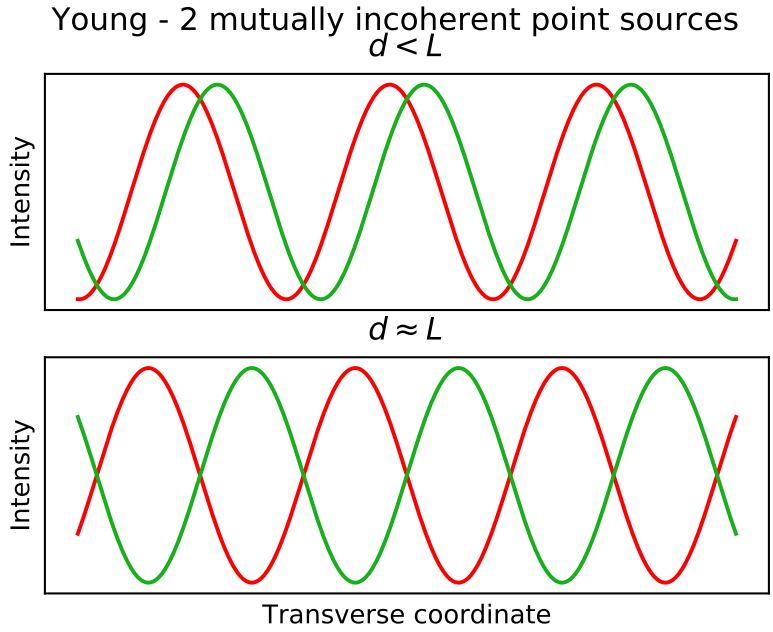

(B) The interference patterns of the two sources in case of a Young's slit experiment with slit separation $d < L$ and $d \approx L$.

FIGURE C.2: A manifestation of the Van Cittert-Zernike theorem, a spatially incoherent source can be considered spatially coherent if the source is small and far away.

are perfectly spatial coherent. See [8, 9] for the implementation. [10] treats CDI in the context of general partial coherence (both temporal and spatial).

Bibliography

[1] E. Hecht. *Optics*. Pearson Education. Addison-Wesley, 2002. ISBN 978-0-8053-8566-3.

[2] David M. Paganin. *Coherent X-Ray Optics*. Number 6 in Oxford Series on Synchrotron Radiation. Oxford University Press, Oxford, 2006. ISBN 978-0-19-856728-8.

[3] Joseph W. Goodman. *Statistical Optics*. John Wiley & Sons, April 2015. ISBN 978-1-119-00946-7.

[4] Max Born and Emil Wolf. *Principles of Optics: Electromagnetic Theory of Propagation, Interference and Diffraction of Light (7th Edition)*. Cambridge University Press, 7th edition, 1999. ISBN 978-0-521-64222-4.

[5] Aura I. González and Yobani Mejía. Nonredundant array of apertures to measure the spatial coherence in two dimensions with only one interferogram. *Journal of the Optical Society of America A*, 28(6):1107, June 2011. ISSN 1084-7529, 1520-8532. doi: 10.1364/JOSAA.28.001107.

[6] David Gauthier. *Imagerie Nanométrique Ultra-Rapide Par Diffraction Cohérente de Rayonnement Extrême-UV Produit Par Génération d'harmoniques d'ordre Élevé*. Thesis, Paris 11, February 2012.

[7] Aura Inés Gonzalez-Angarita. *Single Shot Lensless Imaging with Coherence and Wavefront Characterization of Harmonic and FEL Sources*. Thesis, Paris 11, April 2015.

[8] Garth J. Williams, Harry M. Quiney, Andrew G. Peele, and Keith A. Nugent. Coherent diffractive imaging and partial coherence. *Physical Review B*, 75(10), March 2007. ISSN 1098-0121, 1550-235X. doi: 10.1103/PhysRevB.75.104102.

[9] L. W. Whitehead, G. J. Williams, H. M. Quiney, D. J. Vine, R. A. Dilanian, S. Flewett, K. A. Nugent, A. G. Peele, E. Balaur, and I. McNulty. Diffractive Imaging Using Partially Coherent X Rays. *Physical Review Letters*, 103(24), December 2009. ISSN 0031-9007, 1079-7114. doi: 10.1103/PhysRevLett.103.243902.

[10] Bo Chen, Brian Abbey, Ruben Dilanian, Eugeniu Balaur, Grant van Riessen, Mark Junker, Chanh Q. Tran, Michael W. M. Jones, Andrew G. Peele, Ian McNulty, David J. Vine, Corey T. Putkunz, Harry M. Quiney, and Keith A. Nugent. Diffraction imaging: The limits of partial coherence. *Physical Review B*, 86(23), December 2012. ISSN 1098-0121, 1550-235X. doi: 10.1103/PhysRevB.86.235401.

Appendix D

X-ray interactions with matter

X-rays have some peculiar properties, when compared to e.g. light at optical frequencies, which is why they are so useful from a scientific point of view. This appendix introduces the relevant interactions between X-rays and matter, as well as the expression for the refractive index and the projection approximation, all relevant for this thesis. More detailed derivations can be found in e.g. [1].

D.1 Possible interactions

In X-ray matter interaction, three main mechanisms can be identified: scattering, absorption and pair production. Their corresponding cross-sections σ are plotted in figure D.1 for the case of copper, but the general behavior is the same for all elements. First thing to note is that the overall interaction decreases for increasing X-ray energy; materials become transparent for highly energetic X-rays. Secondly, at low X-ray energies absorption dominates. This is photo-electric absorption, in which the X-ray photon is absorbed by an electron. This photo-electron is then liberated from its shell, with a kinetic energy equal to the photon energy minus the electron binding energy. For the example of copper, soft X-rays up to 1 keV are absorbed by electrons from the M-shell. Above 1 keV the X-ray photon has enough energy to ionize L-shell electrons, and above 8.993 keV the K-shell becomes available. The exact location of these absorption edges is sensitive to the chemical and structural environment of the atom, giving rise to the field of X-ray absorption spectroscopy. The photo-electron leaves a vacant orbital in the atom, which will be occupied by an electron from a higher-energy orbital. The energy-loss of this electron is either emitted in the form of a photon, giving rise to fluorescence, or transferred to yet another electron which will then be ejected from the atom (this is called an Auger electron).

The second effect at low to moderate X-ray energies is scattering. Simply put, scattering can be seen as the photon 'bouncing off' of an electron. In a more accurate picture, the bound electron acts as an oscillator, that starts oscillating with the incoming wavefield. Its dipole oscillation immediately drives the re-emission of a photon. If the emitted photon has the same energy as the incoming photon, scattering is said to be coherent (compare with elastic collisions in a particle picture). If the energy of the emitted photon is different from the incoming photon the scattering is incoherent (inelastic collision). Typically the photon transfers energy to the electron: this is called Compton scattering. When the electron transfers energy to the photon one speaks of inverse Compton scattering (see also chapter 4).

It is elastic scattering that is of most interest to this thesis, as it is the interference between elastically scattered waves that gives rise to coherent diffraction.

Finally, the more exotic of these interactions is pair production, a mechanism that only occurs at extremely high photon energies: it is the conversion of a photon into an electron and a positron. The X-ray photon thus needs to have an energy of at least the

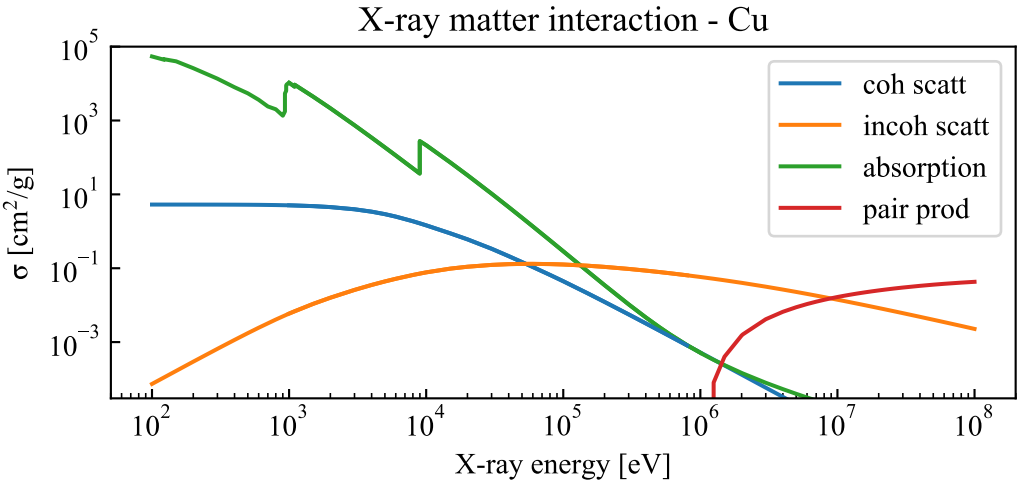

FIGURE D.1: Interaction cross-sections for scattering (coherent and incoherent), absorption and pair production as a function of X-ray energy. The values are given for the element copper, as an example. Data from [2].

sum of the rest mass energies of the electron and the positron ($2\times511\,\text{keV} = 1.022\,\text{MeV}$). It is thus not relevant for the X-ray energy levels in this thesis.

D.2 X-ray refractive index

In Appendix B the Helmholtz equation for free space propagation was derived. In the presence of matter, the Helmholtz equation reads:

$$\left(\nabla^2 + n(x,y,z)k^2\right)\psi(x,y,z) = 0, \tag{D.1}$$

where $n(x,y,z)$ is the refractive index. The effect of absorption can be taken into the refractive index through its imaginary part. Considering the plane wave solution to the Helmholtz equation:

$$\psi^{PW}(x,y,z) = \mathrm{e}^{\mathrm{i}n(x,y,z)(k_x x + k_y y + k_z z)}, \tag{D.2}$$

it is clear that the imaginary part of n causes an exponential decay of propagating field, corresponding to absorption. The real part of the refractive index is very close to unity for X-rays. It is thus customary to write the refractive index as:

$$n = 1 - \delta + \mathrm{i}\beta. \tag{D.3}$$

Figure D.2 plots the values of δ and β as a function of X-ray energy for three materials used in this thesis: silicon nitride (Si3N4), gold (Au) and tantalum nitride (TaN). The absorption edges are clearly visible.

D.3 Projection approximation

As X-rays have such a weak interaction with matter, it is common to model this interaction in the projection approximation: it assumes that the scatterers are sufficiently weak such that the wave exiting the object can be expressed in terms of the phase and amplitude shifts accumulated through the object along the straight paths that the waves would have followed in absence of matter. This assumption was also made in the simulations

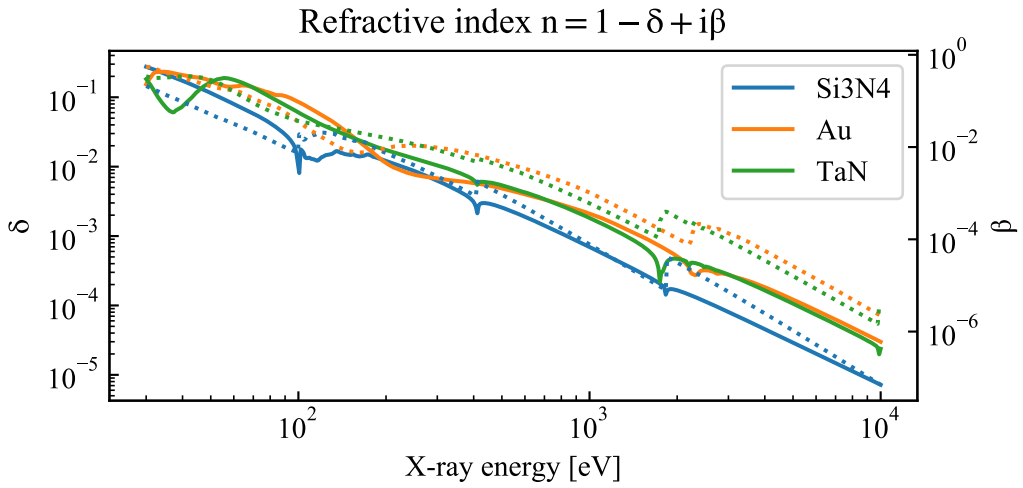

FIGURE D.2: X-ray refractive index as a function of X-ray energy for three materials used in this thesis: silicon nitride, gold and tantalum nitride. δ (left y-axis) is plotted with a solid line, β (right y-axis) is with a dotted line. Data from [3].

performed in this thesis. More formally, one can inject the Ansatz

$$\psi(x,y,z) = \xi(x,y,z)\mathrm{e}^{\mathrm{i}kz} \tag{D.4}$$

into the Helmholtz equation (D.2) to obtain

$$\left\{\nabla^2 + 2\mathrm{i}k\frac{\partial}{\partial z} + k^2\left[n^2(x,y,z) - 1\right]\right\}\xi(x,y,z) = 0. \tag{D.5}$$

To solve this differential equation it is convenient to get rid of the Laplacian: setting $\frac{\partial^2}{\partial z^2}\xi(x,y,z) = 0$ amounts to the paraxial approximation; setting $\frac{\partial}{\partial x}\xi(x,y,z) = 0$, $\frac{\partial}{\partial y}\xi(x,y,z) = 0$ amounts to the projection approximation as these are the only parts of the equation that can transmit information transversely. The resulting partial differential equation

$$\frac{\partial}{\partial z}\xi(x,y,z) \approx \frac{k}{2\mathrm{i}}\left[1 - n^2(x,y,z)\right]\xi(x,y,z) \tag{D.6}$$

is thus easily solved:

$$\xi(x,y,z = z_0) \approx \mathrm{e}^{\frac{k}{2\mathrm{i}}\int_0^{z_0}\left[1-n^2(x,y,z)\right]\mathrm{d}z}\,\xi(x,y,z = 0). \tag{D.7}$$

In addition, for small values of δ and β the quantity $1 - n^2(x,y,z)$ can be linearized, neglecting terms quadratic in δ and β to yield:

$$\xi(x,y,z = z_0) \approx \mathrm{e}^{-\mathrm{i}k\int_0^{z_0}\left[\delta(x,y,z)-\mathrm{i}\beta(x,y,z)\right]\mathrm{d}z}\,\xi(x,y,z = 0). \tag{D.8}$$

Hence, the phase shift $\Delta\phi(x,y)$ and the absorption $A(x,y)$ obtained through propagation through the sample are given by:

$$\Delta\phi(x,y,z_0) = -k\int_0^{z_0}\delta(x,y,z)\mathrm{d}z \tag{D.9}$$

$$A(x,y,z_0) = 1-\mathrm{e}^{-2k\int_0^{z_0}\beta(x,y,z)\mathrm{d}z}. \tag{D.10}$$

When $\Delta\phi \ll 1$ and $A \ll 1$ the object is said to be *optically thin*.

D.4 The first Born approximation

Rather than the macroscopic description of matter employed in the previous section, it is sometimes desirable to model matter as a sum of individual scatterers. This is done for example in the diffraction simulation code *Condor* [4], used in Chapter 4.Then, the weakly interacting property of X-rays is used in the single-scattering approximation, also known as the kinematic or first-Born approximation. If we write the outgoing wave as the sum of the incoming and scattered wave, where the scattered wave is an integral over all scatterers in the sample volume V we obtain:

$$\psi_{out} = \psi_{in} + \psi_{scatt} \tag{D.11}$$

$$= \psi_{in} + \iiint_V \phi(\mathbf{x}')\psi_{out}(\mathbf{x}')\frac{\mathrm{e}^{\mathrm{i}k|\mathbf{x}-\mathbf{x}'|}}{|\mathbf{x}-\mathbf{x}'|}\mathrm{d}\mathbf{x}' \tag{D.12}$$

Here $\phi(\mathbf{x}') = -\frac{k^2}{4\pi}\left[1-n^2(\mathbf{x})\right]$ is the scattering potential. Note that this is not an explicit expression for ψ_{out}, as the scattered wave itself depends on the outgoing wave. The first Born approximation consists in setting $\psi_{out}(\mathbf{x}') = \psi_{in}(\mathbf{x}')$, with $\psi_{in}(\mathbf{x}') = \mathrm{e}^{\mathrm{i}\mathbf{k_0}\cdot\mathbf{x}}$ a plane wave, such that

$$\psi_{out} = \mathrm{e}^{\mathrm{i}\mathbf{k_0}\cdot\mathbf{x}} - \frac{k^2}{4\pi}\iiint_V \left[1-n^2(\mathbf{x})\right]\mathrm{e}^{\mathrm{i}\mathbf{k_0}\cdot\mathbf{x}'}\frac{\mathrm{e}^{\mathrm{i}k|\mathbf{x}-\mathbf{x}'|}}{|\mathbf{x}-\mathbf{x}'|}\mathrm{d}\mathbf{x}'. \tag{D.13}$$

From this first Born approximation it is possible to arrive at the expression for Fraunhofer diffraction (Appendix B). For observation points far away from the object $\mathbf{x}' \ll \mathbf{x}$, then applying the farfield, paraxial and projection approximations (see [1] for the derivation) one arrives at:

$$\psi_{out} \approx \mathrm{e}^{\mathrm{i}\mathbf{k_0}\cdot\mathbf{x}} - \frac{k^2\mathrm{e}^{\mathrm{i}kr}}{2\pi r}\iint\int_0^{z_0}\left[\delta(x',y',z') - \mathrm{i}\beta(x',y',z')\right]\mathrm{d}z'\mathrm{e}^{-\mathrm{i}(\Delta k_x x' + \Delta k_y y')}\mathrm{d}x'\mathrm{d}y'. \tag{D.14}$$

The first term corresponds to the direct beam in the center of the diffraction pattern.

Bibliography

[1] David M. Paganin. *Coherent X-Ray Optics*. Number 6 in Oxford Series on Synchrotron Radiation. Oxford University Press, Oxford, 2006. ISBN 978-0-19-856728-8.

[2] W. T. Elam, B. D. Ravel, and J. R. Sieber. A new atomic database for X-ray spectroscopic calculations. *Radiation Physics and Chemistry*, 63(2):121–128, February 2002. ISSN 0969-806X. doi: 10.1016/S0969-806X(01)00227-4.

[3] B. L. Henke, E. M. Gullikson, and J. C. Davis. X-Ray Interactions: Photoabsorption, Scattering, Transmission, and Reflection at E = 50-30,000 eV, Z = 1-92. *Atomic Data and Nuclear Data Tables*, 54(2):181–342, July 1993. ISSN 0092-640X. doi: 10.1006/adnd.1993.1013.

[4] Max F. Hantke, Tomas Ekeberg, and Filipe R. N. C. Maia. *Condor* : A simulation tool for flash X-ray imaging. *Journal of Applied Crystallography*, 49(4):1356–1362, August 2016. ISSN 1600-5767. doi: 10.1107/S1600576716009213.

Appendix E

Notions on non-linear optics and strong-field physics

Non-linear optics is the branch of optics that describes those phenomena that do not scale linearly with the strength of the electric field driving the phenomena. A powerful example is the polarization of a material due to an electric field $E(t)$, expressed as a power series:

$$P(t) = \epsilon_0 \left[\chi^{(1)} E(t) + \chi^{(2)} E^2(t) + \chi^{(3)} E^3(t) + ... \right], \tag{E.1}$$

where ϵ_0 is the vacuum permittivity, $\chi^{(1)}$ the linear susceptibility, and $\chi^{(2)}$ and $\chi^{(3)}$ the second and third order non-linear susceptibilities, respectively. The process of second harmonic generation (SHG), used for the FROG measurements in Chapter 7, is an example of a $\chi^{(2)}$-process and thus the electric field (intensity) of the second harmonic scales quadratically with the electric field (intensity) of the driving laser. Also the processes of difference frequency generation (DFG) and optical parametric amplification (OPA), at the heart of the laser described in the same chapter, are $\chi^{(2)}$-processes. This Appendix treats some notions of non-linear optics relevant to the work in this thesis. They are based on the standard work on non-linear optics: [1].

E.1 Non-linear index of refraction

Consider the third-order non-linear susceptibility of equation E.1, $\chi^{(3)}$. In the case of a linearly polarized, oscillating field $E(t) = \mathscr{E} \cos \omega t$, the resulting polarization $P^{(3)}(t)$ is given by:

$$P^{(3)}(t) = \epsilon_0 \left[\frac{1}{4} \chi^{(3)} \mathscr{E}^3 \cos 3\omega t + \frac{3}{4} \chi^{(3)} \mathscr{E}^3 \cos \omega t \right]. \tag{E.2}$$

The first term is the expected third harmonic generation, but the second term radiates at the frequency of the incident field. Its effect can thus be absorbed in a non-linear part of the refractive index. The total index of refraction thus becomes:

$$n = n_0 + n_2 I, \tag{E.3}$$

where n_0 is the 'normal', linear index of refraction, n_2 the non-linear part due to $\chi^{(3)}$ and I the intensity. n_2 is then given by:

$$n_2 = \frac{3}{2 n_0^2 \epsilon_0 c} \chi^{(3)}. \tag{E.4}$$

The values of n_2 for a number of gases and glass (fused silica) is given in tabel E.1.

Medium	n_2 [cm^2/W]
Helium	3.6×10^{-21}
Neon	6.5×10^{-21}
Nitrogen	7.6×10^{-20}
Argon	8.5×10^{-20}
Krypton	2.3×10^{-19}
Xenon	6.8×10^{-19}
Fused silica	3.2×10^{-16}

TABLE E.1: Nonlinear refractive index n_2 for different gases and for fused silica. Values calculated from [2].

E.2 Self-phase modulation and temporal solitons

The non-linear part of the refractive index n_2 has important effects on the propagation of intense, ultrashort pulses. For n_2 positive, its effect on a traveling wave after a distance δz is a phase shift of:

$$\Delta\Phi = -k_0 n_2 I \delta z, \tag{E.5}$$

where k_0 is the wave number in vacuum (ω_0/c). At the leading edge of a short pulse, $I(t)$ increases, so each part of the leading edge of the pulse will experience a stronger phase delay than the part before: the frequencies at the leading edge of the pulse are red-shifted. At the trailing edge of the pulse, the opposite occurs and the frequencies are blue-shifted. This phenomenon is called self-phase modulation (SPM). For a formal derivation, see e.g. [1].

The effect of SPM on an ultrashort pulse is thus a spectral broadening, where lower frequencies appear at the front of the pulse and higher frequencies appear at the back. The resulting pulse thus contains a positive chirp. If the pulse is however travelling through a medium with the right amount of anomalous (negative) dispersion (blue faster than red), then it is possible that the SPM and dispersion balance each other and the pulse propagates while maintaining the same shape in time. This is known as a temporal soliton. To describe their behavior first the description of dispersion is recalled:

$$\begin{aligned}\beta_1 &= \left(\frac{\mathrm{d}k}{\mathrm{d}\omega}\right)_{\omega=\omega_0} \\ &= \frac{1}{c}\left[n_0(\omega) + \omega\frac{\mathrm{d}n_0(\omega)}{\mathrm{d}\omega}\right]_{\omega=\omega_0} \equiv \frac{1}{v_g(\omega_0)} \qquad \text{(group delay)}\end{aligned} \tag{E.6}$$

$$\begin{aligned}\beta_2 &= \left(\frac{\mathrm{d}^2k}{\mathrm{d}\omega^2}\right)_{\omega=\omega_0} \\ &= \frac{\mathrm{d}}{\mathrm{d}\omega}\left(\frac{1}{v_g(\omega)}\right)_{\omega=\omega_0} = \left(\frac{1}{v_g^2}\frac{\mathrm{d}v_g}{\mathrm{d}\omega}\right)_{\omega=\omega_0} \qquad \text{(group delay dispersion - GDD)}\end{aligned} \tag{E.7}$$

The propagation of temporal solitons is described by a non-linear Schrödinger equation [1, 3–5]:

$$\mathrm{i}\frac{\partial U}{\partial \xi} + \frac{1}{2}\frac{\partial^2 U}{\partial \tau^2} + N^2|U|^2U = 0, \tag{E.8}$$

with the introduction of a number of dimensionless parameters:

$$\gamma = \frac{\omega_0 n_2(\omega_0)}{cA_{eff}} \qquad \text{(SPM coefficient)} \tag{E.9}$$

$$T = t - \frac{z}{v_g} = t - \beta_1. \qquad \text{(retarded time)} \tag{E.10}$$

$$U = \frac{A}{\sqrt{P_0}} \qquad \text{(normalized field amplitude)} \tag{E.11}$$

$$\xi = \frac{z}{L_D} \qquad \text{(normalized coordinate of propagation)} \tag{E.12}$$

$$L_D = \frac{T_0^2}{|\beta_2|} \qquad \text{(dispersion length)} \tag{E.13}$$

$$\tau = \frac{T}{T_0} \qquad \text{(normalized retarded time)} \tag{E.14}$$

$$N^2 = \frac{L_D}{L_{NL}} = \frac{\gamma P_0 T_0^2}{|\beta_2|} \qquad \text{(soliton order squared)} \tag{E.15}$$

$$L_{NL} = (\gamma P_0)^{-1} \qquad \text{(nonlinear length)} \tag{E.16}$$

where A_{eff}, P_0, T_0 are the effective mode area, peak power and original pulse length respectively. For $N = 1$, the solution is given by:

$$U(\xi, \tau) = \eta \,\mathrm{sech}\,(\eta\tau) \mathrm{e}^{\mathrm{i}\eta^2\xi/2}. \tag{E.17}$$

Here, η is an arbitrary scaling parameter, that shows how, for given amount of dispersion and SPM, the soliton width is inversely proportional to its amplitude. It is clear from equation E.2 that only the phase of the pulse changes during propagation, its shape and spectrum remains constant. This solution for $N = 1$ is called a fundamental soliton. The peak power required to form a fundamental soliton is $P_0 = |\beta_2|/(\gamma T_0^2)$. Perturbation simulations [3] show that the soliton is very stable: if the input pulse does not exactly match the shape of equation E.2, the pulse will adjust its shape and width to a fundamental soliton as long as the input pulse is bell-shaped and $0.5 < N < 1.5$. Excess energy of the pulse will be shed in the form of dispersive waves.

For higher (integer) values of N, higher order solitons are formed. These are superpositions of soliton-like waves, with a peak power of N^2 times that of the fundamental soliton. High order solitons do change shape and spectrum upon propagation, but in a periodic manner with a soliton period z_0:

$$z_0 = \frac{\pi}{2} L_D = \frac{\pi T_0^2}{2|\beta_2|} \approx \frac{T_{FWHM}^2}{2|\beta_2|}. \tag{E.18}$$

Figure E.1 shows the temporal and spectral evolution of a soliton of order 3. At the start of the propagation SPM dominates, broadening the spectrum. As the dispersion 'catches up' the pulse is contracted in time (except for the wings of the pulse, where the intensity is too low for SPM). Propagating further the soliton breaks up, then recombines to the inital shape and one period of the process is completed. The first quarter of this process can be used to compress ultrashort pulses in fibers, as in Chapters 6 and 7. Another application is supercontinuum generation (used as a broadband source in Chapter 3): a femtosecond pulse is launched into a highly nonlinear fiber with a peak power such that $N \gtrsim 10$ and an extremely broad spectrum is generated (these solitons typically break up due to third-order dispersion, neglected in the treatment above).

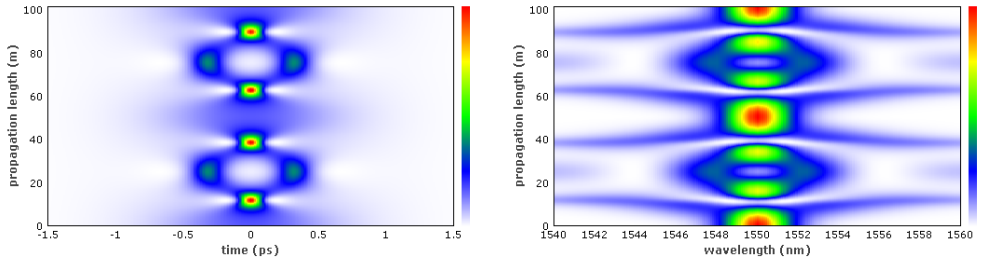

(A) Evolution of the optical power of a soliton of order 3.

(B) Evolution of the power spectral density of a soliton of order 3.

FIGURE E.1: Temporal and spectral evolution of a third order soliton. Taken from [6].

E.3 Quiver motion of a free electron in a laser field

Consider a free electron in an oscillating electric field, $\mathbf{E}(t) = E_x(t)\mathbf{x}$ with:

$$E_x(t) = \mathscr{E} \cos \omega t. \tag{E.19}$$

The equation of motion for the electron is then given by:

$$m\ddot{x} = -e\mathscr{E} \cos \omega t, \tag{E.20}$$

where e is the charge of the electron. For an electron initially at rest, the solution is given by:

$$\dot{x} = -\frac{e\mathscr{E}}{m_e \omega^2} \sin \omega t \tag{E.21}$$

$$x = \frac{e\mathscr{E}}{m_e \omega} \cos \omega t. \tag{E.22}$$

The kinetic energy K of this quiver motion is given by:

$$K = \frac{1}{2} m_e < \dot{x}^2 > \tag{E.23}$$

$$= \frac{e^2 \mathscr{E}^2}{4 m_e \omega^2}. \tag{E.24}$$

This kinetic energy is also called the 'ponderomotive potential' U_P and is an important figure of merit in e.g. high harmonic generation (Chapter 6):

$$U_P = \frac{e^2 \mathscr{E}^2}{4 m_e \omega^2} \tag{E.25}$$

$$= \left(\frac{e^2}{8\pi^2 \epsilon_0 m_e c^3} \right) I \lambda^2, \tag{E.26}$$

where I is the laser intensity and λ the laser wavelength.

In this derivation the effect of the magnetic field of the laser has been neglected. The strength of the magnetic field is given by $B_y = E_x/c$. For the Lorentz force $ev_e \times B_y$ to have an effect comparable to the force of the electric field eE_x, the electron velocity v_e will need to approach c. Thus only when the quiver motion becomes relativistic does the influence of the B-field become appreciable. This is the case when the ponderomotive

potential becomes comparable to the electron rest mass energy, or the ratio a:

$$a = \sqrt{\frac{U_p}{m_e c^2}} \tag{E.27}$$

close to 1. For $\lambda = 800$ nm (the wavelength of the wide-spread Ti-Sapph technology) this corresponds to an intensity of 9×10^{18} W/cm^2. For $\lambda = 3.1\,\mu$m (used in this thesis work) this corresponds to 6×10^{17} W/cm^2. For the intensity regimes in this thesis (and most cases of high harmonic generation) it is thus safe to neglect the influence of the B-field.

E.4 Strong-field physics: Keldysh parameter and ADK model

This appendix is concluded with some notions on strong-field physics. As mentioned in chapter 6, when an atom is in a strong laser field, two ionization mechanisms are identified: multiphoton ionization (MPI) and tunnel ionization[1]. In order to distinguish between the two regimes, Keldysh introduced the adiabaticity parameter γ [7]:

$$\gamma = \sqrt{\frac{I_p}{2Up}} = \frac{2\tau_T}{\tau_L} \tag{E.28}$$

where I_p is the atoms ionization potential and U_p is the ponderomotive potential introduced in the previous section. It is the ratio between the tunneling time of the electron and half a period of the laser, i.e. the time it *takes* the electron to tunnel divided by the time it *has* to do so. $\gamma \gg 1$ is the regime for MPI, as the electron does not have time to tunnel, whereas $\gamma \ll 1$ is the tunneling or quasi-static regime, where the tunneling time τ_T is short compared to the laser period. Hence, at constant laser intensity, increasing the wavelength decreases γ, thus favoring tunnel ionization.

Often one is interested in calculating the amount of ionization induced by a laser pulse (for example in Chapters 6 and 7). The ionization rate can be calculated by the Perelomov, Popov and Terent'ev (PPT) model [8, 9], for arbitrary values of γ. In the tunnel ionization regime, this calculation reduces to the (simpler) ADK model [9, 10]. The ionization rate (ionization probability per unit time) w_{ADK} is given by:

$$w_{ADK} = |C_{n^*l^*}|^2 \, G_{lm} I_p \left(\frac{2F_0}{F}\right)^{2n^* - |m| - 1} \mathrm{e}^{-\frac{2F_0}{3F}} \tag{E.29}$$

with

$$n^* = \frac{1}{\sqrt{2I_p}} \qquad \text{(effective quantum number } n\text{)} \tag{E.30}$$

$$l^* = n_0^* - 1 \qquad \text{(effective quantum number } l\text{)} \tag{E.31}$$

$$|C_{n^*l^*}|^2 = \frac{2^{2n^*}}{(n^* + l^* + 1)!\,(n^* - l^*)} \qquad \text{(Hartree-Fock asymptotic parameter)} \tag{E.32}$$

$$G_{lm} = \frac{(2l+1)(l+|m|)!}{2^{|m|}|m|!\,(l-|m|)!} \tag{E.33}$$

$$F_0 = (2I_p)^{3/2} \qquad \text{(Coulomb field)} \tag{E.34}$$

[1] For very strong fields, the atomic potential barrier disappears completely and a third mechanism comes into play, called Barrier Suppression.

Gas	F_0	n^*	l^*	l	m	$\lvert C_{n^*l^*}\rvert^2$	G_{lm}
Helium	2.42946	0.74387	-0.25613	0	0	4.25575	1
Neon	1.99547	0.7943	-0.2057	1	0	4.24355	3
Argon	1.24665	0.92915	-0.07085	1	0	4.11564	3
Krypton	1.04375	0.98583	-0.01417	1	0	4.02548	3
Xenon	0.84187	1.05906	0.05906	1	0	3.88241	3

TABLE E.2: Values of the ADK coefficients for noble gases. Values taken from [9].

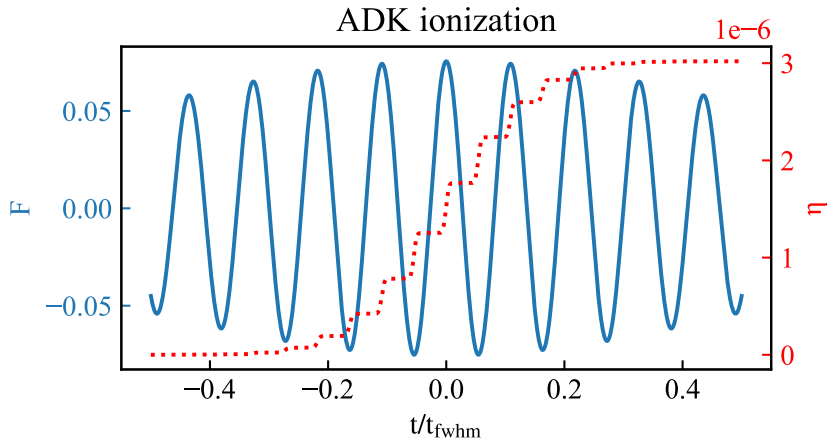

FIGURE E.2: On axis ionization fraction η calculated using the ADK model.

Here n, l, m are the principal, azimuthal and magnetic quantum number of the atom and I_p, F are the ionization potential and the instantaneous electric field strength, respectively. Atomic units are used, so:

$$I_p = \frac{I_p\ [\text{eV}]}{2 \times 13.6} \tag{E.35}$$

$$F = \frac{E\ [\text{V/m}]}{5.14 \times 10^{11}} \tag{E.36}$$

and w_{ADK} gives the ionization probability per atomic unit of time, i.e. 24.2 as. Although typically $\gamma \ll 1$ is stated as criterium for the validity of the ADK model, [11] shows that the model is reasonably accurate up to $\gamma \approx 0.5$. Table E.2 shows values of the ADK coefficients for noble gases. For fields that are small compared to the Coulomb field, i.e. $F \ll F_0$, the contribution of levels with nonzero m can be neglected, so only values for $m = 0$ are given.

Figure E.2 shows the on axis degree of ionization η for a 95 fs pulse at 3.1 µm wavelength and a peak intensity of 2×10^{14} W/cm^2 in helium, as calculated to produce figure 6.5. With these parameters, $\gamma = 0.26$. Note that at a wavelength of 800 nm for the same peak intensity $\gamma = 1.0$, so use of the ADK model would be invalid.

Bibliography

[1] Robert W. Boyd. *Nonlinear Optics, Third Edition*. Academic Press, Inc., Orlando, FL, USA, 3rd edition, 2008. ISBN 978-0-12-369470-6.

[2] H. J. Lehmeier, W. Leupacher, and A. Penzkofer. Nonresonant third order hyperpolarizability of rare gases and N2 determined by third harmonic generation. *Optics Communications*, 56(1):67–72, November 1985. ISSN 0030-4018. doi: 10.1016/0030-4018(85)90069-0.

[3] Govind Agrawal. *Nonlinear Fiber Optics*. Academic Press, 2007. ISBN 978-0-12-369516-1.

[4] Govind Agrawal. *Applications of Nonlinear Fiber Optics*. Academic Press, March 2008. ISBN 978-0-12-374302-2.

[5] Govind P. Agrawal. Nonlinear fiber optics: Its history and recent progress [Invited]. *JOSA B*, 28(12):A1–A10, December 2011. ISSN 1520-8540. doi: 10.1364/JOSAB.28.0000A1.

[6] R. Paschotta. Higher-order solitons. https://www.rp-photonics.com/higher_order_solitons.html.

[7] L. V. Keldysh. Ionization in the field of a strong electromagnetic wave. *Sov. Phys. JETP*, 20(5):1307–1314, 1965.

[8] A. M. Perelomov, V. S. Popov, and M. V. Terent'ev. Ionization of Atoms in an Alternating Electric Field. *Soviet Journal of Experimental and Theoretical Physics*, 23:924, November 1966. ISSN 1063-7761.

[9] Zenghu Chang. *Fundamentals of Attosecond Optics*. CRC Press, Boca Raton, Fla., 2011. ISBN 978-1-4200-8938-7. OCLC: 798923668.

[10] Maxim V. Ammosov, Nikolai B. Delone, and Vladimir P. Krainov. Tunnel Ionization Of Complex Atoms And Atomic Ions In Electromagnetic Field. In *High Intensity Laser Processes*, volume 664, pages 138–141, October 1986. doi: 10.1117/12.938695.

[11] F. A. Ilkov, J. E. Decker, and S. L. Chin. Ionization of atoms in the tunnelling regime with experimental evidence using Hg atoms. *Journal of Physics B: Atomic, Molecular and Optical Physics*, 25(19):4005–4020, October 1992. ISSN 0953-4075. doi: 10.1088/0953-4075/25/19/011.

université PARIS-SACLAY | ÉCOLE DOCTORALE Ondes et Matière (EDOM)

Titre : Imagerie par diffraction cohérente des rayons X en large bande spectrale et développements vers une source harmonique au keV pompée par laser moyen-infrarouge à haut taux de répétition.

Mots clés : génération d'harmoniques d'ordre élevé, rayons X, imagerie par diffraction cohérente, large bande spectrale, force ponderomotrice

Résumé : Des sources laser novatrices basées sur la génération d'harmoniques d'ordre élevé permettent de sonder la matière aux échelles de temps propres aux dynamiques électroniques. Basées sur l'émission d'impulsions attosecondes de rayonnement XUV et X cohérent, ces sources offriront la possibilité de combiner une résolution spatiale au nanomètre avec une résolution temporelle à l'attoseconde. Or, deux défis restent à relever, qui sont chacun adressés dans ce travail de thèse. Premièrement, le rayonnement de ces sources doit être étendu vers les rayons X durs tout en augmentent leur brillance. À cet effet des expériences de génération d'harmoniques ont été réalisées sur un laser OPCPA à une longueur d'onde de 3.1 µm et un taux de répétition de 160 kHz. Plusieurs configurations ont été explorées, dont une particulièrement novatrice regroupant la compression solitonique et la génération d'harmoniques dans une même fibre. Les premiers résultats sont présentés. Deuxièmement, les techniques d'imagerie doivent être adaptées à l'importante largeur spectrale intrinsèque à ces impulsions attosecondes. Une solution innovante en imagerie sans lentille est présentée sous la forme d'une monochromatisation numérique des figures de diffraction large bande. Cette étape dépend uniquement du spectre et de la supposition d'un échantillon spatialement non-dispersif. Combinant simulations et expériences, dans les domaines du visible et des rayons X durs, la méthode est validée pour des largeurs spectrales supérieures à 10 %, compatible avec l'imagerie nanométrique et attoseconde sur les futures sources harmoniques laser.

Title : Broadband Coherent X-ray Diffractive Imaging and Developments towards a High Repetition Rate mid-IR driven keV High Harmonic Source

Keywords : high harmonic generation, X-rays, coherent diffractive imaging, broadband, ponderomotive scaling

Abstract : Novel laser sources based on high order harmonic generation allow measuring dynamics in matter on the natural time scale of electrons. Based on the emission of attosecond pulses of coherent XUV and X-ray radiation, these sources should in principle lead to attosecond temporal resolution combined with nanometer spatial resolution. However, two challenges are yet to be met, both of which are addressed in this thesis. Firstly, the sources need to be extended to the (hard) X-ray regime, while simultaneously increasing their brightness. To this end, high harmonic generation was attempted with an OPCPA driver laser at 3.1 µm wavelength and 160 kHz repetition rate. Several combines soliton compression and high harmonic generation in a single fiber. First results are presented. Secondly, imaging techniques need to be adapted to the large spectral bandwidth inherent to these attosecond pulses. A novel solution is presented in lensless imaging in the form of a numerical monochromatization of the broadband diffraction patterns. This step depends solely on the spectrum and on the assumption of a spatially non-dispersive sample. Through simulations and experiments, both using visible and hard X-ray radiation, the method is shown to work with bandwidths well over 10 %, compatible with attosecond nanometric imaging on high harmonic sources.

Université Paris-Saclay
Espace Technologique / Immeuble Discovery
Route de l'Orme aux Merisiers RD 128 / 91190 Saint-Aubin, France